



TECHNISCHE
UNIVERSITÄT
DARMSTADT

Multifrequency atomic force microscopy for the in-plane and out-of-plane nanomechanical characterization of graphitic surfaces

Dissertation zur Erlangung des akademischen Grades: Doctor rerum naturalium (Dr. rer. nat.)

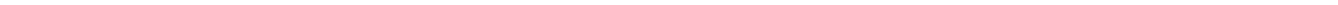
Genehmigte Dissertation von Anna Lisa Eichhorn (M.Sc.) aus Bad Homburg v. d. H.

1. Gutachten: Priv.-Doz. Dr. Christian Dietz
2. Gutachten: Prof. Dr. Regine von Klitzing

Fachbereich Material- und Geowissenschaften

Fachgebiet Physics of Surfaces

Darmstadt 2023



“Multifrequency atomic force microscopy for the in-plane and out-of-plane nanomechanical characterization of graphitic surfaces”

Zur Erlangung des Grades: Doctor rerum naturalium (Dr. rer. nat.)

Genehmigte Dissertation von Anna Lisa Eichhorn (M.Sc.) aus Bad Homburg v. d. H.

Tag der Einreichung: 17.02.2023

Tag der Prüfung: 05.05.2023

1. Gutachten: Priv.-Doz. Dr. Christian Dietz
2. Gutachten: Prof. Dr. Regine von Klitzing

Darmstadt, Technische Universität Darmstadt
Fachbereich Material- und Geowissenschaften
Fachgebiet Physics of Surfaces

Jahr der Veröffentlichung der Dissertation auf TUPrints: 2023

Bitte zitieren Sie dieses Dokument als/Please cite this document as:

URI: <https://tuprints.ulb.tu-darmstadt.de/id/eprint/23856>

URN: <urn:nbn:de:tuda-tuprints-238563>

Dieses Dokument wird bereitgestellt von TUPrints, E-Publishing-Service der TU Darmstadt

<http://tuprints.ulb.tu-darmstadt.de>

tuprints@ulb.tu-darmstadt.de

Diese Arbeit ist urheberrechtlich geschützt.

<http://rightsstatements.org/vocab/InC/1.0/>

This work is protected by copyright.

<http://rightsstatements.org/vocab/InC/1.0/>



Abstract

Graphene is considered as one of the most promising materials for numerous applications such as electronics, photonics, membranes, sensors, heat dissipators, lubricants and many more [1, 2]. In addition to its outstanding electronic properties, in particular, the extraordinary mechanical properties of graphene have become the focus of scientific attention. For example, it has been shown that defect-free graphene has an enormously high Young's modulus of about 1 TPa [3]. However, little research has been done on the local influence of defects on the nanomechanical properties of graphene. Several challenges come to mind as possible reasons, such as (i) imaging graphene with atomic resolution, (ii) simultaneous analysis of sample properties parallel and perpendicular to the sample plane, (iii) preparation of adsorbate-free graphene samples, and (iv) targeted introduction of defects.

To overcome the aforementioned challenges, first, an atomic force microscopy-based method was developed within this work that enables imaging of graphene in air under ambient conditions with atomic resolution. In addition, the method was designed to allow quantification of interaction forces, both, perpendicular and parallel to the graphene surface. This is particularly important to access the complete set of elastic constants of graphene. An important finding of this work is that different adsorbate types could be observed on the graphene surface shortly after the preparation of graphene samples. Therefore, a detailed analysis of the adsorbates was performed using the developed multifrequency atomic force microscopy method. Furthermore, the extent to which oxygen-plasma treatment can be used to remove adsorbates from a graphene sample stored under laboratory air conditions was examined. Adsorbate removal is a basic requirement for the targeted introduction of defects, as well as for the investigation of their influence on the local nanomechanical properties. The effect of oxygen-plasma treatment on different graphene-/graphite-samples was additionally investigated by Raman spectroscopy.

Kurzbeschreibung

Graphen gilt als eines der vielversprechendsten Materialien für zahlreiche Anwendungsbereiche wie z.B. für Elektronik, Photonik, Membranen, Sensoren, Wärmeableiter, Schmiermittel und viele mehr [1, 2]. Neben den besonderen elektronischen Eigenschaften, sind insbesondere auch die außergewöhnlichen mechanischen Eigenschaften von Graphen in den Fokus der Wissenschaft gerückt. So konnte beispielsweise gezeigt werden, dass defektfreies Graphen ein enorm hohes Elastizitätsmodul von etwa 1 TPa [3] aufweist. Wenig erforscht ist allerdings der lokale Einfluss von Defekten auf die nanomechanischen Eigenschaften von Graphen. Als mögliche Ursache für dieses Defizit kommen damit verbundene Herausforderungen in Frage wie z.B. (i) die Abbildung von Graphen mit atomarer Auflösung, (ii) die gleichzeitige Analyse von Probeneigenschaften parallel und senkrecht zur Probenebene, (iii) die Herstellung adsorbatfreier Graphenproben, sowie (iv) das gezielte Einbringen von Defekten.

Um die genannten Herausforderungen zu überwinden, wurde im Rahmen dieser Arbeit zunächst eine Rasterkraftmikroskopie-basierte Methode entwickelt, die die Abbildung von Graphen mit atomarer Auflösung an Luft unter Umgebungsbedingungen ermöglicht. Zudem wurde die Methode dahingehend entwickelt, dass eine Quantifizierung von Wechselwirkungskräften sowohl senkrecht als auch parallel zur Graphenoberfläche erfolgen kann. Dies ist insbesondere wichtig, um die Gesamtheit aller elastischen Konstanten von Graphen zugänglich zu machen. Eine wichtige Erkenntnis dieser Arbeit ist, dass bereits kurz nach der Herstellung von Graphenproben verschiedene Adsorbat-Typen auf der Graphenoberfläche beobachtet werden konnten. Deshalb erfolgte mithilfe der entwickelten multifrequenten Rasterkraftmikroskopie-Methode eine detaillierte Analyse der Adsorbate. Des Weiteren wurde überprüft, inwiefern eine Behandlung mit Sauerstoff-Plasma dazu dienen kann, eine unter Laborbedingungen gelagerte Graphenprobe von Adsorbaten zu befreien. Dies ist eine Grundvoraussetzung für das gezielte Einbringen von Defekten, sowie für die Untersuchung von deren Einfluss auf die lokalen nanomechanischen Eigenschaften. Die Auswirkung der Sauerstoff-Plasma Behandlung auf verschiedene Graphit-/Graphenproben wurde zusätzlich mittels Raman-Spektroskopie untersucht.

Contents

| | |
|---|------------|
| ERKLÄRUNG ZUR DISSERTATION | I |
| ABSTRACT | III |
| KURZBESCHREIBUNG | IV |
| 1. INTRODUCTION | 1 |
| 1.1. GRAPHENE AND GRAPHITE | 3 |
| 1.1.1. CRYSTALLOGRAPHIC STRUCTURE AND SYNTHESIS | 4 |
| 1.2. ATOMIC FORCE MICROSCOPY | 5 |
| 1.2.1. PRINCIPLES AND MODES OF OPERATION..... | 6 |
| 1.2.2. FORCES ACTING BETWEEN TIP AND SAMPLE | 9 |
| 1.2.3. DYNAMIC FORCE MICROSCOPY AND THE EQUATION OF MOTION..... | 10 |
| 1.2.4. HIGH RESOLUTION IMAGING CAPABILITY IN AMPLITUDE MODULATION AFM | 12 |
| 1.2.5. MULTIFREQUENCY ATOMIC FORCE MICROSCOPY | 15 |
| 1.2.6. IDENTIFICATION OF IN-PLANE CANTILEVER EIGENMODES FROM THERMAL NOISE SPECTRA | 17 |
| 1.3. OXYGEN-PLASMA TREATMENT | 19 |
| 1.4. RAMAN SPECTROSCOPY | 20 |
| 1.4.1. RAMAN SPECTRA OF GRAPHENE AND GRAPHITE | 21 |
| 1.5. INDIVIDUAL CONTRIBUTIONS OF AUTHORS | 24 |
| 2. SIMULTANEOUS DECONVOLUTION OF IN-PLANE AND OUT-OF-PLANE FORCES OF HOPG AT THE ATOMIC SCALE UNDER AMBIENT CONDITIONS BY MULTIFREQUENCY ATOMIC FORCE MICROSCOPY | 25 |
| 2.1. INTRODUCTION | 25 |
| 2.2. RESULTS AND DISCUSSION | 28 |
| 2.2.1. TRIMODAL IMAGING IN AMFLEX2-FMTOR1-FMFLEX3 MODE | 28 |
| 2.2.2. DYNAMIC SPECTROSCOPY IN AMFLEX2-FMTOR1-FMFLEX3 MODE..... | 29 |
| 2.2.3. FORCE RECONSTRUCTION USING SADER METHOD | 32 |
| 2.2.4. FORCE RECONSTRUCTION USING FOURIER METHOD | 36 |
| 2.2.5. FLEXURAL AND TORSIONAL EIGENMODE ANALYSIS | 38 |
| 2.2.6. APPLICATION OF FOURIER METHOD TO HOPG FREQUENCY-SHIFT IMAGES FOR IN-PLANE AND OUT-OF-PLANE FORCE RECONSTRUCTION | 40 |
| 2.3. CONCLUSION | 47 |
| 2.4. EXPERIMENTAL SECTION | 48 |
| 2.5. ACKNOWLEDGEMENTS | 49 |
| 3. TORSIONAL AND LATERAL EIGENMODE OSCILLATIONS FOR ATOMIC RESOLUTION IMAGING OF HOPG IN AIR UNDER AMBIENT CONDITIONS | 50 |
| 3.1. INTRODUCTION | 50 |
| 3.2. RESULTS AND DISCUSSION | 54 |
| 3.2.1. IMAGING CAPABILITY OF THE AMFLEX2-OLTOR1-FMLAT1 MODE FOR ATOMIC RESOLUTION | 54 |
| 3.2.2. COMPARISON OF TORSIONAL AND LATERAL FREQUENCY-SHIFT IMAGES AS A FUNCTION OF THE AMPLITUDE SETPOINTS..... | 57 |
| 3.2.3. CALCULATION OF LATERAL AND TORSIONAL FORCES | 62 |
| 3.3. CONCLUSION | 65 |
| 3.4. MATERIALS AND METHODS | 67 |
| 3.5. ACKNOWLEDGEMENTS | 68 |
| 4. IN-PLANE AND OUT-OF-PLANE INTERACTION ANALYSIS OF ADSORBATES ON MULTILAYER GRAPHENE AND GRAPHITE BY MULTIFREQUENCY ATOMIC FORCE MICROSCOPY | 69 |
| 4.1. INTRODUCTION | 69 |
| 4.2. MATERIALS AND METHODS | 72 |
| 4.3. RESULTS AND DISCUSSION | 74 |
| 4.3.1. ANALYSIS OF LARGE- AND SMALL-SCALE ADSORBATES ON A FEW-LAYER GRAPHENE-/GRAPHITE-FLAKE AFTER 14 DAYS OF STORAGE | 74 |

| | | |
|-------------|---|------------|
| 4.3.2. | ANALYSIS OF LARGE-SCALE ADSORBATES ON A FEW-LAYER GRAPHENE-/GRAPHITE-FLAKE AFTER DIFFERENT TIMES OF STORAGE UNDER LABORATORY AIR CONDITIONS AND SUBSEQUENT HEAT OR PLASMA TREATMENT | 81 |
| 4.3.3. | ANALYSIS OF FRICTION ANISOTROPY ON A FEW-LAYER GRAPHENE-/GRAPHITE-FLAKE | 84 |
| 4.4. | CONCLUSION | 89 |
| 4.5. | ACKNOWLEDGEMENT | 90 |
| 5. | ADSORBATE FORMATION/REMOVAL AND PLASMA-INDUCED EVOLUTION OF DEFECTS IN GRAPHITIC MATERIALS..... | 91 |
| 5.1. | INTRODUCTION | 91 |
| 5.2. | RESULTS AND DISCUSSION..... | 93 |
| 5.2.1. | LAYER ANALYSIS OF OXYGEN-PLASMA-TREATED FEW-LAYER GRAPHENE-/GRAPHITE-FLAKES..... | 93 |
| 5.2.2. | DEFECT ANALYSIS OF OXYGEN-PLASMA-TREATED FEW-LAYER GRAPHENE-/GRAPHITE-FLAKES..... | 96 |
| 5.2.3. | DOMAIN PATTERN FORMATION AND SUCCESSIVE REMOVAL BY OXYGEN PLASMA | 98 |
| 5.2.4. | STRIPE-LIKE ADSORBATE AND ISLAND FORMATION SUCCESSIVELY REMOVED BY OXYGEN-PLASMA TREATMENT..... | 102 |
| 5.3. | CONCLUSION | 107 |
| 5.4. | EXPERIMENTAL SECTION..... | 108 |
| 5.5. | ACKNOWLEDGEMENTS | 110 |
| 6. | SUMMARY AND OUTLOOK | 111 |
| 7. | SUPPLEMENTARY INFORMATION | 113 |
| 7.1. | SUPPLEMENTARY INFORMATION TO SECTION 2..... | 113 |
| 7.1.1. | INVERTED AFM IMAGES OF HOPG TAKEN IN AMFlex2-FMTor1-FMFlex3 MODE..... | 113 |
| 7.1.2. | CALIBRATION OF INVERSE OPTICAL LEVER SENSITIVITIES AND OSCILLATION AMPLITUDES | 113 |
| 7.1.3. | INFLUENCE OF CANTILEVER MEAN DEFLECTION IN AM-AFM USING HIGHER EIGENMODES ON ATOMIC-SCALE IMAGING OF HOPG | 115 |
| 7.1.4. | HYSTERETIC BEHAVIOR IN SPECTROSCOPIC EXPERIMENTS | 117 |
| 7.1.5. | COMPARISON OF TOPOGRAPHY, MEAN-DEFLECTION, AND THIRD-EIGENMODE FREQUENCY-SHIFT IMAGES AND CROSS SECTIONS FOR DIFFERENT THIRD-FLEXURAL-EIGENMODE AMPLITUDES | 118 |
| 7.1.6. | CALCULATION OF FORCES FROM SPECTROSCOPIC DATA..... | 120 |
| 7.1.7. | INFLUENCE OF SECOND-FLEXURAL-EIGENMODE AMPLITUDE-SETPOINT ON TORSIONAL AND THIRD-FLEXURAL FREQUENCY SHIFTS | 120 |
| 7.1.8. | CALCULATION OF FORCES FROM FREQUENCY-SHIFT IMAGES USING FOURIER METHOD FOR HIGHER EIGENMODES | 121 |
| 7.1.9. | COMPARISON OF ORIGINAL FREQUENCY-SHIFT DATA WITH FREQUENCY-SHIFT VALIDATION DATA ALONG DISTINCT CROSS SECTIONS | 123 |
| 7.2. | SUPPLEMENTARY INFORMATION TO SECTION 3..... | 126 |
| 7.2.1. | ILLUSTRATION OF IN-PLANE OSCILLATION OPTICAL DETECTION | 126 |
| 7.2.2. | ESTIMATION OF TIP-TRAJECTORY FROM IN-PLANE AND OUT-OF-PLANE DEFLECTION | 126 |
| 7.2.3. | COMPARISON OF ATOMIC RESOLUTION IMAGING ON HOPG IN THE REPULSIVE AND THE ATTRACTIVE REGIME | 128 |
| 7.2.4. | CALIBRATION OF LATERAL OSCILLATION AMPLITUDE INVERSE OPTICAL LEVER SENSITIVITY..... | 129 |
| 7.2.5. | VERTICAL AND LATERAL TIP POSITION ESTIMATED FROM DYNAMIC SPECTROSCOPY AND CONTACT MODE AFM | 132 |
| 7.2.6. | COMPARISON OF TIP TRAJECTORIES IN AMFlex2-FMLat1-FMFlex3 AND AMFlex2-FMTor1-FMFlex3 MODE | 133 |
| 7.2.7. | CALIBRATION OF INVERSE OPTICAL LEVER SENSITIVITIES AND FORCE CONSTANTS | 133 |
| 7.2.8. | COMPARISON OF RESONANCE FREQUENCIES..... | 134 |
| 7.3. | SUPPLEMENTARY INFORMATION TO SECTION 4..... | 135 |
| 7.3.1. | TEMPERATURE AND RELATIVE HUMIDITY DURING STORAGE IN LABORATORY AIR | 135 |
| 7.3.2. | WRINKLE FORMATION DURING AMFlex2-OLTor1-FMLat1-FMFlex3 IMAGING | 136 |
| 7.3.3. | REMOVAL OF LARGE-SCALE ADSORBATES ON A FEW-LAYER GRAPHENE-/GRAPHITE-FLAKE AFTER 7 DAYS OF STORAGE | 136 |
| 7.3.4. | DETERMINATION OF GRAPHENE/GRAPHITE LAYER NUMBERS..... | 139 |
| 7.3.5. | ADSORBATE FORMATION ON A FEW-LAYER GRAPHENE-/GRAPHITE-FLAKE ANALYZED IN AMFlex2-OLTor1-FMLat1-FMFlex3 MODE AFTER DIFFERENT TIMES OF STORAGE | 140 |
| 7.3.6. | ANALYSIS OF THE INFLUENCE OF OXYGEN-PLASMA TREATMENT ON FEW-LAYER GRAPHENE-/GRAPHITE-FLAKE VIA AFM..... | 141 |
| 7.3.7. | ANALYSIS OF THE INFLUENCE OF OXYGEN-PLASMA TREATMENT ON FEW-LAYER GRAPHENE-/GRAPHITE-FLAKE VIA RAMAN-SPECTROSCOPY | 142 |

| | | |
|-------------|--|------------|
| 7.3.8. | ANALYSIS OF FRICTION ANISOTROPY ON AN “AFM-CLEANED” FEW-LAYER GRAPHENE-/GRAPHITE FLAKE | 143 |
| 7.3.9. | ANALYSIS OF THIRD FLEXURAL FREQUENCY-SHIFT AND SECOND FLEXURAL PHASE IMAGES AFTER PLASMA TREATMENT, PRIOR TO AND AFTER ROTATION BY APPROXIMATELY 90° | 147 |
| 7.4. | SUPPLEMENTARY INFORMATION TO SECTION 5 | 149 |
| 7.4.1. | OXYGEN-PLASMA TREATMENT OF HOPG | 149 |
| 7.4.2. | ADSORBATE REMOVAL BY OXYGEN-PLASMA TREATMENT | 150 |
| 7.4.3. | RAMAN INTENSITY RATIOS AS A FUNCTION OF GRAPHENE/GRAPHITE LAYER THICKNESS | 151 |
| 7.4.4. | MULTIFREQUENCY AFM ANALYSIS OF LARGE-SCALE ADSORBATES AND REMOVAL BY OXYGEN-PLASMA TREATMENT | 152 |
| 7.4.5. | GRAPHENE HEIGHT AND LAYER NUMBER EVOLUTION UPON STORAGE AND PLASMA TREATMENT | 153 |
| 7.4.6. | STRIPE-LIKE AND ISLAND STRUCTURE FORMATION ON FEW-LAYER GRAPHENE/GRAPHITE | 154 |
| 8. | LIST OF FIGURES..... | 156 |
| 9. | LIST OF TABLES..... | 167 |
| 10. | LIST OF ABBREVIATIONS | 168 |
| 11. | REFERENCES | 169 |
| 12. | PUBLICATIONS | 182 |
| 13. | CURRICULUM VITAE..... | 183 |
| 14. | ACKNOWLEDGMENTS/DANKSAGUNG | 184 |



1. Introduction

The combination of imaging in air under ambient conditions and the quantification of local forces at the atomic scale is one of the major challenges to thoroughly understand the applicability of graphene-based nanomaterials and nanodevices under operation conditions. In recent years, multifrequency atomic force microscopy has evolved as a promising tool to solve such issues. Currently, most of the atomically resolved quantitative force images were reconstructed from spectroscopic mapping of flexural frequency-shift data. However, the major challenge of this approach under ambient conditions is the significant impact of thermal drift that occurs because of larger data acquisition times compared to those of standard imaging procedures. Additionally, for a sufficient understanding of the functionality of graphene-based nanomaterials, the simultaneous determination of out-of-plane and in-plane forces with atomic resolution is required. The in-plane interaction between two surfaces can cause both friction and shear. However, discriminating between the two mechanisms is a formidable task. The performance of graphene-based nanodevices operated under ambient conditions can also be strongly affected by airborne adsorbates having a high tendency to cover graphitic surfaces. High-resolution atomic force microscopy facilitates the analysis of adsorbate structures on graphene and graphite, however, the discrimination of different types of adsorbates is still a challenging task. Currently, most of the adsorbate analysis is performed by friction force microscopy or tapping mode, providing either insights into the in-plane or the out-of-plane tip-sample interactions. For a thorough understanding of the functionality of graphene-based nanomaterials and their long-term performance, the simultaneous determination of out-of-plane and in-plane interactions with high resolution is required. Additionally, oxygen-plasma treatment can be used for the controlled removal of adsorbates which form on graphene under laboratory air conditions. However, it needs to be considered that cleaning graphitic surfaces with oxygen plasma leads to the introduction of defects into the material.

In Section 2, a trimodal setup based on force microscopy which facilitates the simultaneous acquisition of topography as well as torsional and flexural frequency-shift images with atomic resolution is introduced. We successfully demonstrated the simultaneous deconvolution of in-plane and out-of-plane forces on HOPG with atomic resolution in air under ambient conditions. The approach is based on the Fourier method [4], which allows for the determination of in-plane forces from lateral frequency-shift images. We demonstrated that the Fourier method can be extended for the determination of out-of-plane forces by applying the bimodal approximation [5-7]. Strikingly, we observe significant variations in the in-plane force differences between carbon bonds and hollow sides if the tip motion caused by the torsional

oscillation is oriented in armchair (5 ± 1 pN) or zigzag direction (11 ± 2 pN). Simultaneously, we do not observe this anisotropy in the out-of-plane direction, corroborating (i) the independence of both acquisition directions and (ii) their complementary nature. Remarkably, by additionally recording the mean deflection of the cantilever, long-range attractive tip-sample interactions can be separated from short-range repulsive in- and out-of-plane forces. One of the key findings is the lift of the topmost carbon atoms of the basal plane of graphite during imaging, arising from the weak Van-der-Waals interactions between the graphene layers which has to be considered when designing multi-sheet graphene-based nanodevices.

In Section 3, different trimodal setups based on force microscopy which facilitate the simultaneous acquisition of flexural and torsional or lateral frequency-shift images with atomic resolution are compared. A method for the calibration of the lateral optical lever sensitivity based on imaging a graphene wrinkle is proposed that allowed us to interpret the lateral eigenmode observables in a quantified manner. Thus, torsional and lateral forces have been reconstructed from the corresponding frequency-shift images following an approach based on the Fourier method [4, 8]. Interestingly, we observed significant differences between the in-plane forces determined from torsional and lateral eigenmode oscillations. We found that for small lateral amplitudes a shearing interaction occurred during imaging whereas small torsional amplitudes resulted in strongly localized friction forces. The comparison of the resulting in-plane forces is a relevant contribution towards the discrimination of frictional and shear interaction at the atomic scale under ambient conditions on graphite surfaces. Moreover, imaging with combined flexural-lateral oscillations can facilitate the determination of the full set of elastic constants of graphite and graphene, as well as help to identify the effect of induced defects, which play a major role *e.g.* for the performance of graphene-based nanodevices.

In Section 4, a trimodal setup based on force microscopy was used, which facilitates the simultaneous acquisition of flexural and lateral frequency-shift and drive-amplitude images, resolving small-scale stripe-like adsorbate patterns as well as different adsorbate domains which form on a few-layer graphene-/graphite-sample after storage under laboratory air conditions. Interestingly, we observe distinguishable dissipative and conservative tip-sample interactions as well as differences between the in-plane and out-of-plane tip-sample interactions, allowing for the discrimination of different types of hydrocarbons adsorbing on a few-layer graphene-/graphite-sample. Rotation of the sample by approximately 90° revealed that friction anisotropy was only observable on certain areas of the flake which provides further information on the side group configuration of the adsorbed hydrocarbons as well as the binding of adsorbates to the graphitic surfaces. Additional information on the adsorbates was gained by heat treatment,

causing desorption of water molecules from the surface and by oxygen-plasma treatment, facilitating the removal of large amounts of hydrocarbon adsorbates. We conclude that five different types of adsorbates covered the investigated samples after 14 days of storage, where the amount of coverage increased with further duration of storage.

In Section 5, a multifrequency atomic force microscopy approach was used to simultaneously record lateral frequency-shift and drive-amplitude as well as flexural phase images of graphitic surfaces. The method facilitates the identification of the amount and types of various adsorbates at different length scales and to systematically study the ablation of graphene layers caused by oxygen-plasma treatment as well as defect evolution. The introduction of defects by oxygen-plasma treatment was additionally analyzed by Raman spectroscopy. We demonstrated that numerous adsorbate structures, such as small-scale stripe-like patterns, large-scale islands, small-scale clusters, and large-scale adsorbate domains, form on the surface of few-layer graphene-/graphite-flakes upon storage under laboratory air conditions and oxygen-plasma treatment. The different in-plane and out-of-plane as well as dissipative and conservative tip-sample interactions facilitated the identification of the origin of these adsorbate structures.

1.1. Graphene and graphite

Graphene is a single- or few-layer sheet of graphite. Since the noble price was awarded to Andre Geim and Konstantin Novoselov for their “groundbreaking experiments regarding the two-dimensional material graphene” [9] in 2010, the scientific interest in graphene was rapidly growing. In 2004, Novoselov *et al.* [10] published their invention of fabricating graphene *via* micromechanical exfoliation of graphite. Furthermore, the authors could show that few-layer graphene behaves as a semi-metal with a tiny overlap between valance and conductance band, exhibiting a strong ambipolar electric field effect when applying a gate voltage. Several further outstanding physical properties of monolayer graphene have been reported in the following years such as charge-carrier mobility at room temperature of approximately $200000 \text{ cm}^2(\text{Vs})^{-1}$ [11], optical absorbance of 2.3 % [12], thermal conductivity of approximately $5000 \text{ W}(\text{mK})^{-1}$ [13], specific surface area of $1500 \text{ m}^2\text{g}^{-1}$ [14], geometric pore size of approximately 0.64 \AA [15] and Young’s modulus of approximately 1 TPa [3]. In the presented work, the focus was on a detailed nanomechanical analysis of graphite surfaces down to the atomic level based on a multifrequency AFM approach (see Sections 2 and 3). Here, freshly cleaved highly oriented pyrolytic graphite (HOPG) was used because it turned out that graphene samples started to be

covered by adsorbates already shortly after preparation. This phenomenon was analyzed in detail in Section 4.

1.1.1. Crystallographic structure and synthesis

Graphite is well known as a three-dimensional allotrope of carbon. Due to their sp^2 -hybridization, the carbon atoms are tightly connected by σ -bonds, forming two-dimensional sheets of hexagonally arranged carbon atoms. In graphite, the carbon layers are weakly interconnected by Van-der-Waals forces based on π - π -interactions of the p-orbitals. The most stable arrangement of carbon sheets relative to each other is at a distance of 334.8 pm and in ABA configuration, also known as Bernal-stacking, which is schematically shown in Figure 1-1. Layer A (solid) and B (dotted) are shifted by the length of one carbon-carbon bond (142 pm) in x -direction, which leads to distinguishable carbon atom sides, often named α - and β -side. The differences between α - and β -side becomes clearly visible from Figure 1-1b, where the α -atoms (blue) occur every 334.8 pm and the β -atoms every 669.6 pm in z -direction. The Bernal-stacking in graphite is one of the reasons for the difficulties of imaging the true hexagonal carbon arrangement rather than only the β -atoms when using Scanning Tunneling Microscopy (STM) [16].

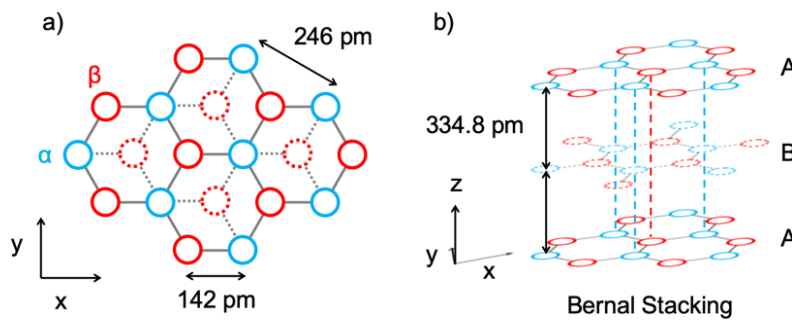


Figure 1-1: Schematic drawing of the crystallographic structure of graphite. a) Top view, b) side view.

Highly oriented pyrolytic graphite, also known as highly ordered pyrolytic graphite (HOPG), is a highly pure synthetic form of graphite which is characterized by a small mosaic spread angle between the ABA-stacked carbon layers. For the synthesis of HOPG, graphite deposited from pyrolysis of methane is subjected to defined pressure- and heat-treatment steps based on experiments of Blackman *et al.* [17]. Due to the fact that fresh and atomically flat graphite

surfaces can be easily prepared by cleaving the material with tape, HOPG is frequently used as a substrate *e.g.* for scanning probe microscopy.

Graphene is in general defined as ten or less layers of graphite. A distinction is made between mono-, bi-, tri- and few-layer graphene, featuring slightly different physical properties [18, 19]. Several different methods for the synthesis of graphene have been developed during the past years, where it is commonly distinguished between top-down (*e.g.* micromechanical exfoliation [10], liquid-phase exfoliation [20, 21]) and bottom-up approaches (*e.g.* epitaxial growth [22], chemical vapor deposition [23-25], laser-related methods [26, 27] and electric discharge [28, 29]). Although its comparably low yield, micromechanical exfoliation is still a strongly relevant method for research purposes. It combines high quality, single crystalline flakes and easy implementation without the requirement of special equipment. Additionally, micromechanical exfoliation facilitates that graphene flakes can be directly prepared on Si/SiO₂-substrates, which avoids the process of graphene transfer from different substrates [30, 31]. Due to the small optical absorbance of graphene [12], the preparation on layered substrates with defined thicknesses (*e.g.* bulk silicon with a 90 nm or 300 nm layer of silicon dioxide) is essential to provide visibility of the graphene samples under optical microscopes [32]. For the experiments shown in Section 4 and 5 of this work, graphene samples were prepared *via* micromechanical exfoliation, following the protocol of Huang *et al.* [33]. The protocol includes the following steps: Graphite flakes are applied on adhesive tape and exfoliated 3-4 times; the Si/SiO₂-substrate is cleaned *via* oxygen-plasma treatment; contact is made between the graphite decorated tape and the substrate; heating for approximately 2 min at 100 °C on a hot-plate; peeling-off the tape. The heating step was introduced in order to remove potentially present gas molecules between graphite flakes and substrate. As a consequence, the contact area between graphite and substrate becomes larger, facilitating the synthesis of more and laterally larger graphene flakes.

1.2. Atomic force microscopy

Scanning Probe Microscopy (SPM) has become strongly relevant for advanced surface analysis of various materials during the last decades. The family of SPM-techniques includes scanning tunneling microscopy (STM), scanning near-field optical microscopy (SNOM) and atomic force microscopy (AFM). All three SPM-techniques exhibit at least two common elements: (i) a sharp tip that serves as a probe and (ii) a feedback-loop-mechanism which allows not only for the detection of the surface topography but additionally facilitates the determination of a variety of different qualitative and quantitative surface and material properties. Depending on the sample

condition and the property of interest, the three SPM-techniques are differently suitable. For “their design of the scanning tunneling microscope” [34], the noble price was awarded to Gerd Binnig and Heinrich Rohrer in 1986. STM is based on sensing the tunneling current between tip and sample [35]. The method allows for ultra-high-resolution imaging down to the atomic scale; however, best results are achieved under ultra-high vacuum (UHV) conditions and both, tip and sample need to be conductive or at least semiconductive. For SNOM, the sample under investigation is analyzed by focusing a laser through the tip onto the sample, where the diameter of the aperture needs to be small compared to the laser wavelength [36, 37]. Hence, it is possible to analyze the near-field instead of the far-field properties, allowing for enhanced optical resolution. The achievable resolution additionally depends on the distance between tip and sample used for imaging. A disadvantage of SNOM is the requirement of specially designed tips. AFM is based on the detection of tip-sample forces [38]. Both, short- and long-range forces can be detected and analyzed without general restrictions to the surface material under investigation. Because we aimed for atomic resolution imaging of graphitic surfaces in air under ambient conditions, AFM was selected for the experiments presented in this work.

1.2.1. Principles and modes of operation

The basic setup for AFM includes a cantilever with an attached tip, a *x-y-z*-piezo sample stage, a controller and a detector unit for the determination of the cantilever deflection during operation. The detector unit typically consists of a detection laser, focused at the cantilever’s back end (where the tip is attached) and a segmented photodiode for the analysis of the reflected laser beam. The deflection of the cantilever is determined from the differences in the induced current between the segments of the photodiode. This detection principle not only allows for the determination of out-of-plane deflection such as required for contact mode AFM (see Figure 1-2a) but also for in-plane deflection such as analyzed in lateral force microscopy (LFM) or friction force microscopy (FFM) (see Figure 1-2b).

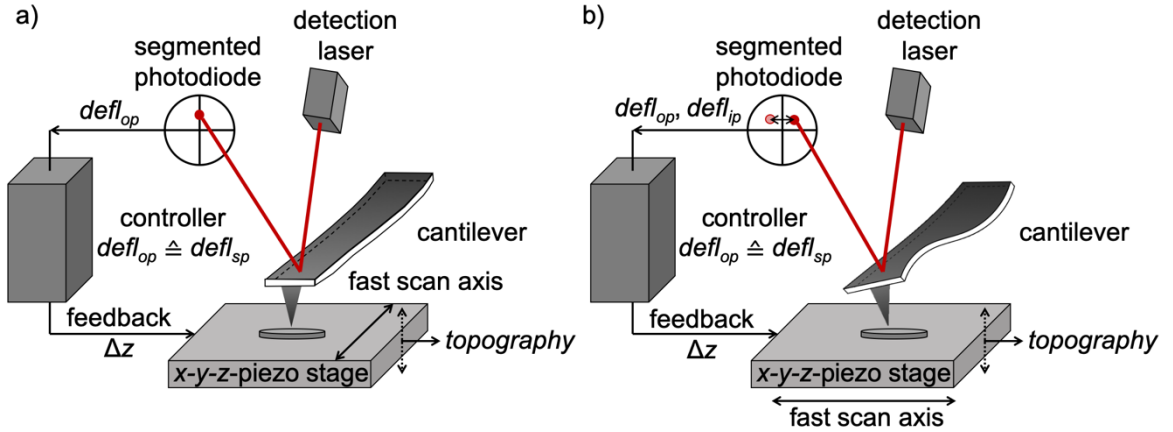


Figure 1-2: Scheme of setup for static AFM modes. a) Contact mode AFM and b) lateral force microscopy (LFM) or friction force microscopy (FFM).

Most of the AFM setups are based on feedback loops *e.g.* for the determination of the sample's topography. Therefore, at least one observable (*i.e.* the out-of-plane deflection) is used as control variable and kept constant by adjusting the z -position of either the piezo-stage or the cantilever. The match between control variable and setpoint value is analyzed within the controller. To optimize the response time for the z -feedback, the error-signal $e(t)$ (difference between control variable and setpoint value) is processed by the help of proportional (P) and integral (I) gains. The resulting actuating variable $\Delta z(t)$ is applied to the z -feedback.

$$\Delta z(t) = P e(t) + I \int e(t) dt \quad (1-1)$$

For both, contact mode AFM and LFM, the out-of-plane deflection is defined as setpoint value. However, in LFM the fast scan axis is perpendicular to the cantilever's long axis, resulting in an in-plane deflection of the cantilever. By applying Hooke's law, lateral or frictional forces (F_{ip}), corresponding to a certain out-of-plane force (F_{op}) applied, can be calculated from the in-plane deflection (δ_{ip}) if the in-plane stiffness (k_{ip}) of the cantilever is known.

$$F_{op} = k_{op} \cdot \delta_{op} \quad (1-2)$$

$$F_{ip} = k_{ip} \cdot \delta_{ip} \quad (1-3)$$

Due to the permanent tip sample contact required for static AFM, the described methods suffer from a high probability of tip and/or sample damage. Additionally, only stick-slip or hollow-side resolution can be achieved instead of true atomic resolution [39].

To overcome these limitations, different dynamic AFM modes were developed, which can be distinguished in amplitude-modulated (AM) [40, 41] and frequency-modulated (FM) modes [42]. The basic setups of AM- and FM-AFM with photothermal excitation are shown in Figure 1-3.

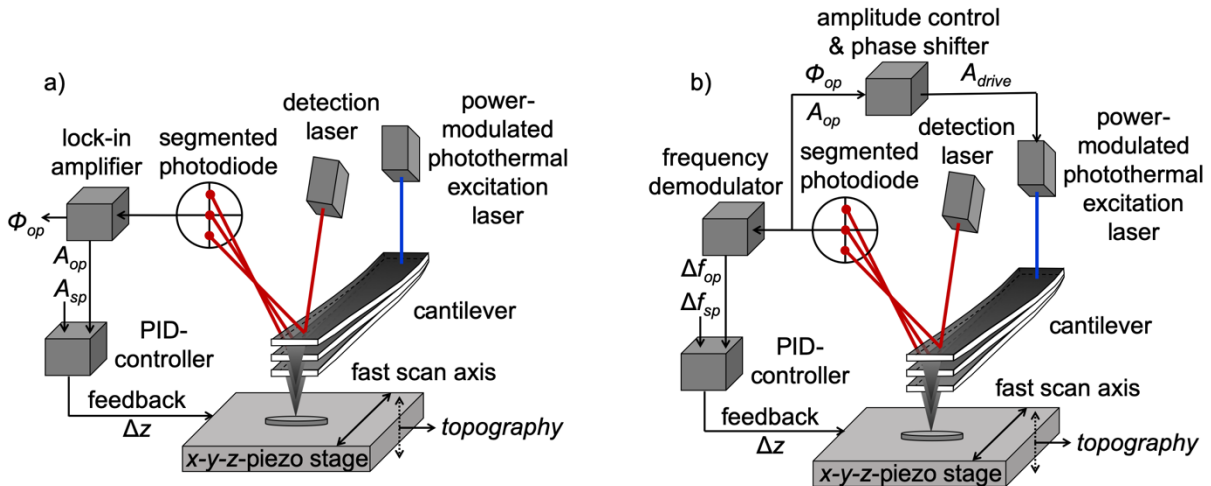


Figure 1-3: Scheme of setup for dynamic AFM modes with photothermal excitation. a) amplitude-modulated (AM) AFM and b) frequency-modulated (FM) AFM.

In contrast to static AFM, in dynamic AFM the cantilever is excited close to or at its resonance frequency, resulting either in intermittent contact or non-contact between tip and sample, depending on the distance. One possibility to excite the cantilever is based on photothermal excitation [43, 44], where a power-modulated laser is focused on the fixed end of the cantilever. The power-modulation of the laser needs to be set so that it matches the respective resonance frequency of the cantilever. If this is the case, the oscillation of the cantilever is induced by local heating of the material as a consequence of the emerging temperature gradient. An alternative and often used approach is acoustic excitation based on piezoelectric actuation [41, 45].

Both, AM- and FM-AFM are resonance techniques, however, for AM-AFM the control variable is the oscillation amplitude, whereas for FM-AFM the frequency shift of the oscillation serves as control variable. As a consequence, the setup requires slightly different components as schematically shown in Figure 1-3.

For AM-AFM (Figure 1-3a), the signal detected by the photodiode is processed by a lock-in amplifier, which provides information on the actual out-of-plane amplitude (A_{op}) and phase (Φ_{op}). The amplitude is compared to the setpoint value and the z -position of the stage or the cantilever is adjusted accordingly.

FM-AFM (Figure 1-3b) requires an additional feedback-loop, which shifts the phase to 90° in order to keep the oscillation at resonance. Therefore, the photodiode signal is on the one hand analyzed by a frequency demodulator, which provides information on the actual out-of-plane frequency shift (Δf_{op}) relative to the original resonance frequency. On the other hand, the detector signal is processed by the amplitude control and phase shifter, which keeps Φ_{op} at 90° and can additionally be used to adjust the drive amplitude (A_{drive}) e.g. for providing a constant oscillation amplitude.

1.2.2. Forces acting between tip and sample

The detection of forces acting between tip and sample is the core principle of AFM. Due to the coexistence of several attractive and repulsive forces acting in different distances between tip and sample, the interpretation of the collected data is a complex task. In air, the most essential forces can be summarized as Van-der-Waals, electrostatic and quantum mechanical forces [46]. All these forces may act attractive or repulsive, depending on the distance between tip and sample. Van-der-Waals forces arising from Keesom interaction (two freely rotating permanent dipoles) or Debye interaction (one permanent and one induced dipole) are on the average always attractive. However, the largest contribution to Van-der-Waals forces in air is the London dispersion interaction (instantaneous polarization due to fluctuations in charge distribution of a neighboring atom or molecule), which is attractive despite for very close distances where electron clouds begin to overlap [46, 47]. The Van-der-Waals force between a sphere of radius R and a flat surface separated by the distance z can be described by [48]

$$F_{vdw} = -\frac{2A_H R^2}{3z^2(z + 2R)^2}, \quad (1-4)$$

where A_H is the Hamaker constant [49], which depends, among other parameters, on the static dielectric constants and the refractive indices of the materials and the separating medium. Only in the rare case, where A_H becomes negative, repulsive Van-der-Waals forces occur [50].

Electrostatic interactions occur in the presence of ions interacting with (i) other ions, (ii) permanent or (iii) induced dipoles. In case (i) electrostatic interaction can be repulsive or attractive depending on the sign of the charging. For case (ii) and (iii) the interaction is always attractive [46, 47].

Quantum mechanical interactions include attractive forces occurring *e.g.* in chemical bonding, however, this is a rarely observed phenomenon in AFM. On the other hand, repulsive quantum mechanical interactions, resulting from steric or Born repulsion are the basis of contact mechanics models [46, 47]. Contact mechanics models allow for the calculation of elastic sample properties such as the Young's modulus and are based on different assumptions regarding the tip-sample interaction. The Hertz model assumes the sample as an isotropic and linear-elastic solid and is based on continuum-elasticity theory, neglecting the influence of adhesion between tip and sample [51]

$$F_{Hertz} = \frac{4}{3}\sqrt{RE_{eff}}\delta^{3/2}, \quad (1-5)$$

where E_{eff} is the effective Young's modulus and δ is the indentation of the tip into the sample

$$E_{eff} = \left(\frac{1 - \nu_{tip}^2}{E_{tip}} + \frac{1 - \nu_{sample}^2}{E_{sample}} \right)^{-1}, \quad (1-6)$$

and ν is the Poisson's ratio.

Derjaguin, Muller and Toporov developed the DMT model which is based on the Hertz model, however, considering a force of adhesion outside the contact area [52]. In a similar way, Johnson-Kendall-Roberts developed the JKR model which is also based on the Hertz model, but considers the adhesion within the contact area [53].

The described contact mechanics models are useful for the nanomechanical analysis of experiments accomplished *via* force-distance curves by static spectroscopy. However, as will be discussed in Sections 2.2.2 and 7.1.3, the analysis of dynamic spectroscopy data, where the cantilever oscillates while approaching and retracting from the surface, is beneficial for highly localized mechanical analysis.

1.2.3. Dynamic force microscopy and the equation of motion

The cantilever oscillation for both AM- and FM-AFM can be described by formally the same equation of motion if the tip-cantilever ensemble is assumed as a point-mass spring [54, 55]

$$m\ddot{z}(t) + \frac{m\omega_0}{Q}\dot{z}(t) + kz(t) = F_{ts}(z_c - z(t)) + F_{exc}(t), \quad (1-7)$$

where m is the mass, $z(t)$ and z_c are the instantaneous tip position and the average tip-sample distance, respectively, ω_0 is the angular resonance frequency, Q is the quality factor, k is the spring constant, F_{ts} is the force acting between tip and sample and $F_{exc}(t)$ is the excitation force. However, there is a fundamental difference between the expression of $F_{exc}(t)$ for AM- and FM-AFM

$$F_{exc,AM}(t) = kA_{exc} \cos(\omega_{exc}t), \quad (1-8)$$

$$F_{exc,FM}(t) = kA_{exc}(t) \cos(\omega_{exc}(t)t), \quad (1-9)$$

where A_{exc} and ω_{exc} are the amplitude and the angular frequency of the driving force, respectively. The key difference between the expressions is that for AM-AFM A_{exc} and ω_{exc} are constant, whereas for FM-AFM both quantities are time-dependent. Consequently, finding a solution for the equation of motion for FM-AFM is even more complicated than for AM-AFM. It is common practice to use approximations in order to find solutions for the equations of motion.

For AM-AFM, analytical solutions were found based on the assumption that no forces are acting between tip and sample ($F_{ts} = 0$). This results in the description of the system as forced harmonic oscillator with damping [56]

$$m\ddot{z}(t) + \frac{m\omega_0}{Q}\dot{z}(t) + kz(t) - kA_{exc} \cos(\omega_{exc}t) = 0. \quad (1-10)$$

Using the steady state solution

$$z(t) = A \cos(\omega t - \Phi), \quad (1-11)$$

the following expressions for amplitude $A(\omega)$ and phase shift Φ can be calculated

$$A(\omega) = \frac{kA_{exc}}{m\sqrt{(\omega_0^2 - \omega^2)^2 + \left(\frac{\omega\omega_0}{Q}\right)^2}} \quad (1-12)$$

$$\tan \Phi = \frac{\omega\omega_0}{Q(\omega_0^2 - \omega^2)}, \quad (1-13)$$

where ω_0 is the resonance frequency without damping. The previously neglected influence of the force gradient close to the sample surface acts as a weak perturbation [56]. Considering the influence of F_{ts} by a parabolic tip-sample interaction potential, the total force can be expressed as

$$F = -kz + \left(\frac{dF_{ts}}{dz} \right)_{z_0} (z - z_0), \quad (1-14)$$

in the case of small displacements from the equilibrium position. Consequently, the effective resonance frequency ω_{eff} is a function of the force gradient

$$\omega_{eff} = \sqrt{\frac{-\frac{dF}{dz}}{m}} = \sqrt{\frac{k - \frac{dF_{ts}}{dz}}{m}}. \quad (1-15)$$

For FM-AFM in constant amplitude operation one can assume that the energy losses due to damping are compensated by the external excitation energy. Hence, both related terms in equation (1-7) can be neglected

$$m\ddot{z}(t) + kz(t) - F_{ts}(z_c - z(t)) = 0. \quad (1-16)$$

Based on those assumptions, Giessibl [57] suggested the calculation of Δf via classical first-order perturbation theory, resulting in

$$\Delta f(d, k, A_0, f_0) = -\frac{1}{2\pi} \frac{f_0}{kA_0} \int_0^{2\pi} F_{ts}(d + A_0 + A_0 \cos \Phi) \cos \Phi d\Phi, \quad (1-17)$$

where d is the distance of closest approach, A_0 is the free amplitude and f_0 is the resonance frequency. Different approaches have been proposed for solving equation (1-17). The two most common methods are the Matrix method introduced by Giessibl [58] and the Sader method introduced by Sader and Jarvis [59, 60]. Another approach for the reconstruction of forces from frequency-shift data is the Fourier method [4, 61]. Details on the force reconstruction methods will be given in Section 2.2.3 and 7.1.6. For a detailed comparison of AM- and FM-AFM also refer to Garcia and Perez [62].

1.2.4. High resolution imaging capability in amplitude modulation AFM

Currently, most of the atomically resolved images are performed using FM-AFM. The main reason for that is the operability under ultra-high vacuum (UHV) conditions. To understand why an operation of AM-AFM under UHV is not possible without further ado, equation (1-18), showing the minimum frequency shift detectable in slope detection due to thermal noise ($\delta(\Delta f)$) [40, 42, 62], needs to be considered

$$\delta(\Delta f) = \delta(f - f_0) = \sqrt{\frac{f_0 k_B T B}{\pi k Q A_0^2}}, \quad (1-18)$$

where k_B is the Boltzmann constant, T is the temperature and B is the detection bandwidth, which here is the reciprocal of the response time τ . Equation (1-18) is valid for both, AM- and FM-AFM. In practice, the largest potential for detection sensitivity improvement is the quality factor which is highest under UHV conditions. However, for AM-AFM, in contrast to FM-AFM, quality factor and bandwidth are not independent of each other

$$\tau_{AM} = \frac{1}{B_{AM}} = \frac{Q}{2f_0}. \quad (1-19)$$

As a consequence, operating AM-AFM in a high-Q environment, such as under UHV conditions, would lead to impracticably long acquisition times. Although, using cantilevers with high resonance frequencies can to some extent compensate for the large Q [63], this is not the perfect choice because it will increase the minimum frequency shift detectable in slope detection due to thermal noise according to equation (1-18). On the other hand, for atomic resolution imaging in air under ambient conditions, improvements in sensitivity can be reached for both, AM- and FM-AFM, by the use of higher spring constants and multifrequency AFM techniques. An alternative approach for using ultra-stiff cantilevers is the utilization of higher cantilever eigenmodes [63-65], where the stiffness of the second (third) eigenmode is approximately 39.31 times (308 times) larger compared to the first eigenmode. On the other hand, the resonance frequency of the second (third) eigenmode is only increased by a factor of approximately 6.27 (17.55) relative to the first eigenmode [66-68].

Furthermore, it was shown by Santos *et al.* [69] that the combination of small free oscillation amplitudes and amplitude setpoints (SASS) allows for ultra-high-resolution imaging due to the tip oscillating in very close proximity relative to the surface of the sample. The authors compared images of double-stranded deoxyribonucleic acid (dsDNA) on mica obtained in the frequency modulated non-contact (NC) and SASS mode. The results are shown in Figure 1-4. They reported that the resolution as well as imaging stability were better and that the tip remained sharper when imaging in SASS compared with NC mode. Additionally, the authors proposed that the high-resolution imaging capability of the SASS method is due to imaging within the hydration layer covering nearly every surface in air under ambient conditions. An illustration of the tip oscillating within the hydration layer in SASS mode is shown in Figure 1-5.

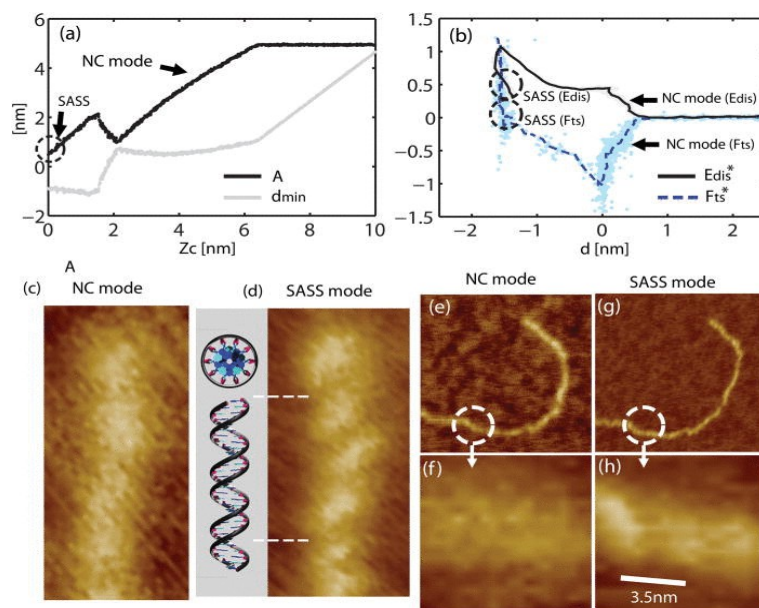


Figure 1-4: Experimental (a) amplitude A (black lines) and minimum distance of approach d_{min} (grey lines) and (b) normalized tip-sample force F_{ts}^* (dashed blue lines) and energy dissipation E_{dis}^* (black lines) as a function of cantilever separation z_c and distance d , respectively. (c)–(h) Experimental examples of images of dsDNA on mica obtained in the NC and SASS modes, respectively. Higher resolution is obtained in the SASS mode provided the tip is sharp enough. Here $R < 5$ nm. (Reprinted from ref. [69], © 2013, with permission from AIP Publishing LLC.)

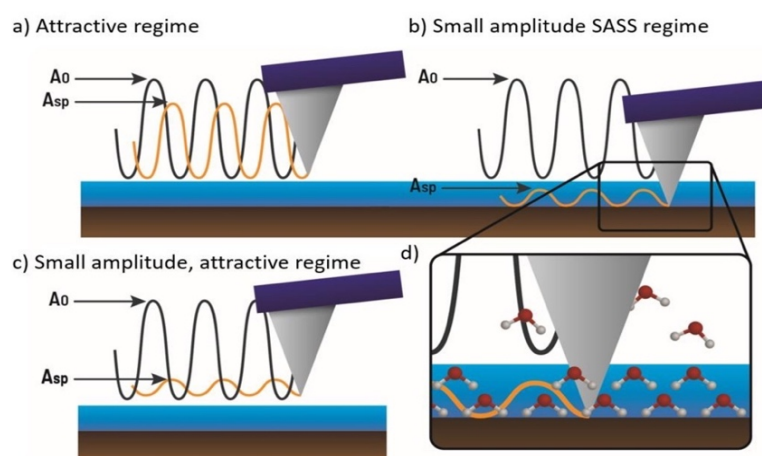


Figure 1-5: Illustration of a cantilever oscillating (a) above the hydration layer with amplitudes (A_{sp}) comparable to the free amplitude A_0 (standard attractive regime imaging), (b) with amplitudes A smaller than A_0 when the tip is permanently immersed in the hydration layer (SASS regime), (c) above the hydration layer with small amplitudes (A_{sp}) much smaller than A_0 (Small amplitude attractive imaging). The inset in (d) is provided to illustrate that in the SASS regime the tip is immersed under the water layer where there might be structure and order. Airborne water molecules are also depicted for illustrative purposes. (Reprinted from ref. [70], <https://doi.org/10.3390/molecules26237083>, © 2021 by the authors. Licensee MDPI, Basel, Switzerland. ¹ Figure caption was slightly adapted.)

¹ This article is an open access article distributed under the terms and conditions of the Creative Commons Attribution (CC BY) license (<https://creativecommons.org/licenses/by/4.0/>).

1.2.5. Multifrequency atomic force microscopy

As set forth in Section 1.2.3, the calculation of forces in standard dynamic AFM is possible, however not straight forward. An essential step towards the quantification of forces and nanomechanical properties was the development of bimodal AFM [71, 72]. The technique is based on the simultaneous excitation of two cantilever eigenmodes, where the amplitude corresponding to the eigenmode with larger resonance frequency is typically much smaller compared to the eigenmode exhibiting the smaller resonance frequency. Bimodal AFM not only leads to a higher amount of accessible quantities but was also shown to provide increased sensitivity towards force variations [5, 73, 74]. One eigenmode oscillation is used for the topography feedback in analogy to monomodal AFM. This feedback-loop can either be performed amplitude or frequency modulated. For the second eigenmode oscillation, three operation options are available; open loop (OL) [75, 76], FM with constant excitation amplitude (CE) and FM with constant oscillation amplitude (CA) [77, 78]. In OL-configuration, the second eigenmode is excited at its resonance with a constant force while amplitude and phase are analyzed. In FM-configuration, the frequency shift, which is required to keep the second eigenmode oscillation at 90° , is acquired. If the oscillation amplitude is additionally kept constant (FM-CA-configuration), frequency shift and drive amplitude can be directly related to conservative and dissipative interactions, respectively [55, 79]. In FM-CE-configuration, such an assignment is not directly accessible, although theoretically a separation of conservative and dissipative interactions is also possible [80-82]. For the quantification of nanomechanical properties, the AM-FM-AFM in CA configuration proved to be highly suitable [78, 83]. A schematic setup of bimodal AM-FM-AFM is shown in Figure 1-6.

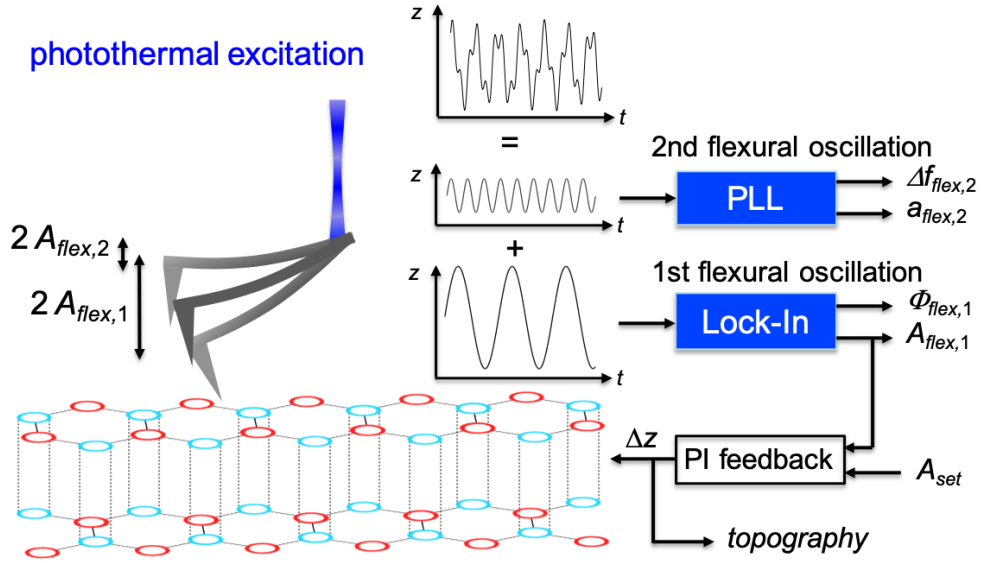


Figure 1-6: Schematic setup of bimodal AM-FM-AFM including a lock-in amplifier for the topography feedback based on amplitude modulation of the first eigenmode and a phase-locked-loop (PLL) for frequency modulation of the second eigenmode oscillation.

As further discussed in Section 2.2.3, the equations for the reconstruction of forces from frequency-shift data differ for the first and the second eigenmode [7]

$$\Delta f_1(d_{min}) = \frac{f_1}{k_1} \frac{1}{\sqrt{2\pi A_1^3}} I_-^{1/2} F(d_{min}), \quad (1-20)$$

$$\Delta f_2(d_{min}) = \frac{f_2}{2k_2} \frac{1}{\sqrt{2\pi A_1}} D_-^{1/2} F(d_{min}), \quad (1-21)$$

where $I_-^{1/2}$ is the half-fractional integral and $D_-^{1/2}$ is the half-fractional derivative. Equation (1-20) and (1-21) are valid if A_1 is larger than the typical length scale of the interaction force. An example for the half-fractional integral and derivative of a model function is shown in Figure 1-7.

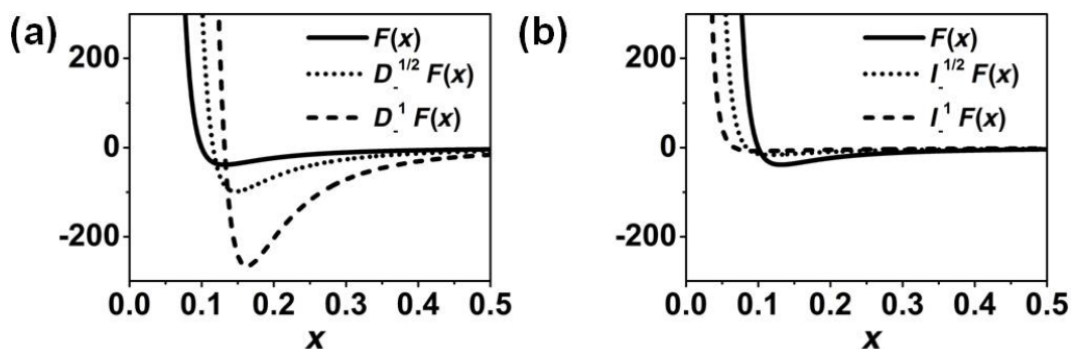


Figure 1-7: Fractional operators of $(0.1^4/x^6 - 1/x^2)$. (a) The function, half-derivative and derivative are plotted. (b) The function, half-integral and integral are plotted. (Reprinted from ref. [7], <https://doi.org/10.3762/bjnano.3.22>, © 2012 Herruzo and Garcia; licensee Beilstein-Institut.²)

Standard bimodal AFM configuration based on the simultaneous excitation of the first and the second flexural eigenmode was further developed into two main directions. One direction was the development of trimodal or tetramodal AFM [84-86]. The second direction was the combination of out-of-plane flexural with in-plane torsional or lateral eigenmodes for bimodal AFM operation [6, 87, 88]. The combination of both approaches, *i.e.* trimodal AFM with in-plane and out-of-plane oscillation components was a focus of this work. Details on possibilities to achieve atomic resolution and deconvolution of in-plane and out-of-plane-forces can be found in Sections 2 and 3.

1.2.6. Identification of in-plane cantilever eigenmodes from thermal noise spectra

It needs to be mentioned that the discrimination between torsional and lateral oscillation eigenmodes is rarely done in literature. This is on the one hand comprehensible because in theory the lateral oscillation should not be visible based on laser beam detection, such as illustrated by Ding *et al.* and shown in Figure 1-8.

² This is an Open Access article under the terms of the Creative Commons Attribution License (<http://creativecommons.org/licenses/by/2.0>), which permits unrestricted use, distribution, and reproduction in any medium, provided the original work is properly cited.

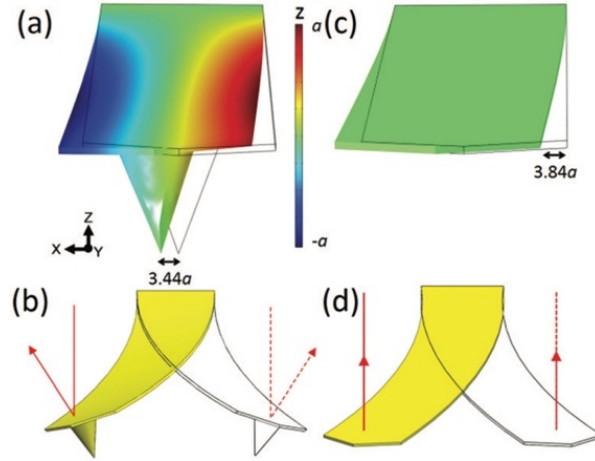


Figure 1-8: Effect of a tip on the fundamental lateral resonance of a cantilever with a rectangular cross section. (a) Finite element analysis (FEA) simulation for a cantilever with a tip height of 16 μm . The cantilever thickness is 1 μm . The colored part indicates the cantilever at the maximum movement of an oscillation; the uncolored part indicates the cantilever in the equilibrium position. The scale bar indicates the deflection of the cantilever in the z -direction. (b) Schematic of the lateral resonance for a cantilever with a tip. (c) FEA simulation for a tipless cantilever. The cantilever thickness is 1 μm . (d) Schematic of the lateral resonance for a tipless cantilever. (Reprinted from ref. [89], © 2016, with permission from Nanoscale.)

However, due to the tip attached to the cantilever, a small torsional movement is induced. If thermal noise spectra of the in-plane cantilever oscillation are acquired, two peaks occur, which nicely fit to the torsional and the lateral eigenmode resonance frequency if compared with equations from beam theory [90, 91]

$$f_{tor,1} = \frac{1}{4L} \sqrt{\frac{GK}{\rho J_p}}, \quad (1-22)$$

$$f_{lat,1} = \frac{1.875^2 b}{2\pi L^2} \sqrt{\frac{E}{12\rho}}, \quad (1-23)$$

where L , b , G , K , ρ , J_p and E are length, width, shear modulus, torsional constant, mass density, second moment of inertia and Young's modulus of the cantilever, respectively. Both, J_p and K depend on the width b and the thickness t of the cantilever

$$J_p \approx \frac{b^3 t}{12}, \quad (1-24)$$

$$K \approx \frac{bt^3}{3}. \quad (1-25)$$

A detailed discussion on the opportunities and benefits from using lateral as well as torsional eigenmodes for AFM can be found in Section 3.

1.3. Oxygen-plasma treatment

Plasma chambers are typically used for three different applications; activation, coating cleaning or etching of samples. All techniques are based on the ionization of gas molecules within a plasma chamber. In a low-pressure plasma chamber such as the one used for the experiments shown in Sections 4 and 5, the plasma is produced by applying energy to a vacuum chamber, using a high-frequency (HF)-generator. The setup of a low-pressure plasma chamber for the removal of carbon *via* oxygen plasma is schematically shown in Figure 1-9.

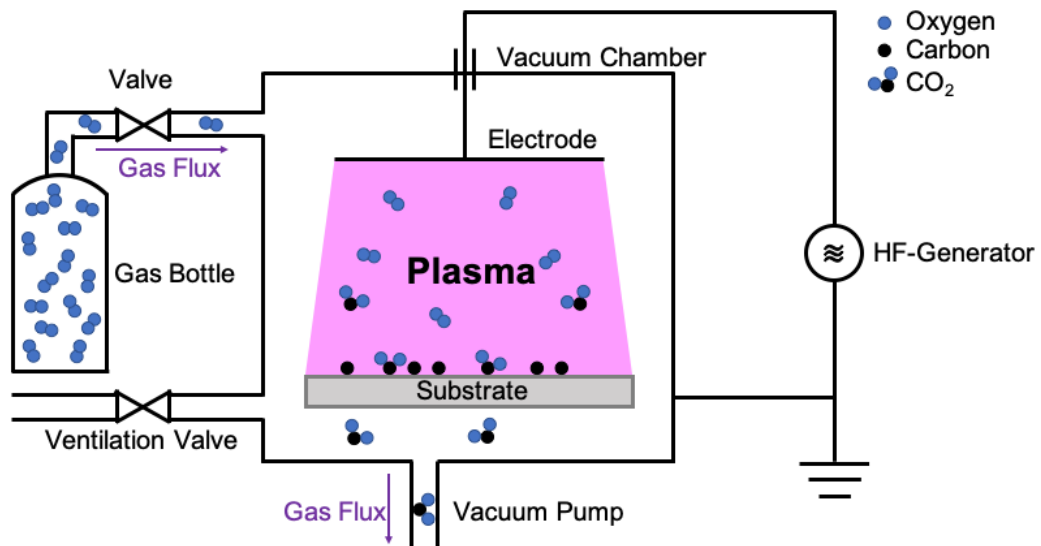


Figure 1-9: Schematic setup of a low-pressure plasma chamber.

Due to the energy applied between the vacuum chamber and the electrode, not only oxygen ions and electrons, but also UV-radiation is produced. As a consequence, three different interaction mechanisms with the substrate or the adsorbate material (carbon in Figure 1-9) potentially occur: (i) mechanical removal *via* ion bombardment, (ii) chemical removal *via* reactions of ions with the substrate or adsorbate or (iii) bond splitting by interaction with UV radiation. By adjusting the process parameters, such as vacuum pressure, power, process time and gas flow, the plasma treatment can be adjusted according to the user's needs. In the presented work, plasma treatment was used for cleaning Si/SiO₂-substrates and for the removal of ambient adsorbates as well as individual graphene-layers from few-layer graphene-/graphite-samples (see Sections 4 and 5).

1.4. Raman spectroscopy

The Nobel Prize in Physics 1930 was awarded to Sir Chandrasekhara Venkata Raman "for his work on the scattering of light and for the discovery of the effect named after him" [92]. Raman spectroscopy is based on inelastic scattering of monochromatic light such as schematically depicted in Figure 1-10.

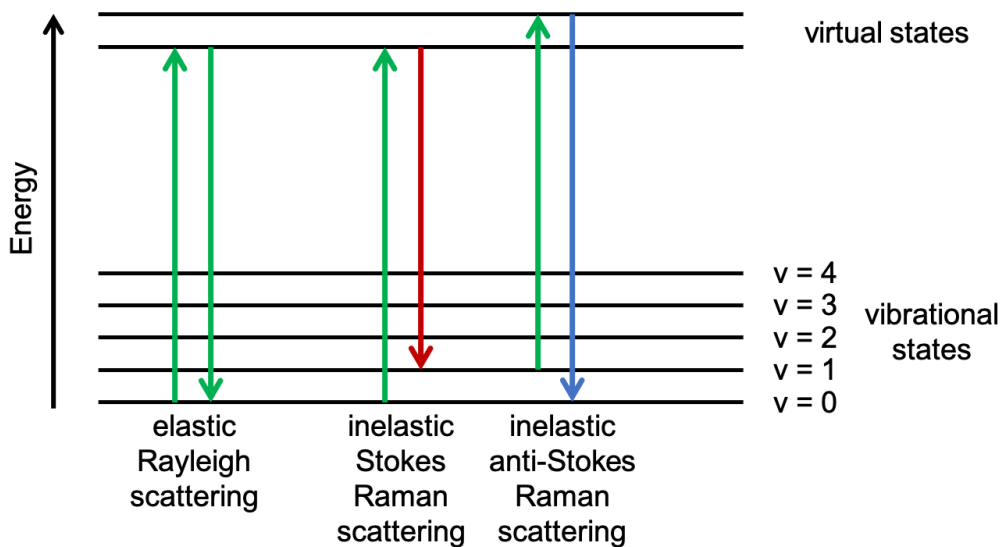


Figure 1-10: Schematic energy diagram comparing Rayleigh and Raman scattering.

The incident photon excites the molecule to virtual states. In contrast to elastic Rayleigh scattering, inelastic Raman scattering results in an energy shift between the photon prior to and after vibrational interaction with the sample. Depending on the vibrational states involved, inelastic Raman scattering can either result in a downshift (Stokes) or in an upshift of the photon's energy (anti-Stokes). This shift in energy is measured in Raman spectroscopy by means of the "Raman shift", being the reciprocal of the wavelength. It needs to be mentioned that Raman scattering occurs much less frequently compared to Rayleigh scattering. Furthermore, Stokes Raman scattering occurs with a higher probability than anti-Stokes Raman scattering.

Since its invention, advanced Raman spectroscopy methods have been developed [93] and the technique became an essential tool not only for the identification of molecules, but also for the analysis of *e.g.* defects or stresses within materials [94]. However, the applicability of Raman spectroscopy is based on the material of interest being Raman-active or not. Basically, molecules, where the polarizability changes during the vibration, are Raman-active [95]. By the help of group theory, it is possible to predict which Raman-active modes will be seen in Raman spectroscopy. Therefore, character tables are used, which summarize all symmetry properties of each point group [96].

1.4.1. Raman spectra of graphene and graphite

Raman spectroscopy is an essential tool for the analysis of graphene and graphite in terms of identifying layer numbers and defectiveness [97, 98]. The Raman spectra of defect-free graphene and graphite, taken with a laser wavelength of 532 nm, typically include the G-peak at around 1580 cm^{-1} and the 2D-peak at around 2700 cm^{-1} . Typical Raman spectra of 1-5 layers thick graphene and graphite samples are shown in Figure 1-11 [99].

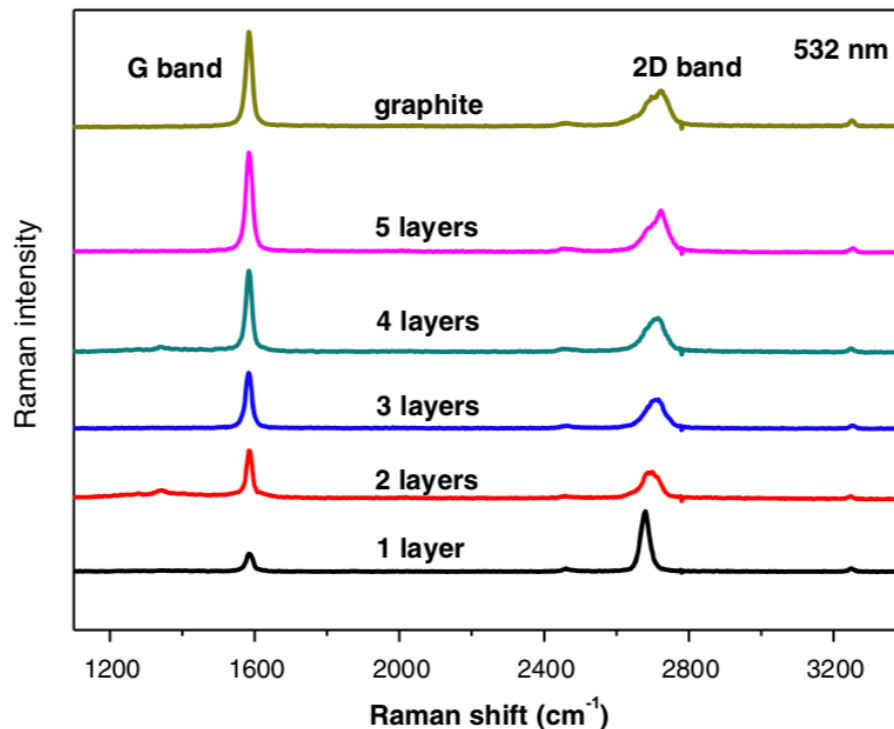


Figure 1-11: Raman spectra of 1 to 5 layers thick graphene and graphite samples acquired with a laser wavelength of 532 nm. (Reprinted from ref. [99], <https://doi.org/10.1186/1556-276X-8-335>, © 2013.³ Figure caption was adapted.)

The Raman spectra of mono-, bi-, tri- and four-layer graphene can be distinguished by the ratio between the intensity of the G- and the 2D-peak. For five-layer graphene the Raman spectrum already resembles the one of graphite. To understand the occurrence of the peaks within the Raman spectra of graphene and graphite, phonon dispersion curves need to be analyzed. Figure 1-12 exemplarily shows the phonon dispersion curves of monolayer graphene [100-102] and in Figure 1-13, the real space unit cell (a) as well as the first Brillouin zone of monolayer graphene (b) are depicted. Additionally, the “breathing” mode corresponding to the D-peak as well as the

³ This article is distributed under the terms of the Creative Commons Attribution 2.0 International License (<https://creativecommons.org/licenses/by/2.0>), which permits unrestricted use, distribution, and reproduction in any medium, provided the original work is properly cited.

vibration of carbon atoms causing the G-peak are shown in Figure 1-13c and d, respectively [102, 103].

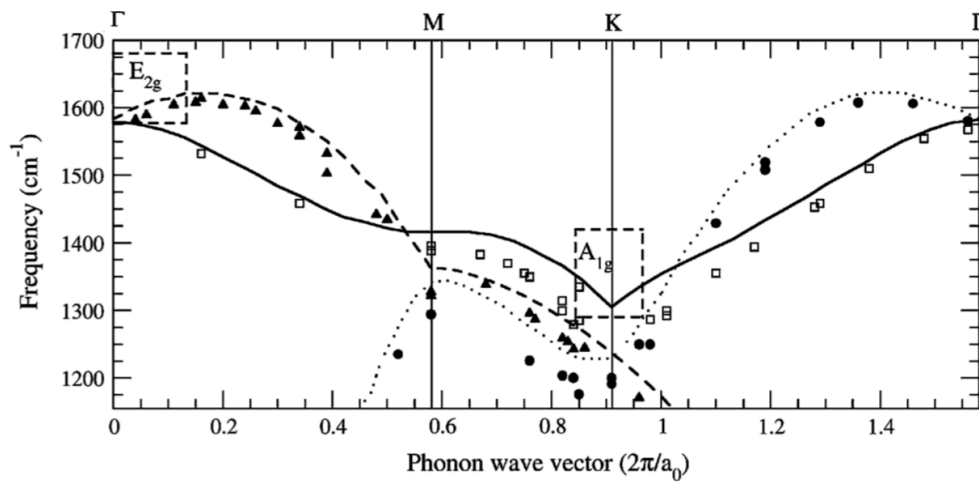


Figure 1-12: Phonon dispersion plot of a single-layer graphene, calculated (lines) [100] and experimental (points) [101]. Different experimental points correspond to the different branches, where the filled triangles correspond to the longitudinal optical (LO) branch, open squares to the in-plane transverse optical (iTO) branch and the filled dots to the longitudinal acoustic (LA) branch. (Reprinted from ref. [102], <https://doi.org/10.1007/s10853-010-4673-3>, © 2010.⁴ Figure caption was slightly adapted.).

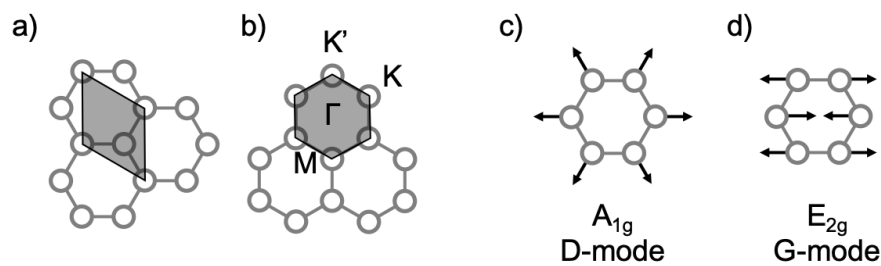


Figure 1-13: Schematic drawing of graphene in (a) real space and (b) reciprocal space. The shaded areas mark the unit cell in (a) and the first Brillouin zone in (b). The vibration of carbon atoms in (c) the A_{1g} D-mode or “breathing” mode and in (d) the E_{2g} G-mode are shown [102, 103].

Since the unit cell of monolayer graphene contains two atoms, the phonon dispersion curves consist of three acoustic (A) and three optical (O) phonon modes. Each of those modes corresponds to out-of-plane phonon modes (o) while the remaining four are in-plane (i) phonon

⁴ This is an open access article distributed under the terms of the Creative Commons Attribution Noncommercial License (<https://creativecommons.org/licenses/by-nc/2.0>), which permits any noncommercial use, distribution, and reproduction in any medium, provided the original author(s) and source are credited.

modes, splitting up into transverse (T) and longitudinal (L) branches. Consequently, the six phonon dispersion curves can be assigned to LO, iTO, oTO, LA, iTA, and oTA phonon modes [104]. According to group theory, the LO and iTO phonon modes at the center of the Brillouin zone (Γ -point) are the only Raman active modes, corresponding to the two-dimensional E_{2g} phonon, being the origin of the G-peak [102]. The 2D-peak represents the overtone of the D-peak which corresponds to modes associated with iTO phonons around the edge of the Brillouin zone (K-point) [105]. While the D-peak is only visible in defective graphene and graphite, the 2D-peak is always visible. This behavior was shown by Thomsen *et al.* [106] to originate from the double resonance (DR) activation mechanism. In a DR process, Raman scattering includes four steps. As a first step, an electron–hole pair is generated *via* Laser irradiation. Secondly, electron–phonon scattering occurs with an exchanged momentum and third, electron scattering from a defect takes place, whose recoil absorbs the momentum of the electron–hole pair. The mechanism finishes with electron–hole recombination as the fourth step [105]. Due to the fact, that in defect-free graphene or graphite the requirement of momentum conservation would be violated by the DR process, the D-peak is not visible. However, since the process responsible for the occurrence of the 2D-peak involves two phonons with opposite momentum vectors, momentum conservation is fulfilled and thus, the 2D-peak is always visible in graphene and graphite [102, 105]. Additionally, within the K-point a further scattering process can be observed in defective graphene and graphite. The process is known as intravalley process, where phonons with small momentum are activated, leading to the occurrence of the D'-peak at around 1620 cm^{-1} [102, 107]. Based on the previous considerations, the distinguishability between the Raman spectra of mono-, bi-, tri-, four-layer graphene and graphite can be explained with their slightly different electronic band structures [97, 105]. Besides the influence of the graphene layer number on the Raman spectra, the evolution of the D- and the D'-peak in defective graphene and graphite depend on the type of defect present. Depending on the intensity ratio between D- and D'-peak, it can be distinguished between predominantly sp^3 -type ($I_D/I_{D'} \approx 13$), vacancy type ($I_D/I_{D'} \approx 7$) and boundary-like defects ($I_D/I_{D'} \approx 3.5$) [108]. Additionally, information on the type of defect present can be gained from the ratio between D- and G-peak [109].

1.5. Individual contributions of authors

Sections 2, 3, 4 and 5 of this work have been prepared in collaboration with Christian Dietz. For the preparation of Sections 4 and 5, Marvin Hoffer was additionally involved. Katharina Bitsch performed part of the experimental work presented in Section 5. All authors are working or have been working for the group “Physics of Surfaces” which is part of the Materials Science department at TU Darmstadt. In the following the individual contributions will be specified.

Section 2 was published as “Simultaneous Deconvolution of In-Plane and Out-of-Plane Forces of HOPG at the Atomic Scale under Ambient Conditions by Multifrequency Atomic Force Microscopy” by A. L. Eichhorn and C. Dietz in *Advanced Materials Interfaces*, 2021, 8(20). My contribution to the publication was the planning and execution of experiments, the adaption of the Fourier method for trimodal AFM setups, the calculation of forces as well as drafting the manuscript. Christian Dietz conceived the initial idea for the publication, supported me with method development, discussed the results and reviewed and edited the manuscript.

Section 3 was published as “Torsional and lateral eigenmode oscillations for atomic resolution imaging of HOPG in air under ambient conditions” by A. L. Eichhorn and C. Dietz in *Scientific Reports*, 2022, 12(1): p. 8981. For this publication, I extended the AFM measurement method, performed the experiments, conducted data analysis and drafted the manuscript. Christian Dietz and I designed the experiment together. Christian Dietz proposed the basic idea for the method, discussed the results, and revised the manuscript.

Section 4 was published as “In-plane and Out-of-plane Interaction Analysis of Adsorbates on Multilayer Graphene and Graphite by Multifrequency Atomic Force Microscopy” by A. L. Eichhorn, M. Hoffer and C. Dietz in *Carbon*, 2022, 8(20). Marvin Hoffer and I contributed equally to this publication. We did the formal analysis and investigation together. Marvin Hoffer did most of the experimental work. Christian Dietz and I optimized the methodology and I drafted the original manuscript. Christian Dietz was additionally responsible for conceptualization, project administration, supervision, review and editing of the manuscript.

Section 5 was submitted as “Adsorbate Formation/Removal and Plasma-Induced Evolution of Defects in Graphitic Materials” by A. L. Eichhorn, M. Hoffer, K. Bitsch and C. Dietz to *Small Methods*, 2023. Marvin Hoffer and I contributed equally to this publication. The experimental work was done by Katharina Bitsch and Marvin Hoffer. Interpretation of Raman and AFM data was supervised by Christian Dietz and myself and frequently discussed with all co-authors. Marvin Hoffer and I drafted the manuscript. Christian Dietz additionally reviewed and edited the manuscript.

2. Simultaneous deconvolution of in-plane and out-of-plane forces of HOPG at the atomic scale under ambient conditions by multifrequency atomic force microscopy⁵

Multifrequency atomic force microscopy (AFM) is shown to be an excellent tool for imaging crystal structures at atomic resolution in different spatial directions. However, determining the forces between single atoms remains challenging, particularly in air under ambient conditions. Developed here is a trimodal AFM approach that simultaneously acquires torsional and flexural frequency-shift images and spectroscopic data to transfer these observables into in-plane and out-of-plane forces between single bonds of highly oriented pyrolytic graphite (HOPG) at atomic resolution in air under ambient conditions based on the Fourier method. It is found that the cantilever mean deflection is an excellent indicator to understand that strong attractive interactions between the tip and the surface of HOPG in dynamic AFM imply a local lift of the topmost carbon layer when using higher eigenmodes for the topographical feedback. Cross-talk between torsional and flexural-oscillation modes is shown to be negligible. Interestingly, significant differences are observed in the in-plane forces depending on the orientation of the carbon bonds relative to the direction of torsional oscillation.

2.1. Introduction

Highly oriented pyrolytic graphite (HOPG) is well known as atomically flat substrate for various experimental setups and advanced sensors [110, 111]. Graphene, the basal plane of HOPG, has been shown to be a promising material as membrane or for future applications, such as in electronics [2]. However, although there have been some studies of how defects affect the nanomechanical properties of graphene [109, 112, 113], it remains challenging to analyze the local effect of different types of defects on the in-plane and out-of-plane elastic properties at the atomic level. Also, because graphene devices are exposed to environmental influences, measurements in air under ambient conditions are more relevant than those under ultrahigh vacuum (UHV). While imaging graphitic surfaces at the atomic scale has become a standard procedure using atomic force microscopy (AFM) under UHV [6], at low temperatures [16, 114-116] or in a liquid environment [117], it remains a challenging task to obtain comparable high resolution in air under ambient conditions.

⁵ This Section was published as “Simultaneous Deconvolution of In-Plane and Out-of-Plane Forces of HOPG at the Atomic Scale under Ambient Conditions by Multifrequency Atomic Force Microscopy” by A. L. Eichhorn and C. Dietz in *Advanced Materials Interfaces*, 2021. 8(20). © 2021 The Authors. *Advanced Materials Interfaces* published by Wiley-VCH GmbH. This is an open access article under the terms of the Creative Commons Attribution License (<https://creativecommons.org/licenses/by/4.0/>), which permits use, distribution and reproduction in any medium, provided the original work is properly cited. References were adapted to provide continuous numbering throughout the whole work.

In 2014, Wastl *et al.* were the first to demonstrate atomic resolution of HOPG in air under ambient conditions, using stiff quartz tuning-fork force sensors (qPlus sensors [118]) in the flexural-frequency modulation mode [119]. A major advantage of using qPlus sensors is that they allow the cantilever to oscillate with ultrasmall amplitudes (<1 nm) because of their high stiffness. However, although the combination of in-plane and out-of-plane oscillation modes is feasible, the implementation is not straightforward because qPlus sensors require some nonstandard AFM equipment [120-122]. Another option for achieving ultrasmall oscillation amplitudes is to exploit higher flexural cantilever eigenmodes because they are stiffer than the fundamental eigenmode. Atomic resolution has been shown successfully on different substrates in air when higher eigenmodes were used for the amplitude or frequency-shift feedback [63-65]. Multifrequency AFM has also been shown to be capable of atomic-resolution imaging using the first and second flexural eigenmode [5, 6, 123]. Also, some research groups have achieved atomic resolution with flexural-torsional approaches, but not under ambient conditions [6, 87]. Most of the benchmark images in terms of high resolution were obtained with CO-functionalized tips [124, 125], but unfortunately they cannot be used in air under ambient conditions and they suffer from bending while imaging [126]. Although there are several approaches for imaging with atomic resolution, determining forces remains a challenging task if measurements are performed in air under ambient conditions. In water under UHV and/or low temperatures, out-of-plane forces have been determined successfully with atomic resolution in spectroscopic experiments [127-131], but unfortunately it is challenging to obtain atomic resolution in air under ambient conditions with spectroscopic mapping because of long image-acquisition times and the associated thermal drift that is substantial when imaging at the atomic scale. Recently, Seeholzer *et al.* developed an approach to deconvoluting forces from lateral frequency-shift images at the molecular level using the Fourier method [4]. The advantage of this method over others is that the force determination from a single image is much faster than that from a complete set of spectroscopic data. Because of the applicability to single images, the method is assumed to be particularly suitable for force deconvolution in air under ambient conditions. To date, the Fourier method has been used for only in-plane force determination.

In the present work, we extend the method to determine in-plane and out-of-plane forces simultaneously from torsional and flexural frequency-shift data, respectively, to unravel the interactions between single carbon atoms of HOPG in air under ambient conditions. For acquiring atomically resolved images, we have developed a trimodal approach [84, 85] based on the AMFlex-FMTor method [88] demonstrated by Dietz. This mode uses photothermal excitation to drive the cantilever [43, 44]. The blue excitation laser spot is placed at the fixed

end of the cantilever but at a considerable distance from the length symmetry axis [87]. This enables the simultaneous excitation of flexural and torsional eigenmodes by modulating the power of the laser periodically with frequencies matching the flexural and torsional resonance frequencies. The first flexural-eigenmode amplitude of the cantilever is used for topographical feedback (AMFlex). Hence, by adjusting the flexural-amplitude setpoint, the indentation into the sample can be controlled. From the resulting phase shift between oscillation and excitation, dissipative sample properties in the out-of-plane direction can be obtained. Additionally, a phase-locked loop (PLL) is used to frequency-modulate the torsional oscillation of the cantilever (FMTor). Thus, the torsional phase shift is always kept at 90° to maintain the oscillation at resonance when the tip interacts with the surface. Additionally, the torsional oscillation amplitude is kept constant by adjusting the drive amplitude. From the drive amplitude, dissipative information about the in-plane sample properties can be deduced. The frequency shift of the torsional oscillation provides information about the elasticity of the sample in its in-plane direction [88]. Applying the described method for stiff samples such as HOPG requires some modifications of the setup as shown in Figure 2-1. To achieve a 3D analysis of the interacting forces, the method was extended to a trimodal setup, where the second flexural eigenmode was used for the topographic feedback in amplitude modulation (AMFlex2), the frequency-modulated torsional oscillation (FMTor1) provided access to the in-plane forces and the frequency-modulated third-eigenmode flexural oscillation (FMFlex3) gave access to the out-of-plane forces.

Inspired by Kawai *et al.* [65] and Korolkov *et al.* [64], we use the amplitude of the second flexural eigenmode for the topographical feedback to take advantage of the fact that this particular eigenmode is stiffer than the fundamental eigenmode. In combination with the small amplitude small setpoint (SASS) method introduced by Santos *et al.* [69], we reach a sufficiently small tip-sample distance to routinely achieve atomic resolution on HOPG surfaces. To sense in-plane and out-of-plane forces simultaneously, we also excite the third flexural eigenmode oscillation. Similar to the torsional eigenmode, the third flexural eigenmode is driven as frequency-modulated in constant-amplitude mode to establish a second PLL circuit. Hereinafter, according to the excited modes and feedbacks, we designate the mode as the AMFlex2-FMTor1-FMFlex3 mode. The advantages of amplitude modulation for feedback control over other methods are straightforward implementation, stable operation, and fast response in air under ambient conditions [62].

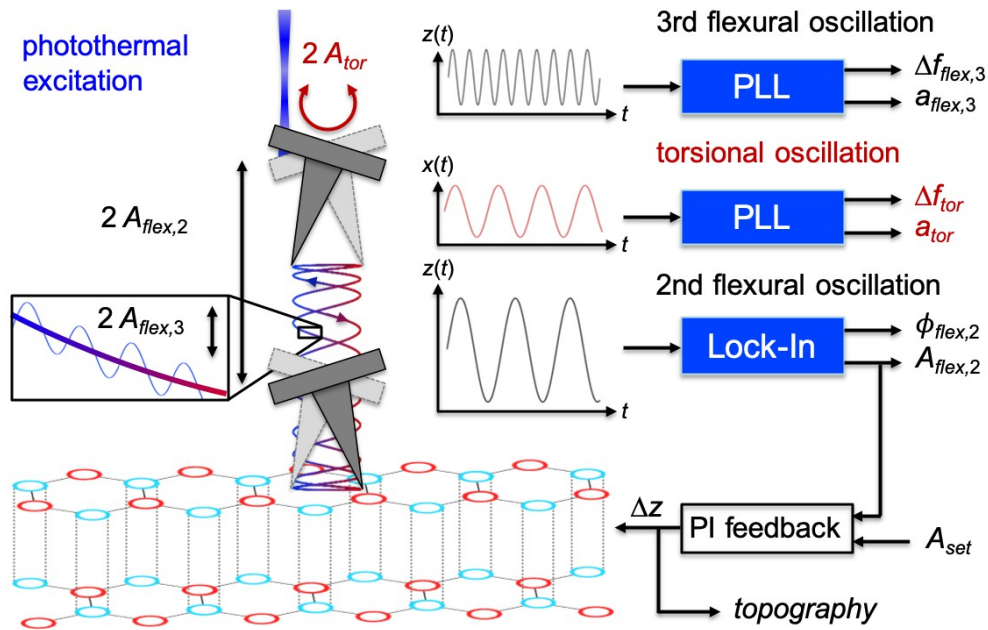


Figure 2-1: Schematic of AMFlex2-FMTor1-FMFlex3 mode for atomic-resolution imaging of HOPG. Out-of-plane forces can be determined from the third-eigenmode flexural frequency shift, whereas in-plane forces can be calculated from the torsional-eigenmode frequency shift (Reprinted from ref. [8], <https://doi.org/10.1002/admi.202101288>, © 2021.⁶).

2.2. Results and discussion

2.2.1. Trimodal imaging in AMFlex2-FMTor1-FMFlex3 mode

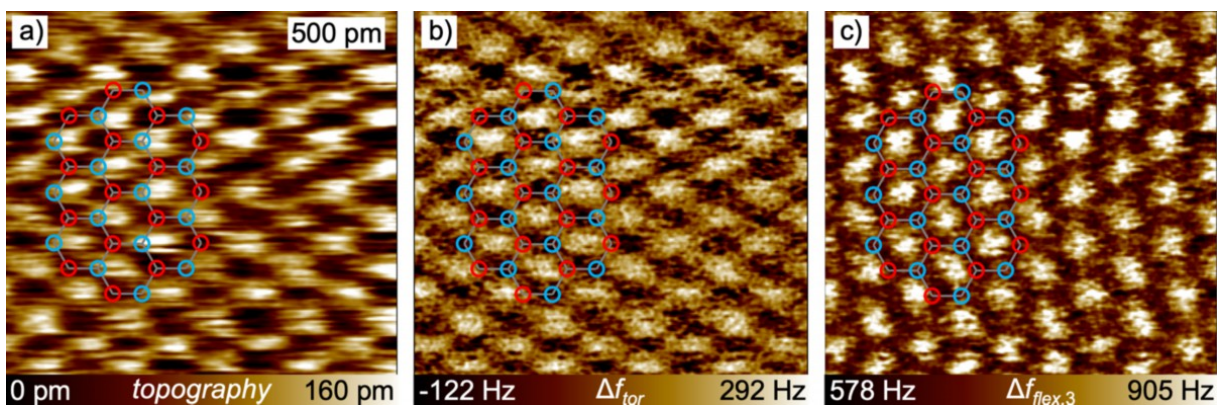


Figure 2-2: AFM images of HOPG taken in AMFlex2-FMTor1-FMFlex3 mode: a) topography image, and b) torsional and c) flexural frequency-shift images. Imaging parameters: $A_0(flex,2) = 770$ pm, $A_{flex,2} = 100$ pm, $A_{tor} = 80$ pm, $A_{flex,3} = 220$ pm (Reprinted from ref. [8], <https://doi.org/10.1002/admi.202101288>, © 2021.⁷).

^{6,7} This is an open access article under the terms of the Creative Commons Attribution License (<https://creativecommons.org/licenses/by/4.0/>), which permits use, distribution and reproduction in any medium, provided the original work is properly cited.

Figure 2-2 shows AFM images of HOPG taken simultaneously in the AMFlex2-FMTor1-FMFlex3 mode. Atomic contrast is observed in a) the topography image and b) the torsional and c) third-eigenmode flexural frequency-shift images, in which the atoms appear as dark spots and the hollow sides as bright protrusions. In the topography image (Figure 2-2a) and the torsional frequency-shift image (Figure 2-2b) we did not observe the honeycomb structure of HOPG, whereas the third-eigenmode frequency-shift image (Figure 2-2c) resolves carbon hexagons, however, compared to the high quality images shown by Wastl *et al.* [119] with inverted contrast (see Figure 7-1 in the Supplementary Information (Section 7.1.1) for an inverted image to compare). This inverted contrast is well known for AFM imaging in frequency-modulation mode when operating the instrument in the attractive regime [6, 16]. Nevertheless, in our case the assignment of atomic sides requires some further explanation because both the third-eigenmode frequency-shift image shown in Figure 2-2c and the phase of the second-eigenmode oscillation (not shown) suggest that imaging was performed in the repulsive regime. Also, we observed a small offset between the frequency-shift images and the topography image along the fast scan axis, as well as an unexpected high corrugation of up to 160 pm peak-to-peak. We found that these effects can be attributed to a significant mean deflection of the cantilever during imaging with topographic feedback on a higher eigenmode [132, 133]. Details about the relationship between mean deflection and contrast formation are given in Figure 7-2 in the Supplementary Information (Section 7.1.3).

2.2.2. Dynamic spectroscopy in AMFlex2-FMTor1-FMFlex3 mode

To clarify further the contrast formation of the atomically resolved images in Figure 2-2, we performed dynamic spectroscopy experiments at the alleged carbon-atom location on HOPG using the AMFlex2-FMTor1-FMFlex3 mode. Therefore, the amplitude feedback was turned off and the amplitude of the second flexural eigenmode oscillation was free to change upon approach and retract while triggering at 10 % of the free oscillation amplitude (determined at 200 nm above the surface). Besides the change in the second-eigenmode amplitude, we also recorded the changes in the second-eigenmode phase, the mean deflection, the third-eigenmode frequency shift, and the torsional frequency shift as functions of the tip-sample distance d . The results are shown in Figure 2-3a, and details about the calibration of the different eigenmode amplitudes and the deflection are given in the Supplementary Information (Section 7.1.2).

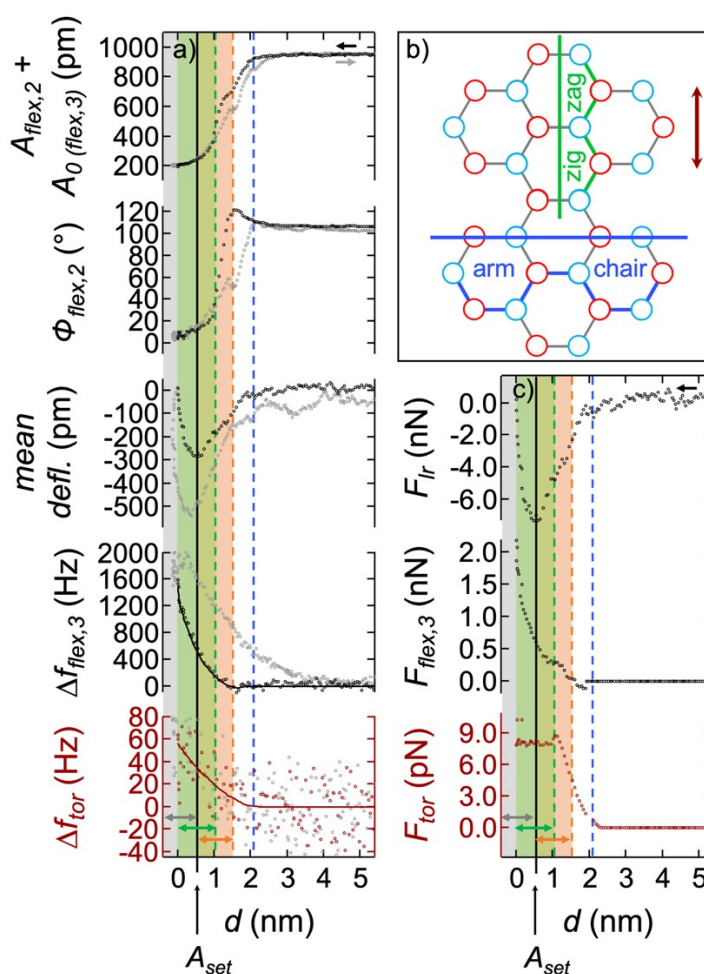


Figure 2-3: Dynamic spectroscopy at alleged carbon-atom location of HOPG in air under ambient conditions. a) Amplitude, phase, mean deflection, and flexural and torsional frequency shifts versus tip–sample distance d . The approach curves are shown in black/red (flexural/torsional), the retract curves are shown in gray, and the solid lines represent the fitted frequency-shift data of the approach curves. b) Scheme of zigzag and armchair orientation of carbon hexagons. Here, the torsional oscillation direction (red double-headed arrow) is along the zigzag direction of the hexagonal carbon structure. c) Long-range interaction F_{lr} between tip and sample calculated from mean deflection and force deconvolution from fitted flexural and torsional frequency-shift data (solid lines in (a)) using the Sader method. The setpoint amplitude at which images were taken is marked by the black vertical lines. Some characteristic regions of the approach curves are colored gray, green, and orange and marked by double-headed arrows. The dashed vertical lines mark the starts of the characteristic areas (Reprinted from ref. [8], <https://doi.org/10.1002/admi.202101288>, © 2021.⁸).

Figure 2-3a shows hysteresis between the approach and retract curves, which we attribute on the one hand to the existence of water layers covering the surfaces at both sides, tip and sample. On the other hand, we assume that a significant portion of the hysteresis is caused by the local

⁸ This is an open access article under the terms of the Creative Commons Attribution License (<https://creativecommons.org/licenses/by/4.0/>), which permits use, distribution and reproduction in any medium, provided the original work is properly cited.

lift of the topmost carbon layers [134]. The assumption was corroborated by comparative spectroscopic measurements performed on HOPG and silicon as shown in Figure 7-3 in the Supplementary Information (Section 7.1.4). We have marked some characteristic regions of the approach curves as colored areas separated by dashed lines. Starting from the largest tip-sample distance (right side of the graph), the blue dashed line marks the onset of attractive forces at ≈ 2 nm from the surface, which results in a reduction of the second flexural amplitude and the mean deflection and an increase in the second flexural phase. While the third-eigenmode frequency stays at initial resonance, a small increase in the torsional frequency shift is noticeable from the fit of the original data (solid line), but with a high uncertainty as can be estimated from the scattered data points. Here, the torsional oscillation direction was along the zigzag orientation of the carbon hexagons, as shown schematically in Figure 2-3b. The orange dashed line at ≈ 1.5 nm from the sample surface marks the maximum attractive force sensed by the tip, notable for the second-flexural-eigenmode phase shift that results in a significant change of the gradient of the second-flexural-eigenmode amplitude. At that point, the mean-deflection changes in gradient, which can be interpreted as an increase in the average attractive force, whereas the third-eigenmode frequency shift starts to increase (stronger repulsion). The average torsional frequency shift starts to increase when the tip is moved closer than 2 nm to the surface. The green line at a tip-sample distance of ≈ 1 nm marks where the approach curve coincides with the retract curve for the second-eigenmode amplitude and phase upon approach, although we noticed large hysteresis for the mean deflection and the third-eigenmode frequency shift. While the gradient of the decreasing mean deflection remains constant, that of the third flexural frequency shift again increases. The minimum mean cantilever deflection is reached at the second-eigenmode amplitude setpoint marked by the black dashed line. Consequently, for smaller tip-sample distances, the mean deflection and the third-eigenmode frequency shift both increase, but the mean deflection remains predominantly attractive. From these observations, we conclude that using the AMFlex2-FMTor1-FMFlex3 setup provides three different overlapping contrast regimes, which are marked in gray ($d < 0.5$ nm), green ($d \approx 0-1$ nm), and orange ($d \approx 0.5-1.5$ nm) in Figure 2-3a. In the orange regime, the gradients of the mean deflection and third-flexural-eigenmode frequency shift show opposite trends, whereas at closer tip-sample distances (gray) the trends coincide. The green regime represents the area close to the minimum mean cantilever deflection, *i.e.*, the sign of the gradient might differ between the atomic sites. We were able to show that a variation of the third-eigenmode oscillation amplitude enables imaging in the three different described contrast-formation regimes (see Figure 7-4 in the Supplementary Information (Section 7.1.5) for details). This implies that imaging in the gray (resp. orange) area results in equal (resp. inverted) contrasts of the mean-deflection and

third-eigenmode frequency-shift images. For images taken in the green area, we expect differently pronounced offsets between the maxima and minima of the mean deflection and the third-eigenmode frequency shift. At the same time, we observed that the mean-deflection images and the topography images show nearly the same patterns, however, with inverted contrast. Hence, the topography signal seems to be strongly influenced by the mean cantilever deflection during imaging, which might explain on the one hand the unexpected high corrugation of the atomic structure of HOPG in Figure 2-2a and on the other hand the small lateral offset between the topography image (Figure 2-2a) and the torsional and flexural frequency-shift images (Figure 2-2b, c). However, due to the fact that the spectroscopy and imaging measurements cannot be accomplished simultaneously, a direct proof of the hypothesis remains challenging. With the knowledge gained from the spectroscopic experiments, we conclude that for the images shown in Figure 2-2, the tip-sample distance was most likely in the range of 0–1 nm around the minimum mean deflection. This could have caused the small offset in the observed structure between the topography and frequency-shift images on the one hand and the appearance of hollow sides as maxima and the atoms as minima in the frequency-shift images on the other hand, although positive frequency shifts imply imaging in the repulsive regime. Additionally, we assume that imaging is influenced by a local lift of the topmost carbon layer, as suggested by the retract curves.

2.2.3. Force reconstruction using Sader method

Having clarified the contrast formation, we seek quantities that are physically more meaningful, such as the forces between the different carbon atoms. From the mean-deflection signal, we can simply approximate the average long-range attractive force F_{lr} by multiplication with the static force constant. More meaningful short-range forces can be determined from the frequency-shift data. There are two standard approaches to quantifying forces from the frequency-shift data of FM-AFM measurements: the Sader method [60] developed by Sader and Jarvis and the matrix method [58] developed by Giessibl. The Sader method is based on a Laplace transform and uses the large-amplitude approximation—which presumes that the oscillation amplitude is larger than the characteristic length scale of the interaction force—to reconstruct forces by inverting the frequency-shift data. The matrix method is based on a transformation matrix that converts the frequency-shift data into forces. Both methods rely on the frequency-modulation mode with constant oscillation amplitude. Because the amplitude of the second flexural eigenmode is smaller than that of the third eigenmode at tip-sample distances that are relevant for imaging, we assume that the standard force-deconvolution

methods are valid for the present imaging conditions after modifying the equations slightly. This modification is based on the observation that the height signal is dominated by the mean cantilever deflection and so the corrected tip–sample distance can be approximated as a constant height, similar to the situation in frequency modulation. Unlike frequency modulation, we must consider the varying oscillation amplitude upon approach, whereupon the modified version of the formula derived by Sader and Jarvis [59] is given by

$$F_{flex,3}(d) = k_{flex,3} \sqrt{2\pi(A_{flex,2}(d) + A_{0(flex,3)})^3} D_-^{1/2} \frac{\Delta f_{flex,3}(d)}{f_{0(flex,3)}}, \quad (2-1)$$

where $k_{flex,3}$ is the stiffness of the third flexural eigenmode, $A_{flex,2}$ is the tip–sample-distance-dependent amplitude of the second flexural eigenmode, $A_{0(flex,3)}$ is the amplitude setpoint of the third flexural eigenmode, and $\Delta f_{flex,3}$ and $f_{0(flex,3)}$ are the frequency shift and resonance frequency, respectively, of the third flexural eigenmode. The force deconvolution uses the half-fractional derivative $D_-^{1/2}$ applied to the frequency-shift data [7].

Several authors have shown that for bimodal AFM, the formula for calculating forces from frequency-shift data differs for the first and second eigenmodes [5-7, 135, 136]. From considering the amplitude ratios, we assume that we can treat the system as a bimodal AFM setup with both flexural eigenmodes (plus torsional eigenmode) being frequency-modulated. The corresponding formula has been shown to be valid for both flexural–flexural [5] and flexural–torsional [6] setups. The modified formula for determining the torsional force can be expressed as

$$F_{tor}(d) = 2k_{tor} \sqrt{2\pi(A_{flex,2}(d) + A_{0(flex,3)})} I_-^{1/2} \frac{\Delta f_{tor}(d)}{f_{0(tor)}}, \quad (2-2)$$

where k_{tor} is the torsional stiffness, and Δf_{tor} and $f_{0(tor)}$ are the frequency shift and resonance frequency, respectively, of the torsional eigenmode. Here, the force deconvolution relies on the half-fractional integral $I_-^{1/2}$ of the torsional frequency-shift data. Details about determining the underlying formula can be found in refs. [7, 59, 60] and information about implementing the formula in a MATLAB code is given in the Supplementary Information (Section 7.1.6).

The bimodal approach presumes that the two eigenmodes under consideration can oscillate independently of each other and that one oscillation amplitude is much smaller than the other. From dynamic spectroscopy with different oscillation amplitudes, we found no considerable

coupling between the modes; potential cross-talk will be analyzed in more detail by means of imaging data. Also, note that calibrating the inverse optical lever sensitivity (invOLS) for the torsional eigenmode and the third flexural eigenmode is not straightforward (see the Supplementary Information (Section 7.1.2) for details of the calibration). Despite the fact that the condition $A_{0(flex,3)} \gg A_{0(tor)}$ might not be valid for every constellation of parameters, we assume that the bimodal approach can be used because of the spatial difference in oscillation direction.

The resulting forces after deconvolution of the fitted frequency-shift curves (solid lines in Figure 2-3a) are shown in Figure 2-3c. Additionally, the long-range forces determined from the mean-deflection curve in Figure 2-3a are plotted against the tip-sample distance. The strongest attractive force during approach is at a tip-sample distance of ≈ 500 pm and is 7.3 nN in absolute value. The strongest attractive force as determined from the retract curve is nearly twice as large (14 nN).

Compared to the study by Chiesa and Lai [137], who measured the attractive tip-sample forces under multiple aging conditions of HOPG, in the range of 0.7–1.3 nN, we found values that are approximately ten times higher. Calo *et al.* [138] observed an increase in the attractive force with increasing tip radius, which is unlikely to be the reason in our case. We assume that using diamond-like carbon (DLC) tips instead of the mostly used silicon tips might cause the higher tip-sample attraction originating from a larger Hamaker constant of DLC compared to that of silicon oxide [139]. The short-range flexural force ($F_{flex,3}$) shows a similar trend to that of the third-eigenmode flexural frequency shift, although note a major difference in the region between the blue and orange dashed lines (tip-sample distance of 2–1.5 nm), where the short-range flexural force shows a small attractive region. During approach, starting from the orange dashed line, the repulsive force increases initially with a very small gradient. In the center between the orange and green dashed lines, note a jump to an overall repulsive force with a 250 pN increase in absolute value. Around the green dashed line, a small plateau of ≈ 500 pm width forms, where the repulsive force remains constant at 250 pN. Upon further approach, from $d < 750$ pm the force increases with increasing gradient. The maximum repulsive force reached is 2 nN, and the force at the setpoint amplitude is ≈ 480 pN. Interestingly, the in-plane force deduced from the torsional frequency shift increases constantly (tip-sample distance of 2–1 nm) up to a maximum repulsive value of ≈ 9 pN. The maximum torsional tip-sample force is reached at the position of the green dashed line, and further approach of the tip leads to a slightly decreased force plateau of 8 pN. Note the effects of this force behavior in the frequency-

shift images: while the choice of the second- flexural-eigenmode amplitude setpoint influenced the torsional frequency-shift image only slightly, it had a clear influence on the third-eigenmode frequency-shift image. Details are given in Figure 7-5 in the Supplementary Information (Section 7.1.7).

Consequently, quantifying forces from dynamic spectroscopy data in the AMFlex2-FMTor1-FMFlex3 mode is indispensable for understanding contrast formation in images. Nevertheless, we encountered a few obstacles when using this method of force deconvolution with atomic resolution in air under ambient conditions. First, the determination of forces depends strongly on the actual tip-sample distance, thereby involving the correction for the mean deflection of the cantilever. The mean-deflection signal measured by the induced photocurrent on the photodiode is always accompanied by oscillations and/or tilt during approach and retract. Hence, the associated calibration is not straightforward and therefore prone to errors. This in turn influences the determination of all forces deduced from spectroscopy data. Second, hysteresis between approach and retract curves involves further sources of errors for the quantification. Third, the quantification of torsional forces is imprecise because of the high noise level of the frequency-shift data. Fourth, discriminating the atomic sides *via* dynamic spectroscopy at room temperature in air is challenging, a major cause being the influence of thermal drift. To the best of our knowledge, atomic-resolution dynamic spectroscopy in air under ambient conditions has not been demonstrated until now. For all these reasons, we decided to focus on a different approach suggested by Weymouth *et al.* [61] and Seeholzer *et al.* [4] who determined lateral tip-sample forces from dynamic lateral-force microscopy images using the Fourier method. This line-by-line approach relies on the same physical background as that of the Sader and matrix methods for force deconvolution from frequency-shift data. Consequently, we assume that our approximation of the setup as a trimodal one in frequency modulation is still reasonable. The Fourier method emerged because both standard methods can lead to errors in force deconvolution for certain force curves and amplitudes, in particular at the regions of local extrema [140]. Because of the substantial number of inflection points in our data, we decided to calculate forces based on the Fourier method with the images obtained on HOPG. It needs to be mentioned that the Fourier method is not applicable for the analysis of individual spectroscopy curves such as shown in Figure 2-3. For the acquirement of periodic structures necessary for the Fourier method, complete spectroscopic maps are needed. However, this is challenging on the atomic scale in air under ambient conditions due to thermal drift issues. Consequently, we cannot provide a direct comparison between the two reconstruction methods.

2.2.4. Force reconstruction using Fourier method

The Fourier method bears the idea that a periodic function such as the lateral frequency shift can be decomposed into a Fourier series. It has been shown that the Fourier method reproduces forces with higher accuracy compared to the Sader and matrix methods, especially at the local extrema of force curves [4]. Until now, the Fourier method was used only for monomodal AFM operation and the lateral oscillation of the cantilever in combination with a qPlus sensor. We assume that the same approach can be adapted for the deconvolution of lateral forces involved in the torsional cantilever oscillation. Additionally, we extended the Fourier method for the bimodal operation by modifying the formulae according to the bimodal approximation [5-7]. In general, the tip-sample forces can be determined from

$$F_{ts}(x) = \sum_{n=1}^N -a_n \frac{2\pi n}{L} \cos\left(\frac{2\pi n}{L}x\right) + b_n \frac{2\pi n}{L} \sin\left(\frac{2\pi n}{L}x\right). \quad (2-3)$$

as described in detail elsewhere, where L is the line length and N is the Nyquist frequency, which is half of the sampling rate s [4]

$$N = \frac{s}{2L}. \quad (2-4)$$

The difference between the monomodal and bimodal approaches appears in the prefactors a_n and b_n in Equations (2-5)–(2-8)

$$a_{n(mono)} = -\frac{2k_{tor}}{f_0(tor)} \alpha_n \left(\frac{A_{tor}L}{4\pi n}\right) \frac{1}{J_1\left(\frac{2\pi n A_{tor}}{L}\right)}, \quad (2-5)$$

$$b_{n(mono)} = -\frac{2k_{tor}}{f_0(tor)} \beta_n \left(\frac{A_{tor}L}{4\pi n}\right) \frac{1}{J_1\left(\frac{2\pi n A_{tor}}{L}\right)}, \quad (2-6)$$

$$a_{n(bi)} = -\frac{2k_i}{f_0(i)} \alpha_n \left(\frac{L}{2\pi n}\right)^2 \frac{1}{J_0\left(\frac{2\pi n A_{tor}}{L}\right)}, \quad (2-7)$$

$$b_{n(bi)} = -\frac{2k_i}{f_0(i)} \beta_n \left(\frac{L}{2\pi n}\right)^2 \frac{1}{J_0\left(\frac{2\pi n A_{tor}}{L}\right)}, \quad (2-8)$$

where J_0 and J_1 are the Bessel functions of the first kind (J) of zero and first order, respectively and i represents the eigenmode which was additionally used for bimodal imaging in frequency modulation. Details about determining a_n and b_n in the bimodal case are provided in the Supplementary Information (Section 7.1.8). As in the work of Seeholzer *et al.* [4], the factors a_n and β_n are determined from the scalar projection of the data on the relevant sine or cosine function divided by a normalization factor. To control the precision to which the Fourier method can reproduce the original frequency-shift data, it is helpful to calculate additional validation images of the frequency-shift data using

$$\Delta f_{mono (val)}(x) = \frac{f_0(i)}{2k_i} \sum_{n=1}^N -a_n \left(\frac{4\pi n}{A_{tor}L} \right) \sin \left(\frac{2\pi n}{L} x \right) J_1 \left(\frac{2\pi n A_{tor}}{L} \right) - b_n \left(\frac{4\pi n}{A_{tor}L} \right) \cos \left(\frac{2\pi n}{L} x \right) J_1 \left(\frac{2\pi n A_{tor}}{L} \right), \quad (2-9)$$

$$\Delta f_{bi (val)}(x) = \frac{f_0(i)}{2k_i} \sum_{n=1}^N -a_n \left(\frac{2\pi n}{L} \right)^2 \sin \left(\frac{2\pi n}{L} x \right) J_0 \left(\frac{2\pi n A_{tor}}{L} \right) - b_n \left(\frac{2\pi n}{L} \right)^2 \cos \left(\frac{2\pi n}{L} x \right) J_0 \left(\frac{2\pi n A_{tor}}{L} \right). \quad (2-10)$$

To implement the formulas numerically, the MATLAB code provided by Seeholzer *et al.* was used and extended for the bimodal case. Unlike Seeholzer and co-workers who determined the lateral forces acting between tip and sample while moving over an adsorbate, we aimed to determine the forces that occur during scanning on an HOPG surface. Therefore, it must be considered that the Fourier method is based on the assumption that the frequency-shift data start and end with 0 Hz. Because this is not necessarily the case for the frequency shift data measured while scanning an HOPG surface, applying the algorithm to the data shifts the average frequency-shift data to 0 Hz, and therefore a relevant amount of force might be neglected. For now, we can correct for this discrepancy by adding manually the offset force determined from the spectroscopic force–distance data. Also, note that i) the Fourier method is limited to the analysis of periodic structures that are larger than the torsional oscillation amplitude, ii) the number of pixels collected during imaging is essential for the success of the Fourier algorithm, and iii) due care must be taken in using the Fourier method for the bimodal approach because we know from the spectroscopic experiments that the flexural amplitude is larger compared to the torsional one. However, as stated in Section 2.2.3 entitled “Force reconstruction using Sader method” we assume that the approach is valid because of the

different oscillation directions in space. To corroborate this assumption, we analyzed the frequency-shift histograms of several images (HOPG, $5 \text{ nm} \times 5 \text{ nm}$) taken with systematically changed amplitude values for the torsional eigenmode and the third flexural eigenmode, and the results are shown in Figure 2-4.

2.2.5. Flexural and torsional eigenmode analysis

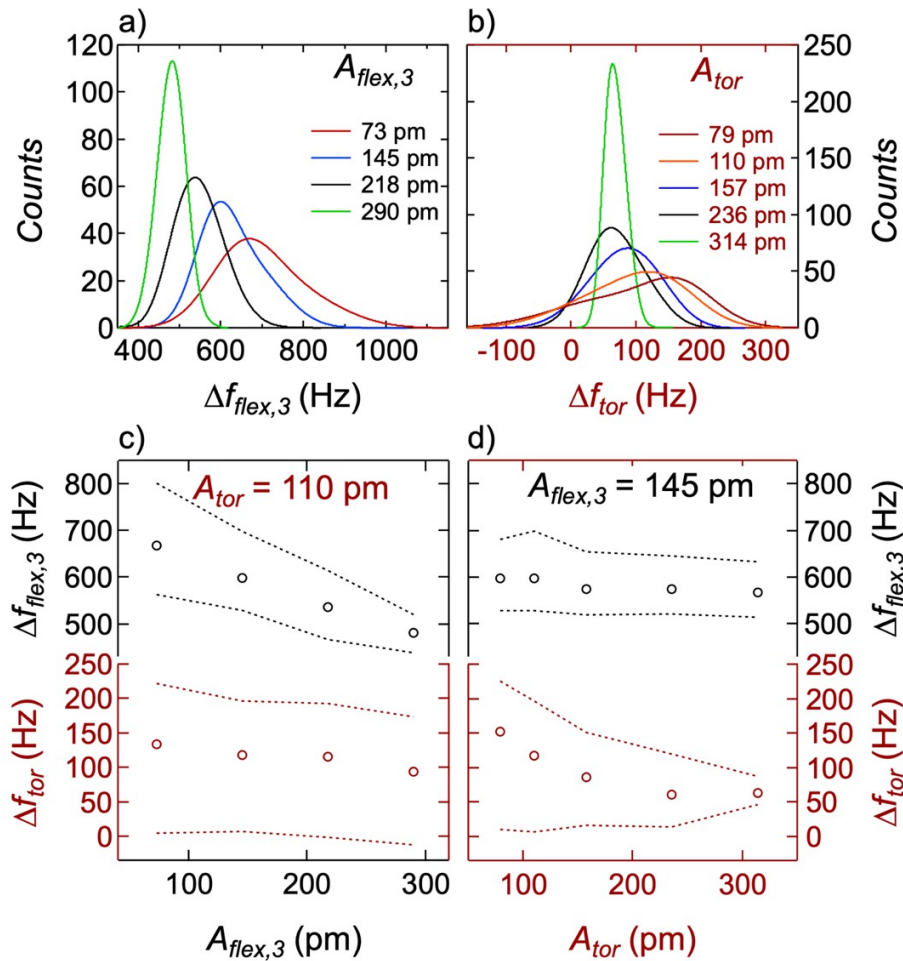


Figure 2-4: Influence of torsional and third-eigenmode flexural-oscillation amplitudes on observed frequency shifts at a second-flexural-eigenmode amplitude setpoint of 110 pm. a) Histograms of third-eigenmode flexural-frequency-shift images for different third-eigenmode flexural amplitudes. b) Histograms of torsional-frequency-shift images for different torsional amplitudes. Third-eigenmode flexural and torsional frequency shifts at maximum counts (open circles) and at full width at half-maximum (FWHM) (dashed lines) as a function of c) third-flexural-eigenmode amplitude at constant torsional-eigenmode amplitude of 110 pm and d) torsional-eigenmode amplitude at constant third-flexural-eigenmode amplitude of 145 pm (Reprinted from ref. [8], <https://doi.org/10.1002/admi.202101288>, © 2021.⁹).

⁹ This is an open access article under the terms of the Creative Commons Attribution License (<https://creativecommons.org/licenses/by/4.0/>), which permits use, distribution and reproduction in any medium, provided the original work is properly cited.

In Figure 2-4a, b, we show histograms of the frequency-shift values from images taken at a constant second-eigenmode amplitude setpoint of 120 pm. The histograms in Figure 2-4a represent the distribution of the third-eigenmode flexural frequency shift with increasing third-eigenmode flexural amplitude (73–290 pm) at a constant torsional-eigenmode amplitude of approximately 110 pm. The histograms in Figure 2-4b represent the distribution of the torsional frequency shift with increasing torsional-eigenmode amplitude (79–314 pm) at a constant third-eigenmode flexural amplitude of 145 pm. In Figure 2-4c, d, the corresponding frequency shifts at the maximum positions of the histograms in Figure 2-4a, b are shown as open circles, and the frequency shifts at full width at half- maximum (FWHM) are shown with dashed lines. Additionally, the cross-talk behavior between the torsional and third flexural frequency shifts and amplitudes was analyzed. Figure 2-4c shows that varying the third-flexural-eigenmode amplitude from 73 to 290 pm has little influence on the torsional-frequency- shift histogram, and Figure 2-4d shows that varying the torsional amplitude from 79 to 314 pm also has no significant influence on the third-eigenmode flexural frequency shift. However, we see that the frequency-shift values at maximum counts decrease with increasing amplitude, and the corresponding FWHM values decrease with increasing amplitude. Note the linear decrease for the third flexural frequency shift, whereas the torsional frequency shift seems to reach a plateau for torsional amplitudes of 157–236 pm. This seems reasonable because in this range the tip moves across more than one carbon hexagon during one oscillation cycle. Surprisingly, it was still feasible to achieve atomic resolution in the torsional-frequency-shift channel if the direction of torsional oscillation was along the zigzag direction of the carbon hexagons. However, no honey- comb structure was resolved for torsional amplitudes larger than the interatomic spacing of the carbon atoms in zigzag direction. We assume that this originates from the symmetry along this direction, which allows lattice resolution, although the torsional amplitude was larger compared to the interatomic spacings. This observation also helped us to determine the torsional oscillation sensitivity, such as described in more detail in the Experimental Section 2.4 and in the Supplementary Information (Section 7.1.2). Another interesting observation was the increasing asymmetry of the peaks in the histograms in Figure 2-4a, b when decreasing the amplitude of the third flexural eigenmode or the torsional eigenmode, respectively, although the same position was scanned. Surprisingly, the frequency shift at maximum counts was shifted to less-repulsive flexural frequency shifts such as shown in Figure 2-4a, c, whereas with decreasing amplitude it was shifted to more-repulsive torsional frequency shifts such as shown in Figure 2-4b, d. We interpret this as another indicator for the independence of the oscillations of the torsional and third flexural eigenmodes and therefore the validity of the bimodal approximation. It impressively demonstrates that for larger third-flexural-eigenmode

amplitudes, attractive long-range Van-der-Waals forces become increasingly dominant, which is not the case for sensing the in-plane interactions because of the (relatively) steady oscillation distance with respect to the HOPG surface. Consequently, the monomodal Fourier method [4] allows us to determine in-plane forces along the direction of the torsional oscillation based on the torsional-eigenmode frequency-shift data. The modified bimodal Fourier method can be used to calculate forces that are directed out of plane from the third-eigenmode frequency-shift data along the direction of the torsional-eigenmode oscillation.

2.2.6. Application of Fourier method to HOPG frequency-shift images for in-plane and out-of-plane force reconstruction

In Figure 2-5, we show images of the forces (a, b, e, f) deconvoluted from frequency-shift images, as well as the validation images of the torsional (c, d) and third flexural frequency shift (g, h) on HOPG using the Fourier method. The red-framed images a–d) were calculated from the frequency-shift images shown in Figure 2-2. Here, the deconvolution direction was from top to bottom because the image was taken with a scan angle of 0° . This resulted in a cantilever torsional-oscillation direction (indicated by the white arrows in Figure 2-5a, c) that was perpendicular to the fast scan axis. The blue-framed images e–h) were deconvoluted from left to right because the scan angle was 90° . This resulted in a cantilever torsional-oscillation direction (indicated by the white arrows in Figure 2-5e, g) that was parallel to the fast scan axis.

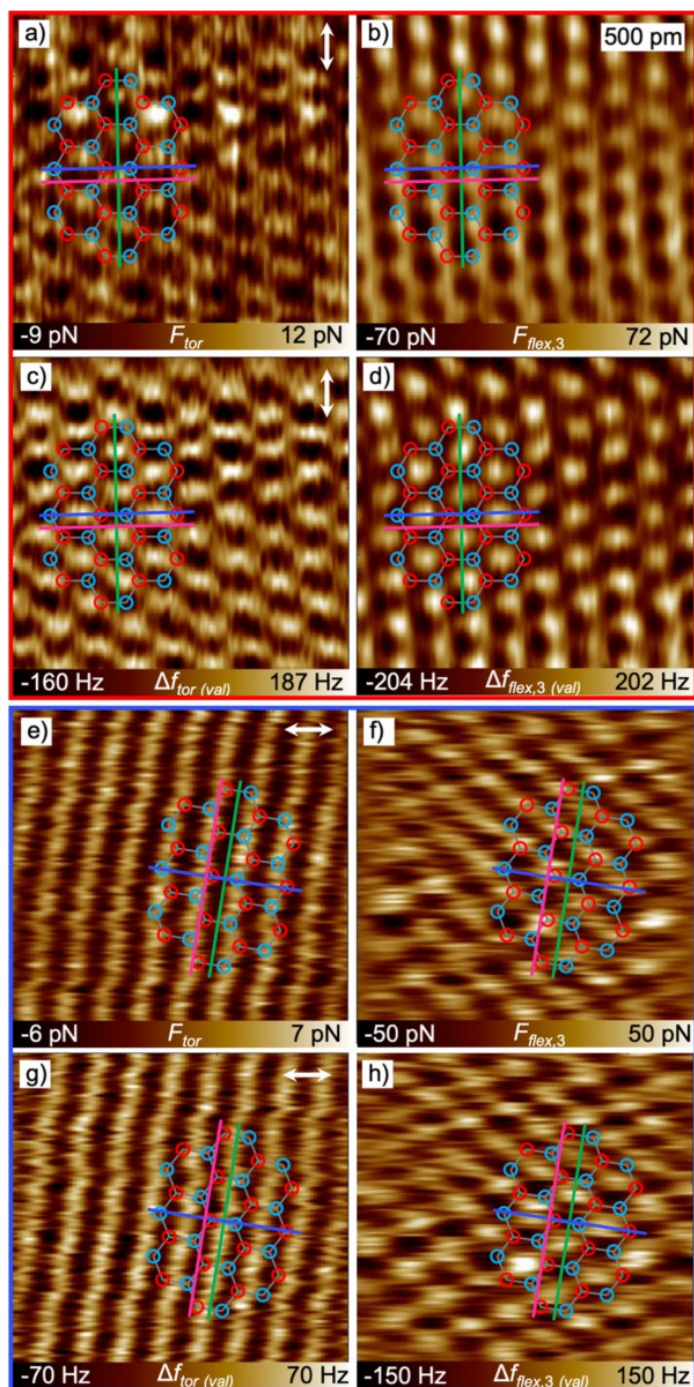


Figure 2-5: a, b, e, f) Forces and c, d, g, h) frequency-shift validation data determined from frequency-shift images using the Fourier method without offset correction. a, c, e, g) Torsional data were calculated using the monomodal Fourier method, b, d, f, h) flexural data were calculated using the bimodal Fourier method. Red: scan angle = 0° , $A_{tor} = 80$ pm, $A_{flex,2} = 100$ pm, $A_{0(flex,2)} = 770$ pm, $A_{flex,3} = 220$ pm. Blue: scan angle = 90° , $A_{tor} = 110$ pm, $A_{flex,2} = 90$ pm, $A_{0(flex,2)} = 770$ pm, and $A_{flex,3} = 150$ pm (Reprinted from ref. [8], <https://doi.org/10.1002/admi.202101288>, © 2021.¹⁰).

¹⁰ This is an open access article under the terms of the Creative Commons Attribution License (<https://creativecommons.org/licenses/by/4.0/>), which permits use, distribution and reproduction in any medium, provided the original work is properly cited.

Figure 2-5 shows that the deconvolution of forces from frequency-shift images was successful. The frequency-shift validation images calculated from Equations (2-9) and (2-10) show a constant frequency-shift offset relative to the original frequency-shift images, but the contrast is reproduced with satisfying accuracy (compare Figure 2-2b, c and Figure 2-5c, d). The comparison results in a torsional frequency-shift offset of 72 Hz and a flexural frequency-shift offset of 742 Hz. Very similar offset values (74 and 736 Hz, respectively) were determined for the blue-framed images, where the torsional oscillation direction was perpendicular to the fast scan axis. Consequently, an offset value of ≈ 8 pN must be added to the torsional forces and ≈ 480 pN to the flexural forces.

Although the angle between the fast scan axis and the orientation of the carbon hexagons was very similar ($\approx 10^\circ$ deviation) for the red-framed images (Figure 2-5a–d) and the blue-framed ones (Figure 2-5e–h), we can observe clear differences in the contrast formation. This might be partially due to the slightly different imaging parameters, but we assume that most of the variations can be attributed to the difference in the torsional oscillation direction relative to the carbon hexagons. This assumption was corroborated by the observation that the differences between the torsional frequency-shift images in Figure 2-5c, g are much more pronounced compared to those between the flexural frequency-shift images shown in Figure 2-5d, h. The most reasonable explanation for the striped appearance of the contrast in the torsional force and frequency-shift images in Figure 2-5e, g is the larger torsional amplitude ($\approx 30\%$) compared to the amplitude set for the torsional images in Figure 2-5a, c. From this consideration, the striped appearance of the torsional frequency-shift images would originate from lateral averaging, although note that we never observed atomically resolved contrast when the torsional oscillation direction was oriented along the armchair direction of the carbon hexagons. Obviously, the frequency-shift images and the force images are displaced slightly along the direction of the torsional oscillation, and this is a direct consequence of the relationship between force and frequency shift such as introduced by Giessibl [57] and Sader [60]. and Jarvis. Interestingly, we can observe an inversion of the contrast in the flexural-force image (Figure 2-5b) compared to the flexural-frequency-shift image (Figure 2-5d). This seems counterintuitive at first glance, but it is rational considering that the force is influenced predominantly by the gradient of the frequency shift. To compare the force and frequency-shift data directly, we took cross sections along the green, pink, and blue lines marked in Figure 2-5, and the results are shown in Figure 2-6. The frequency-shift cross sections were determined from the original data. The frequency-shift validation data and the original data are compared in Figure 7-6 and Figure 7-7 in the Supplementary Information (Section 7.1.9).

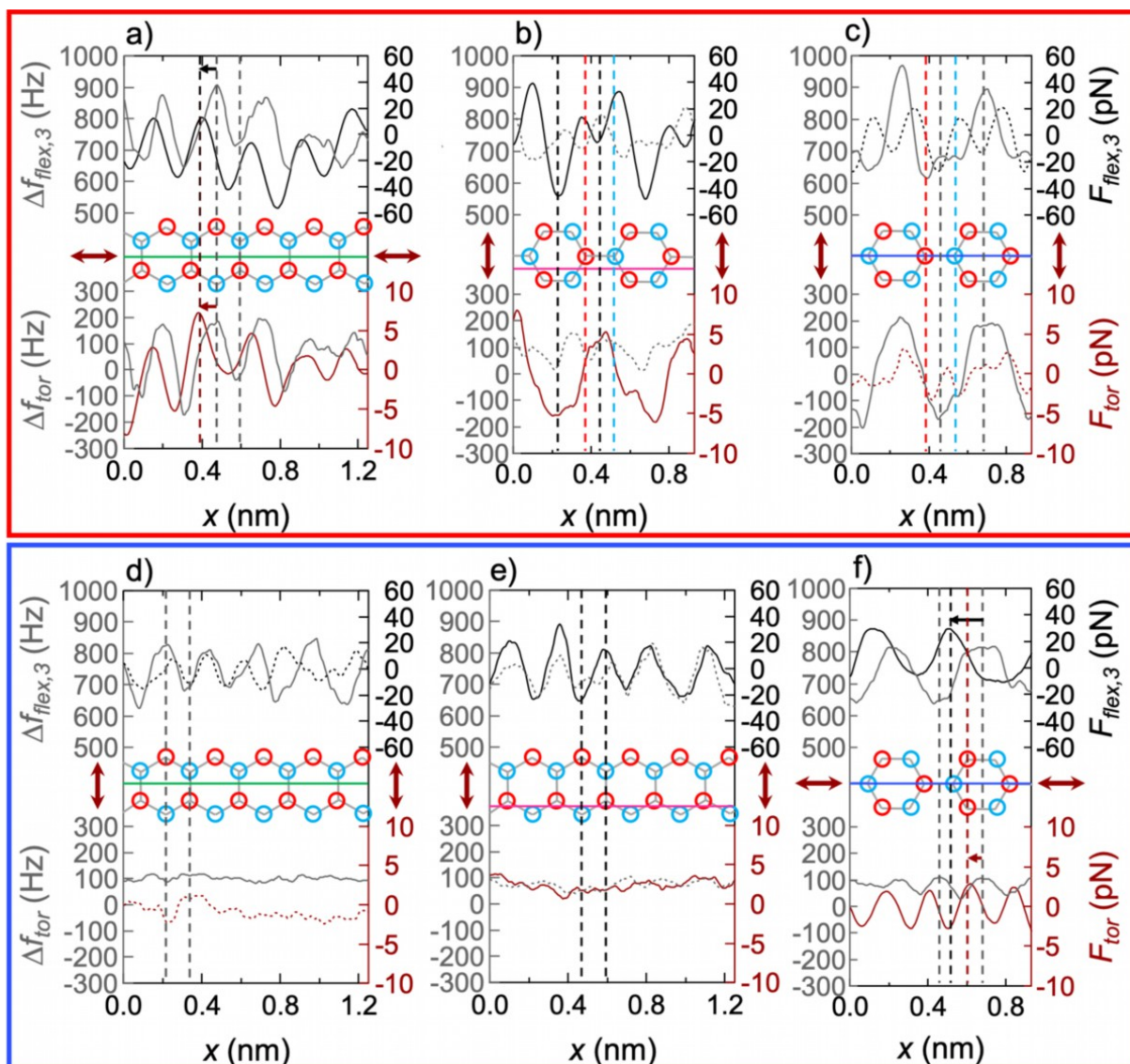


Figure 2-6: Cross-sectional profiles through force and frequency-shift images of HOPG along the green, pink, and blue lines in Figure 2-5. Profiles and axis labels are shown in gray for the frequency shift, black for the flexural forces, and red for the torsional forces. The vertical dashed lines mark the positions of characteristic local extrema of the profiles, following the same color code. The torsional oscillation was aligned approximately along the zigzag (resp. armchair) direction of the carbon hexagons for the cross sections shown within the red frame a–c) (resp. blue frame d–f)). The cross sections in (a), (d), and (e) are in the zigzag direction of the carbon hexagons, and those in (b), (c), and (e) are in the armchair direction. The cross sections marked a, d) green and c, f) blue cut the center of the hollow side, whereas those marked b, e) pink are offset from the center of the hollow side by the particular torsional amplitude values to enable analysis of force extrema (black and red arrows) (Reprinted from ref. [8], <https://doi.org/10.1002/admi.202101288>, © 2021.¹¹).

¹¹ This is an open access article under the terms of the Creative Commons Attribution License (<https://creativecommons.org/licenses/by/4.0/>), which permits use, distribution and reproduction in any medium, provided the original work is properly cited.

First, we analyzed the cross-sectional profiles (solid gray) of the frequency shifts shown in Figure 2-6a, c, d, f, which correspond to the green and blue lines marked in Figure 2-5c, d, e, h. As discussed in the previous sections and confirmed by the cross sections, the flexural frequency-shift maxima and minima (marked by gray dashed vertical lines) appear at the hollow sides and at the carbon bonds, respectively. Interestingly, it was feasible to distinguish between the atomic sides (red and light-blue dashed vertical lines) from the blue cross section (Figure 2-6c) through the flexural frequency-shift image by the local maxima or minima, respectively, which are different in magnitude. In contrast, the atomic sides could not be discriminated in the corresponding flexural frequency-shift images of Figure 2-2c (original) and Figure 2-5d (validation). The capability to discriminate between the atomic sides when imaging HOPG originates from the Bernal stacking of the carbon layers [115] (see schematic in Figure 2-1). This observation helps to explain the contrast inversion of the flexural-force image in Figure 2-5b compared to the flexural frequency-shift image in Figure 2-5d, which can be attributed to the existence of additional maxima and minima. The torsional frequency-shift maxima appear at the hollow sides in Figure 2-6a, c, if the torsional oscillation direction was along the zigzag direction of the carbon hexagons. Interestingly, we observe negative torsional frequency-shift values at the locations of the carbon bonds. This is surprising if we consider that the flexural frequency shift appears exclusively repulsive. On the other hand, such a behavior of the lateral frequency shift was also observed by Weymouth *et al.* [141] on the carbon bonds of 3,4,9,10-perylenetetracarboxylic dianhydride (PTCDA). A completely different distribution was observed if the torsional oscillation direction was approximately along the armchair direction of the carbon bonds, such as visible in Figure 2-6d, f. The torsional frequency shift in Figure 2-6d is approximately constant, whereas we observe an extra maximum at the position of the carbon bonds in Figure 2-6f, which corresponds to the position of the minimum flexural frequency shift (see gray dashed vertical lines). As discussed in Section 2.2.6 entitled “Application of Fourier method to HOPG frequency-shift images for in-plane and out-of-plane force reconstruction” this might be a consequence of the torsional oscillation amplitude, which was 30 pm larger for the images and cross sections shown in the blue frames in Figure 2-5e–h and 6d,e ($A_{tor} \approx 110$ pm) compared to the images and cross sections shown in the red frames in Figure 2-5a–d and 6a–c ($A_{tor} \approx 80$ pm). We assume that the smaller the oscillation amplitude in the lateral direction, the more sensitive the tip becomes to local variations in the interaction potential. This argument is corroborated by the observation that the torsional frequency shift does not sense attractive interactions for the images shown in Figure 2-6d, f, which indicates that the tip interacts with more than one carbon hexagon during one oscillation cycle.

From Figure 2-6a, f, it can be deduced that the shift of the flexural-force maxima relative to the frequency-shift maxima along the torsional oscillation direction (marked by black arrows and dashed lines) is approximately as large as the particular torsional amplitude (80 pm in Figure 2-6a and 110 pm in Figure 2-6f). This is also the case for the torsional-force profiles in Figure 2-6a, whereas the shift between torsional-force and frequency-shift profiles in Figure 2-6f is approximately half as large as the torsional amplitude (marked by red arrows and dashed lines). As a consequence, if the cross sections are drawn perpendicular to the torsional oscillation direction and through the center of the hollow sides (extrema of the frequency shift) such as indicated in Figure 2-6c, d (red/black dotted profiles), the curves do not include the force maxima and minima. Therefore, we show the frequency shifts as solid profiles and the forces as dotted profiles for the cross sections in Figure 2-6c (blue) and d (green). We additionally drew the cross sections marked in pink in Figure 2-6b, e, which are shifted from the center of the hollow side by the value of the particular torsional-oscillation amplitude. Thus, the profiles along the pink cross sections allow for the analysis of the force extrema (solid profiles) and do not include the extreme values of the frequency shifts (dotted profiles).

The maximum flexural forces in Figure 2-6b, originating from the carbon atoms, are distinguishable for the different atomic sides (red and blue vertical dashed lines). This appears nonintuitive at first glance because previously we always found that the maximum frequency shifts take place at the hollow sides rather than at the position of the carbon atoms. The contrast inversion originates from the direction dependence of the algorithm behind the Fourier method. In other words, if the algorithm is applied from top to bottom of the image instead from bottom to top, the force image will appear inverted. For the quantitative interpretation of the force deconvoluted with the Fourier method, it has to be considered that forces do not reflect absolute values but relative differences between the atomic sides. To this end, the mean values and standard deviations of the different local extrema of the forces were determined from the number of values that appear over a cross sectional length of 2 nm. Consequently, from the black solid profile in Figure 2-6b we can determine the flexural-force difference between the red and blue marked atoms to be 24 ± 4 pN. The force difference between the blue marked atom and the hollow side is 81 ± 4 pN, and that between the red marked atom and the hollow side is 57 ± 4 pN. The force difference between the center of the carbon bond and the hollow side is 48 ± 5 pN if determined from Figure 2-6b and 44 ± 10 pN if determined from Figure 2-6a, being a good match. Compared to similar studies from the literature on pentacene molecules [126], the determined values are in good agreement but are slightly larger than the literature value (≈ 37 pN). For the torsional forces, we can measure a force difference of

10 ± 2 pN between the carbon bonds (red dashed line) and the hollow sides for Figure 2-6a and of 11 ± 2 pN for Figure 2-6b if the torsional oscillation direction was along the zigzag direction of the carbon bonds. From Figure 2-6e, we observe that the flexural-force difference between the carbon bonds and the hollow sides is 48 ± 9 pN, and from Figure 2-6f the force difference was measured as 41 ± 10 pN. The torsional force difference between the hollow sides and the carbon bonds can be determined from Figure 2-6f as 5 ± 1 pN if the torsional oscillation direction was approximately along the armchair direction of the carbon bonds. From the cross sections shown in Figure 2-6e, it was not possible to determine reliable torsional force-difference values because of the striped pattern of the frequency-shift distribution as discussed in the previous section. Consequently, the flexural-force differences between the carbon bonds and the hollow sides are in good agreement, regardless of the direction of the torsional oscillation. Interestingly, torsional forces between the different sides differ remarkably depending on the direction of the torsional oscillation relative to the orientation of the carbon hexagons (armchair or zigzag). To gain more understanding of the torsional frequency-shift and respective force images, it might help to consider symmetry reasons for the direction of the torsional oscillation with respect to the alignment of the carbon hexagons. Although the torsional oscillation amplitude is very small, the tip interacts with several atoms of the hexagonal lattice during one cycle. For the alignment of the carbon hexagons with respect to the tip oscillation as shown in the schemes of Figure 2-6a–c (zigzag orientation), we observe very high symmetry, *i.e.*, along the drawn cross sections, the tip senses the same atom sides (red and blue) during both oscillation half cycles. If the torsional oscillation direction is oriented along the armchair direction of the carbon hexagons as shown in Figure 2-6d–f, this symmetry is broken. This explains the striped appearance of the frequency- shift and force images. On the other hand, it is reasonable to believe and highly expected to sense differences in the local in-plane forces depending on the oscillation direction relative to the orientation of the carbon hexagons. Although the elastic constants of graphite do not imply an in-plane anisotropy [142], in-plane forces determined locally on the atomic scale can differ depending on the oscillation direction because of the different numbers of carbon bonds involved, as demonstrated in the present study.

2.3. Conclusion

Force quantification by AFM is indispensable for understanding the mechanical characteristics of materials, in particular at the atomic scale and in air under ambient conditions. We presented a multifrequency methodology that simultaneously determines the in-plane and out-of-plane force differences within the topmost graphene layer of HOPG with atomic resolution. By analyzing the mean deflection of the cantilever, we showed that this graphene layer is lifted locally from the bulk by the exerted tip forces that exceed the weak Van-der-Waals interactions between the basal planes. This effect must be addressed when analyzing forces from dynamic force spectroscopy data. In addition, we detected a comparably large hysteretic behavior between approach and retract curves on HOPG in air under ambient conditions. This was partially assigned to the presence of water films on the surface, but we assume that hysteresis originates mainly from the local lift of the topmost carbon layers, which complicates interpretation of spectroscopic data. We showed that the in-plane force differences between carbon bonds or carbon atoms and the hollow sides exist depending on the alignment of the shear direction relative to the alignment of the carbon bonds. In contrast, the force differences in the out-of-plane direction are independent of the shear direction. To quantify atom-atom interactions, we presumed validity of the bimodal approximation for lateral tip oscillations. As a key result, we determined the in-plane force between carbon bonds and hollow sides to be 11 ± 2 or 5 ± 1 pN when shearing carbon hexagons along the zigzag or armchair direction, respectively. This shows the strong anisotropic mechanical behavior of HOPG at the atomic level that must be considered when designing graphene-based nanomaterials.

2.4. Experimental Section

Sample. The HOPG sample (grade 2) was purchased from SPI Supplies (Structure Probe, Inc., West Chester, PA, USA) and had a mosaic spread angle of as little as $0.8 \pm 0.2^\circ$. Prior to the AFM experiments, it was cleaved with adhesive tape in air under ambient conditions to expose a fresh clean surface.

Cantilevers. Supersharpest cantilevers of the type HiResC15/Cr-Au were purchased from Mikromasch (Innovative Solutions Bulgaria Ltd., Sofia, Bulgaria). The cantilevers used for the experiments shown in this study were chosen to exhibit very similar force constants and free vibration resonance frequencies ($\leq 2\%$ relative aberration). Representative values of the resonance frequencies were $f_{0\text{ (flex,1)}} \approx 266$ kHz, $f_{0\text{ (flex,2)}} \approx 1.67$ MHz, $f_{0\text{ (flex,3)}} \approx 4.62$ MHz, and $f_{0\text{ (tor)}} \approx 1.73$ MHz. The respective force constants were determined as $k_{\text{flex,1}} \approx 26$ N m⁻¹, $k_{\text{flex,2}} \approx 644$ N m⁻¹, $k_{\text{flex,3}} \approx 3489$ N m⁻¹, and $k_{\text{tor}} \approx 472$ N m⁻¹ (details are given in the Supplementary Information (Section 7.1.2)). The manufacturer assures a tip radius of <1 nm realized by an extra tip consisting of hydrophobic DLC.

Environmental conditions. The temperature in the AFM chamber while imaging was 26–27 °C, and the relative humidity was 22–31 % for the different experiments. Neither the temperature nor the relative humidity was actively controlled, but the imaging conditions remained stable during imaging.

Trimodal AFM setup. Experiments were performed with a Cypher S atomic force microscope (Asylum Research, Oxford Instruments, Santa Barbara, CA, USA) equipped with a blueDrive photothermal excitation of the cantilever. The torsional and third-eigenmode flexural frequency shifts were tracked with additional phase-locked loops (HF2PLL, Zurich Instruments, Zurich, Switzerland). The gains of the PLLs ($P \approx 45\text{--}46$, $I \approx 32\ 000\text{--}49\ 000$ for the cantilever used) were adjusted following numbers suggested by the “PLL Advisor” of the ziControl software (Zurich Instruments, Zurich, Switzerland), providing stable tracking of the torsional and the third flexural eigenmode resonance frequencies. Proper gains for the amplitude feedback (constant-amplitude frequency modulation, $P \approx 1$, $I \approx 1000\text{--}4000$) were sought by toggling the setpoint amplitude between two values (typically in the range of $\approx 50\%$ of the measurement setpoint amplitude) ensuring that the time signal resulted in a decent rectangular shape. Two PID controllers built into the same instrument were used to adjust the drive amplitudes to maintain constant torsional and third-eigenmode flexural amplitudes.

Calibration of torsional inverse optical lever sensitivity. First, the torsional force constant of the cantilever was determined using the Sader method [143, 144]. Subsequently, the calibration of the torsional resonance invOLS was accomplished by fitting the torsional resonance peak in the lateral thermal noise spectrum to the algorithm developed in refs. [145, 146]. However, it needs to be mentioned that the determination of the torsional force constant using the Sader method is prone to errors due to the strong dependency of the obtained values on the dimensions of the cantilever. Hence, the torsional invOLS value was corrected based on the results of the histogram analysis in Figure 2-4b, d. It is assumed that an asymmetric peak distribution in the histogram is a strong indication of a sufficiently small torsional amplitude reflecting values smaller than the interatomic spacing of carbon atoms. Hence, the transition between the torsional amplitudes corresponding to symmetric and asymmetric histograms was taken as reference value where the oscillation matches the interatomic spacing of carbon atoms in zigzag direction. Further details on the calibration procedure are given in the Supplementary Information (Section 7.1.2).

Data processing. The topography images shown were first-order flattened to remove any tilt from the images using the Igor Pro v6.36 software (WaveMetrics Inc., Lake Oswego, OR, USA). All images resulting directly from AFM measurements were treated with a 3×2 Gauss filter to remove noise from the images. This step was additionally required to enable the successful application of the Fourier method. MATLAB R2018a (MathWorks Inc., Natick, MA, USA) was used for the implementation of the Fourier method into a program code based on the script provided by Seeholzer *et al.* [4]. Subsequently, the calculated force images were smoothed with a Savitzky–Golay filter over nine points with a first-order polynomial. The same smoothing procedure was accomplished to reduce noise in the cross sections shown.

2.5. Acknowledgements

The authors thank Niklas Scheer for helping with the MATLAB code and the Deutsche Forschungsgemeinschaft (Project number 407750697) for financial support.

3. Torsional and lateral eigenmode oscillations for atomic resolution imaging of HOPG in air under ambient conditions¹²

Combined in-plane and out-of-plane multifrequency atomic force microscopy techniques have been demonstrated to be important tools to decipher spatial differences of sample surfaces at the atomic scale. The analysis of physical properties perpendicular to the sample surface is routinely achieved from flexural cantilever oscillations, whereas the interpretation of in-plane sample properties *via* force microscopy is still challenging. Besides the torsional oscillation, there is the additional option to exploit the lateral oscillation of the cantilever for in-plane surface analysis. In this study, we used different multifrequency force microscopy approaches to attain better understanding of the interactions between a super-sharp tip and an HOPG surface focusing on the discrimination between friction and shear forces. We found that the lateral eigenmode is suitable for the determination of the shear modulus whereas the torsional eigenmode provides information on local friction forces between tip and sample. Based on the results, we propose that the full set of elastic constants of graphite can be determined from combined in-plane and out-of-plane multifrequency atomic force microscopy if ultrasmall amplitudes and high force constants are used.

3.1. Introduction

Understanding the in-plane nanomechanical behavior of graphitic surfaces at the atomic scale under ambient conditions in air is of utmost importance to predict the long-term performance of graphene-based nanodevices such as Van-der-Waals heterostructures [147] or for DNA sequencing [148]. Multifrequency atomic force microscopy (AFM) [68] was shown to be an excellent tool for the quantification of forces at the nanoscale in out-of-plane as well as in-plane direction [8, 127, 131]. The out-of-plane force deconvolution and determination of elastic moduli from bimodal AFM spectroscopy data using the Sader method [60] or the matrix method [58] are well established. In contrast, the determination of in-plane forces and shear moduli from spectroscopic data is still challenging [6, 88]. One issue is the difficulty to excite the cantilever in the in-plane direction. This problem can either be addressed by using qPlus sensors [61, 122, 149] or by photothermal excitation [43, 44]. The photothermal excitation technique is based on a power-modulated laser focused at the base of the cantilever and a few micrometers

¹² This Section was published as “Torsional and lateral eigenmode oscillations for atomic resolution imaging of HOPG in air under ambient conditions” by A. L. Eichhorn and C. Dietz in *Scientific Reports*, 2022. 12(1): p. 8981. This is an open access article under the terms of the Creative Commons Attribution License (<https://creativecommons.org/licenses/by/4.0/>), which permits use, distribution and reproduction in any medium, provided the original work is properly cited. References were adapted to provide continuous numbering throughout the whole work.

off the cantilever length symmetry axis. This results in an in-plane oscillation if the excitation frequency matches the resonance frequency of the desired eigenmode. Photothermal excitation facilitated atomic resolution imaging using the torsional-eigenmode oscillation in bimodal AFM [87]. A second issue is the discrimination between torsional and lateral eigenmodes. In most publications the term “lateral” is used as synonym for both, the torsional and lateral eigenmode. This might originate from the fact that in theory the lateral-eigenmode oscillation should not be observable using the beam detection methods as schematically explained by Ding *et al.* [89] and illustrated in Figure 7-8. However, they rationalized that the tip attached to the cantilever can induce coupling between lateral and torsional eigenmodes facilitating the detection of the lateral resonance using a standard detection laser and segmented photodiodes. The authors demonstrated that both eigenmodes are useful for imaging and that the lateral oscillation might be advantageous over the torsional one. The main issue in using the lateral eigenmode for imaging is the calibration of the inverse optical lever sensitivity (invOLS) to attain quantitative or semi-quantitative data. There are a few approaches for the determination of the torsional invOLS [146, 150-153], whereas there is currently no procedure for the determination of the lateral invOLS to the best of our knowledge.

In this study, we compared the suitability of the torsional and the lateral eigenmodes for atomic resolution imaging of HOPG in air under ambient conditions. The comparison is based on our recently published methodology named AMFlex2-FMTor1-FMFlex3 mode introduced in Ref. [8] with a slightly modified setup (AMFlex2-FMLat1-FMFlex3). Both setups exploit the second flexural eigenmode for the topographical feedback in amplitude modulation (AM) whereas the first torsional, first lateral and third flexural mode are frequency-modulated (FM) and controlled by phase-locked-loop (PLL) electronics. Inspired by the work of colleagues in the field, we used higher flexural eigenmodes which were shown to be beneficial for atomic resolution imaging due to the enhanced stiffness compared to the first flexural eigenmode [64, 65]. Additionally, the combination of small free amplitudes and small amplitude setpoints was used for imaging as it was shown by Santos *et al.* [69, 70] and Lai *et al.* [154] that the method can lead to a very close proximity between tip and sample, being essential for high resolution imaging.

For some of the super-sharp tips we used, it was impossible to excite the second flexural and the first torsional eigenmode individually due to the close proximity of their resonance frequencies. Interestingly, the coupling of the two eigenmodes facilitated atomic resolution imaging. A scheme of possible setups as well as the resulting movement of the tip are

schematically shown in Figure 3-1. If there is coupling between the second flexural and the first torsional eigenmode, the torsional oscillation cannot be controlled individually (open loop (OL)). From the second flexural and the first torsional phase shifts, dissipation in out-of-plane and in-plane direction can be determined, respectively. Unfortunately, the AMFlex2-OLTor1 mode is not suitable for the deconvolution of in-plane or out-of-plane forces. Consequently, we extended the AMFlex2-OLTor1 mode, by two phase-locked loops (PLL) for frequency modulation (FM) of the first lateral and the third flexural eigenmode. The resulting AMFlex2-OLTor1-FMLat1-FMFlex3 mode such as schematically depicted in Figure 3-1 facilitates quantification of in-plane and out-of-plane forces, reconstructed from lateral- and third-eigenmode flexural frequency-shift data.

In this work, we analyzed the imaging capability of coupled flexural/torsional oscillations as well as the suitability of the first lateral eigenmode for atomic resolution imaging and provide an approach for the calibration of the lateral eigenmode optical lever sensitivity. In addition, we calculated in-plane forces from torsional and lateral frequency-shift data and analyzed the origin of the forces regarding friction or shear. Analyzing the tip-trajectories, effective torsional and lateral amplitudes as well as the maximum indentation of the tip into the surface (with and without compression) were estimated. The plausibility of the determined lateral forces was confirmed by calculating the lateral displacement using the literature value of the shear modulus of HOPG.

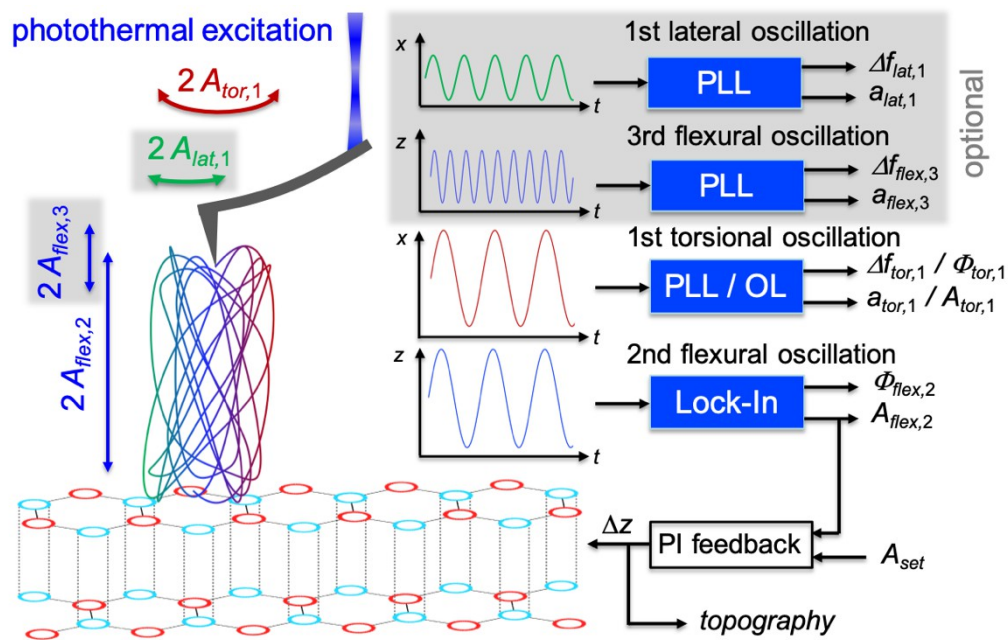


Figure 3-1: Schematic illustration depicting the setup of the AMFlex2-OLTor1-FMLat1-FMFlex3 mode. Topographical feedback is driven at the coupled resonance frequency of the second flexural and the first torsional eigenmode using the flexural component for amplitude modulation. The first-torsional-eigenmode amplitude and phase are recorded at the same frequency in an open-loop configuration. Optionally, the setup can be expanded by one or two phase-locked loops, tracking the phase at resonance of the first lateral and/or the third flexural eigenmode which allowed us to quantify forces in in-plane and/or out-of-plane direction from the respective frequency-shift data. Dissipative tip-sample interactions can be analyzed from the drive amplitudes ($a_{lat,1}$, $a_{flex,3}$) and the respective phase shifts ($\Phi_{flex,2}$, $\Phi_{tor,1}$). The cantilever dimension was substantially reduced for simplicity (Reprinted from ref. [182], <https://doi.org/10.1038/s41598-022-13065-9>, © 2022.¹³).

¹³ This is an open access article under the terms of the Creative Commons Attribution License (<https://creativecommons.org/licenses/by/4.0/>), which permits use, distribution and reproduction in any medium, provided the original work is properly cited.

3.2. Results and discussion

3.2.1. Imaging capability of the AMFlex2-OLTor1-FMLat1 mode for atomic resolution

From Figure 3-2, we get an overview of the capability of different imaging channels for atomic resolution imaging in air under ambient conditions depending on the z -sensor position. Increasing z -sensor position (from left to right) causes a reduction of the average tip-sample distance. Figure 3-2a–e show schemes of the expected tip-trajectory corresponding to the AMFlex2-OLTor1-FMLat1 mode with a lateral-eigenmode amplitude setpoint of $A_{lat,1} = 863$ pm. The shown tip-trajectories were calculated by plotting the out-of-plane deflection $z(t)$ vs. the in-plane deflection $x(t)$ of the cantilever using linear combinations of cosine functions such as shown by Benaglia *et al.* [155] for the z -component and assuming that $\Phi_{tor,1} = 90^\circ$ (see eqs. (3-4, 3-5) and Figure 7-9 of the Supplementary Information (Section 7.2.2) for details). The lateral-eigenmode invOLS was calibrated by imaging a wrinkle of a graphene layer on an HOPG sample with different lateral amplitude setpoints while oscillating perpendicular to the wrinkle and comparing the images with the results of a Savitzky-Golay-filtered reference image. A detailed description of the technique can be found in Section 4 (Calibration of lateral-oscillation-eigenmode sensitivity) of the Supplementary Information. From Figure 3-2a–e the second flexural-eigenmode-amplitude setpoint is reduced from 700 to 454 pm, causing a reduction of the torsional amplitude due to the coupling of both modes (Figure 3-2, second row). The corresponding approximate z -sensor position can be taken from the third row of Figure 3-2. From spectroscopic experiments (local amplitude distance curves recording all available observables), we can visualize the dependence of the second flexural amplitude (Figure 3-2f), the first torsional amplitude (Figure 3-2l) and the first lateral frequency shift (Figure 3-2r) on the z -sensor position. The crossed circles mark the positions where the AFM images of Figure 3-2 where taken. The height images are shown in Figure 3-2g–k, the “error images” of the first torsional amplitude in Figure 3-2m–q and the first lateral frequency-shift images in Figure 3-2s–w. “Error images” of the first torsional amplitude here means the deviation of the actual torsional amplitude relative to the torsional-amplitude setpoint corresponding to the second flexural-amplitude setpoint due to the coupling of both eigenmodes.

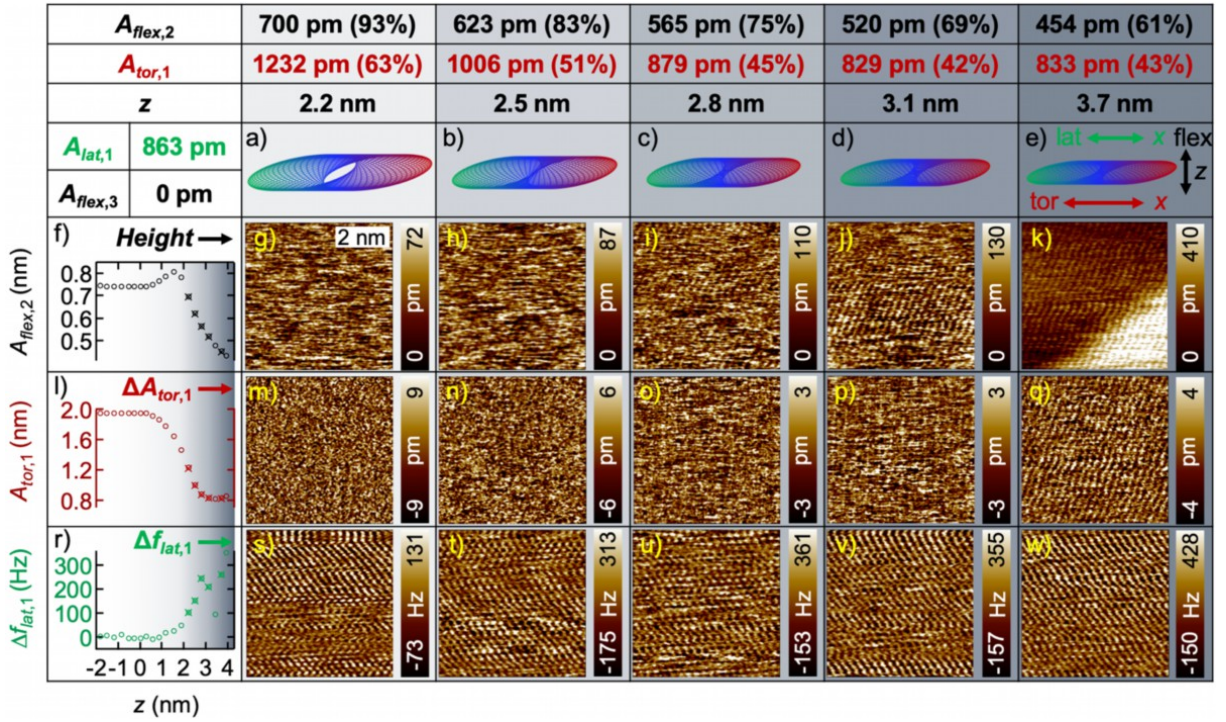


Figure 3-2: Imaging and spectroscopy on HOPG at a covered step edge in AMFlex2-OLTor1-FMLat1 mode with 863 pm lateral-eigenmode-amplitude setpoint. (a–e) Schemes of the tip trajectory for the coupled second flexural and first torsional cantilever oscillation for decreasing second flexural-eigenmode-amplitude setpoints $A_{flex,2}$. The setpoints of $A_{flex,2}$ are listed in the first, the corresponding setpoints of the first-torsional-eigenmode amplitude $A_{tor,1}$ in the second row and the approximate z -sensor position at the third row. The values in brackets represent the percentages of the setpoints from the free amplitudes $A_{0(flex,2)}$ and $A_{0(tor,1)}$. (f) Second flexural-, (l) first torsional-eigenmode amplitude $A_{tor,1}$ and (r) first lateral frequency shift $\Delta f_{lat,1}$ vs. z -sensor position, where the crossed circles mark the positions at which the images were taken. (g–k) Height, (m–q) first torsional-eigenmode amplitude error $\Delta A_{tor,1}$ and (s–w) $\Delta f_{lat,1}$ images at decreasing $A_{flex,2}$. Note, that $\Phi_{tor,1}$ was assumed to be 90° for the calculation of the tip-trajectories shown in (a–e) (Reprinted from ref. [182], <https://doi.org/10.1038/s41598-022-13065-9>, © 2022.¹⁴).

Comparing the amplitude vs. z -position curves in Figure 3-2f and l, it becomes evident that although the second flexural and the first torsional oscillations are coupled, they show different dependencies on the tip-sample distance. These differences are consistent with results from uncoupled flexural–torsional AFM studies in open-loop configuration [87]. The lateral frequency shift vs. z -sensor position curve in Figure 3-2r shows an increasing repulsive interaction with decreasing tip-sample distance. Atomic resolution imaging was feasible in all three channels as e.g. visible in Figure 3-2k, q, w at a z -sensor position of approximately 3.7 nm.

¹⁴ This is an open access article under the terms of the Creative Commons Attribution License (<https://creativecommons.org/licenses/by/4.0/>), which permits use, distribution and reproduction in any medium, provided the original work is properly cited.

Interestingly, the lateral frequency-shift images show atomically resolved structures at setpoint ratios up to 93 % of the second flexural-eigenmode amplitude as observable in Figure 3-2s, which corresponds to a z -sensor value of approximately 2.2 nm. Compared to imaging with “uncoupled” cantilevers, where atomic resolution imaging was impossible to achieve using setpoint ratios larger than 15 %, it is reasonable to believe that performing measurements with “coupled” cantilevers implies more gentle conditions, preserving the integrity of both, tip and sample. Note, that the torsional amplitude ratio was already at 63 % which fits to our observation that the stiffness of the second flexural eigenmode was higher compared to the first torsional eigenmode stiffness for the type of cantilevers used in this study (see “Materials and methods” (Section 3.4) for details). At this position, however, neither in the height image (Figure 3-2g) nor in the torsional-amplitude error image (Figure 3-2m) atomic contrast could be resolved. Lowering the second flexural-eigenmode-amplitude setpoint, atomic contrast becomes more and more apparent in the height images (Figure 3-2m–q). The growing corrugation amplitude (measured vertical distance between atomic and hollow side) is assumed to originate from an increase in the mean cantilever deflection [87, 132, 133]. Strikingly, the height image at a z -sensor position of 3.7 nm (Figure 3-2k) shows a step which matches the height of individual graphene layers. This step is neither observable in the $\Delta A_{tor,1}$ image (Figure 3-2q) nor in the $\Delta f_{lat,1}$ image at the same z -sensor position. Consequently, the topographic feedback seems to function extremely precise. Another interesting observation is, that the atomic structure at both, the lower and the upper plateau of the graphene step, exhibit the same arrangement of carbon atoms. This leads us to the conclusion that we imaged a monoatomic step edge covered by a small number of graphene layers which is in line with results shown by Aboalizadeh *et al.* [156]. From this observation the question arises why we were not able to resolve the step at smaller z -sensor positions. To answer the question, we exemplarily drew two cross sectional profiles through the height images shown in Figure 3-2k, j (see Figure 7-10 in the Supplementary Information (Section 7.2.3)). We assume that the visibility of the step edge depends on whether the average tip-sample force (represented by the mean deflection, averaged over several oscillation cycles) is predominantly attractive or repulsive. On the right side of Figure 7-10, we schematically sketched the alleged interaction between tip and sample on a covered step edge. In the predominantly attractive regime, we assume that several graphene layers cover the step such as depicted in the top right part of Figure 7-10. As discussed in our recent work and by others [8, 134], it is reasonable to believe that the topmost carbon layers are lifted by the attractive tip-sample interactions. Consequently, the tip will not sense the step edge. If imaging takes place in the predominantly repulsive regime, we assume that

the graphene cover layers are tightly stretched over the step edge as sketched in the bottom right of Figure 7-10.

From the imaging results shown in Figure 3-2 we can conclude that the coupled motion of the cantilever (AMFlex2-OLTor1) seems to promote atomic resolution at higher setpoint ratios ($A_{flex,2}/A_{0(flex,2)}$) compared to uncoupled ones. This can, on the one hand, be attributed to the enhanced dynamic stiffness of the coupled flexural/torsional oscillation of the cantilever and, on the other hand, to the oval shape of the tip trajectory. This might lead to a reduced influence of the interactions far away from the center of the oscillation, because the tip will have the closest distance to the sample and therefore the highest interaction at the currently measured local position. Nevertheless, the largest drawback of imaging with coupled cantilever modes is that the relation between the flexural and the torsional amplitudes cannot be set individually. Additionally, it needs to be considered that the combined in-plane oscillation of torsional and lateral components needs to be analyzed in detail in order to get a better understanding regarding the interaction with the sample. An idea for future studies would be tailoring cantilevers *e.g.* by a controlled introduction of holes at different positions of the cantilever such as shown by Eslami *et al.* [157], in order to analyze the influence of different resonance-frequency ratios.

3.2.2. Comparison of torsional and lateral frequency-shift images as a function of the amplitude setpoints

In order to gain deeper insights into the different oscillation behaviors of the torsional and the lateral eigenmodes, we analyzed several $5 \times 5 \text{ nm}^2$ frequency-shift images taken in the AMFlex2-FMLat1-FMFlex3 mode and the AMFlex2-FMTor1-FMFlex3 mode at different lateral- and torsional-eigenmode setpoints. The results are shown in Figure 3-3. In Figure 3-3a, e and Figure 3-3d, h lateral and torsional frequency-shift images ($2.5 \times 2.5 \text{ nm}^2$ zoom-in) taken at $A_{lat,1} = 518 \text{ pm}$ (a), $A_{lat,1} = 3451 \text{ pm}$ (e) and $A_{tor,1} = 158 \text{ pm}$ (d), $A_{tor,1} = 628 \text{ pm}$ (h) are shown exemplarily. The corresponding histograms of the lateral and the torsional frequency-shift images can be seen in Figure 3-3b, c, respectively. The open circles in Figure 3-3f, g show the lateral and torsional frequency shifts at maximum counts and the dashed lines represent the full width at half maximum (FWHM) as a function of the lateral- and torsional-amplitude setpoints, respectively.

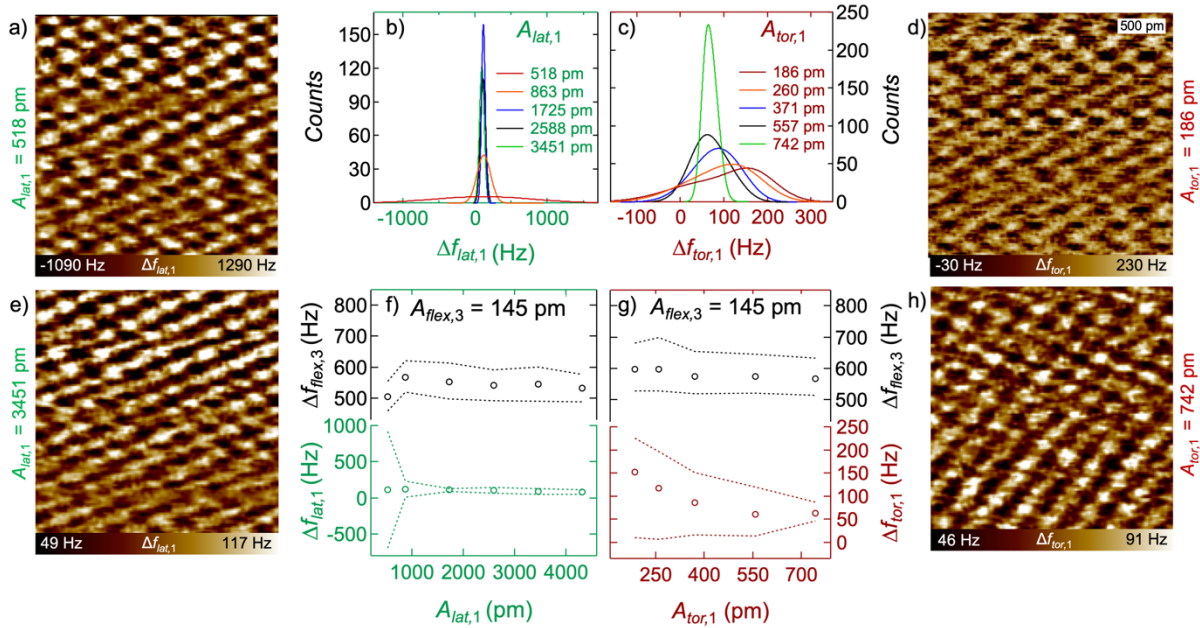


Figure 3-3: Influence of the lateral- and the torsional-amplitude setpoints on the frequency shifts in AMFlex2-FMLat1-FMFlex3 mode and in AMFlex2-FMTor1-FMFlex3 mode respectively. Frequency-shift images are shown exemplarily taken at $A_{lat,1} = 518$ pm in (a), $A_{lat,1} = 3451$ pm in (e) and $A_{tor,1} = 158$ pm in (d), $A_{tor,1} = 628$ pm in (h). Histograms of lateral (b) and torsional frequency-shift images (c) at different lateral-/torsional-amplitude setpoints. Third-eigenmode flexural and lateral (f)/torsional (g) frequency shifts at maximum counts (open circles) and at FWHM (dotted lines) as a function of the lateral-/torsional-amplitude setpoints at a constant third flexural-eigenmode amplitude of 145 pm and a constant second flexural-eigenmode amplitude of 110 pm (Reprinted from ref. [182], <https://doi.org/10.1038/s41598-022-13065-9>, © 2022.¹⁵).

If we compare the frequency-shift images taken in the AMFlex2-FMLat1-FMFlex3 mode in Figure 3-3a, e with the images taken in the AMFlex2-FMTor1-FMFlex3 mode in Figure 3-3d, h we observe that atomic contrast was achieved in all images but the range of the frequency-shift values strongly differs. While the lateral and torsional frequency-shift images taken at the higher-amplitude setpoints ($A_{lat,1} = 3451$ pm and $A_{tor,1} = 628$ pm) shown in Figure 3-3e, h show similar frequency-shift ranges, the frequency-shift images at smaller-amplitude setpoints ($A_{lat,1} = 518$ pm and $A_{tor,1} = 158$ pm) in Figure 3-3a, e clearly differ regarding their frequency-shift ranges and the distribution of the values. This becomes even more evident by looking at the histograms corresponding to frequency-shift images taken at five different lateral- (Figure 3-3b) and torsional-amplitude (Figure 3-3c) setpoints. In general, the full width at half maximum (FWHM) of the peaks increases with decreasing amplitude setpoints (lateral/torsional). The histograms of the lateral frequency-shift images remain symmetric around a center value of

¹⁵ This is an open access article under the terms of the Creative Commons Attribution License (<https://creativecommons.org/licenses/by/4.0/>), which permits use, distribution and reproduction in any medium, provided the original work is properly cited.

approximately 120 Hz, whereas the histograms of the torsional frequency-shift images become asymmetric for torsional-amplitude setpoints smaller than 314 pm. As a result, the maxima of the histograms are shifted to more repulsive values. Moreover, the third eigenmode flexural frequency shift is only slightly influenced by the lateral- or torsional-eigenmode amplitude which corroborates the assumption of the independency of the in-plane (lateral/torsional) and the out-of-plane (flexural) eigenmodes (Figure 3-3f, g (top graphs)). Interestingly, we observe that although the torsional- and lateral-amplitude setpoints are in most cases substantially larger than the interatomic spacing of the carbon atoms, we can still obtain atomic contrast in the frequency-shift images. To further investigate this phenomenon, we calculated the tip-trajectory resulting from the combined lateral-flexural (Figure 3-4a, b) or torsional-flexural (Figure 3-4c, d) oscillations of the cantilever according to equations (3-4, 3-5) for two different lateral and torsional amplitudes, respectively.

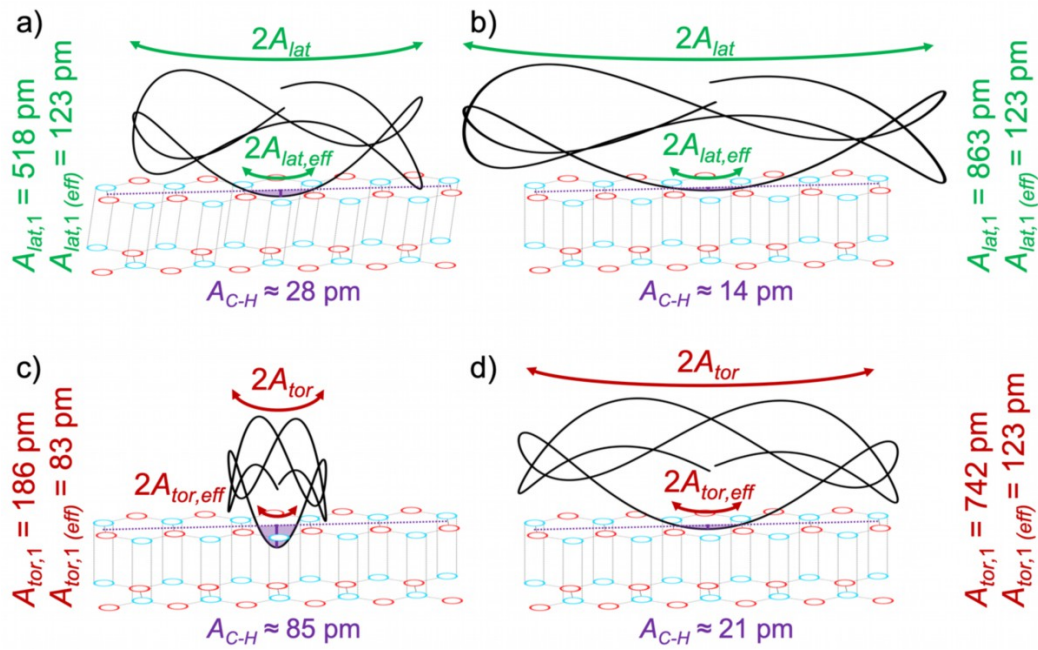


Figure 3-4: Extract of the calculated tip-trajectory of a cantilever oscillating in the AMFlex2-FMLat1-FMFlex3 mode (a, b) or in the AMFlex2-FMTor1-FMFlex3 mode (c, d) with $A_{flex,2} = 110$ pm and $A_{flex,3} = 145$ pm. The trajectories are shown for two different torsional- and lateral-oscillation eigenmodes: (a) $A_{lat,1} = 518$ pm, (b) $A_{lat,1} = 863$ pm, (c) $A_{tor,1} = 186$ pm and (d) $A_{tor,1} = 742$ pm. Additionally, the effective amplitudes ($A_{lat,1}^{(eff)}$ and $A_{tor,1}^{(eff)}$) as well as the determined corrugation amplitudes A_{C-H} are shown. The minimum possible distance between two hydrophobic surfaces (tip and sample) of 300 pm [158] was neglected for the schematic drawing to improve the comprehensibility (Reprinted from ref. [182], <https://doi.org/10.1038/s41598-022-13065-9>, © 2022.¹⁶).

It needs to be mentioned that in Figure 3-4 only an extract of the full oscillation trajectory is shown. While imaging one position, almost every point in the area spanned by $A_{flex,2} + A_{flex,3}$ and $A_{tor,1}$ or $A_{lat,1}$, respectively, is reached such as plotted in the Supplementary Information (Figure 7-13). From Figure 3-4 it becomes obvious that the interaction between tip and sample strongly depends on the curvature of the tip. For the situations shown in Figure 3-4a, b, d we interpret, that the minimum distance from the lower turning point of the tip-trajectory to the intersection of the tip-trajectory and the horizontal line (purple dotted) defined by the interatomic spacing between two atoms (here 246 pm, due to the tip oscillating perpendicular to the carbon bonds) determines the indent (without distortion of the carbon atoms) of the tip into the carbon ring (vertical purple line). This indent without distortion of carbon atoms corresponds to the corrugation amplitude (A_{C-H}). Thus, we defined the effective in-plane amplitudes as half of the horizontal distance between two carbon atoms (here: $A_{lat,1}^{(eff)} = A_{tor,1}^{(eff)} = 123$ pm because the

¹⁶ This is an open access article under the terms of the Creative Commons Attribution License (<https://creativecommons.org/licenses/by/4.0/>), which permits use, distribution and reproduction in any medium, provided the original work is properly cited.

tip oscillates perpendicular to the carbon bonds) for the situations shown in Figure 3-4a, b, d. From the situation shown in Figure 3-4c we found that if the tip-trajectory shows a higher curvature, the effective amplitude is no longer equivalent to half of the distance between two carbon bonds. This is a result of the maximum possible corrugation amplitude which was reported by Kawai *et al.* to equal 85 pm in the repulsive regime [134]. This value was additionally verified by performing dynamic spectroscopy experiments such as shown in Figure 7-12 of the Supplementary Information. Consequently, the effective amplitude is still determined by the intersection between the tip-trajectory and the horizontal line (purple dotted) defined by the interatomic spacing between two atoms, but it becomes smaller than 123 pm due to the limited corrugation amplitude. If we calculate the effective torsional amplitude from the tip-trajectory in Figure 3-4c, assuming a corrugation amplitude of 85 pm, it would be approximately 83 pm, which is in line with the 79 pm determined in our recent work [8]. We can conclude that imaging the atomic structure of HOPG in the frequency-shift channel is also possible with in-plane oscillations larger than half of the interatomic spacing, but the resolution in the height images is strongly reduced due to the small corrugation amplitudes. Additionally, it needs to be considered that the frequency-shift images reflect the tip-sample interaction averaged over a few carbon hexagons. This needs to be kept in mind if forces are determined from the frequency-shift images. Nevertheless, due to the formation of plateaus in the torsional and lateral frequency shift values for larger in-plane oscillation amplitudes (see Figure 3-3f, g (bottom graph)), we propose that conclusions about different interaction mechanisms, *i.e.* friction or shear, as a function of the different in-plane oscillation amplitudes can be drawn.

We point out that the most obvious way of determining the corrugation amplitude would be the analysis of the topography images. Unfortunately, the topography images are strongly influenced by the mean cantilever deflection, so that the corrugation amplitude is not directly accessible [8].

3.2.3. Calculation of lateral and torsional forces

From Figure 3-3, we additionally observed that the full width at half maximum becomes much broader for the smaller lateral-amplitude setpoints compared to the torsional-amplitude setpoints. In order to identify the origin of the differences between torsional and lateral frequency-shift behavior, we calculated the forces from the images taken at $A_{lat,1} = 518$ pm and $A_{tor,1} = 158$ pm ($A_{flex,2} = 110$ pm and $A_{flex,3} = 145$ pm), respectively. The results are presented in Figure 3-5. Schemes of the interaction between tip and sample are shown in Figure 3-5a, d. The lateral and torsional frequency-shift images are shown in Figure 3-5b, e. In Figure 3-5c, f forces calculated from the frequency-shift images in Figures 5b, e by using the Fourier method [4, 8] are shown.

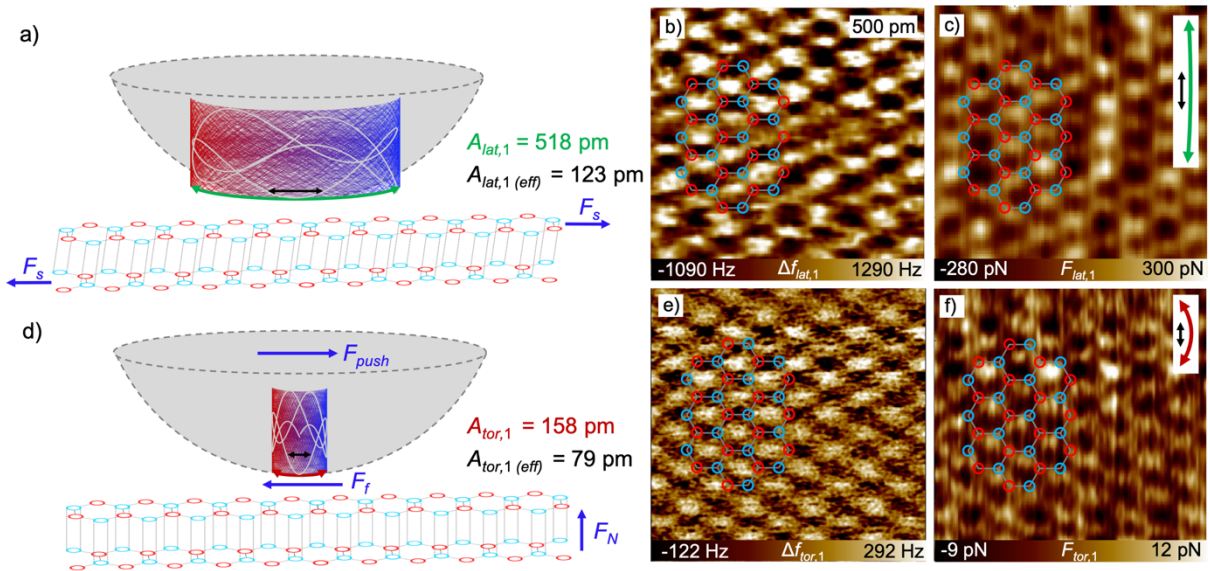


Figure 3-5: Scheme of the interaction between tip and HOPG surface for (a) a shearing interaction resulting from imaging in the AMFlex2-FMLat1-FMFlex3 mode with $A_{lat,1} = 518$ pm (F_s : shear force) and (d) a frictional interaction resulting from imaging in the AMFlex2-FMTor1-FMFlex3 mode with $A_{tor,1} = 158$ pm, where F_N is the normal force acting perpendicular to the surface, F_{push} is the force originating from the movement of the tip in the direction of the in-plane oscillation and F_f is the frictional force counteracting F_{push} ($A_{flex,2} = 110$ pm and $A_{flex,3} = 145$ pm). (b, e) lateral and torsional frequency-shift images. (c, f) corresponding lateral and torsional force images calculated by the Fourier method and using the effective lateral/torsional amplitudes $A_{lat,1(eff)} = 123$ pm and $A_{tor,1(eff)} = 79$ pm (Reprinted from ref. [182], <https://doi.org/10.1038/s41598-022-13065-9>, © 2022.¹⁷).

¹⁷ This is an open access article under the terms of the Creative Commons Attribution License (<https://creativecommons.org/licenses/by/4.0/>), which permits use, distribution and reproduction in any medium, provided the original work is properly cited.

Obviously, both, the torsional and the lateral force image in Figure 3-5c, f reproduce the hexagonal structure of graphene. It needs to be mentioned that this is only the case if the forces are calculated by using the effective torsional or lateral amplitude. Interestingly, forces determined from the lateral frequency-shift image in Figure 3-5b are around 50 times larger compared to the forces (Figure 3-5f) calculated from the torsional frequency-shift images in Figure 3-5e. We propose that this large difference in forces originates partially from the difference in force constants but also/mainly from different types of interaction mechanisms between tip and sample, *i.e.* friction and shear. While Weymouth *et al.* [61, 159] observed “non-contact friction” during imaging of an H-terminated Si(100) surface in dynamic lateral force microscopy using a qPlus sensor [122], we assume that the lateral frequency shift determined on HOPG at 518 pm lateral amplitude mainly originates from a local shear due to relatively weak van-der-Waals interactions between the carbon layers. We assume this to happen for two reasons: First, the angle under which the tip touches the surface at the respective local position is less steep for the shown lateral oscillation compared to the torsional one. Second, the lateral stiffness of the cantilever is higher compared to the torsional stiffness which might lead to shear for a certain range of lateral oscillation amplitudes whereas torsional amplitudes of the same magnitude result in frictional interaction between tip and sample. In order to verify our assumption about shearing interaction for the constellation shown in Figure 3-5a–c we calculated the lateral displacement Δx of the topmost carbon layer relative to the second one if we assume a shear modulus of 4.18 GPa in x - z -direction [142]. In a simple approximation, the shear modulus G_{xz} can be calculated by

$$G_{xz} = \frac{F_{lat} \cdot d}{\Delta x \cdot A_c}, \quad (3-1)$$

where d is the distance between two carbon layers (334 pm) and A_c is the contact area between tip and sample which can be calculated according to Hertz from the tip radius R and the indentation δ [51]

$$A_c = \pi R \delta. \quad (3-2)$$

In order to determine the indentation δ which is caused by the tip oscillating over a carbon atom, we used Hertz contact mechanics model [51]

$$F = \frac{4}{3} E^* \sqrt{R \delta^3}, \quad (3-3)$$

where E^* is the effective Young's modulus which can be considered here as equal to the Young's modulus E_{zz} of graphite due to the high stiffness of the diamond-like-carbon tip. The maximum value of $F_{flex,3}$ was calculated in our recent work to be approximately 520 pN for the AMFlex2-FMTor1-FMFlex3 mode [8]. Due to the similarity of the third-eigenmode flexural frequency-shift values we chose this value as representative for all the other experiments. By rearranging equation (3-3) and inserting $E_{zz} = 36.5$ GPa as reported by Blakslee *et al.* [160] we determined an indentation of approximately 50 pm. Using $\delta = 50$ pm and rearranging equation (3-1), we calculated a local displacement of approximately $\Delta x = 157$ pm between the first and the second graphene layer. This implies a shift by the length of approximately one carbon-carbon bond (142 pm) which seems to be reasonable in distance. We corroborated our findings by performing additional friction force microscopy images, however, using a comparably large vertical deflection setpoint (43 nm \pm 1100 nN) in order to ensure permanent contact between tip and sample. By means of the analysis of cross sections drawn through lateral deflection trace and retrace images, the actual lateral tip-position was calculated. The results are shown in Figure 7-12 of the Supplementary Information. As expected, the typical stick-slip movement of the tip imaging an HOPG surface was observed [161], however, the stiction was stretched out over a region of approximately 150 pm, which can be interpreted as a temporary shift of the topmost carbon layer relative to the second one.

For the tip-trajectory of the torsional oscillation shown in Figure 3-5d, we observe a very similar oscillatory behavior, however, much more compact in the in-plane direction, resulting from the smaller torsional amplitude. As a consequence, the angle at which the tip approaches and finally touches the surface is much steeper and therefore a negligible shifting of the first carbon layer relative to the second is assumed to take place. We suppose that the torsional forces involved in this mechanism can be interpreted as strongly localized frictional forces which is on the one hand in accordance with the magnitude of frictional forces on graphene determined by Lee *et al.* [162]. On the other hand, the interpretation is in compliance with the observation of direction dependent torsional forces observed in our recent work [8]. Additionally, it needs to be highlighted, that the flexural/torsional oscillation of the cantilever simulated here is symmetric in out-of-plane direction but not in in-plane direction such as schematically shown in Figure 7-13 of the Supplementary Information. This can explain the shift between topography and frequency-shift images such as shown in our recent work [8]. For the flexural/lateral oscillation the tip-trajectory is overall symmetric in both, in-plane and out-of-plane direction (see Figure 7-13). Here, no shift between the height and the frequency-shift images could be observed. However, it needs to be mentioned that the resolution in the height images was

strongly reduced if imaging was accomplished with the lateral instead of the torsional eigenmode. The effect can be attributed to the shear interaction between tip and sample. If the lateral or the torsional amplitudes become larger in size, we observe averaged friction along the surface which might explain the formation of the plateaus in the frequency shifts in Figure 3-3f, g (bottom graph). Here, we also observed that the flexural frequency-shift values and therefore the flexural forces are only slightly influenced by the in-plane oscillation amplitudes. In theory, it should additionally be possible to determine the in-plane Young's moduli $E_{xx} = E_{yy}$ and E_{xy} by using higher torsional or lateral eigenmodes of the cantilever. Unfortunately, it is nontrivial to control these higher eigenmodes and determine their invOLS as well as the corresponding force constants.

Nevertheless, this approach could be considered as an alternative method for the determination of the Young's modulus of graphene instead of the frequently used techniques where graphene is spanned over membranes or holes and E_{xx} is calculated from nanoindentation experiments [109, 112]. Therefore, we propose that the simultaneous determination of strongly localized in-plane and out-of-plane sample properties such as shear moduli and Young's moduli using multifrequency AFM is feasible if very small amplitudes and adequate force constants are used for the analysis. The main advantage of determining elastic properties at the atomic scale is the possibility to locally assess the influence of atomic defects in the material, which were shown to strongly influence the mechanical stability of graphene samples on a larger scale [109]. Serving the large scientific interest to analyze the origin of friction anisotropy on graphene and graphite samples [163-166], we are convinced that our presented multifrequency AFM method can substantially contribute to gain deeper insights into in-plane sample properties by comparing the mechanical properties on the atomic scale with that on the nano-/micrometer scale. The ability to compare material properties at different length scales in air under ambient conditions is of particular interest for the analysis of adsorbate formation [165, 166] or ripples [163, 164] on a graphitic surface which strongly influences the performance of graphene-based nanodevices. Additionally, the availability of torsional and lateral eigenmodes extends the spectrum of oscillation modes, facilitating the simultaneous acquisition of different in-plane sample properties, using one and the same cantilever.

3.3. Conclusion

In summary, we demonstrated that performing multifrequency AFM with in-plane and out-of-plane components of the tip-motion has additional potential for atomic resolution imaging of

HOPG surfaces. The coupling of the second flexural and the first torsional eigenmode facilitates imaging with atomic contrast at higher amplitude-setpoint ratios, although the quantitative interpretation of the results is challenging if the torsional and the lateral oscillation amplitude are simultaneously excited. In order to estimate the inverse optical lever sensitivity of the lateral cantilever eigenmode, a calibration procedure was proposed which is based on imaging a graphene wrinkle with different lateral amplitude setpoints while oscillating perpendicular to the wrinkle and comparing the images with the results of a Savitzky-Golay-filtered reference image. We compared the results from imaging in the AMFlex2-FMLat1-FMFlex3 and the AMFlex2-FMTor1-FMFlex3 mode. Analyzing the tip-trajectories and the in-plane forces resulting from both modes with the respective amplitudes, we proposed that imaging with small lateral amplitudes can result in localized shear of the first graphite layer with respect to the second one with a relative displacement of 157 pm. The applied out-of-plane forces caused an indentation of approximately 50 pm of the top graphene layer. Both values are in a reasonable range to propose that the AMFlex2-FMLat1-FMFlex3 method can be used for the simultaneous determination of $E_{xx} = E_{yz}$ and $G_{xz} = G_{yz}$. Imaging with the AMFlex2-FMTor1-FMFlex3 in contrast, promotes rather frictional forces which we mainly attributed to the smaller force constant and the curved tip-trajectory compared to the lateral eigenmode. Based on our findings, we suggest that the use of higher in-plane cantilever eigenmodes or generally stiffer cantilevers can provide a strategy to determine the shear moduli on HOPG and graphene also with torsional eigenmodes. The method carries great potential for future assessment of graphene in nanodevices where local differences in mechanical properties *e.g.* induced by defects or adsorbates, play a major role. To this end, the in-plane oscillation amplitudes need to be in the range of the interatomic spacings, which is still challenging to achieve while imaging in air under ambient conditions due to the small signal-to-noise ratio. With the presented method we aim to promote the analysis of friction anisotropy observed on graphene by the comparison of atomic and nano-/micrometer resolution images at different relative orientations between the hexagonal carbon lattice and the in-plane cantilever oscillation using torsional and/or lateral eigenmodes. This can help to investigate the origin of fundamental friction mechanisms underlying graphene-based systems. Additionally, we expect that the presented method might not only be limited to the analysis of stiff samples but also can be applied for a broad range of materials, including soft matter, facilitating a complete in- and out-of-plane sample surface characterization.

3.4. Materials and methods

Sample. The HOPG sample (grade 2, mosaic spread angle: $0.8 \pm 0.2^\circ$) was purchased from SPI Supplies (Structure Probe, Inc., West Chester, PA, USA). Cleaving was performed prior to the AFM experiments with adhesive tape in air under ambient conditions to expose a fresh clean surface.

Cantilevers. Super-sharp cantilevers of the type HiResC15/Cr-Au purchased from Mikromasch (Innovative Solutions Bulgaria Ltd., Sofia, Bulgaria) were used. Although of the same type, the cantilevers showed slightly varying resonance frequencies resulting in “coupled” and “uncoupled” eigenmodes. For the AFM images shown in Figure 3-2 we used a cantilever with “coupled” second flexural and first torsional eigenmodes as it depicted a close proximity of both resonance frequencies. For the AFM images shown in Figure 3-3 and Figure 3-5 cantilevers with “uncoupled” eigenmodes were used. The resonance frequencies, quality factors and force constants of the used cantilevers are listed in Table 3-1. Details for the determination of the force constants are given in Section 7.2.7 of the Supplementary Information. The tip radius of the cantilevers was $R = 1$ nm according to the manufacturer’s data sheet.

Table 3-1: Resonance frequencies, quality factors and force constants of the “coupled” and “uncoupled” cantilevers HiResC15/Cr-Au. The cantilever indexed by “Tor” was used for the images taken in AMFlex2-FMTor1-FMFlex3 mode and by “Lat” in the AMFlex2-FMLat1-FMFlex3 mode (Reprinted from ref. [182], <https://doi.org/10.1038/s41598-022-13065-9>, © 2022.¹⁸).

| HiResC15/ Cr-Au | f_0 in MHz | | | Q | | | k in N/m | |
|---------------------------|--------------|-------------|-------|-----------|-------------|------|-------------|------|
| | “coupled” | “uncoupled” | | “coupled” | “uncoupled” | | “uncoupled” | |
| | | Tor | Lat | | Tor | Lat | Tor | Lat |
| 1 st flexural | 0.274 | 0.266 | 0.263 | 606 | 594 | 585 | 26 | 25 |
| 2 nd flexural | 1.718 | 1.667 | 1.653 | 97 | 951 | 708 | 644 | 473 |
| 3 rd flexural | - | 4.615 | 4.562 | | 381 | 296 | 3489 | 2406 |
| 1 st torsional | 1.735 | 1.730 | 1.720 | 1438 | 1341 | 1383 | 472 | 483 |
| 1 st lateral | 1.913 | 1.887 | 1.872 | 1546 | 1692 | 1634 | 1440 | 1395 |

In Section 7.2.8 of the Supplementary Information we list the ratios between the flexural, torsional and lateral resonance frequencies determined for several cantilevers of the type HiResC15/Cr-Au for further considerations.

¹⁸ This is an open access article under the terms of the Creative Commons Attribution License (<https://creativecommons.org/licenses/by/4.0/>), which permits use, distribution and reproduction in any medium, provided the original work is properly cited.

Environmental conditions. The AFM-lab was equipped with a controlled ventilation system, which provided stable environmental conditions also inside the AFM chamber. The temperature and the relative humidity in the AFM chamber were tracked by sensors and remained stable during imaging (relative humidity: 22 ± 2 %, temperature: 26 ± 2 °C).

AFM setup. A Cypher S atomic force microscope (Asylum Research, Oxford Instruments, Santa Barbara, CA, USA) equipped with a built-in blueDrive photothermal excitation setup for dynamic AFM modes was used for all experiments. The blueDrive laser was focused at the fixed end of the cantilever and the lateral position was optimized by finding the spot that led to the maximum possible in-plane amplitude. A scheme for the approximate positioning of the laser spots on the cantilever is shown in Figure 7-8e of the Supplementary Information (Section 7.2.1). The respective frequency shifts (depending on the method used) were tracked with additional phase-locked loops (HF2PLL, Zurich Instruments, Zurich, Switzerland). The drive amplitudes of the frequency-modulated eigenmodes were adjusted in order to maintain constant amplitudes by two PID controllers implemented in the same instrument.

Data processing. The topography and the torsional-amplitude error images were first-order flattened to remove any tilt from the images using the Igor Pro v6.36 software (WaveMetrics Inc., Lake Oswego, OR, USA). In order to remove noise from the small-scale images a 3×2 Gauss filter was applied to all AFM images except for the ones used for the determination of the lateral invOLS (Figure 7-11). For the calculation of the torsional and the lateral force images in Figure 3-5 we wrote a Matlab code (MATLAB R2018a, MathWorks Inc., Natick, MA, USA) for the implementation of the Fourier method based on the script provided by Seeholzer *et al.* [4, 8]. The calculated force images were smoothed with a Savitzky–Golay filter over nine points with a first-order polynomial.

3.5. Acknowledgements

The authors thank the Deutsche Forschungsgemeinschaft (Project number 407750697) for financial support.

4. In-plane and out-of-plane interaction analysis of adsorbates on multilayer graphene and graphite by multifrequency atomic force microscopy¹⁹

Graphene and graphite are generally considered as materials exhibiting friction anisotropy. However, it was demonstrated by friction force microscopy experiments that friction anisotropy most likely originates from adsorbates aligning in well-ordered stripes on graphitic surfaces. In this study, we analyzed the evolution of adsorbates on a few-layer graphene-/graphite-flake on top of a Si/SiO₂-substrate after different times of storage using a multifrequency force microscopy approach. The method allows for the simultaneous in-plane and out-of-plane sample analysis as well as the discrimination of conservative and dissipative tip-sample interactions directed parallel and perpendicular to the surface and thus offers a myriad of complementary physical information. We found that friction anisotropy was observable at distinct areas of the graphene-/graphite-flake after 14 days of storage when exposed to air, albeit not throughout the whole flake, indicating different types of adsorbates. High-resolution imaging revealed that friction anisotropy occurred not only at positions where stripe-like structures were visible, but also on areas which were completely covered with adsorbates. Additionally, we demonstrated that after removal of the adsorbate material by oxygen-plasma treatment, no friction anisotropy was observable on the graphene-/graphite-flake, corroborating adsorbate driven nature of friction anisotropy on graphitic surfaces.

4.1. Introduction

Within the last years graphene has become subject of increased interest in the field of tribology due to its ability to significantly reduce friction and wear [167, 168]. These noteworthy tribological properties allow for application of graphene as a solid lubricant, *e.g.* for micro- and nanoelectromechanical systems (MEMS and NEMS) [169, 170]. On the other hand, graphene was also evaluated to be suitable for molecular sieving, facilitating controlled gas separation through porous graphene membranes [171, 172]. Both applications have in common that precise knowledge about the surface of graphene is required to provide a reliable and reproducible performance of the devices. If these devices are operated under ambient conditions, it needs to be considered that adsorbates tend to self-assemble in stripe-like

¹⁹ This Section was published as “In-plane and Out-of-plane Interaction Analysis of Adsorbates on Multilayer Graphene and Graphite by Multifrequency Atomic Force Microscopy” by A. L. Eichhorn, M. Hoffer and C. Dietz in *Carbon*, 2022, 8(20). Reprinted with permission from Elsevier Ltd., © 2022. This article is protected by copyright. References were adapted to provide continuous numbering throughout the whole work.

structures with a periodicity between 4 and 6 nm on graphene surfaces as observed by means of atomic force microscopy (AFM) [165, 166, 173-175].

The occurrence of ordered stripe structures was reported by Choi *et al.* [163, 164, 176] to be the origin of friction anisotropy observed by friction force microscopy (FFM) on graphene, however, they assigned the formation of the ordered stripes to stress-induced rippling of the graphene surface. Gallagher *et al.* [165, 166] compared the friction anisotropy found on graphene and hexagonal boron nitride *via* transverse force microscopy. Due to the similarities of the stripe periodicity noticed on both investigated materials they ascribed the friction anisotropy to the formation of ordered adsorbate structures, and hence, it cannot originate from stress-induced rippling due to the differences in bending stiffness and response to stress [177]. Temiryazev *et al.* [175] showed that imaging in dissipative mode (DM) AFM enabled high resolution imaging of the adsorbate stripe patterns on graphene, graphite plates and highly oriented pyrolytic graphite (HOPG).

It was shown by Weymouth *et al.* [61, 159] on an H-terminated Si(100) surface that friction can also be analyzed without tip-sample contact using the dynamic lateral force microscopy method. The authors demonstrated that frictional forces can be determined from lateral frequency-shift data. This appears unusual at first glance because frequency-shift data is generally assigned to conservative tip-sample interaction [57, 59] whereas dissipative interactions, such as friction, can be analyzed from drive amplitudes in frequency modulation AFM [178, 179]. However, it was shown by Gotsmann *et al.* [180] that in case of hysteretic forces or friction coefficients, the frequency-shift data is slightly influenced also by dissipative interactions and the drive-amplitude values contain a certain degree of conservative tip-sample interaction information as well. Recently, Tan *et al.* [181] analyzed dynamic friction by means of the dissipated energy calculated from torsional phase shift images, using a bimodal AFM setup.

The possibility and advantages to use lateral eigenmodes alternative to torsional eigenmodes for dynamic in-plane AFM imaging were reported by Ding *et al.* [89]. In our recent work [182], we demonstrated the feasibility to distinguish between frictional or shear interaction while imaging an HOPG surface at the atomic scale by analyzing torsional and lateral tip-sample interactions. We found that the deconvolution of torsional and lateral frequency-shift data using the Fourier method [4] resulted in forces of different magnitudes if small amplitudes were used [69]. The study also revealed that imaging with small lateral amplitudes (<518 pm) results in (conservative) shear interaction whereas imaging with torsional eigenmodes or larger lateral

amplitudes predominantly resulted in (dissipative) frictional interaction. The different interaction mechanisms were attributed to originate from differences in the tip-trajectories and force constants between the torsional and the lateral eigenmode.

In the present study we investigated (i) the formation of adsorbate structures on graphene and graphite upon storage and (ii) the influence of conservative and dissipative tip-adsorbate forces by performing experiments using the multifrequency force microscopy setup AMFlex2-OLTor1-FMLat1-FMFlex3 as recently introduced [182]. This technique is based on the simultaneous photothermal excitation of different eigenmodes of the cantilever (torsional, lateral and flexural). Thus, the related frequency-shift data allows for the discrimination of in-plane and out-of-plane conservative tip-sample interactions. Additionally, the phase and drive-amplitude values provide information on the in-plane and out-of-plane dissipative tip-sample interaction. By performing spectroscopic experiments using this multifrequency AFM approach, in-plane and out-of-plane sample properties such as shear and elastic modulus can be deduced *via* force deconvolution of the frequency-shift data [6, 59, 182].

The aim of this study was to identify the effect of adsorbate formation on the tribology of few layer graphene-/graphite-flakes upon storage. To this end, the formation and physical/mechanical properties of adsorbates on a graphene-/graphite-flake were investigated using the AMFlex2-OLTor1-FMLat1-FMFlex3 method after short-term (≤ 14 days) and long-term storage (87–209 days). To gain further insight into the nature of the adsorbates, the sample was heated for 5 min at 100 °C after 95 days and plasma treated for 6 s after 209 days. Additionally, friction anisotropy was analyzed by rotating the graphene-/graphite-flake by approximately 90° prior to and after plasma treatment. Note that it was shown by Chen *et al.* [183] *via* conductivity experiments that graphene on an Si/ SiO₂-substrate was stable for at least 500 days of storage in air under ambient conditions.

4.2. Materials and methods

The few-layer graphene-/graphite-sample was fabricated by micromechanical exfoliation of natural graphite-flakes (ProGraphite GmbH, Untergriesbach, Germany) on a silicon substrate that was covered with a 300 nm thick layer of SiO₂ [10], following the protocol of Huang *et al.* [33]. The sample was stored in a polypropylene storage box under laboratory air conditions, ranging between 9 and 69 % in relative humidity and 16–26 °C in temperature (see Figure 7-14 in Section 7.3.1 for details). Heating of the sample after 95 days of storage was performed on a hotplate for 5 min at 100 °C. For the oxygen-plasma treatment, the sample was treated for 6 s at 55 W in a FEMTO plasma chamber (Diener electronic GmbH + Co. KG, Germany, Ebhausen) after 209 days of sample storage.

All experiments were performed using a Cypher S atomic force microscope (Asylum Research, Oxford Instruments, Santa Barbara, CA, USA), equipped with a blueDrive photothermal excitation setup. For implementing the AMFlex2-OLTor1-FMLat1-FMFlex3 method [182], the blueDrive laser was power-modulated, matching the different resonance frequencies of the cantilever and focused at the fixed end of the cantilever, however, some micrometers off the length symmetry axis. In this way, flexural [43, 44], torsional [87, 88] and lateral cantilever eigenmodes [89] could be simultaneously excited. For this study we used cantilevers of the types HQ:NSC15/Cr-Au and HiRes-C15/Cr-Au purchased from Mikromasch (Innovative Solutions Bulgaria Ltd., Sofia, Bulgaria), which, according to the manufacturer, differ exclusively by their tip radius, being 8 nm and 1 nm, respectively. Their resonance frequencies and force constants were chosen to be as similar as possible and are listed in Table 4-1. Details on the determination of the force constants can be found in our recent publications [8, 182].

Table 4-1: Flexural, torsional and lateral resonance frequencies and approximate force constants of the cantilever types HQ:NSC15/Cr–Au and HiRes-C15/Cr–Au (Reprinted from ref. [225], <https://doi.org/10.1016/j.carbon.2022.08.005>, © 2022.²⁰).

| | 1 st flexural | 2 nd flexural | 3 rd flexural | 1 st torsional | 1 st lateral |
|---------------------------------|--------------------------|--------------------------|--------------------------|---------------------------|-------------------------|
| Resonance frequency f_0 (kHz) | 252–263 | 1604–1689 | 4452–4709 | 1594–1680 | 1851–2005 |
| Force constant k (N/m) | ≈ 25 | ≈ 520 | ≈ 2820 | ≈ 465 | ≈ 1380 |

²⁰ This article is protected by copyright. © 2022 Elsevier Ltd. All rights reserved.

Using the second flexural eigenmode amplitude-modulated (AMFlex2) for the topography feedback turned out to promote high-resolution imaging down to the atomic scale [8, 64, 65]. Due to the close proximity of the second flexural and the first torsional resonance frequencies of the cantilevers selected in this study, these eigenmodes could not be controlled individually. Consequently, we assigned the torsional oscillation as “open loop” (OLTor1) configuration. To distinguish between conservative and dissipative tip-sample interaction we operated the lateral (FMLat1) and the third flexural eigenmode (FMFlex3) in constant amplitude frequency-modulation mode using two phase-locked loops (PLL) and two PID controllers (HF2PLL, Zurich Instruments, Zurich, Switzerland). A scheme of the setup and further details for the implementation of the AMFlex2-OLTor1-FMLat1-FMFlex3 method can be found in our recent publication [182]. The method facilitates to simultaneously acquire conservative tip-sample interactions from the frequency-shift and dissipative interactions from the drive-amplitude values for both, in-plane (FMLat1) and out-of-plane (FMFlex3) direction. Due to a limited number of channels which can be monitored during imaging we decided not to record the third flexural drive amplitude because dissipative out-of-plane information was also gained from the second flexural phase. Details on the calibration of the inverse optical lever sensitivities (invOLS) of the different eigenmodes can be found in our recent publications [8, 182].

4.3. Results and discussion

The few-layer graphene-/graphite-sample was first analyzed 4 h after preparation such as shown in Figure 7-15 in Section 7.3.2. Surprisingly, adsorbates were already present at the surface although the sample was freshly prepared. This effect was also reported by Martinez-Martin *et al.* [184] who could show by a combination of desorption and Kelvin probe force microscopy experiments plus theoretical calculations that polycyclic aromatic hydrocarbons (PAH) are, among the molecules compatible with physisorption, the main contaminant for graphitic surfaces in air under ambient conditions, facilitating the monolayer coverage of graphitic surfaces within 1 h. Additionally, it was observed that imaging with a second flexural eigenmode setpoint ratio of 55 % with respect to the free amplitude caused wrinkle formation of the graphene-flake as shown in Figure 7-15d in Section 7.3.2. A reasonable explanation for the wrinkle formation was found by Androulidakis *et al.* [185]. By analyzing compressive behavior of fully embedded graphene they found that the critical strain to compression failure decreases with the increase in thickness of graphene as a result of low resistance to shear. After 7 days of storage under ambient air conditions, the same area was imaged again using different second flexural and first lateral amplitude setpoints. The results are shown in Figure 7-16 in Section 7.3.3, where images were taken in the order of a-h. Interestingly, we observed that the combination of reduced second flexural amplitude setpoint ratios and increased lateral amplitudes resulted in a removal of large-scale adsorbate structures on the surface. After 14 days of storage, we focused on a different area of the few-layer graphene-/graphite-flake which was analyzed in detail within this study. This area includes a portion of the Si/SiO₂-substrate and a partially folded graphene-flake consisting of an eight layers thick graphene-region and a 16 layers thick graphite-region as shown in Figure 7-17 in Section 7.3.4.

4.3.1. Analysis of large- and small-scale adsorbates on a few-layer graphene-/graphite-flake after 14 days of storage

In Figure 4-1 we show the results of the large- and small-scale analysis of adsorbates on a few layer graphene-/graphite-flake, analyzing the topography (a-d), the second flexural phase (e-h), the lateral drive-amplitude (i-l), the lateral frequency-shift (m-p) and the third flexural frequency-shift (q-t) images at different scan sizes after 14 days of storage under ambient air conditions within the laboratory (see Figure 7-14 in Section 7.3.1 for details on temperature and relative humidity).

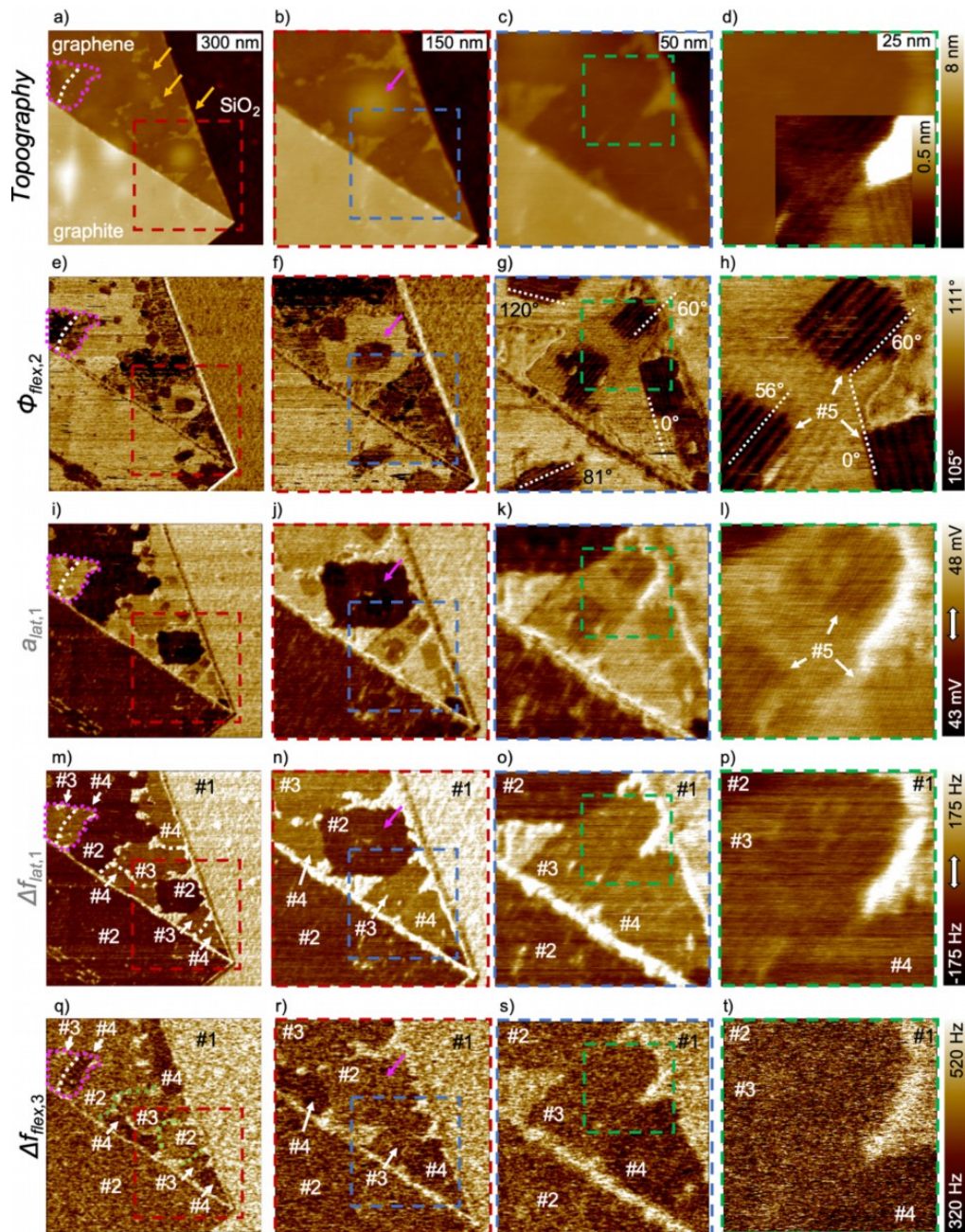


Figure 4-1: Large- and small-scale adsorbate formation on a few layer graphene-/graphite-flake analyzed at different magnifications in AMFlex2-OLTor1-FMLat1-FMFlex3 mode in out-of-plane (a-h, q-t) and in-plane direction (i-l) after 14 days of storage under ambient conditions in air. Topography (a–d), second flexural phase (e–h), lateral drive-amplitude (i–l), lateral frequency-shift (m–p) and third flexural frequency-shift images (q–t). $A_{0(flex,2)} = 675$ pm, $A_{flex,2} = 600$ pm, $A_{lat,1} = 1.766$ nm, $A_{flex,3} = 75$ pm. White arrows within the color bars indicate the direction of lateral oscillation. White arrows within the frequency-shift images (m–t) point out regions where different adsorbates numerated from #1 to #5 are assumed. Yellow arrows in (a) exemplarily mark unordered large-scale adsorbates and the pink arrows in the second column highlight the hillock observed on the graphene-portion of the flake (Reprinted from ref. [225], <https://doi.org/10.1016/j.carbon.2022.08.005>, © 2022.²¹).

²¹ This article is protected by copyright. © 2022 Elsevier Ltd. All rights reserved.

In Figure 4-1a we marked the different materials of the analyzed sample, namely the Si/SiO₂-substrate (darkest area), the graphene-portion (brownish area) and the graphite-portion of the flake (brightest area). First, we focus on the large-scale unordered adsorbate structures which are visible in all images shown in Figure 4-1 and are exemplarily marked by yellow arrows in Figure 4-1a. From the topography images shown in Figure 4-1a–d we observed that unordered large-scale adsorbates (as reported by Temiryazev *et al.* [175]) were formed predominantly at the edges but also appeared as small islands within the plane graphene-portion of the flake. These non-structured large-scale adsorbates were also clearly visible in the lateral and third flexural frequency-shift images (Figure 4-1m–p and q–t), reflecting the highest lateral and vertical forces acting between tip and sample at those areas. On the other hand, these large-scale adsorbate regions induce only a small decrease of the second flexural phase (Figure 4-1e–h) and a slight increase of the lateral drive amplitude (Figure 4-1i–l) compared to the rest of the flake, indicating only a slight increase in dissipated energy in out-of-plane direction [178, 179] as well as in in-plane-direction. Additionally, it becomes obvious that in all four channels related to physical properties of the sample ($\Phi_{flex,2}$, $a_{lat,1}$, $\Delta f_{lat,1}$ and $\Delta f_{flex,3}$) the respective value on the unordered large-scale adsorbates was similar compared to the value on the Si/SiO₂-substrate (#1 in Figure 4-1m–t), indicating the same type of adsorbate material on both areas. It is reasonable to believe that water molecules adsorb on the Si/SiO₂-substrate due to the hydrophilicity of the SiO₂-surface. Graphite is well known as a hydrophobic material and it was reported by Kazakova *et al.* [186] that the hydrophobicity of graphene/graphite increases with layer number. This is in accordance with the observation that no unordered large-scale adsorbates were present on the graphite-area of the flake. This corroborates the interpretation that the unordered-large-scale adsorbates, which solely form at the graphene-portion of the flake, can be attributed to water molecules. If we compare the $1 \times 1 \mu\text{m}^2$ images shown in Figure 4-1e, i, m and q, we notice that different large-scale domains formed, especially on the graphene-portion of the flake. On some areas of the graphene, the respectively measured physical quantities equal the ones measured on nearly every position of the graphite-portion of the flake (#2 in Figure 4-1m–t). Li *et al.* [187] showed that pristine graphitic surfaces are hydrophilic and that the actual hydrophobicity mainly originates from the coverage with airborne hydrocarbons. Thus, we interpret these areas of the flakes as covered by airborne hydrocarbons, which prevent the surface from being covered with water molecules. Due to the fact that no stripe-like patterns could be observed in the #2-areas we assume that the adsorbing hydrocarbons were most likely of aromatic origin. This is in line with the study of Martinez-Martin *et al.* [184] who found that polycyclic aromatic hydrocarbons (PAH) are, among the molecules compatible with physisorption, the main contaminant for graphitic surfaces in air

under ambient conditions. Note that the sample was stored in a polypropylene box, and hence, 2,6-di-tert-butyl-2,5-cyclo-hexadiene-1,4-dione, dibutyl phthalate (DBP) or butylated hydroxytoluene (BHT) could also be the origin of the adsorbates [188, 189]. Additionally, we find areas on the graphene-portion of the flake (#3 and #4 in Figure 4-1m–t) which show physical quantities that are different from both, the Si/SiO₂-substrate (#1 in Figure 4-1m–t) and the graphene-/graphite-area most probably covered by PAH (#2 in Figure 4-1m–t). As can be seen from Figure 4-1m, the non-structured large-scale adsorbates predominantly form at the edges of these areas #3 and #4, exemplarily highlighted by the pink dotted line in the first column of Figure 4-1. Interestingly, in the areas marked as #3 and #4 in Figure 4-1m–t, the in-plane properties (Figure 4-1i and m) were measured to be very similar in both areas, whereas the out-of-plane properties (Figure 4-1e and q) indicate clearly discriminable interactions. On the other hand, in the areas marked as #2 and #3 in Figure 4-1m–t, clearly discriminable in-plane interactions could be observed, whereas very similar out-of-plane interactions were identified. This implies the adsorption of different types of airborne hydrocarbon adsorbates, where the strength of the interaction with the graphene-/graphite-flake seems to be distinguishable in in-plane and out-of-plane direction. To further analyze the origin of these different areas #2, #3 and #4, we consecutively reduced the scan size of the AFM images to 500 × 500 nm² (Figure 4-1b, f, j, n, r (red framed)), 240 × 240 nm² (Figure 4-1c, g, k, o, s (blue framed) and 95 × 95 nm² (Figure 4-1d, h, l, p, t (green framed)). In the topography image in Figure 4-1b, we clearly observe a bright hillock marked by the pink arrow. This hillock might either originate from a particle or gas inclusions covered by the graphene-/graphite-flake during preparation *via* micromechanical exfoliation. The formation of unordered adsorbates (most probably water molecules) seems to be promoted by such irregularities. If we now compare the area marked by the pink arrow in the topography image (Figure 4-1b), with the same area of the second flexural phase image shown in Figure 4-1f, we find that in the center of the hillock the out-of-plane phase is smaller compared to the surrounding, indicating a smaller amount of dissipated energy perpendicular to the surface, compared to the direct surrounding [178, 179]. The same effect can be observed for the energy dissipated parallel to the sample surface, indicated by an area of lower lateral drive amplitude in the center of the hillock surrounded by an area of higher lateral drive amplitude as indicted by the pink arrow in Figure 4-1j. Interestingly, for the lateral as well as the third flexural frequency-shift image shown in Figure 4-1n and r, there is no such difference visible between the center of the hillock and the surrounding which indicates that the tip-sample interaction is predominantly dissipative directly above the hillock. Similar effects can be observed for the small-scale adsorbate structure formation in areas #2, #3 and #4, which does not appear in the frequency-

shift images (Figure 4-1o and s) but in the second flexural phase (Figure 4-1g) and the lateral drive amplitude images (Figure 4-1k), marked as #5. Analyzing Figure 4-1g in detail, we can unambiguously identify domains of adsorbates exhibiting stripes of different orientations (indicated by the white dotted lines) predominantly on graphene but also sporadically on the graphite-portion of the flake. On the graphene-portion, the 60°-orientation of the stripes relative to each other can be identified attributable to the 60°-rotational symmetry of the hexagonal graphene-lattice [166]. An exception of the 60°-orientation of stripe domains can be observed on the graphite-portion of the flake, where an angle of 81° was determined. This observation is not surprising because the graphite-portion corresponds to a folded area of the graphene-flake, leading to a different orientation of the hexagonal carbon lattice of the topmost layer. These stripes are apparent in the lateral drive amplitude image (Figure 4-1k) as well, but not in the topography (Figure 4-1c) or the frequency-shift images (Figure 4-1o, s). Interestingly, we realized that the stripes were predominantly observable on areas of increased dissipated energy in out-of-plane direction (lower $\Phi_{flex,2}$ compared to the surrounding in Figure 4-1g) as well as in in-plane direction (higher $a_{lat,1}$ compared to the surrounding in Figure 4-1k). From the green-framed images (highest magnification, Figure 4-1d, h, l, p) it became obvious that the stripe structure of the adsorbates is also visible in the topography image (Figure 4-1d) after adjusting the color scale. Additionally, it is noticeable in the second flexural phase image (Figure 4-1h) that adjacent stripe domains are not always accurately aligned in orientation (difference of approximately 4°), which was also reported by others [190]. The periodicity of the stripes was determined to be approximately 5.3 nm which is in line with previous reports [166, 175], where the occurrence of ordered adsorbate patterns was attributed to airborne hydrocarbons. Gallagher *et al.* [166] proved that the stripe-like patterns formed along the armchair direction of the carbon hexagons. It is reasonable to believe that the formation of stripe-like adsorbate patterns can be attributed to hydrocarbons of aliphatic origin, where the carbon-chains align most probably perpendicular to the observed adsorbate patterns with 4–6 nm periodicity. In a recent study, Pálinkás *et al.* [191] confirmed that the stripe-like structures on graphitic surfaces originate from normal alkanes with lengths of 20-26 carbon atoms. By performing low temperature (9 K) scanning tunneling microscopy (STM) experiments they visualized that the alkane chains aligned along the zigzag orientation of the graphitic surface, where adjacent stripes tend to be shifted by a half-molecule width. As a consequence, the periodicity of the stripe-like adsorbate patterns observed at room temperature corresponds to the length of the alkane molecules. Note that the inner structure of the stripes cannot be visualized at room temperature due to the smectic nature of the alkane monolayer [192].

To sum up, we observed that after 14 days of storage various types of domains can be discerned on the few layer graphene-/graphite-flake in all available channels representing dissipative (Figure 4-1e-l) and conservative interactions (Figure 4-1m-t) as well as out-of-plane (Figure 4-1e-h and q-t) and in-plane interactions (Figure 4-1i-p). For in-plane interactions, two different large-scale domains (#2 and #3 \triangleq #4 in Figure 4-1m-p)) are visible, where #2 was attributed as most probably covered by aromatic hydrocarbons [184]. Area #3 and #4 contain a large amount of small-scale adsorbate structures which are likely to originate from normal alkanes [191], however, a large portion of area #3 and #4 does not show stripe-like structures which implies the presence of a different type of adsorbates, presumably of organic aromatic origin as for region #2. Also, for out-of-plane interactions, two different large-scale domains (#2 \triangleq #3 and #4 in Figure 4-1q-t) are visible. Consequently, it is likely to believe, that three different types of aromatic hydrocarbons adsorbed on the few-layer graphene-/graphite-flake, where the molecules present on #2 and #3 are assumed to obtain similar out-of-plane but different in-plane binding to the graphene-/graphite-flake. On the other hand, the molecules present on #3 and #4 most probably show similar in-plane, but different out-of-plane interactions with the sample. This could *e.g.* be caused by different side groups within the adsorbed molecules, leading to distinguishable adsorbate-graphene or tip-adsorbate interactions, respectively. However, based on the work of Martinez-Martin *et al.* [184] who found that PAH is, among the molecules compatible with physisorption, the predominant adsorbate species on graphitic surfaces, it is reasonable to assume that the differences in in-plane and out-of-plane interaction behavior of the adsorbates with the AFM tip originated from differences in the aromatic ring structures rather than differences in side groups. Li *et al.* [193] predicted by density functional theory (DFT) analysis that on the one hand the adsorption energy increases with the number of aromatic rings in the adsorbates and on the other hand that the most stable adsorption configuration can be “top”- (*e.g.* benzo[k]fluoranthene) or “bridge”-configuration (*e.g.* fluoranthene) depending on the arrangement of the aromatic rings. A schematic drawing of the different adsorption configurations according to Li *et al.* [193] is shown in Figure 4-2.

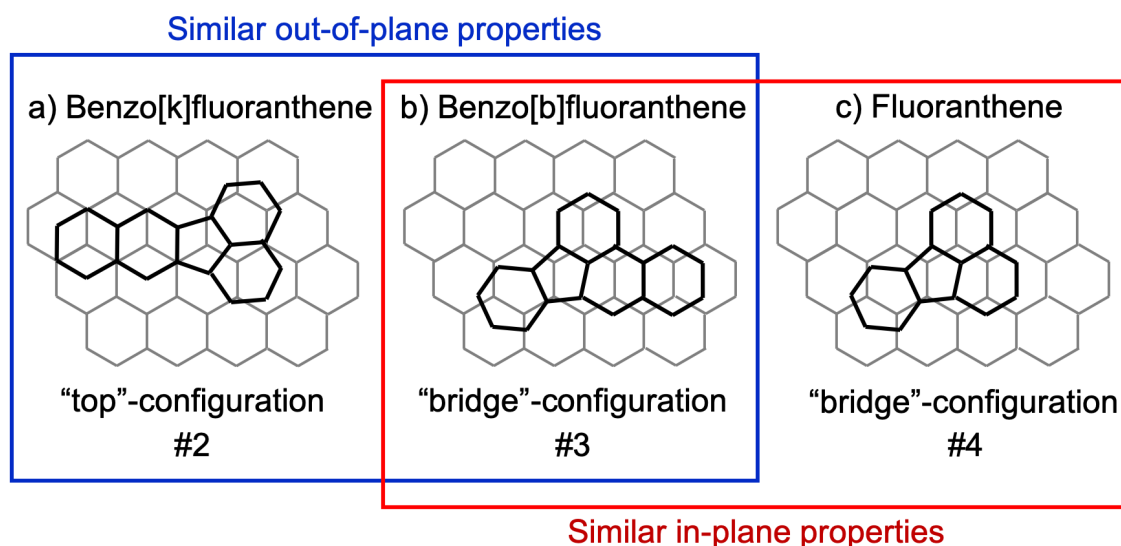


Figure 4-2: Scheme of stable adsorption configurations of different polycyclic aromatic hydrocarbons (PAH) on graphene in a) “top”-configuration (benzo[k]fluoranthene) and b, c) “bridge”-configuration (benzo[b]fluoranthene, fluoranthene) according to Li *et al.* [193] (Reprinted from ref. [225], <https://doi.org/10.1016/j.carbon.2022.08.005>, © 2022.²²).

By comparing the adsorption energies and adsorption configurations of different PAH we suggest different molecules which could be responsible for the differences/similarities in in-plane and out-of-plane properties observed in the areas #2, #3 and #4 as marked in Figure 4-1. It is reasonable to believe that there is a correlation between similar adsorption energies and similar out-of-plane properties of adsorbates covering graphitic surfaces. On the other hand, it seems reasonable that molecules adsorbing in “top”- or “bridge”- configuration show distinguishable response to shear interaction as induced by the laterally oscillating tip. Based on these assumptions we propose that area #2 (Figure 4-1) might *e.g.* have been covered with benzo[k]fluoranthene which adsorbs in “top”-configuration such as schematically shown in Figure 4-2a. Benzo[k]fluoranthene obtains a similar adsorption energy as benzo[b]fluoranthene, which adsorbs in “bridge” configuration (Figure 4-2b) and might have been covering area #3. From Figure 4-1 we found that the areas #2 and #3 show similar out-of-plane but distinguishable in-plane properties which is in line with the characteristics of the proposed adsorption molecules. Additionally, it was found from Figure 4-1 that in area #3 and #4 similar in-plane but different out-of-plane properties were observed. The adsorption of fluoranthene (Figure 4-2c) in area #4 could explain this observation because it adsorbs in the same configuration (“bridge”) but exhibits a smaller adsorption energy compared to benzo[b]fluoranthene (area #3). Li *et al.* [193] additionally reported that based on their

²² This article is protected by copyright. © 2022 Elsevier Ltd. All rights reserved.

calculations the adsorption energy of PAH is reduced on stressed graphitic areas. As a consequence, at positions exerted to stress, the PAH could be easier replaced by other adsorbates such as alkanes forming the stripe-like adsorbate patterns. This finding is in line with the occurrence of stripe-like adsorbate patterns on top of the hillock as *e.g.* observed in Figure 4-1g. Consequently, from the images taken in the AMFlex2-OLTor1-FMLat1-FMFlex3 mode shown in Figure 4-1 five different types of adsorbates (presumably three different PAH (*e.g.* benzo[k]fluoranthene, benzo[b]fluoranthene and fluoranthene), alkanes with chain-lengths between 20 and 26 carbon atoms and water) can be discriminated on the surface of the few-layer graphene-/graphite-flake after storage in air under ambient conditions for 14 days. To verify the suggested adsorbate species, we performed Raman spectroscopic experiments of the few-layer graphene-/graphite-flake after storage (see Figure 7-20, Section 7.3.7). Unfortunately, we could not identify any additional peaks compared to the spectrum of a freshly prepared graphene-/graphite-sample. This could on the one hand be attributed to the small amount of adsorbate material covering the surface. On the other hand, the Raman spectra of fluoranthenes resemble the Raman spectra of graphene or graphite, complicating the identification of the adsorbate peaks [194]. It needs to be mentioned that other groups also reported on ordered stripes originating from nitrogen adsorption on graphitic surfaces [173, 195]. However, Wang *et al.* [196] reported that graphene nanoplatelets can be used as an adsorption agent for efficient cleaning of air from volatile organic compounds (VOCs) such as PAH which corroborates the high affinity of hydrocarbons on graphitic surfaces. Thus, we assume that the adsorption of VOCs is much more likely to occur under ambient conditions than the adsorption of nitrogen.

4.3.2. Analysis of large-scale adsorbates on a few-layer graphene-/graphite-flake after different times of storage under laboratory air conditions and subsequent heat or plasma treatment

To gain further insights into the formation of adsorbates on graphene-/graphite-flakes upon storage at ambient conditions we imaged the same area of the flake as analyzed in Figure 4-1 in the AMFlex2-OLTor1-FMLat1-FMFlex3 mode after longer periods of time and additionally analyzed the effect of heating and plasma-treating the samples, respectively, aiming to reduce/remove the adsorbates. In Figure 4-3, the resulting lateral drive amplitude images are shown. The corresponding second flexural phase, lateral and third flexural frequency-shift images are shown in the Supplementary Information (Figure 7-18, Section 7.3.5).

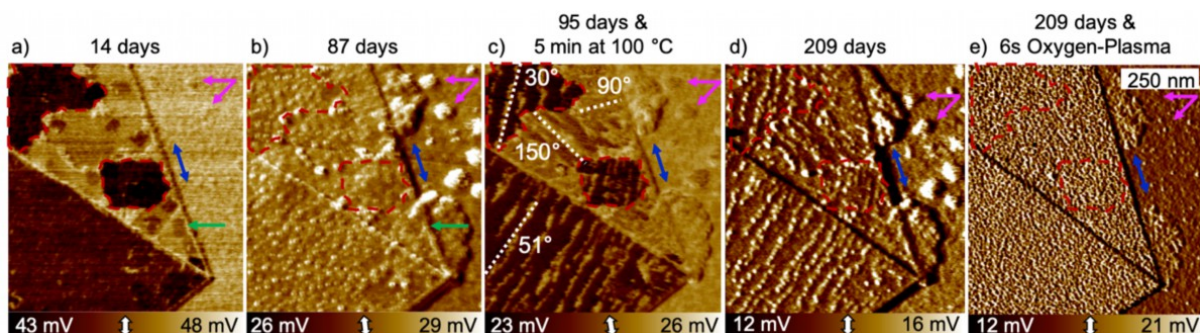


Figure 4-3: Adsorbate formation on the same few-layer graphene-/graphite-flake as shown in Figure 4-1 analyzed by means of the lateral drive amplitude acquired in the AMFlex2-OLTor1-FMLat1-FMFlex3 mode upon storage for 14 days (a), 87 days (b) and 95 days & heating for 5 min at 100 °C (c), 209 days (d) and 209 days & 6 s oxygen-plasma treatment (e). $A_{0(flex,2)} = 675$ pm, $A_{flex,2} = 600$ pm, (a–c): $A_{lat,1} = 1.766$ nm, $A_{flex,3} = 75$ pm, (d, e): $A_{lat,1} = 833$ pm, $A_{flex,3} = 150$ pm. The white arrows within the color bar indicate the direction of the in-plane cantilever oscillation. Pink and blue arrows point out positions where adsorbates were formed on the Si/SiO₂-substrate. The green arrow exemplarily indicates the position of a small-scale ordered stripe domain (Reprinted from ref. [225], <https://doi.org/10.1016/j.carbon.2022.08.005>, © 2022.²³).

Comparing the image after 14 days of storage (Figure 4-3a) to the image taken after 87 days of storage (Figure 4-3b) it is obvious that the amount of adsorbate material strongly increased during storage. As indicated by pink and blue arrows, larger conglomerates of adsorbates formed on the Si/SiO₂-substrate after 87 days of storage next to the graphene-flake which were not present after 14 days of storage. Additionally, on the sample stored for 87 days, the large-scale domains, which are clearly apparent after 14 days of storage as shown in Figure 4-3a and described in detail in Figure 4-1, were no longer observable in Figure 4-3b. Nevertheless, some of the small-scale domains which were clearly visible after 14 days of storage in Figure 4-3a could be identified in the lateral drive-amplitude image in Figure 4-3b after 87 days of storage as marked by green arrows in both images. We hypothesize that the small-scale domains clearly visible in Figure 4-3a were covered by a different type and layer of adsorbate material during the long-term storage resulting in the disappearance of the domains encircled in red (cf. Figure 4-3a with Figure 4-3b). In order to validate whether the large amount of coverage could more likely originate from inorganic molecule adsorption or from organic adsorbates such as hydrocarbons the sample was heated for 5 min at 100 °C after 95 days of storage. First, it becomes obvious by comparing the positions pointed out by pink and blue arrows on the Si/SiO₂-substrate prior to (Figure 4-3b) and after heating (Figure 4-3c) that some areas with larger amount of adsorbate material were still present after heating. Xie *et al.* [197] showed

²³ This article is protected by copyright. © 2022 Elsevier Ltd. All rights reserved.

that cleaning of graphene-surfaces from hydrocarbons requires temperatures larger than 500 °C which corroborates our assumption that different types of adsorbates were formed on the surfaces (graphene/graphite and SiO₂) upon storage. The heating of the sample most probably resulted in the removal of inorganic molecule adsorptions (most likely water) whereas adsorbates of organic origin remained at the surface. Interestingly, we observed that after the heat treatment, the large-scale domains which are apparent in Figure 4-3a can be identified again in Figure 4-3c as marked by the red dotted framed areas. Surprisingly, in every large-scale domain, stripe structures with a periodicity of approximately 50 nm formed which are again oriented in 60°-angles relative to each other (see white dotted lines in Figure 4-3c for relative orientation). In contrast to the small-scale adsorbate structures analyzed in Figure 4-1g, the large-scale ordered adsorbate structures appeared 30°-rotated. Consequently, based on the finding of Gallagher *et al.* [166], claiming that small-scale adsorbate structures assemble along the armchair direction, we assume that the ordered large-scale adsorbates observed after heating assembled along the zigzag direction of the hexagonal graphene-lattice. Small-scale adsorbate structures were not apparent in the images of the flake after storage for 95 days and heating for 5 min at 100 °C. It is likely to assume that the heat treatment of the sample led to a rearrangement of the hydrocarbons resulting in the formation of the large-scale adsorbate patterns. After storage of 209 days the large-scale oriented adsorbates were still visible as can be seen from Figure 4-3d, however, their domains marked by the red dotted frame were less pronounced compared to the ones in Figure 4-3c. The lateral drive-amplitude image shown in Figure 4-3e shows the same sample after 209 days of storage and 6 s oxygen-plasma treatment. On the Si/ SiO₂-substrate we observed that the quantity of adsorbates at the locations indicated by pink arrows was strongly reduced after plasma treatment, however, the adsorbates which were first observed after 87 days of storage (indicated by blue arrow) were still visible after 6 s of plasma irradiation. Interestingly, neither large- nor small-scale adsorbate patterns or different domains were visible on the graphene-/graphite-flake area after plasma treatment. This is a strong corroboration for the interpretation of Gallagher *et al.* [166] that the stripes and domains observed in Figure 4-3a–d originate from adsorbates that can be removed by the plasma irradiation rather than stress-induced rippling. Additionally, the fact that the lateral drive-amplitude values on the graphene-/graphite-flake area was homogeneously distributed and clearly distinguishable from the lateral drive amplitude on the substrate area indicates imaging of pristine surfaces. However, it needs to be mentioned that the surface of the graphene-/graphite-flake appears perforated to a certain degree, which implies that not only the adsorbates were removed but also some modification of the graphene-/graphite-surface took place. In order to analyze whether the oxygen-plasma treatment resulted in ablation of

graphene layers as *e.g.* reported by Al-Mumen *et al.* [198] or not, we drew averaged cross-sections (over 10 lines) through the topography images taken after 14 days of storage, 209 days of storage and after subsequent plasma etching for 6 s such as shown in Figure 7-19 in Section 7.3.6. The comparison revealed that no ablation of complete graphene-layers was induced by the plasma-treatment. However, it was clearly visible that the adsorbates were removed and that a slight increase of surface roughness on the graphene-/graphite area took place. From Raman spectroscopic measurements of the graphene-/graphite-flake treated for 6 s with oxygen-plasma (see Figure 7-20, Section 7.3.7) we observed that the D-peak as well as the D'-peak occurred after the plasma treatment which indicates the introduction of defects into the material [199]. Based on the results presented in Figure 4-3, we compared images taken in the AMFlex2-OLTor1-FMLat1-FMFlex3 mode after storage and plasma treatment before and after rotation by approximately 90° in order to analyze the origin of friction anisotropy.

4.3.3. Analysis of friction anisotropy on a few-layer graphene-/graphite-flake

First, we analyzed the few-layer graphene-/graphite-flake after storage of 87 days before and after rotation of approximately 90°. The results are shown in Figure 4-4 with focus on the lateral frequency-shift images.

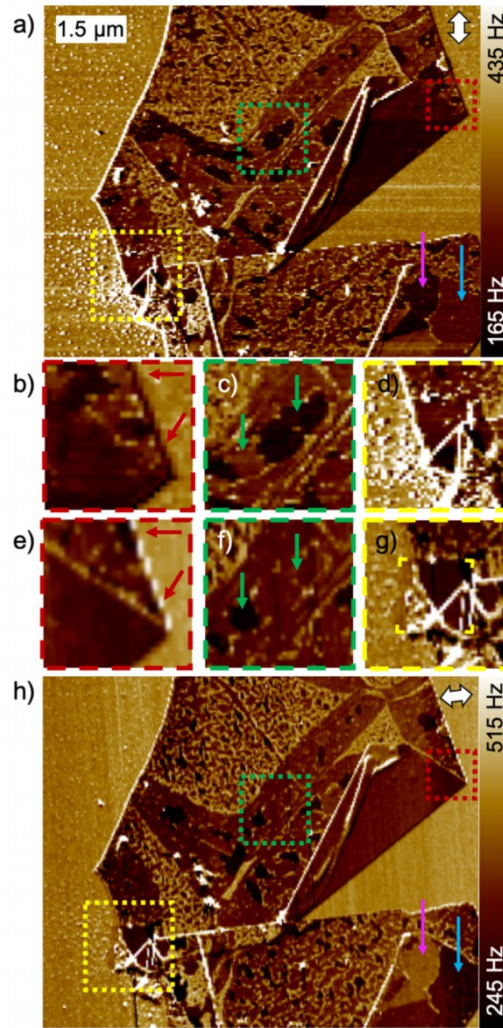


Figure 4-4: Lateral frequency-shift images of a few layer graphene-/graphite-flake taken in the AMFlex2-OLTor1-FMLat1-FMFlex3 mode before (a–d) and after rotation by approximately 90° (e–h). The areas framed in a and h by the yellow, green and red dotted squares are shown enlarged in b and e ($1 \times 1 \mu\text{m}^2$), c and f ($1.4 \times 1.4 \mu\text{m}^2$) and d and g ($1.9 \times 1.9 \mu\text{m}^2$), respectively. $A_0(\text{flex},2) = 675 \text{ pm}$, $A_{\text{flex},2} = 600 \text{ pm}$, $A_{\text{lat},1} = 1.766 \text{ nm}$, $A_{\text{flex},3} = 75 \text{ pm}$. Arrows point out regions where the color contrast was inverted after sample rotation by approximately 90° (Reprinted from ref. [225], <https://doi.org/10.1016/j.carbon.2022.08.005>, © 2022.²⁴).

Figure 4-4a and h show the overview images of the few-layer graphene-/graphite-flake which was already analyzed in the previous sections. The lateral oscillation direction of the cantilever is indicated by the white arrow on the top right of the images. The areas marked by the yellow, green and red dotted boxes are shown enlarged in Figure 4-4b–g for a more detailed comparison. At first glance, we noticed that large areas of the lateral frequency-shift images in Figure 4-4a and h show the same color contrast. Nevertheless, distinct domains such as exemplarily highlighted by the pink and the blue arrows, show an inverted contrast if Figure

²⁴ This article is protected by copyright. © 2022 Elsevier Ltd. All rights reserved.

4-4a is compared to Figure 4-4h. A similar effect can be observed if the area within the red dotted squares, which is shown enlarged in Figure 4-4b and e, is examined. This area was already analyzed in Figure 4-1 and Figure 4-3 and it becomes obvious that the domains which were observed in the areas #3 and #4, marked in Figure 4-1m-t exhibit inverted contrast after 90°-rotation of the sample as indicated by the red arrows. Interestingly, the areas marked as #2 in Figure 4-1m-t did not show contrast inversion after sample rotation which is another strong corroboration for the assumption that different types of hydrocarbons adsorbed on the graphene-/graphite-flake. The same effect can be observed within the area marked by the green dotted square, which is shown enlarged in Figure 4-4c and f, highlighted by green arrows. The observation that no friction anisotropy could be found in area #2 is additionally in line with the suggestion that benzo[k]fluoranthene or at least a molecule adsorbing in “top”-configuration (see Figure 4-2) might have been covering the respective areas. Due to the fact that the “top”-configuration resembles the stacking of graphene layers in graphite, exhibiting isotropic shear behavior [142], it is reasonable to believe that a coverage with *e.g.* benzo[k]fluoranthene results in isotropic frictional response. In contrast, for the “bridge”-configuration, such as proposed for areas #3 and #4 (*e.g.* benzo[b]fluoranthene and fluoranthene), anisotropic frictional behavior seems to be likely due to the incommensurability of the graphitic and the adsorbate lattice. These observations are a strong indication that the lateral frequency-shift images of the stored graphene-/graphite-flake taken in the AMFlex2-OLTor1-FMLat1-FMFlex3 mode contain strongly surface sensitive information of the tip/adsorbates/graphene interaction. Additionally, it becomes obvious that the images of unordered large-scale adsorbates such as *e.g.* visible in Figure 4-4c and f at the top left corner were also not significantly influenced by the sample rotation. It is likely to believe that these adsorbate structures originate from water adsorption due to the similarity of the lateral frequency-shift value compared to the SiO₂-substrate area. In Figure 4-4d and g the enlarged images of the area marked by the yellow dotted square in Figure 4-4a and h are shown. At this position the images shown in Figure 7-16 in Section 7.3.3 were taken, where we observed that imaging with high lateral amplitudes (17.26 nm) and second flexural amplitude setpoint ratios <78 % caused large-scale adsorbates removal from the few-layer graphene-/graphite-flake. The scan area chosen for the tip-particle removal (Figure 7-16 in Section 7.3.3) can be particularly identified in Figure 4-4g (small yellow markers). It approves the finding that adsorbates can be manipulated on the graphene-sample or the sample can be “cleaned” by the tip. By comparing Figure 4-4d to g, we additionally found that no anisotropy was observable on the “cleaned” area which further confirms that the friction anisotropy is strongly driven by adsorbates. To analyze this observation in more detail, we imaged the “cleaned” area of the flake (yellow dotted frame

in Figure 4-4a, d, g, h) with two different second flexural and first lateral eigenmode amplitudes before and after rotation, as shown in Figure 7-21 and Figure 7-22 of the Supplementary Information (Section 7.3.8). As a result, we found that the lateral frequency-shift values on the graphene-/graphite-flake did not significantly change during imaging with different lateral- or second flexural-amplitude setpoints. The lateral drive amplitude, however, was increased for the large lateral amplitude when the sample was rotated, indicating a higher amount of energy dissipated between tip and sample. Nevertheless, within the frame of uncertainty no anisotropic behavior could be found in this area by comparing the results prior to and after the 90° rotation of the sample as it was already recognized by the yellow-framed zoom-in shown in Figure 4-4d and g. Motivated by the observation from the 6 s of oxygen-plasma treatment that led to a strong reduction of adsorbate material (Figure 4-3e) we analyzed the treated sample prior to and after rotation by approximately 90° in order to confirm the assumption that friction anisotropy is mainly driven by adsorbates forming on the surface. The results are shown in Figure 4-5.

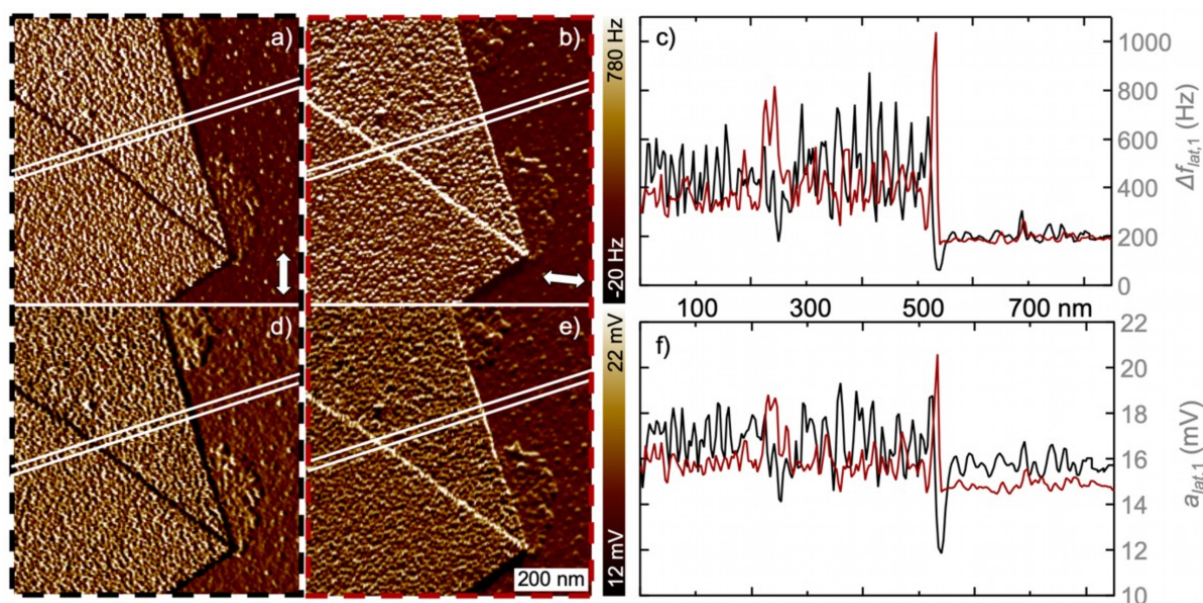


Figure 4-5: Lateral frequency-shift (a, b) and drive-amplitude images (d, e) of a few-layer graphene-/graphite-flake which was stored for 209 days and oxygen-plasma treated for 6 s afterwards. The black-framed images (a, d) show the sample prior to and the red-framed images (b, e) after rotation by approximately 90°. The lateral tip oscillation directions with respect to the sample orientation are indicated by the white arrows in a and b. In c and f, the averaged cross-sections (four pixel) taken at the positions marked with white lines (a, b, d, e) are shown. $A_0(flex,2) = 675$ pm, $A_{flex,2} = 600$ pm, $A_{lat,1} = 883$ pm, $A_{flex,3} = 150$ pm (Reprinted from ref. [225], <https://doi.org/10.1016/j.carbon.2022.08.005>, © 2022.²⁵).

²⁵ This article is protected by copyright. © 2022 Elsevier Ltd. All rights reserved.

By comparing the lateral frequency-shift images prior to (Figure 4-5a) and after 90°-rotation (Figure 4-5b) after 6 s of oxygen-plasma treatment, the largest differences were observed at the steps or edges of the graphene-/graphite-flake, most probably caused by a delayed response of the feedback loop. However, the corresponding averaged cross-sections (Figure 4-5c) confirm that no substantial anisotropy in the lateral frequency shift was observed neither on the graphene-/graphite-flake nor on the Si/SiO₂-substrate. Because it is well known that the dissipative tip-sample interaction can be imaged by visualizing of the drive-amplitude channel, we additionally compared the lateral drive-amplitude images prior to (Figure 4-5d) and after 90°-rotation (Figure 4-5e) of the graphene-/graphite-flake. The tiny offset (1 mV) in the drive amplitude value can be attributed to a slight change of the detection laser during sample unmounting for rotation (for detailed explanation, see Supplementary Information, Section 7.3.9). Compared to the anisotropic behavior of the same flake observed after storage for 14 days as shown in Figure 4-4 we conclude that both, the conservative component of the interaction (shear) and the dissipative component (friction) are isotropic on oxygen-plasma treated graphene-/graphite- and SiO₂-surfaces.

By analyzing the results of Figure 4-5 it needs to be considered that the 6 s of oxygen-plasma treatment not only led to a removal of the adsorbate material but also slightly modified the morphology of the few-layer graphene-/graphite-flake such as shown in Figure 7-19 in Section 7.3.6. Additionally, it was pointed out *via* Raman spectroscopy that the plasma treatment led to the introduction of defects into the material, resulting *e.g.* in the oxidation of the topmost graphene-layers. Nevertheless, we assume that the isotropic frictional behavior of the few-layer graphene-/graphite-flake after plasma-treatment was most probably not caused by a change of the intrinsic graphene/graphite properties. The assumption is based on the work of Berman *et al.* [200] who could show that graphene oxide exhibits even higher friction anisotropy compared to graphene. To clearly confirm the interpretation that friction anisotropy is caused by adsorbates covering the surface, it might help to adjust the multifrequency AFM technique to UHV conditions. However, it needs to be mentioned that amplitude-modulation AFM as used here is challenging to perform under UHV conditions because of the high-Q environment that increases the settling time of the tip oscillation to unpracticable time spans. Hence, a frequency-modulated multifrequency setup has to be developed which does not guarantee comparable results. Additionally, the preparation of graphene-/graphite-samples without any surface contamination would be an essential requirement because adsorbates which are present on graphitic surfaces will not completely be removed under UHV conditions [191].

4.4. Conclusion

In this study we found that the formation of adsorbates on graphene-/graphite-flakes started to take place directly after preparation of the sample under laboratory air conditions. After 14 days of storage we observed different types of adsorbates: (I) unordered large-scale adsorbates (most probably water), (II) large-scale domains (presumably PAH) and (III) small-scale ordered stripes (most likely normal alkanes with chain-lengths between 20 and 26 carbon atoms) oriented along the armchair direction of the topmost graphene layer. The unordered large-scale adsorbates were observed in all acquired channels (second eigenmode flexural phase shift, first eigenmode lateral drive amplitude and frequency shift, third eigenmode flexural frequency shift), whereas the contrast of the large-scale domains differed between channels related to in-plane and out-of-plane properties as well as conservative and dissipative interaction. The small-scale stripe domains exhibited an expected 60° -orientation relative to each other and their appearance was most prominent in the second flexural-phase and the first lateral drive-amplitude images indicating a predominantly dissipative nature of the interaction. We found that upon long-term storage of the sample the amount of adsorbate material increased on both, the graphene-/graphite-flake and the Si/SiO₂-substrate. Heating the sample for 5 min at 100 °C after 95 days of storage led to a partial removal of the adsorbate material (most likely water), however, a significant proportion of adsorbates remained at the sample. Interestingly, after the heat-treatment, large-scale domains formed again on the graphene-/graphite-area and a large-scale ordered stripe pattern was formed, most probably along the zigzag direction of the topmost graphene layer. Further storage of the sample resulted in a disappearance of the large-scale domains, presumably due to readsorption with water molecules. Additionally, we discovered that a plasma treatment of the long-term stored sample resulted in a strong reduction of adsorbate material, especially on the graphene-/graphite-flake area. The adsorbate driven origin of friction anisotropy was confirmed by analyzing the sample stored for 14 days and after oxygen-plasma treatment prior to and after rotation by approximately 90° . After 14 days of storage, the contrast of several large-scale domains in the lateral drive-amplitude and frequency-shift images showed inverted contrast after rotation of the sample, indicating friction anisotropy. However, some of the large-scale domains remained unchanged after the 90° -rotation, indicating the presence of different types of adsorbates, which only partially led to friction anisotropy. Based on a DFT study of Li *et al.* [193] dealing with adsorption energy and adsorption configuration of different PAH, we suggest three different molecules (benzo[k]fluoranthene (#2), benzo[b]fluoranthene (#3) and fluoranthene (#4)) that could be present on the surface and would fit to the observations of Figure 4-1. After 209 days of storage

and subsequent plasma-treatment no substantial change in conservative or dissipative interaction was observed prior to and after rotation of the sample, indicating neither friction nor shear anisotropy on “cleaned” graphene-, graphite- or SiO₂-surfaces.

In summary, we could demonstrate that imaging with small amplitudes using the AMFlex2-OLTor1-FMLat1-FMFlex3 method opens up new avenues for a very sensitive and comprehensive surface analysis. We found that the separation of in-plane and out-of-plane as well as dissipative and conservative interactions facilitates the discrimination of different types of adsorbates covering graphene-/graphite-surfaces. We conclude that the frictional behavior of graphitic surfaces strongly depends on the storage conditions and the type of airborne adsorbates. Both attributes have to be taken into account for the design of devices where stable frictional properties are essential.

4.5. Acknowledgement

The authors thank the Deutsche Forschungsgemeinschaft (Project number 407750697) for financial support.

5. Adsorbate formation/removal and plasma-induced evolution of defects in graphitic materials²⁶

The preparation of adsorbate-free graphene with well-defined layer numbers is a current challenge in materials and surface science. One strategy to tailor the number of layers is oxygen-plasma treatment of few-layer graphene-/graphite-flakes. However, when graphitic materials are stored in air under ambient conditions, it is almost inevitable that adsorbates are deposited on their surfaces. When precisely removing individual graphene layers from graphite and graphene flakes by oxygen-plasma treatment, the amount and type of adsorbates strongly affect the required plasma-treatment process and duration. To examine the removal/etching mechanism involved in removing such layers, few-layer graphene-/graphite flakes, with areas of different layer numbers, were stored in ambient air and stepwise exposed to oxygen plasma in a shielded configuration. The flakes were then successively analyzed by multifrequency atomic force microscopy in combination with Raman spectroscopy, focusing on the etching rate and adsorbate and defect evolution. Combined in-plane and out-of-plane tip-adsorbate-substrate interaction analysis facilitated discrimination of different types of adsorbates (water, polycyclic aromatic hydrocarbons, and linear alkanes) and their formation with time.

5.1. Introduction

Since its invention in 2004 [10], graphene has emerged as a promising material as electrical component in storage and energy conversion devices, such as batteries [201] and solar cells [202] paving the way towards alternative energy sources [203, 204]. Depending on the application, graphene with a specific number of layers is required, and mono-, bi-, and trilayer graphene are of particular technological interest [205-207]. To distinguish graphene consisting of up to four layers, Raman spectroscopy has been shown to be reliable: The intensity ratio between the G- and the 2D-peak can provide information about the sample thickness [97]. Despite several graphene preparation methods being realized within the last few years [10, 208-211], the synthesis of graphene with a well-defined number of layers is still challenging. A promising approach for the controlled ablation of graphene layers is plasma treatment. Several different gases have been used for thinning multilayer graphene to monolayer graphene, such

²⁶ This Section titled “Adsorbate Formation/Removal and Plasma-Induced Evolution of Defects in Graphitic Materials” was submitted as a manuscript by A. L. Eichhorn, M. Hoffer, K. Bitsch and C. Dietz. The final version was published as “Adsorbate Formation/Removal and Plasma-Induced Evolution of Defects in Graphitic Materials” by A. L. Eichhorn, M. Hoffer, K. Bitsch and C. Dietz in *Advanced Materials Interfaces*, 2023. 2300256. © 2023 The Authors. *Advanced Materials Interfaces* published by Wiley-VCH GmbH. This is an open access article under the terms of the Creative Commons Attribution License (<https://creativecommons.org/licenses/by/4.0/>), which permits use, distribution and reproduction in any medium, provided the original work is properly cited. References were adapted to provide continuous numbering throughout the whole work.

as N₂, H₂, H₂O₂, and O₂, or combinations of these gases [198, 212-214]. The time required for the ablation of single layers is strongly dependent on the type of gas used [214] and on ablation parameters, such as the discharge power, plasma chamber pressure, and distance of the sample from the powered electrode [215-217]. Oxygen plasma is strongly effective in graphene layer ablation; however, the ablation parameters must be carefully adjusted in order to prevent the sample from becoming severely damaged. Eckmann *et al.* [108] analyzed the Raman spectra of defective graphene samples, distinguishing between a “stage 1” and “stage 2” of defect generation. The transition between stage 1 and stage 2 was characterized by a maximum in the D- and G-peak ratio as a function of plasma-treatment time. They showed that the ratio between the D- and the D'-peak is a suitable indicator of the predominant type of defect. They also found that for stage 1, $I_D/I_{D'} \approx 13$ indicated that sp³-type defects were predominant, while $I_D/I_{D'} \approx 7$ indicated that vacancy-like defects were predominant. Smaller intensity ratios between the D- and the D'-peak (≈ 3.5) were attributed to boundaries in the graphite. Lee *et al.* [218] defined the transition between sp³- (stage 1, crystalline defects) and vacancy-type defects (stage 2, nanocrystalline defects) at $I_D/I_{D'} \approx 7$. They extended the model by a third stage, which was defined by reaching a plateau at $I_D/I_{D'} \approx 3.5$, indicating the presence of amorphous carbon [219]. Zandiatashbar *et al.* [109] reported that the introduction of defects in graphene samples during plasma treatment could be strongly reduced by placing the sample upside down in the chamber between two glass slides, resulting in a shielded configuration. Additionally, they found that the ratio between the D- and G-peak as a function of plasma-treatment time of monolayer graphene had a local maximum at the transition between predominantly sp³-type and predominantly vacancy-type defects [109]. Because the number of defects and the number of layers both influence the Raman spectra of few-layer graphene-/graphite-samples, we examined the effect of plasma treatment on the few-layer graphene-/graphite-samples during stepwise ablation of the graphene layers. This was done in a shielded configuration, and the samples were interrogated using Raman spectroscopy and atomic force microscopy (AFM). Graphene samples have a high tendency to become covered by adsorbates, which, depending on the duration of storage and surrounding conditions, form stripe-like structures with periodicities of 4–6 nm [165, 166, 173, 175, 190, 195, 220-224]. Recently, we demonstrated (using AFM) that different types of adsorbates covering graphitic surfaces could be distinguished by analyzing the flexural and torsional/lateral cantilever vibrational modes simultaneously (AMFlex2-OLTor1-FMLat1-FMFlex3 mode), when the tip interacted with the adsorbates [225]. On top of the stripe-like patterns identified by Pálincás *et al.* [224], which originated from normal alkanes with chain lengths between 20–26 carbon atoms, we found another four types of adsorbates that could be attributed to three different polycyclic aromatic

hydrocarbons (PAHs) and water [225]. Consequently, when removing individual carbon layers from graphitic surfaces, it is essential to remove adsorbates at an earlier stage.

We also examined the controlled removal of adsorbates by shielded oxygen-plasma treatment in order to obtain cleaned and pure graphitic surfaces. The effect of incremental oxygen-plasma treatment on a few-layer graphene-/graphite-sample stored for different durations under ambient laboratory conditions was analyzed by using AFM, with the recently introduced AMFlex2-OLTor1-FMLat1 AFM method [182]. This multifrequency approach was chosen because of its capability of distinguishing different types of adsorbates by their in-plane and out-of-plane interactions with the AFM tip. Additionally, this approach facilitated the examination of whether surfaces were covered with adsorbates [225].

5.2. Results and discussion

5.2.1. Layer analysis of oxygen-plasma-treated few-layer graphene-/graphite-flakes

To elucidate the effect of oxygen-plasma treatment on layer number and defect generation within a few-layer graphene-/graphite-sample, AFM and Raman spectroscopy experiments were performed. The sample was placed in a plasma chamber in a shielded configuration, as schematically depicted in Figure 5-1b. After each step of oxygen-plasma treatment, the sample was analyzed using amplitude modulation (AM) AFM and Raman spectroscopy; scans across the different layers of a graphene flake were acquired. The sample was oxygen-plasma-treated for the durations listed in Table 5-1 of the Experimental Section.

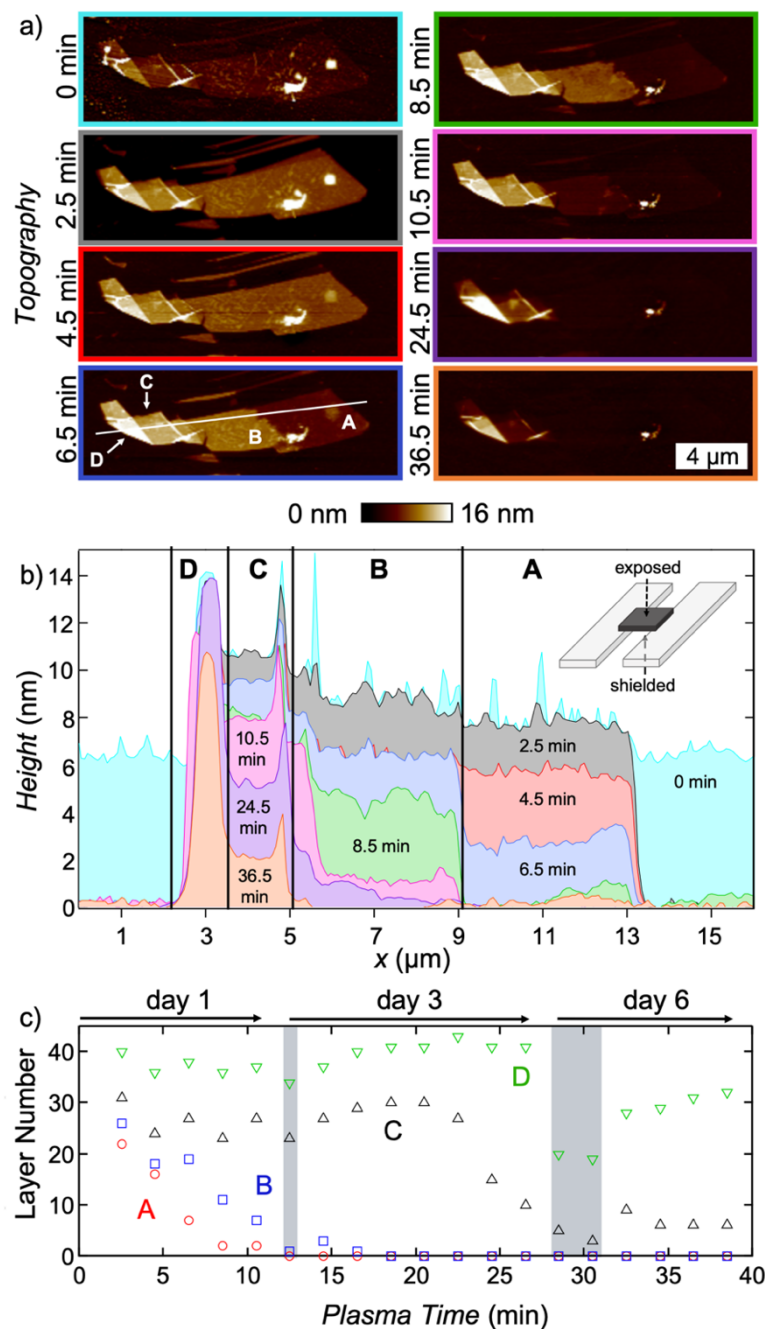


Figure 5-1: AFM topography imaging and analysis of a few-layer graphene-/graphite-sample treated by oxygen plasma. AFM topography images (a) and cross-sections (b) of a few-layer graphene-/graphite-flake before (light blue) and after 2.5 min (grey), 4.5 min (red), 6.5 min (blue), 8.5 min (green), 10.5 min (pink), 24.5 min (purple), and 36.5 min (orange) of oxygen-plasma treatment in a shielded configuration (inset in b). (c) Number of carbon layers of the different areas A (red circle), B (blue square), C (black triangle), and D (green triangle), as marked in (b), as a function of plasma-treatment time (Reprinted from ref. [226], <https://doi.org/10.1002/admi.202300256>, © 2023.²⁷ Figure and caption were slightly adapted).

²⁷ This is an open access article under the terms of the Creative Commons Attribution License (<https://creativecommons.org/licenses/by/4.0/>), which permits use, distribution and reproduction in any medium, provided the original work is properly cited.

Figure 5-1 shows the evolution of layer thickness for a few-layer graphene-/graphite-sample stepwise treated by oxygen plasma in a shielded configuration, as schematically depicted in Figure 7-24. In Figure 5-1a, AFM topographic images of a few-layer graphene-/graphite-sample are shown prior to (light blue) and after 2.5 min (grey), 4.5 min (red), 6.5 min (blue), 8.5 min (green), 10.5 min (pink), 24.5 min (purple), and 36.5 min (orange) of plasma treatment. The corresponding cross-sections along the white line in Figure 5-1a (blue framed image) are shown in Figure 5-1b. Additionally, areas A, B, C, and D, representing graphene/graphite with different layer thicknesses, are marked in Figure 5-1a (blue frame) and in Figure 5-1b. Surprisingly, the height of the few-layer graphene-/graphite-sample determined from the cross-section of the AFM images of the sample prior to oxygen-plasma treatment (light blue frame) is less than the height determined after 2.5 min (grey frame) of oxygen-plasma treatment. However, if the corresponding topographic images in Figure 5-1a (light blue and grey framed) are analyzed in detail, it becomes obvious that prior to plasma treatment, the substrate was covered significantly by adsorbates (left and right portions of the cross-section). This phenomenon was also observed and analyzed in detail in our recent publication [225], in which we showed that different types of adsorbates formed on both, graphene-/graphite-sample and Si/SiO₂-substrate. Consequently, it is reasonable to assume that a larger quantity of adsorbates covered the Si/SiO₂-substrate area compared to the graphene-/graphite-sample, resulting in an apparently smaller thickness of the graphene-/graphite-sample prior to plasma treatment. By analyzing cross-sections of AFM topographic images taken after 30 s, 1 min, 1.5 min, and 2 min, shown in Figure 7-25 of the Supplementary Information, we can show that the adsorbate coverage was stepwise removed from the substrate. Eventually after 4.5 min of plasma treatment, the sample was cleaned, removing a large quantity of adsorbates. The height difference between area A and B became clearly visible after 6.5 min of plasma treatment. Interestingly, the etching rate of graphene layers was strongly dependent on the initial number of layers, as can be deduced from Figure 5-1c. The larger the initial number of graphene layers, the slower the etching rate. We assume that this is because of the presence of different types of adsorbates on the substrate/sample, and the associated differences in adsorption energies. The removal of the thinner graphene layers (areas A and B) started immediately after the adsorbates were removed, whereas 24.5 min elapsed before a clear reduction in thickness was visible in area C and after 32.5 min in area D. Interestingly, there was a continuous removal of material within areas A and B until exposure of the substrate after 8.5 min and 12.5 min, respectively. The etching rates within areas A (2.5–8.5 min), B (6.5–12.5 min), and C (24.5–28.5 min) were 3.0–3.5 layers per minute, *i.e.*, 16–21 s were required to remove a single layer of graphene.

5.2.2. Defect analysis of oxygen-plasma-treated few-layer graphene-/graphite-flakes

To study the effect of stepwise oxygen-plasma treatment on defect evolution in the few-layer graphene-/graphite-sample, we took Raman measurements after each step of plasma treatment, immediately after the AFM topographic images (c.f. Section 5.2.1) were taken. The results are summarized in Figure 5-2.

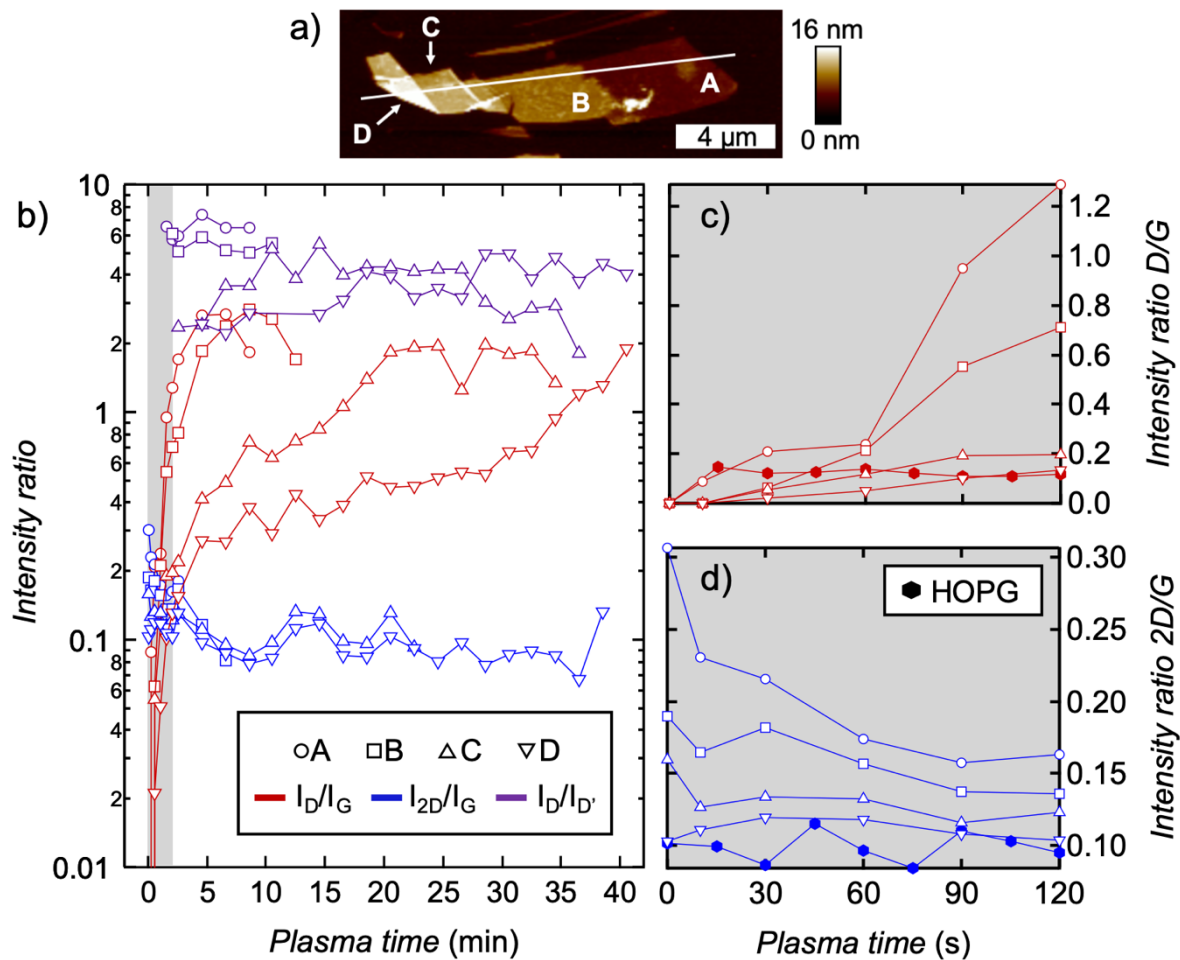


Figure 5-2: Raman intensity ratios measured within areas A (circle), B (square), C (triangle pointing up), and D (triangle pointing down), as marked in (a), as a function of oxygen-plasma treatment time (b). The intensity ratio between the D- and G-peak is shown in red, between the 2D- and G-peak in blue and between the D- and D'-peak in purple color. Zoom-in images of the grey marked area in (b) for the intensity ratios D/G and 2D/G are shown in (c) and (d), respectively. For comparison, the intensity ratios determined on highly oriented pyrolytic graphite (HOPG) for stepwise oxygen-plasma treatment in the shielded configuration are added to (c) and (d) by means of filled hexagons (Reprinted from ref. [226], <https://doi.org/10.1002/admi.202300256>, © 2023.²⁸ Figure and caption were slightly adapted).

²⁸ This is an open access article under the terms of the Creative Commons Attribution License (<https://creativecommons.org/licenses/by/4.0/>), which permits use, distribution and reproduction in any medium, provided the original work is properly cited.

The AFM topographic image taken after 6.5 min of plasma treatment is shown in Figure 5-2a and indicates areas A, B, C, and D, where the Raman spectra were taken. Results of the Raman-spectroscopic analysis are shown in Figure 5-2b in the form of the intensity ratios D/G (red, measure for defect density), 2D/G (blue, measure for layer number), and D/D' (purple, measure for defect type) determined within the areas A (circle), B (square), C (triangle pointing up), and D (triangle pointing down). Additionally, a zoom-in for the first two minutes of cumulative oxygen-plasma treatment is provided in Figure 5-2c and d for the intensity ratios D/G and 2D/G, respectively. For comparison, the results of a highly oriented pyrolytic graphite (HOPG) sample, stepwise treated for 120 s, are included in Figure 5-2c and d (filled hexagons). The experiments on HOPG were performed for two reasons: (i) The Raman spectrum of plasma-treated HOPG is predominantly influenced by the introduced defects. Due to the relatively large HOPG sample thickness, there should be a negligible effect from the number of graphene layers beneath the topmost on the etching rate. (ii) A double-sided freshly cleaved HOPG sample allows analysis of the exposed and the shielded area of the sample that result from one and the same plasma treatment process. This facilitates a direct comparison of both treatment options, as shown in Figure 7-24 of the Supplementary Information.

Each of the areas A, B, C, and D show an initial increase in the intensity ratio D/G. Interestingly, for areas A and B a maximum in the intensity ratio between the D- and G-peaks at ≈ 3 was reached shortly before the area was completely removed as a consequence of oxygen-plasma treatment. Such a maximum was also observed by Zandiatashbar *et al.* [109] at $I_D/I_G \approx 4$, which was interpreted as a transition between predominantly sp^3 -type and vacancy-type defects. However, the authors observed a complementary decrease in $I_D/I_{D'}$, which was not observed in our experiments [109]. This may be because Zandiatashbar *et al.* investigated monolayer graphene, whereas we focused on controlled ablation of few-layer graphene-/graphite-samples. In contrast, for the intensity ratio D/D' (Figure 5-2b, purple) no clear trend was observable. For areas A and B, $I_D/I_{D'}$ was stable at approximately 6.4 ± 0.5 and 5.5 ± 0.4 , respectively; there was slightly more variance for areas C and D (3.6 ± 1 and 3.7 ± 0.8). Based on the experiments done by Eckmann *et al.* [108] on graphene, the predominant types of defects would be the vacancy type (≈ 7) in areas A and B and the boundary type (≈ 3.5) in areas C and D. However, this is in contrast to the interpretation by Zandiatashbar *et al.* [109] that the maximum of I_D/I_G marks the transition between sp^3 -type and vacancy-type defects in graphene. We assume that this discrepancy mainly originates in our case having analyzed few-layer graphene-/graphite-samples, in which not only the number of defects, but also the number of layers influences the Raman spectra [227]. This argument is supported by the trend of the intensity ratio I_{2D}/I_G

(Figure 5-2b and d, blue), which was initially larger for thinner areas of the flake, but decreased with plasma-treatment time. Lee *et al.* [218] found that during stage 1 (prior to reaching the maximum value of I_D/I_G) oxygen tended to adsorb on the graphene surface to form sp^3 -type defects, such as epoxy, carbonyl, and ether groups. The epoxy groups exhibited, according to the authors, the lowest defect formation energy and were energetically favored to form on the graphene surface. The transition between stage 1 and 2 represented the conversion of sp^3 - to vacancy-type defects.

Additionally, we observed that the D-peak already appeared after 30 s of oxygen-plasma treatment at the latest for all areas of the investigated few-layer graphene/graphite flake including the HOPG sample (see Figure 5-2c). This was unexpected because, for short plasma-treatment times, the graphene-/graphite-flakes were still covered by large quantities of adsorbates (Figure 5-1). Consequently, we decided to analyze the process of adsorbate removal by successive oxygen-plasma treatment in more detail by applying the recently introduced AMFlex2-OLTor1-FMLat1 AFM method. This method allows a detailed analysis of the in-plane and out-of-plane interactions of a sharp tip with adsorbates and graphitic surfaces [182]. Based on the findings of Zandiatashbar *et al.* [109] and Lee *et al.* [218], we propose that for 30 s of plasma treatment predominantly sp^3 -type defects, such as epoxy, carbonyl, and ether groups, should be visible. Depending on the thickness of the few-layer graphene-/graphite-sample, longer plasma-treatment durations should either lead to the formation of further sp^3 -type defects or to vacancies whose presence we also aimed to confirm by our AFM method.

5.2.3. Domain pattern formation and successive removal by oxygen plasma

Based on the knowledge obtained from our previous work [225], we expect at least three different types of adsorbates to become evident upon storage, *i.e.* water (islands), PAHs (domains), and alkanes (stripe-like patterns). Firstly, we analyzed the second flexural phase and lateral drive amplitude AFM images acquired on a stored and oxygen-plasma-treated few-layer graphene-/graphite-flake at a relatively large scale ($8 \times 8 \mu\text{m}^2$). The results are shown in Figure 5-3.

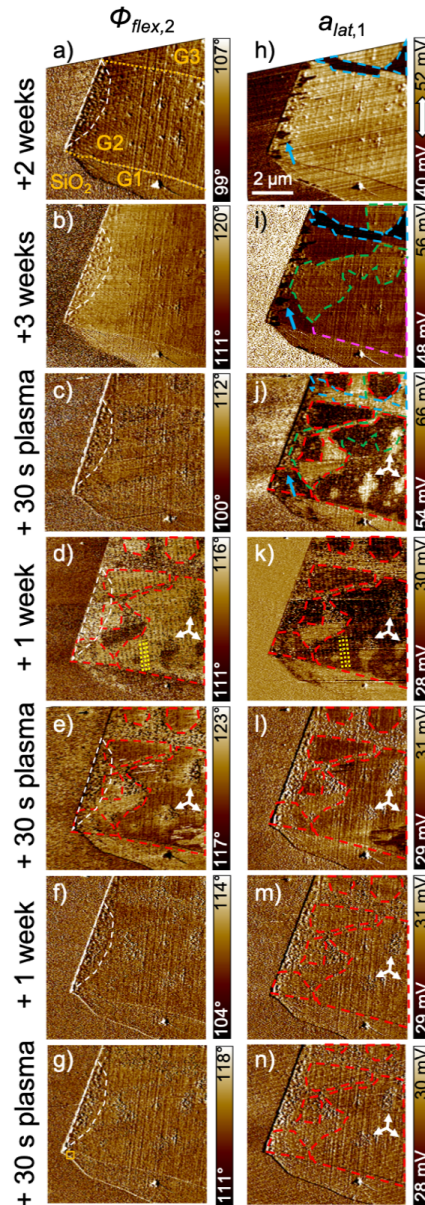


Figure 5-3: Adsorbate formation on a few-layer graphene-/graphite-flake analyzed by means of second flexural phase (a–g) and lateral drive-amplitude (h–n) after different durations of storage and oxygen-plasma treatment and in AMFlex2-OLTor1-FMLat1 AFM mode. $A_0 (flex,2) = 675$ nm, $A_{flex,2} = 600$ nm, and $A_{lat,1} = 1.766$ nm. The few-layer graphene-/graphite-flake consists of three areas (G1, G2, and G3, as marked in (a)) with different numbers of graphene layers, where the layer number increases from G1 to G3. The white arrow within the color bar (h) indicates the direction of lateral oscillation. Dashed lines (blue, green, pink, and red) highlight the shape of the different domains found on the few-layer graphene-/graphite-flake surface. Large-scale islands are enclosed by white dashed lines in the flexural phase images (a–g). The yellow square in (g) marks the area (350×350 nm²) where the high-resolution images shown in Figure 5-4 were taken (Reprinted from ref. [226], <https://doi.org/10.1002/admi.202300256>, © 2023.²⁹ Figure and caption were slightly adapted).

²⁹ This is an open access article under the terms of the Creative Commons Attribution License (<https://creativecommons.org/licenses/by/4.0/>), which permits use, distribution and reproduction in any medium, provided the original work is properly cited.

For the images shown in Figure 5-3, the sample was first stored for two weeks (Figure 5-3a, h), then for another three weeks (Figure 5-3b, i), and then treated with oxygen-plasma for 30 s in the shielded configuration (Figure 5-3c, j). Subsequently, we repeated a procedure of one week's storage (Figure 5-3d, f, k, m and Figure 7-27a, c) and 30 s of plasma treatment (Figure 5-3e, g, l, n and Figure 7-27b, d) three times, to study the desorption and re-adsorption process of adsorbates.

After the initial storage of the prepared graphene/graphite sample for two weeks, the accumulation of adsorbates on the few-layer graphene-/graphite-flake was characterized by different domains apparent, as highlighted by the blue arrow and dashed lines in the lateral drive-amplitude image in Figure 5-3h. Interestingly, the domains were not visible in the corresponding second flexural phase image (Figure 5-3a). However, the flexural phase image indicated the presence of adsorbates forming large-scale islands within the area marked by the white dashed line in Figure 5-3a. These islands were also observed in our recent study [225], and most likely originated from adsorbed water. After storing the sample for another three weeks, additional domains became apparent, as highlighted by the green and pink dashed lines in the lateral drive-amplitude image in Figure 5-3i. These domains can only be guessed in the flexural phase image in Figure 5-3b. This matches our previous observations: We proposed the presence of different PAHs adsorbing on graphitic surfaces under laboratory air conditions [193, 225]. We also proposed that the dissipative interaction between the tip and all types of adsorbates was similar in out-of-plane direction, but distinguishable in in-plane direction. The large-scale islands within the area marked by the white dashed lines in Figure 5-3b were still present. Interestingly, after the first oxygen-plasma treatment of 30 s, the domain structure was still visible in the lateral drive-amplitude images of the few-layer graphene-/graphite-surface. However, the appearance of the domains changed, which is clear when comparing the red with the blue, pink, and green dashed lines in Figure 5-3j. There are bright circular-shaped domains of around 1–2 μm in size, as indicated by white arrows; there are also relatively dark domains at the upper flake region and close to the flake edge, as marked by the red dotted lines in Figure 5-3j. Interestingly, only within the areas marked by the blue dashed lines, the lateral drive amplitude remained constant in value, however, at a higher value compared to the image taken before plasma treatment (Figure 5-3i). In the green and pink marked areas, the lateral drive amplitude partially changes, resulting in new domains (the red dotted lines in Figure 5-3j). This indicates that adsorbates were partially removed by plasma treatment. Neither the variation in domains, nor the effect of plasma treatment, are visible in the corresponding phase image (Figure 5-3c); here, the large-scale islands forming from water are still present (white dashed

line). After another week of storage, a domain structure similar to that obtained directly after plasma treatment (Figure 5-3j) was observed on the flake surface in the lateral drive-amplitude image, as indicated by the red dashed lines in Figure 5-3k. Interestingly, stripes with a periodicity of 200–250 nm appeared on a large proportion of the flake, indicated by the yellow dashed lines in Figure 5-3k. These stripes are also clearly visible in the corresponding phase image in Figure 5-3d. We observed a similar phenomenon in our recent study [225], where stripes with a periodicity of approximately 50 nm could be detected on graphitic surfaces after heating as well as subsequent storage. The stripes were predominantly aligned along the zigzag direction of the hexagonal carbon lattice. Some of the plasma-induced domains were visible in the flexural phase images, as marked by the white arrows and red dotted lines in Figure 5-3d. This is an interesting observation because it indicates that the plasma treatment and the re-adsorption within these areas changed the tip-sample out-of-plane dissipative interactions. Consequently, it is reasonable to assume that the material adsorbing during one week's storage is different from the previously present type of adsorbate. Interestingly, the large-scale islands are not visible in Figure 5-3d (white dashed lines), indicating that the re-adsorbing material covered these islands during the one week of storage. As shown in Figure 5-3l, after the second plasma treatment of 30 s in the shielded configuration, the overall domain structure remains the same; however, the stripes disappear and the bright domains (indicated by white arrows) resemble the contrast attributed to water island formation (marked by white dashed lines in the corresponding flexural phase image (Figure 5-3e)). This was initially surprising because we expected removal of material induced by plasma treatment rather than water island formations. However, this phenomenon has been observed by others and will be discussed in detail in Section 5.2.4. Plasma-induced water island formation also explains the presence of bright and dark domains in the corresponding phase image in Figure 5-3e after the second plasma-treatment step. After another week of storage, the bright and dark domains became less distinct in both the flexural phase and the lateral drive-amplitude image (see Figure 5-3f and m). Nevertheless, the islands (marked by the white dashed lines and white arrows in Figure 5-3f and outside the red dashed marked areas in Figure 5-3m) were still apparent. This is indicative of coverage by a single type of adsorbate, however, one that possesses pockets of water. Similar observations were made after the next 30 s plasma-treatment step, as shown in Figure 5-3g and n and after another one week's storage (Figure 7-27a, c) and 30 s plasma treatment (Figure 7-27b, d), where bright and dark domains were hardly visible. It can be assumed that the adsorbate material was completely removed from the surface, and that subsequent storage for one week was insufficient to form distinct domains. To further understand adsorbate formation and removal, we analyzed the topographic images corresponding to the ones shown in Figure

5-3. We determined the height of the different areas G1, G2, and G3 relative to the Si/SiO₂-substrate and found that after the first two weeks of storage, both areas G1 and G2 were lower compared to the substrate (for details see Figure 7-28). Consequently, we confirmed that larger quantities of adsorbates were deposited on the Si/SiO₂-substrate compared to the few-layer graphene-/graphite-flake areas. Additionally, larger quantities of adsorbates were removed from the Si/SiO₂-substrate during the 30 s of plasma treatment compared to the graphene-/graphite-areas. Both effects complicate the accurate measurement of the number of graphene layers and hindering the determination of the plasma-treatment time needed to remove the adsorbates from the graphitic surfaces. However, using the information in Figure 5-2 and Figure 5-3, we propose that large quantities of adsorbates were already removed after 30 s of plasma treatment; and after another 30 s of plasma treatment, the sample was almost completely adsorbate-free, except for areas where water islands grew. This is in agreement with the Raman spectroscopy results (Figure 5-2) that show that defects were already introduced after a short plasma treatment (30 s) in the shielded configuration. However, solely observing topographic images is insufficient to corroborate this thesis because the complete removal of adsorbates from the Si/SiO₂-surface takes approximately four times longer than the complete removal from the graphitic flake areas. In order to corroborate the proposed theory, we recorded and thoroughly analyzed high-resolution images of the same few-layer graphene-/graphite-flake, within the area marked by the yellow square in Figure 5-3g.

5.2.4. Stripe-like adsorbate and island formation successively removed by oxygen-plasma treatment

In addition to the adsorbates forming different domains, we also expect stripe-like patterns to form on graphitic surfaces upon storage [165, 166, 173, 175, 190, 195, 220-224]. Based on the results of our previous study [225], we analyzed the effect of plasma treatment on the stripe-like patterns by using the second flexural phase images, as shown in Figure 5-4. The corresponding lateral drive-amplitude images, in which the stripe-like patterns are also visible, are shown in Figure 7-29 of the Supplementary Information.

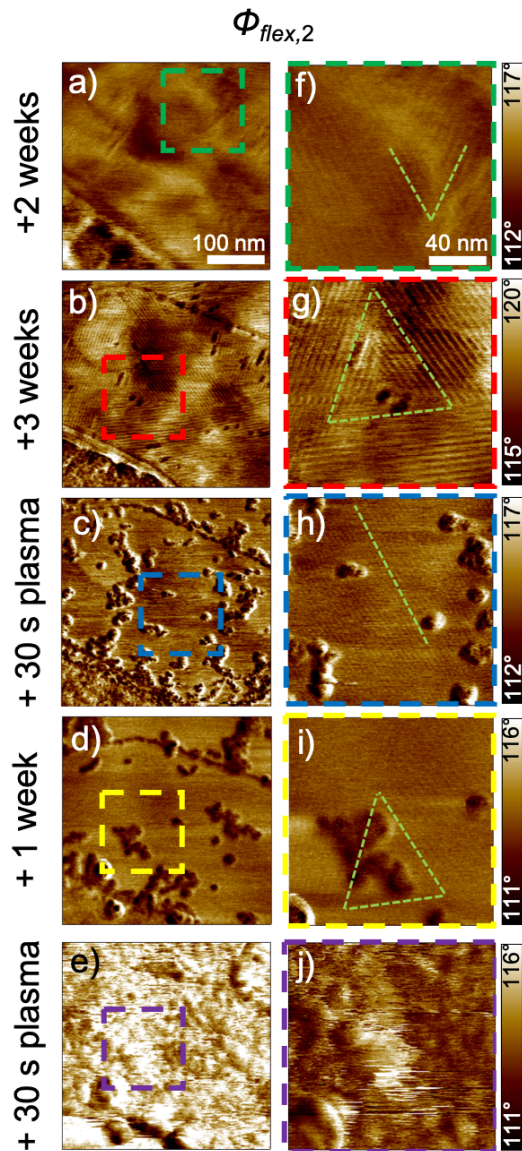


Figure 5-4: Stripe-like and island structure formation on a few-layer graphene-/graphite-flake analyzed using the second flexural phase images at two magnifications (a–e: $350 \times 350 \text{ nm}^2$ and f–j: $150 \times 150 \text{ nm}^2$). Analysis took place after different durations of storage and stepwise oxygen-plasma treatment measured by the AMFlex2-OLTor1-FMLat1 AFM mode. $A_0(\text{flex},2) = 675 \text{ nm}$, $A_{\text{flex},2} = 600 \text{ nm}$, and $A_{\text{lat},1} = 1.766 \text{ nm}$ (Reprinted from ref. [226], <https://doi.org/10.1002/admi.202300256>, © 2023.³⁰ Figure and caption were slightly adapted).

The stripe-like pattern formation shown in Figure 5-4 was analyzed using the second flexural phase images recorded with two different magnifications (Figure 5-4a–e: $350 \times 350 \text{ nm}^2$ and Figure 5-4f–j: $150 \times 150 \text{ nm}^2$) in the AMFlex2-OLTor1-FMLat1 AFM mode. Figure 5-4a and f

³⁰ This is an open access article under the terms of the Creative Commons Attribution License (<https://creativecommons.org/licenses/by/4.0/>), which permits use, distribution and reproduction in any medium, provided the original work is properly cited.

show that the stripe-like pattern of adsorbates is already visible after two weeks of storage, marked by the green dashed lines in Figure 5-4f, however, not that distinct. Almost the whole scan area of $350 \times 350 \text{ nm}^2$ was covered with adsorbates, forming a stripe-like pattern after another three weeks of sample storage (Figure 5-4b and g). The stripe-like pattern consists of domains with three different orientations that have a 60° -symmetry with respect to each other, as highlighted by the green dashed lines in Figure 5-4g. The 60° -symmetry of the stripe-like pattern domains originates from the 60° -rotational symmetry found in the hexagonal, honeycomb graphene structure [166]. The periodicity of the stripes is approximately 5 nm, which is in agreement with our recent work [225] and within the range of 4–6 nm mentioned by others [165, 166, 173, 175, 190, 195, 220-224]. Pálincás *et al.* [224] performed scanning tunneling microscopy (STM) measurements at a temperature of 9 K to clarify the origin of this stripe-like pattern. They showed that the pattern is formed by adsorption of linear alkanes with a length of 20–26 carbon atoms aligned along the zigzag direction of the graphene surface. According to Pálincás *et al.* [224], the periodicity of these stripes (5 nm) at room temperature is equal to the length of the linear alkanes. Consequently, the stripes reflect the orientation of the armchair direction of the graphene lattice. However, it was not possible in our AFM measurements to resolve the molecular structure of the stripe-like pattern at room temperature because the alkane molecules are present in the smectic phase.

After the first 30 s of oxygen-plasma treatment, the stripe-like pattern was still visible on the surface of the investigated flake (Figure 5-4c and h). In contrast to the acquired phase image taken prior to plasma treatment (Figure 5-4b and g), the stripe-like pattern was not distinct suggesting that a considerable portion of the adsorbates was removed from the surface of the flake. We conclude that linear alkanes exhibit a sufficiently high binding energy to the graphitic surfaces to at least partly withstand a plasma treatment of 30 s duration in the shielded configuration. To gain a better understanding of the occurrence of the stripe-like pattern before and after the first oxygen-plasma treatment, the corresponding topographic and lateral frequency-shift images were analyzed (Figure 7-30 of the Supplementary Information). The three stripe-like pattern domains with the aforementioned 60° -symmetry can be seen, as indicated by the green dashed lines in the topographic image in Figure 7-30a. In contrast, no stripe-like pattern is visible in the topography image (see Figure 7-30b) acquired after 30 s of oxygen-plasma treatment. Comparing the lateral frequency-shift images prior to and after plasma treatment (see Figure 7-30c and d), shows that the orientation of the stripe-like pattern changes upon plasma treatment within the same areas (colored polygons); however, some of the stripes remain in their original orientation. The reorientation of the stripe-like pattern was

most likely caused by a partial removal of the adsorbates from the graphitic surface due to the first 30 s of plasma treatment. Interestingly, in close proximity to the stripe-like pattern in Figure 5-4c and h, islands with a diameter between 50–100 nm can be observed after the first plasma treatment on the surface of the few-layer graphene-/graphite-flake. We assume that these islands formed by/during the 30 s of oxygen-plasma treatment, as already implied in Section 5.2.3. Zhou *et al.* [228] analyzed the contact angle of water on graphene prior to and after oxygen-plasma treatment. They observed that the oxygen-plasma treatment caused an increase in the hydrophilicity of graphene, and, therefore, a higher tendency for the graphene to adsorb water molecules on its surface. Hence, one potential explanation for the island formation is the adsorption of water molecules on the oxygen-plasma-treated graphene surface. Another possible explanation is that the islands were created by reactive oxygen from the plasma itself, reacting with the graphene surface to form sp^3 -type defects. Following the previous discussion on defect evolution upon oxygen-plasma treatment, based on Raman spectroscopy experiments (Section 5.2.1), sp^3 -type defect generation substantiates the interpretation of Zandiatashbar *et al.* and Lee *et al.* [109, 218]. Both groups concluded that prior to reaching a maximum in the intensity ratio between the D-peak and G-peak as a function of plasma-treatment time (transition between stage 1 and stage 2), sp^3 -type defects occurred predominantly for graphene samples.

Using scanning probe microscopy techniques, *i.e.*, AFM and STM, Paredes *et al.* [229, 230] investigated the initial stages of oxidation of graphitic surfaces caused by oxygen plasma. The authors observed small protrusions of 1–5 nm in size after a short plasma treatment of 4–6 s with the graphite surface directly facing the plasma source (exposed configuration). These protrusions were not visible in their recorded AFM topographic images, but they were in the lateral force images [231]. Therefore, the authors argued that the occurrence of the protrusions had an electronic origin. They interpreted these protrusions as vacancies formed by oxygen-plasma treatment. Paredes *et al.* [232] suggested that the friction contrast of the protrusions in lateral force images originated from the occurrence of symmetry-forbidden vibrational lattice modes arising from the symmetry breaking by the formed vacancies. They assigned the contrast visible in the STM images to an increased number of electrons near the Fermi level available for excitation in the vicinity of the vacancies of the graphene lattice. Li *et al.* [233] also observed these protrusions in their recorded STM images after ozone treatment of HOPG and developed a model to explain the occurrence of the protrusions. Based on the work by Paredes *et al.* [229] and Li *et al.* [233] we propose a model for oxygen-plasma induced water island formation, schematically shown in Figure 5-5.

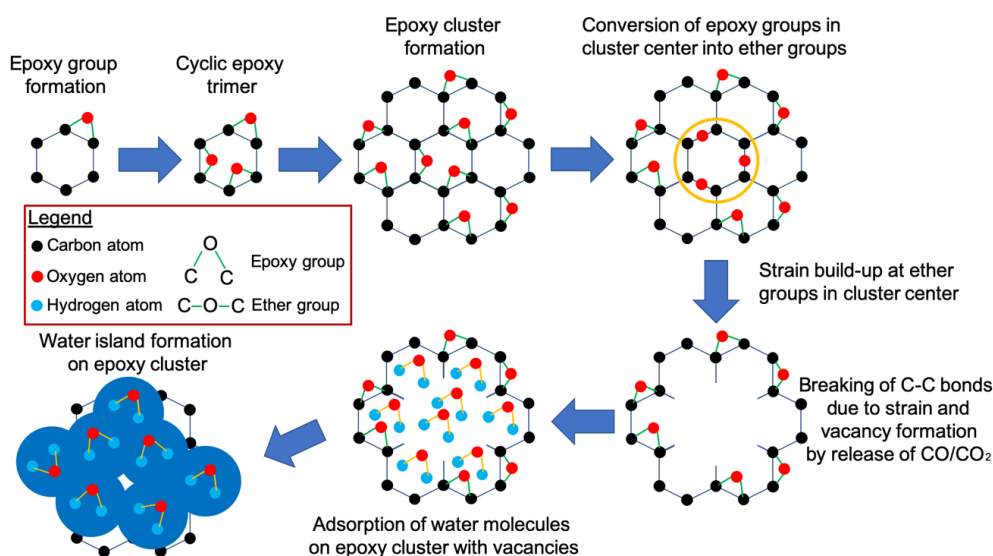


Figure 5-5: Scheme for oxygen-plasma induced water island formation on graphitic surfaces based on the theories of Paredes *et al.* [229] and Li *et al.* [233] (Reprinted from ref. [226], <https://doi.org/10.1002/admi.202300256>, © 2023.³¹ Figure and caption were slightly adapted).

Li *et al.* [233] proposed that oxygen from ozone becomes bound in form of epoxy groups at the bridging sites of the graphene lattice, since epoxy groups, compared with other oxygen functional groups (*e.g.*, carbonyl, ether) have a very low defect formation energy. Three oxygen atoms can adsorb at one carbon hexagon to form a cyclic epoxy trimer. The epoxy groups are mobile according to Paredes *et al.* [229] which means that the cyclic epoxy trimers migrate along the graphene lattice until they meet each other to form a network or cluster. Epoxy groups located in the center of these epoxy clusters change into ether groups, and strain occurs within the center of the cluster. Li *et al.* [233] suggested that the ether groups escape from the epoxy cluster due to strain build-up, resulting in the release of reaction products, such as CO and CO₂. Consequently, vacancies are formed in the center of the epoxy cluster. The epoxy groups together with the vacancies are hydrophilic. Hence, water molecules adsorb on these hydrophilic epoxy clusters and fill the vacancies to form water islands on them [234].

The white spots between the islands visible in the lateral frequency-shift image in Figure 7-30d are of a similar size (5–10 nm) when comparing with the size of the protrusions reported by Paredes *et al.* [229] and Li *et al.* [233]. Thus, we propose that the first plasma treatment step

³¹ This is an open access article under the terms of the Creative Commons Attribution License (<https://creativecommons.org/licenses/by/4.0/>), which permits use, distribution and reproduction in any medium, provided the original work is properly cited.

in a shielded configuration also creates epoxy clusters with vacancies in their center, and that islands represent water molecule agglomerations on epoxy clusters with vacancies.

Comparing Figure 5-4d and i with Figure 5-4c and h shows that the arrangement of the islands changes after one week of storage, possibly either due to diffusion of the islands or manipulation of their position while AFM imaging, as it was reported in our recent work [225]. However, the corresponding $8 \times 8 \mu\text{m}^2$ images in Figure 5-3d and k, in which a large-scale stripe-like arrangement of adsorbates (yellow dashed lines) can be seen, show that this effect is likely caused by a rearrangement of the epoxy clusters/vacancies and their associated water islands along the zigzag direction of the hexagonal lattice. We observed that the small-scale stripe-like pattern was still observable after one week's storage, as indicated by the green dashed lines in Figure 5-4i. After another plasma treatment step of 30 s, the stripe-like pattern was completely removed from the sample (Figure 5-4e and j). Surprisingly, the water islands were not completely removed, and the graphitic surfaces appeared perforated. Following the conclusions drawn in Section 5.2.3, we argue that after 1 min of plasma treatment, the sample was almost completely cleaned from adsorbates, except for some water islands remaining because of the induced epoxy/vacancy clusters. Here we emphasize that despite the fact that the sample was plasma-treated in the shielded configuration, a strongly defective graphene surface was evident after the second plasma-treatment step of 30 s. This must be kept in mind when considering oxygen-plasma treatment as a tool for cleaning graphitic surfaces from adsorbates.

5.3. Conclusion

We found that airborne adsorbates were present on both Si/SiO₂-substrate and few-layer graphene-/graphite-flakes. These adsorbates initially prevented the removal of graphene layers from the investigated flakes. Removal of graphene layers occurred after approximately 2.5 min of plasma treatment. A further plasma treatment of 16–21 s was required to remove individual layers of graphene (3.0–3.5 layers per minute). Using Raman spectroscopy, we showed that defects had been already introduced after ≈ 30 s of plasma treatment of the graphitic material. From other studies about oxygen-plasma treatment performed on monolayer graphene [108, 109, 218], however, we could not draw unambiguous conclusions on the predominant type of defect *via* analysis of the D/G- and D/D'-peak ratios. Hence, we proposed that this was because the peak ratios were not only influenced by the defectiveness of the sample, but also by the number of graphene layers. However, from an energetic perspective, the creation of sp³-type defects was more likely to occur for shorter plasma-treatment times, whereas the creation of

vacancy-type defects was more likely to occur for longer ones [218]. We verified this hypothesis by means of high-resolution multifrequency AFM analysis. Additionally, we focused on a controlled removal of adsorbates from a few-layer graphene-/graphite-sample to establish a method for cleaning graphitic surfaces. Specifically, we performed stepwise oxygen-plasma treatment of 30 s duration and subsequent storage for one week. Several types of adsorbates and defects were observed at different length scales and after different plasma-treatment and storage durations. At the microscale, different domains with sizes of about 1–2 μm in diameter originating from different species of adsorbed polycyclic aromatic hydrocarbons (PAHs) [225]. PAHs featured different contrasts in the lateral drive-amplitude images associated with differences in energy dissipation between the AFM tip and graphene surface under investigation. Interestingly, the formed domains were differently affected by plasma treatment, indicating that the interaction of the adsorbed PAHs with oxygen-plasma depended on the PAH type. At the nanoscale, islands of approximately 50–100 nm in diameter were observed after the first oxygen-plasma-treatment step. These islands represented agglomerated water molecules because oxygen-plasma treatment induced the formation of oxygen functional groups, such as epoxy, carbonyl, and ether groups; these groups increased the hydrophilicity of the graphene surface. This reflected the evolution of sp^3 -type defects after short-period oxygen-plasma treatment. Additionally, stripe-like patterns, with a periodicity of approximately 5 nm, were observed in three different orientations with 60° symmetry. These patterns were formed by the adsorption of linear alkanes, consisting of 20–26 carbon atoms [224]. Interestingly, the orientation of some of these stripes changed by 60° upon plasma treatment, indicating the presence of different layers of stripe-like adsorbates stacked on each other.

5.4. Experimental Section

Few-layer graphene-/graphite-sample preparation. The few-layer graphene-/graphite-samples were prepared *via* micromechanical exfoliation, following the protocol of Huang *et al.* [33]. The peculiarity of the approach lies in the supplemental heating step when the graphite-flake-decorated tape is in contact with the Si/SiO₂-substrate. Consequently, gases present between the graphite flakes and the substrate evaporate easier than they would without heating; and the probability of synthesizing laterally larger and vertically thinner flakes is increased.

Oxygen-plasma treatment. We used a FEMTO plasma device (Diener electronic GmbH + Co. KG, Ebhausen, Germany) which was evacuated to a pressure of 4 mbar. The chamber was then

flushed with oxygen gas for 1 min before gas discharge was initiated at a power of 55 W. The various steps of sample treatment and the cumulative plasma-treatment times for the samples are summarized in Table 5-1.

Table 5-1: Oxygen-plasma times for treatment of the few-layer graphene-/graphite-flake as analyzed in Figure 5-1 and Figure 5-2 (Reprinted from ref. [226], <https://doi.org/10.1002/admi.202300256>, © 2023.³²).

| | Step 1 | Step 2 | Step 3-6 | Step 7-25 |
|---------------------------|--------|--------|--------------------------------|---|
| Treatment time | 10 s | 20 s | 30 s | 2 min |
| Cumulative treatment time | 10 s | 30 s | 1 min, 1.5 min, 2 min, 2.5 min | 4.5 min, 6.5 min, 8.5 min, 10.5 min, 12.5 min, 14.5 min, 16.5 min, 18.5 min, 20.5 min, 22.5 min, 24.5 min, 26.5 min, 28.5 min, 30.5 min, 32.5 min, 34.5 min, 36.5 min, 38.5 min, 40.5 min |

Raman spectroscopy. A sample was analyzed with a WiTec Raman microscope (Oxford Instruments, Ulm, Germany), equipped with a 532 nm laser at a laser power of 1 mW. Image-scans of the few-layer graphene-/graphite-flake were performed with a pixel size of approximately $250 \times 250 \text{ nm}^2$ and an integration time of 0.8 s. The peak intensity ratios were determined by averaging the extracted spectra that can be attributed to one of the areas marked with A, B, C, and D in Figure 5-1a. Owing to the differences in size of the examined areas, the averaged Raman spectra were determined using 36 spectra for A, 16 spectra for B, nine spectra for C, and two spectra for D. The peak intensities were determined by Lorentz fitting of the averaged spectra using Igor Pro v6.36 software (WaveMetrics Inc., Lake Oswego, OR, USA).

Atomic force microscopy. Two different atomic force microscopes were used for the experiments presented in this work. The topography measurements shown in Figure 5-1a were performed using a Dimension Icon (Bruker AXS, Santa Barbara, CA) in standard amplitude modulation mode ($A_{flex,1}/A_0 \approx 50\text{-}75\%$) using cantilevers of the type HQ:NSC18/Cr-Au ($k_{flex,1} \approx 2.8 \text{ N/m}$, $f_{flex,1} \approx 76 \text{ Hz}$). Multifrequency AFM measurements were performed using a Cypher S atomic force microscope (Asylum Research, Oxford Instruments, Santa Barbara, CA). The instrument was equipped with a blueDrive photothermal excitation setup, allowing for simultaneous in-plane and out-of-plane excitation of the cantilever if the power-modulated laser is focused at the fixed end of the cantilever, however, some micrometers off the length

³² This is an open access article under the terms of the Creative Commons Attribution License (<https://creativecommons.org/licenses/by/4.0/>), which permits use, distribution and reproduction in any medium, provided the original work is properly cited.

symmetry axis. Details of the setup for performing the AMFlex2-OLTor1-FMLat1-FMFlex3 AFM method can be found in our recent publications [8, 182, 225]. Here we used cantilevers of the type HiRes-C15/Cr-Au purchased from Mikromasch (Innovative Solutions Bulgaria Ltd., Sofia, Bulgaria).

5.5. Acknowledgements

The authors thank Alena Bell for supporting us with analysis of the Raman measurements and the Deutsche Forschungsgemeinschaft (Project number 407750697) for financial support.

6. Summary and outlook

The key element for all the content presented within this thesis was the development of a multifrequency atomic force microscopy method for simultaneous in-plane and out-of-plane analysis of graphitic surfaces in air under ambient conditions. In Section 2, it was shown that the method facilitates atomic resolution imaging of HOPG in air under ambient conditions, when the second flexural eigenmode was used for the topographic feedback. In addition, the method also allows for a quantitative analysis of tip-sample forces being capable to discriminate between atomic and hollow sides of the hexagonal crystal lattice of graphitic surfaces.

With respect to the determination of local elastic properties Section 3 focuses on the accessibility of different in-plane and out-of-plane elastic constants such as in-plane and out-of-plane Young's and shear modulus. It was proposed that different in-plane oscillation modes of the cantilever, *i.e.* torsional and lateral eigenmodes, facilitate the discrimination of frictional or shear interactions between tip and sample. The existence of both processes complicates the determination of in-plane elastic components. However, a discrimination was possible if ultrasmall in-plane oscillation amplitudes (< 1 nm) were used. The experiments presented in Sections 2 and 3 were performed on HOPG instead of graphene. This was done for two reasons; (i) preventing the tip from becoming blunt while searching for the perfect spot on a graphene flake and (ii) providing a clean surface by cleaving the sample with tape directly before imaging.

During the performance of the experiments shown in Section 4 it turned out that the few-layer graphene-/graphite-flakes under investigation were strongly covered by different types of adsorbates. Consequently, it was not possible to achieve atomic resolution on the samples prepared *via* micromechanical exfoliation on Si/SiO₂-substrates. However, the developed multifrequency AFM method proved to be advantageous for the discrimination of different types of adsorbates (water, three different PAHs and hydrocarbons) covering the surface. The discrimination could be achieved based on a comparison between the recorded observables (in-plane *vs.* out-of-plane and conservative *vs.* dissipative). Additionally, it was shown that the adsorbates could be removed by oxygen-plasma treatment. However, the plasma treatment not only caused a removal of adsorbates but also introduced some defects into the material as confirmed by Raman spectroscopy.

To return to the original idea of analyzing graphene surfaces with atomic resolution, we performed oxygen-plasma treatment experiments on few-layer graphene-/graphite-flakes, intending to achieve two goals: (i) to prepare graphene with defined numbers of layers and (ii) to clean the flakes in a controlled manner. The results are presented in Section 5. Although, the

samples were treated for initially small time-periods (10 s) and in a shielded configuration, defects were introduced into the few-layer graphene-/graphite-flakes as analyzed by Raman spectroscopy. This was surprising because it was shown by AFM experiments that the samples were still strongly covered by adsorbates. Using the developed multifrequency AFM method it was possible to show different stages of sample coverage with adsorbates after alternating storage and 30 s of oxygen-plasma treatment. However, once the adsorbate material was completely removed, the sample appeared perforated although a mild oxygen-plasma treatment was chosen. Further plasma treatment additionally allowed for the removal of entire graphene layers. Due to the comparably large roughness of the few-layer graphene-/graphite-flakes after oxygen-plasma treatment, atomic resolution imaging was unfortunately not possible until now. Nevertheless, understanding the significant occurrence of adsorbate coverage on graphene was an essential step not only towards the investigation of the local elastic properties but also for the interpretation of friction and shear properties of graphene which are strongly influenced by adsorbates. Additionally, the developed multifrequency AFM method including both, in-plane and out-of-plane cantilever oscillations facilitates to analyze whether the sample is covered by adsorbates or not, which is challenging to achieve by standard AFM methods.

To sum up, within the frame of this thesis, several important steps towards the analysis of the effect of individual defects of graphene on the local elastic properties were achieved. However, the issue of strong adsorbate coverage of graphene surfaces under laboratory air conditions needs to be overcome. One possible option could be the optimization of the plasma-treatment process, *e.g.* by using different gases or by further adjusting parameters such as the power for initiating the gas discharge. Another approach could be the performance of the sample preparation as well as all the experiments under clean room conditions. Additionally, different graphene preparation methods could be tested. However, based on the results shown in Sections 4 and 5, it is not likely to assume that adsorbate coverage upon storage can be prevented by choosing a different graphene preparation method.

Besides the analysis of defects, the developed multifrequency AFM method is proposed to serve as a versatile tool for the in-plane and out-of-plane analysis of various materials. Depending on the type of cantilever used, further eigenmodes could become usable, allowing for a true three-dimensional quantitative nanomechanical analysis of different materials, ranging from soft to stiff.

7. Supplementary Information

7.1. Supplementary Information to Section 2

7.1.1. Inverted AFM images of HOPG taken in AMFlex2-FMTor1-FMFlex3 mode

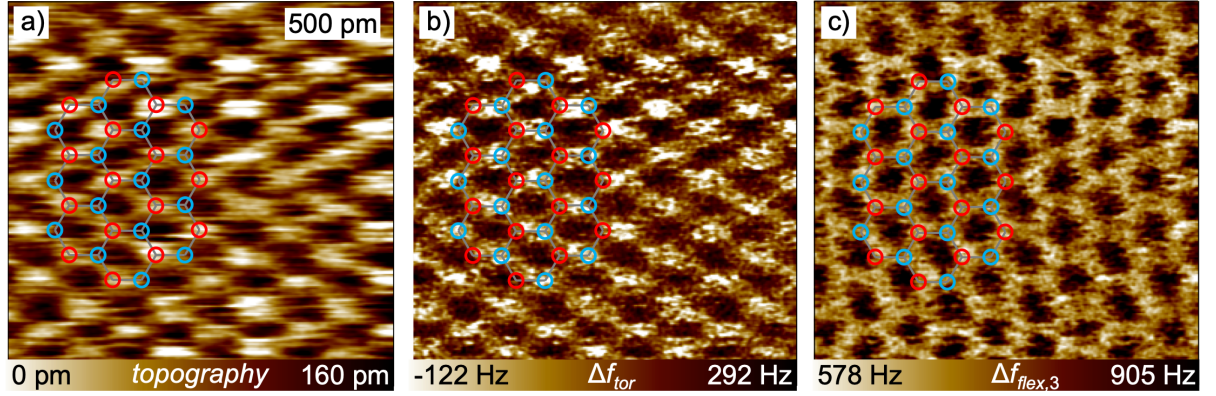


Figure 7-1: Inverted AFM images of HOPG taken in AMFlex2-FMTor1-FMFlex3 mode: a) topography image, and b) torsional and c) flexural frequency-shift images. Imaging parameters: $A_{0(flex,2)} = 770$ pm, $A_{flex,2} = 100$ pm, $A_{tor} = 80$ pm, $A_{flex,3} = 220$ pm.

7.1.2. Calibration of inverse optical lever sensitivities and oscillation amplitudes

The inverse optical lever sensitivity (invOLS) was calibrated from the gradient of a curve of static deflection versus z -sensor position with a comparably low voltage setpoint to trigger, to protect the tip from wearing off. The calibration of the deflection has a major impact on the interpretation of the spectroscopy data because it is required for determining the actual tip-sample distance d . Consequently, calibrating the dynamic sensitivity from curves of amplitude versus tip-sample distance also depends on the accuracy of the static-deflection calibration. That is why we determined the amplitude sensitivities from thermal-tune data based on the equipartition theorem [235-237]. Therefore, the flexural and lateral thermal noise spectra were collected and the observed power spectral densities (PSDs) were fitted by [145, 146]

$$\gamma_{flex} = \sqrt{\frac{2k_B T}{\pi k_{flex} f_{0,flex} P_{DC} Q_{flex}}}, \quad (7-1)$$

$$\gamma_{tor} = \sqrt{\frac{2k_B T}{\pi k_{tor} f_{0,tor} P_{DC} Q_{tor}}}, \quad (7-2)$$

where γ is the InvOLS, k_B is the Boltzmann constant, T is the absolute temperature, f_0 is the resonance frequency, P_{DC} is the PSD of the oscillator at DC, and Q is the quality factor. The

flexural-force constants k_{flex} of the first two bending eigenmodes and the torsional torque constant k_{ϕ} were determined by using the Sader method [143, 238]:

$$k_{flex} = 0.1906\rho b^2 L Q_{flex} f_{0,flex}^2 \Gamma_i^{flex}(f_{flex}), \quad (7-3)$$

$$k_{\phi} = 0.1592\rho b^4 L Q_{tor} f_{0,tor}^2 \Gamma_i^{tor}(f_{tor}), \quad (7-4)$$

where ρ is the density of air, b is the width and L is the length of the cantilever, and Γ_i is the imaginary part of the hydrodynamic function. In the limit of small torsion angle, the torsional force constant can be calculated from the torsional torque constant by [144]

$$k_{tor} = \frac{k_{\phi} L}{(L - \Delta L) h^2}, \quad (7-5)$$

where $L/(L - \Delta L)$ accounts for the influence of the tip set-back ΔL , and h is the tip height.

Note that γ_{tor} as determined from Equation (7-2) was around twice that estimated from imaging. It is well known that it is not straightforward to determine the torsional sensitivity, which is why we used the results of atomically resolved imaging for the calibration in the end. We observed that the torsional frequency shift at maximum counts of the image histograms decreased asymptotically with increasing torsional amplitude, and we assigned the beginning of the asymptotic value to amplitude values that were larger than half of the interatomic spacings. Consequently, the torsional sensitivity was estimated as being 11 nm/V. Currently to the best of our knowledge there is no method available that provides a higher accuracy for the calibration of the dynamic torsional invOLS. The improvement of the calibration methods for the dynamic torsional invOLS is of high importance for further research in this field.

Unfortunately, it was not possible to determine the third-flexural-eigenmode sensitivity and force constant from Equations (7-1) and (7-3) because of the small response of the resonance peak in the thermal spectrum. That is why we derived the values from the first- and second-eigenmode values. The force constant was calculated using the equation introduced by Labuda *et al.* [237] for flexural eigenmodes:

$$k_n = k_1 \left(\frac{f_n}{f_1} \right)^{\xi}, \quad (7-6)$$

where the power-law exponent ξ can be determined from the known values for the second eigenmode as 1.76. The third-eigenmode sensitivity was estimated as being $\gamma_{flex,3} = 10$ nm/V from the second-eigenmode sensitivity using the relations introduced by Garcia *et al.* [68] for rectangular cantilevers.

7.1.3. Influence of cantilever mean deflection in AM-AFM using higher eigenmodes on atomic-scale imaging of HOPG

In general, it is not straightforward to assign the atomic positions from AFM images taken on HOPG. Several groups have shown that the appearance of the topographical contrast depends on whether imaging is accomplished in the attractive or repulsive regime, and the shown height image resembles a checkerboard pattern, which was also predicted and observed by other groups working in the field of AFM or scanning tunneling microscopy (STM) [239-241]. In a theoretical study, Sasaki *et al.* showed that the contrast that can be observed on HOPG in the repulsive regime depends strongly on the configuration of the tip [239]. Besides the number and type of tip atoms involved in the imaging process, the tilt angle of the tip and the bond length and tip orientation relative to the surface were also predicted to influence the contrast of the height images. Another explanation for the appearance of the twofold symmetry was introduced by Wong *et al.* and Xu *et al.* [240-242] for STM images. They showed that the offset of the topmost carbon layer relative to the second one as well as the increased coupling between these layers can also result in a checkerboard pattern. Because of the observation that the topography images of HOPG showed a certain offset between trace and retrace, which depends on the scan velocity as well as the scan angle, in our setup we assume that the checkerboard pattern might originate from a tip-induced shift of the topmost carbon layer relative to the one beneath. Based on this assumption, it must be clarified how the first layer of carbon atoms can be lifted despite the fact that we observe exclusively repulsive phase and frequency-shift values in the second and third eigenmode channel, respectively. The solution to this puzzle was found by observing the mean deflection of the cantilever. In general, the cantilever deflection is assumed to play a minor role in dynamic spectroscopy, which is especially the case for large amplitudes and stiff cantilevers. However, as shown by Kawai and coworkers [132] and recently in work by Yalcin *et al.* [133], in particular at close tip-sample distances, the mean deflection of the cantilever cannot be neglected in dynamic spectroscopy. To understand better how the cantilever deflection influences the oscillation behavior, we obtained curves of mean deflection versus tip-sample distance including first-, second-, and third-eigenmode excitation, and simultaneously we recorded the deflection values while triggering at an amplitude value that was $\sim 10\%$ of the free second flexural amplitude. Additionally, we measured static deflection versus tip-sample distance (no dynamic drive) with the same cantilever. As shown in Figure 7-2a, the tip-sample distance d was calculated from the z -sensor position minus the tip height h plus the mean deflection as known from static spectroscopy, where the deflection is defined as negative for attractive and positive for repulsive long-range tip-sample interaction. The results of the curves of (mean) deflection versus tip-sample distance are shown in Figure 7-2b.

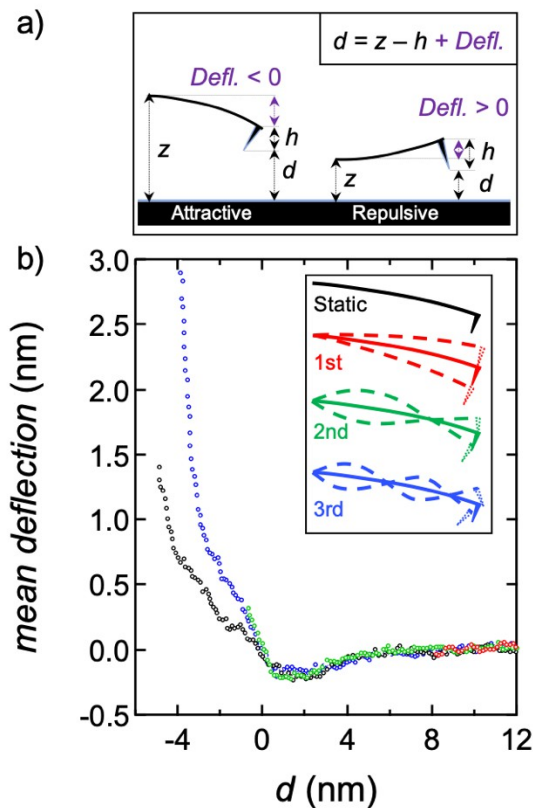


Figure 7-2: Comparison of mean deflection for different eigenmode oscillations as well as the static case on HOPG upon approach. a) Scheme for determining tip-sample distance from z -sensor position, tip height, and mean deflection (purple). b) Plot of mean deflection vs. tip-sample distance for static case (black), first flexural eigenmode (red), second flexural eigenmode (green), and third flexural eigenmode (blue).

Interestingly, the curves of mean deflection versus tip-sample distance show the same overall trend for all three dynamic modes and strongly resemble the trend of the curve of static deflection versus distance (up to $d = -1$ nm). Furthermore, it becomes evident that with higher eigenmodes, significantly higher mean deflections can be reached at similar amplitude setpoint ratios, which is a consequence of the enhanced dynamic stiffness. The curve of mean deflection versus tip-sample distance for the first-eigenmode oscillation additionally explains why we could not show atomic resolution: the smallest tip-sample distance achievable was still ~ 8 nm. Consequently, this observation corroborates the general assumption that the mean cantilever deflection can be neglected for the standard tapping mode with the first-eigenmode oscillation. However, we strongly recommend analyzing the mean-deflection behavior when using higher-eigenmode oscillations for feedback operation for a reliable interpretation of the obtained images.

7.1.4. Hysteretic behavior in spectroscopic experiments

Because we noticed an unexpectedly high hysteresis between the approach and retract curves of the (mean) deflection versus tip–sample distance, to clarify the origin of the hysteresis we made additional static-deflection measurements with the same tip on freshly cleaved HOPG and silicon stored under ambient conditions. The resulting plots as well as a schematic of the possible scenarios on the two different materials close to the surface are shown in Figure 7-3.

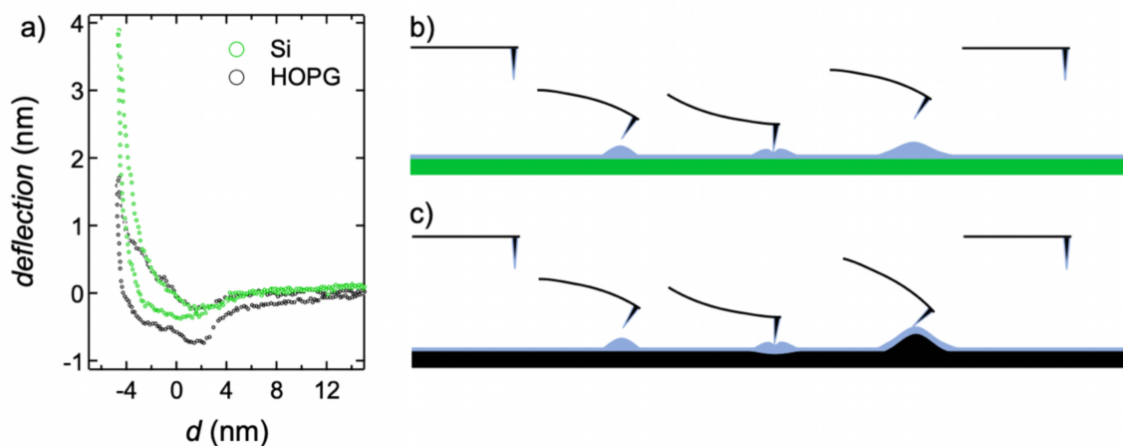


Figure 7-3: Comparison of hysteretic behavior upon approach and retract for silicon and HOPG with a DLC AFM tip. a) Deflection vs. tip–sample distance on silicon (green) and HOPG (black). b) and c) Scheme of tip–sample interactions on silicon and HOPG, respectively.

Usually, hysteretic behavior is observed for viscous materials such as polymers and biological cells because of the indentation of the stiff cantilever into the softer material, which causes plastic deformation, dissipation within the material, and strong attractive forces between tip and sample. On stiff and hydrophobic substrates such as HOPG and silicon, we expect neither a strong indentation nor a strong attractive tip–sample interaction or dissipation in general. However, the very close proximity of the tip to the sample means that Van-der-Waals attraction and capillary interaction of water layers, which are present at both tip and sample under ambient conditions, cannot be neglected and are most likely responsible for the hysteresis. However, the question arises as to where the difference between the retract curves taken on silicon and on HOPG comes from. Figure 7-3a shows that the approach behavior of the DLC-coated tip to the silicon and the HOPG surface is very similar, and this behavior can be explained by the similar water wettability of the substrates. Both freshly cleaved HOPG and silicon stored under ambient conditions were shown to have a water contact angle of $\sim 60^\circ$ [243, 244]. However, the Hamaker constant between silicon and carbon is approximately half of that for HOPG [139]. This information matches the observation of stronger hysteresis on HOPG. Figure

7-3b and c show schematically the different interaction scenarios on silicon and HOPG. During approach, we assume that capillary interaction forces dominate the deflection of the cantilever on both substrates, whereas we assume an additional effect of a strong Van-der-Waals adhesion on HOPG. This can lead to a local lift of the topmost carbon layer during retraction of the cantilever [134]. Consequently, this effect is also very likely to occur during imaging, which might have caused the contrast inversion of the images shown in the main text.

7.1.5. Comparison of topography, mean-deflection, and third-eigenmode frequency-shift images and cross sections for different third-flexural-eigenmode amplitudes

Figure 7-4 shows the topography (left) and third-eigenmode frequency-shift images (right) taken with three different values of $A_{flex,3}$. Additionally, the cross sections along the pink line marked in all the images can be seen in the center, while also plotted are the cross sections through the mean-deflection images (not shown). By comparing the results, it becomes apparent that the mean deflection compensates for a large amount of the height signal, as mentioned in the main text. This explains why we see such a high corrugation amplitude in the topography images. Second, we see from Figure 7-4b, e, and h that the minimum in the frequency shift always appears at the bond and the maximum at the hollow side. This is also the case for the height signal in Figure 7-4h where $A_{flex,3} = 509$ pm. In contrast, for $A_{flex,3} = 364$ pm, the minimum in height appears at the hollow side and the maximum at the bonds, which means that the contrast is inverted. For $A_{flex,3} = 436$ pm, the height signal has its inflection points at the positions of the carbon bonds and the hollow sides, resulting in a shifted appearance of both images. We assume that the different contrast relations originate from the different distances relative to the surface while imaging, which result from the variation of the third-eigenmode amplitude.

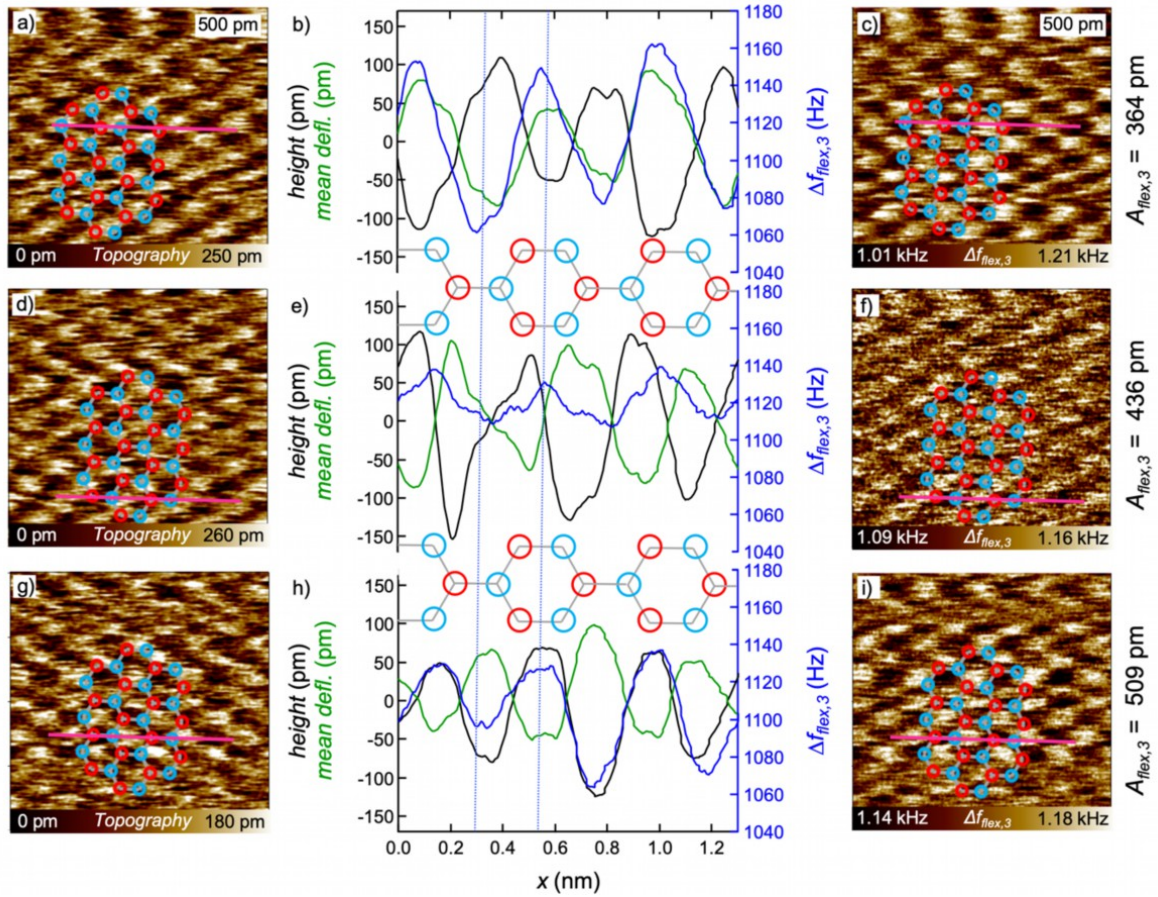


Figure 7-4: Comparison of topography, mean-deflection, and third-eigenmode frequency-shift images and cross sections for three different third-flexural-eigenmode amplitude setpoints. a), d), g) Topography images, b), e), h) cross sections drawn along the pink lines, and c), f), i) third-eigenmode frequency-shift images at $A_{flex,3} = 364$ pm (a–c), $A_{flex,3} = 436$ pm (d–f), and $A_{flex,3} = 509$ pm (g–h). Further imaging parameters: $A_{flex,2} = 68$ pm, $A_{tor} = 0$ pm.

7.1.6. Calculation of forces from spectroscopic data

The out-of-plane ($F_{flex,3}$) and in-plane (F_{tor}) forces were calculated from the frequency-shift data based on the approach of Sader and Jarvis [59]. The modified formulas for the multimodal approach used in this study, which can be implemented in a MATLAB code, are

$$F_{flex,3}(d) = \frac{2k_{flex,3}}{f_0(flex,3)} \int_d^\infty \left(1 + \frac{\sqrt{A_{flex,2} + A_0(flex,3)}}{8\sqrt{\pi(x-d)}} \right) \Delta f_{flex,3}(x) - \frac{\sqrt{(A_{flex,2} + A_0(flex,3))^3}}{\sqrt{2(x-d)}} \frac{d\Delta f_{flex,3}(x)}{dx} dx, \quad (7-7)$$

$$F_{tor}(d) = -\frac{2k_{tor}}{f_0(tor)} \int_d^\infty \left(1 - \sqrt{2(A_{flex,2} + A_0(flex,3))} \right) \frac{\Delta f_{flex,3}(x)}{\sqrt{(x-d)}} dx, \quad (7-8)$$

where $k_{flex,3}$ (resp. k_{tor}) is the third flexural (first torsional) eigenmode stiffness, $A_{flex,2}$ is the tip-sample-distance-dependent amplitude of the second flexural eigenmode, $A_0(flex,3)$ is the amplitude setpoint of the third flexural eigenmode, and $\Delta f_{flex,3}$ (resp. Δf_{tor}) and $f_0(flex,3)$ (resp. $f_0(tor)$) are the frequency shift and resonance frequency, respectively, of the third flexural (first torsional) eigenmode.

7.1.7. Influence of second-flexural-eigenmode amplitude-setpoint on torsional and third-flexural frequency shifts

Figure 7-5 shows the histograms resulting from atomically resolved (a) third-eigenmode and (b) torsional frequency-shift images of HOPG for varying second-eigenmode amplitude setpoints. In Figure 7-5c, the frequency shifts at maximum counts are plotted as a function of the second-flexural-eigenmode amplitude setpoint. Additionally, the frequency shifts at FWHM of the histograms in Figure 7-5a and b are shown with dotted lines. From Figure 7-5c, it becomes evident that the third-eigenmode frequency-shift images are much more influenced by the second-flexural-eigenmode amplitude setpoint compared to the torsional frequency-shift images.

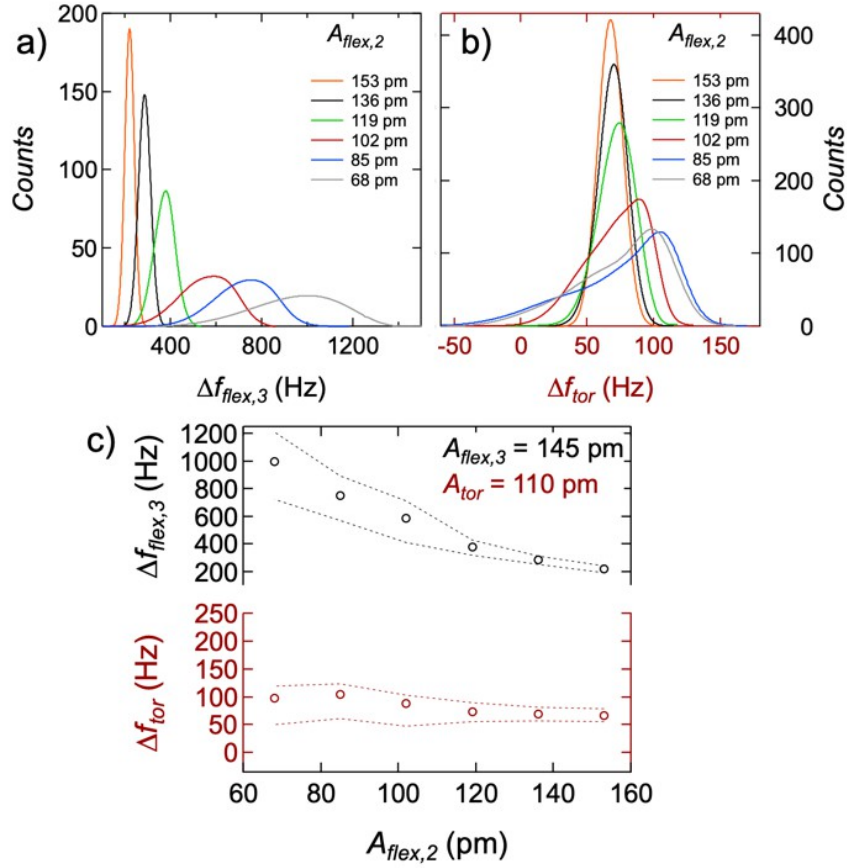


Figure 7-5: Influence of second-eigenmode flexural-oscillation amplitude setpoint on the observed frequency shifts. Histograms of a) third-eigenmode flexural and b) torsional frequency-shift images for different second-eigenmode flexural-amplitude setpoints. Third-eigenmode flexural and torsional frequency shifts at maximum counts (open circles) and at FWHM (dotted lines) as a function of the second-flexural-eigenmode amplitude setpoint at a constant torsional-eigenmode amplitude of 110 pm and a constant flexural-eigenmode amplitude of 145 pm.

7.1.8. Calculation of forces from frequency-shift images using Fourier method for higher eigenmodes

We modified the Fourier method to reconstruct the forces in z -direction from the flexural frequency shift of the higher eigenmodes. The formula for the frequency shift as a function of the force for the second eigenmode was introduced by Herruzo *et al.* [7] based on the work of Giessibl *et al.* [57]. Kawai and coworkers showed that the relation between frequency shift and forces is also valid for higher flexural as well as for torsional eigenmodes [6]:

$$\Delta f_i(x) = -\frac{f_i}{2\pi k_i} \int_{-A_{sp}}^{A_{sp}} F'_{ts}(x+q) \frac{1}{\sqrt{A_{sp}^2 - q^2}} dq, \quad (7-9)$$

where Δf_i is the frequency shift, f_i is the resonance frequency, and k_i is the force constant of the i^{th} eigenmode. A_{sp} is the setpoint amplitude of the oscillation used for the topographical feedback, and F'_{ts} is the first derivative of the force.

Introducing the variable $q = A_{sp} \cos\left(\omega t - \frac{\pi}{2}\right)$ allows the convolution of the force gradient with the semicircle $\frac{2A_{sp}^2}{\pi} \sqrt{A_{sp}^2 - q^2}$ [7, 57]. Equivalently to Seeholzer et al. we used the exact formula for Δf_i [4, 57, 58]:

$$\Delta f_i(x) = \frac{f_i}{2k_i} \langle k_{ts} \rangle(x), \quad (7-10)$$

where $\langle k_{ts} \rangle$ is the weight force gradient. The first derivative of the tip-sample force, F'_{ts} , can be expressed as

$$F'_{ts}(x + q) = -k_{ts}(x + q). \quad (7-11)$$

From Equations (7-9–7-11), it follows that

$$\langle k_{ts} \rangle(x) = \frac{1}{\pi} \int_{-A_{sp}}^{A_{sp}} k_{ts}(x + q) \frac{1}{\sqrt{A_{sp}^2 - q^2}} dq. \quad (2-22)$$

The tip-sample stiffness k_{ts} can be determined from the second derivative of the tip-sample energy E_{ts} expressed by a Fourier series with the components a_n and b_n :

$$k_{ts}(x) = \sum_{n=1}^N -a_n \left(\frac{2\pi n}{L}\right)^2 \sin\left(\frac{2\pi n}{L}x\right) - b_n \left(\frac{2\pi n}{L}\right)^2 \cos\left(\frac{2\pi n}{L}x\right) = \frac{d^2 E_{ts}(x)}{dx^2}, \quad (2-23)$$

where L is the line length and N is the Nyquist frequency, which is half of the sampling rate s :

$$N = \frac{s}{2L}. \quad (2-24)$$

By substituting the formula for k_{ts} into that for $\langle k_{ts} \rangle$, we obtain

$$\begin{aligned} \langle k_{ts} \rangle(x) = & \sum_{n=1}^N -a_n \left(\frac{2\pi n}{L}\right)^2 \sin\left(\frac{2\pi n}{L}x\right) J_0\left(\frac{2\pi n A_1}{L}\right) \\ & - b_n \left(\frac{2\pi n}{L}\right)^2 \cos\left(\frac{2\pi n}{L}x\right) J_0\left(\frac{2\pi n A_1}{L}\right), \end{aligned} \quad (2-25)$$

where J_0 is the Bessel function of the first kind and zero order. Assuming that the frequency-shift data of the line can be expressed as a Fourier series with the components a_n and β_n , i.e.,

$$\Delta f_i(x) = \sum_{n=1}^N \alpha_n \sin\left(\frac{2\pi n}{L}x\right) + \beta_n \cos\left(\frac{2\pi n}{L}x\right), \quad (2-26)$$

we can determine the expressions for a_n and b_n via direct comparison of the formulas. As in the work of Seeholzer *et al.*, the factors a_n and β_n were determined from the scalar projection of the data on the relevant sine or cosine function divided by a normalization factor [4]:

$$\alpha_n = \int \frac{2\Delta f_i(x)}{L} \sin\left(\frac{2\pi n}{L}x\right) dx, \quad (2-27)$$

$$\beta_n = \int \frac{2\Delta f_i(x)}{L} \cos\left(\frac{2\pi n}{L}x\right) dx. \quad (2-28)$$

This allows the determination of forces from frequency-shift data of higher eigenmodes, such as shown in the main text.

7.1.9. Comparison of original frequency-shift data with frequency-shift validation data along distinct cross sections

Figure 7-6 shows that the frequency-shift validation images determined with the Fourier method match the contrast of the original images. The main difference between the original and validation images is the frequency-shift offset, which results from the assumptions behind the Fourier method, as discussed in the main text. Additionally, the validation images appear much smoother than the original images, which is a consequence of the Fourier algorithm. To directly compare some distinct lines, we show the cross sections marked in the original and validation images in Figure 7-7. The positions of the cross sections are the same as those in the main text.

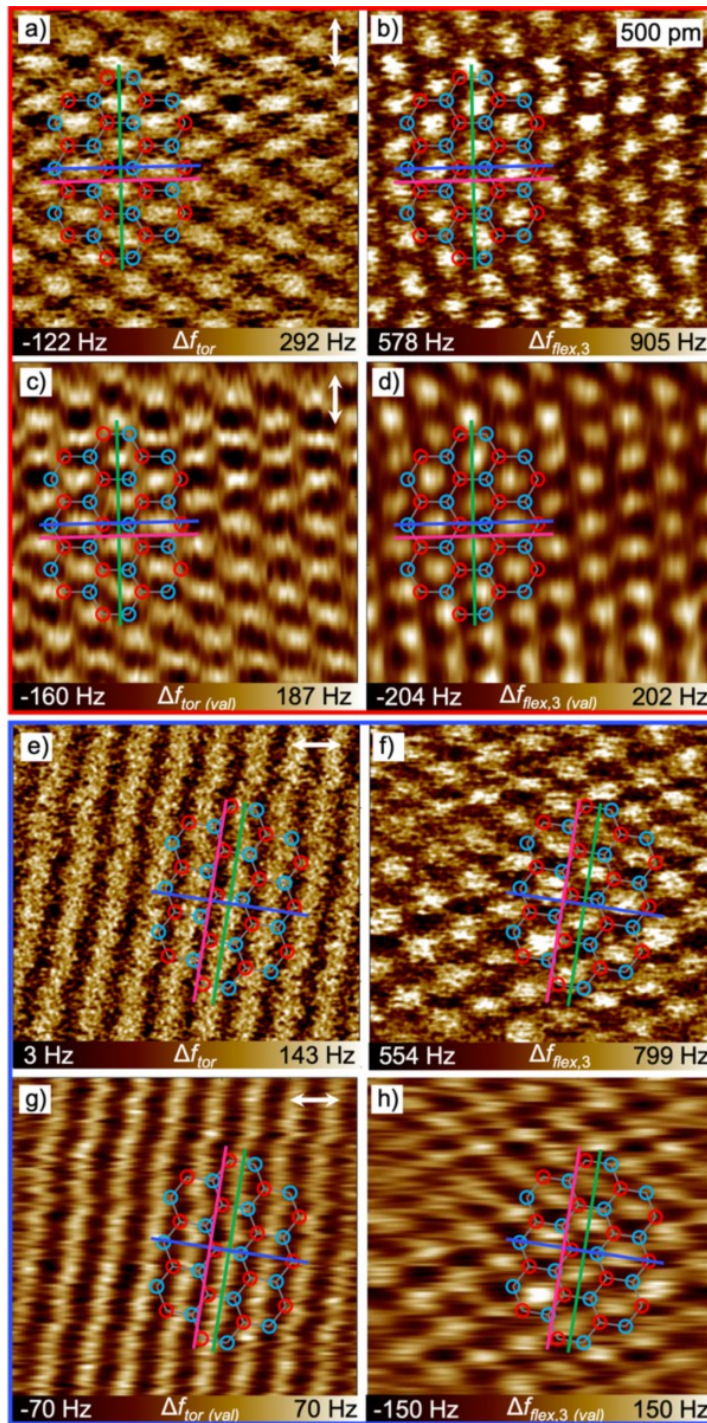


Figure 7-6: Original frequency-shift images (a, b, e, f) and frequency-shift validation images (c, d, g, h) determined by using the Fourier method. The torsional validation data (a, c, e, g) were calculated using the monomodal Fourier method, and the flexural validation data (b, d, f, h) were calculated using the bimodal Fourier method. Red: scan angle = 0° , $A_{tor} = 80$ pm, $A_{flex,2} = 100$ pm, $A_{0(flex,2)} = 770$ pm, $A_{flex,3} = 220$ pm. Blue: scan angle = 90° , $A_{tor} = 110$ pm, $A_{flex,2} = 90$ pm, $A_{0(flex,2)} = 770$ pm, $A_{flex,3} = 150$ pm.

Figure 7-7 shows that the frequency-shift validation images reproduce the original frequency-shift data nicely at the positions of the hollow sides and the carbon bonds, as seen in a, c, d,

and f. Nevertheless, in Figure 7-7c the flexural frequency shift is not reproduced perfectly at the distinguishable atomic sides. For the pink cross sections in Figure 7-7b and e, the discrepancies between the validation and original frequency-shift data are slightly larger. This must be considered when interpreting the force images, but the overall reproduction of the frequency-shift images is satisfying.

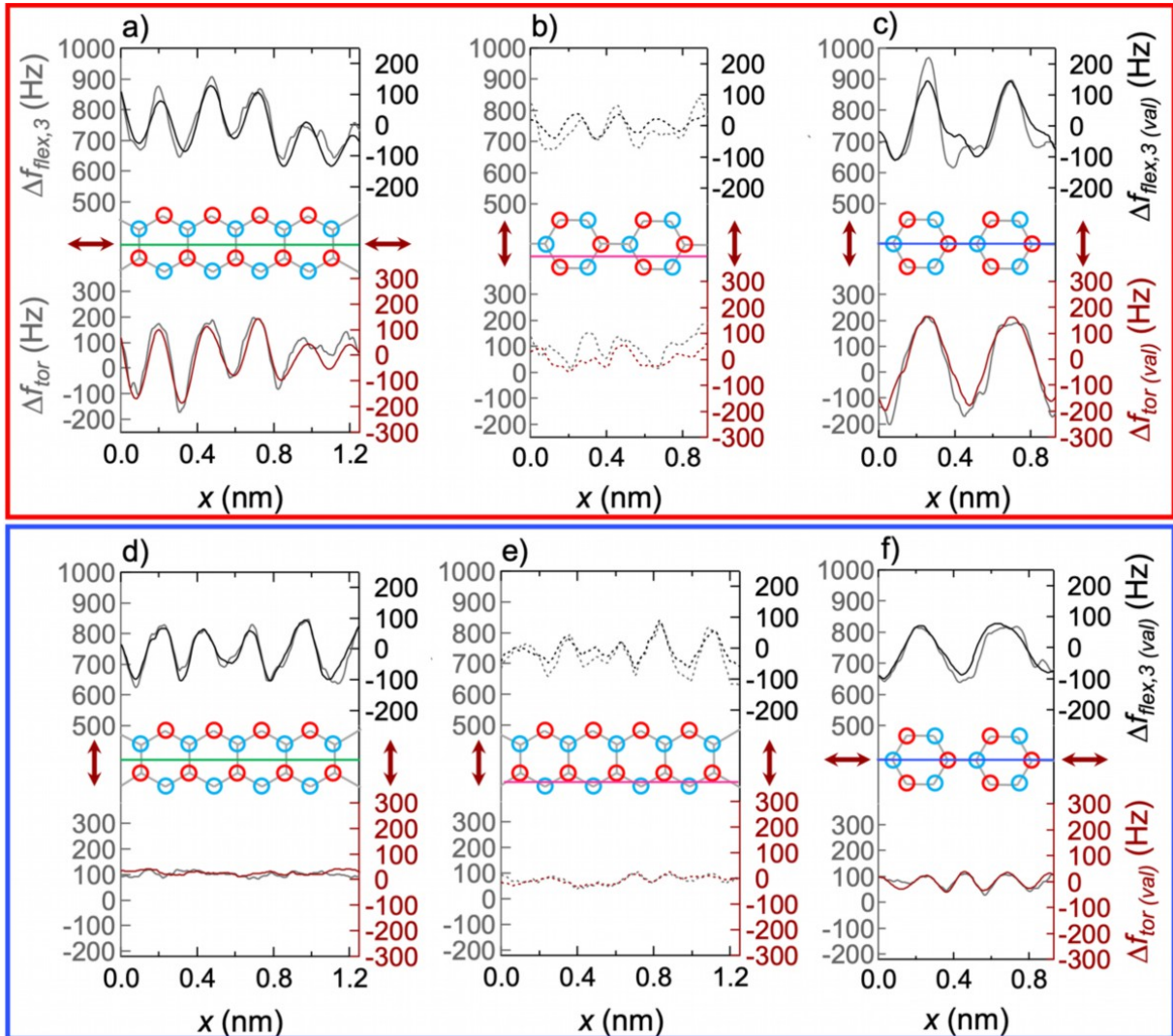


Figure 7-7: Cross-sectional profiles drawn through the original and validation frequency-shift images of HOPG along the pink, blue, and green lines in Figure 7-6. Profiles and axis labels are shown in gray for the original frequency-shift data, black for the flexural validation frequency-shift data, and red for the torsional validation frequency-shift data. The torsional oscillation was aligned approximately along the zigzag (resp. armchair) direction of the carbon hexagons for the cross sections shown in the red frame (a–c) (resp. blue frame (d–f)). The cross sections in a), d), and e) were drawn along the zigzag direction and in b), c), and e) along the armchair direction of the carbon hexagons. The a), d) green and c), f) blue marked cross sections cut the center of the hollow side, whereas the b), e) pink marked cross sections are offset from the center of the hollow side by the particular torsional amplitude values.

7.2. Supplementary Information to Section 3

7.2.1. Illustration of in-plane oscillation optical detection

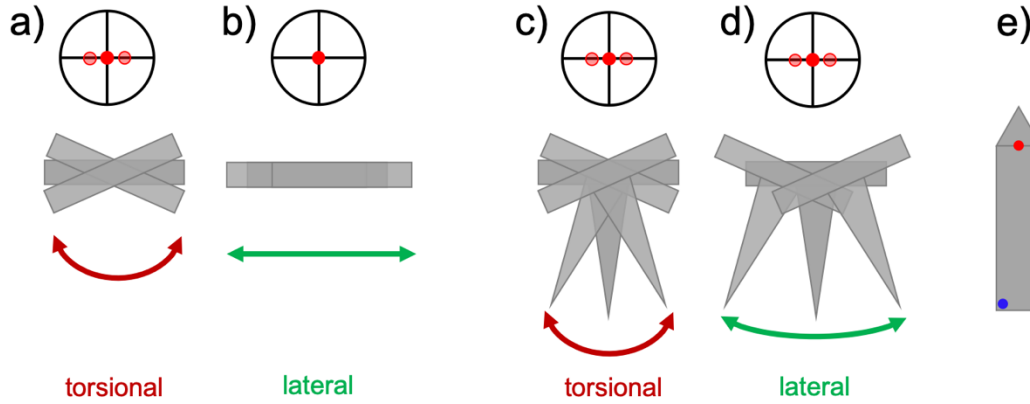


Figure 7-8: Illustration of a torsional (a, c) and a lateral eigenmode oscillation (b, d) for tip-less (a, b) and tip-containing cantilevers (c, d) and scheme of the detection (red) and photothermal excitation laser (blue) (e). Due to the rotational motion induced by the torsional eigenmode oscillation, the amplitude can be optically detected on a segmented photodiode for tip-less (a) and tip-containing cantilevers (c) in the same way. On the other hand, it is not possible to detect the lateral oscillation of a tip-less cantilever (b) by means of the standard optical beam detection technique. Nevertheless, as explained by Ding *et al.* [89], due to the small torsional motion induced by the tip attached to the cantilever, the lateral oscillation can be detected using the standard optical beam detection technique. To determine the optical lever sensitivity, additional considerations are required as discussed in detail in Section 7.2.4 “Calibration of lateral oscillation amplitude inverse optical lever sensitivity” of this Supplementary Information.

7.2.2. Estimation of tip-trajectory from in-plane and out-of-plane deflection

The cantilever oscillation in out-of-plane (z) and in-plane (x) direction can be estimated by linear combinations of cosine functions including the amplitude setpoints A_i , the resonance frequencies $f_{0(i)}$, the time t and the phase Φ_{AM} of the oscillation used for the topographic feedback in amplitude modulation [155]. The static components z_0 and x_0 have been neglected for simplicity. For the calculations behind the figures of the tip-trajectories shown in the main text, equations (3-4, 3-5) were used

$$z(t) = z_0 + z_{flex,2}(t) + z_{flex,3}(t) \approx A_{flex,2} \cos(2\pi f_{0(flex,2)} t - \Phi_{flex,2}) + A_{flex,3} \cos(2\pi f_{0(flex,3)} t - \Phi_{flex,3}), \quad (7-12)$$

$$x(t) = x_0 + x_{tor}(t) + x_{lat}(t) \approx A_{tor} \cos(2\pi f_{0(tor)}t - \Phi_{tor}) \quad (7-13)$$

$$+ A_{lat} \cos(2\pi f_{0(lat)}t - \Phi_{lat}).$$

If the respective channel is frequency modulated, the phase equals $\pi/2$. For the tip-trajectories shown for the AMFlex2-OLTor1-FMLat1 mode, the phase of the torsional oscillation was assumed to be 90° due to the lack of channels which could be detected simultaneously. In order to analyze the influence of the torsional phase, we simulated tip-trajectories with $\Phi_{tor,1} = 30^\circ, 45^\circ, 60^\circ, 90^\circ, 100^\circ$ and 120° as shown in Figure 7-9.

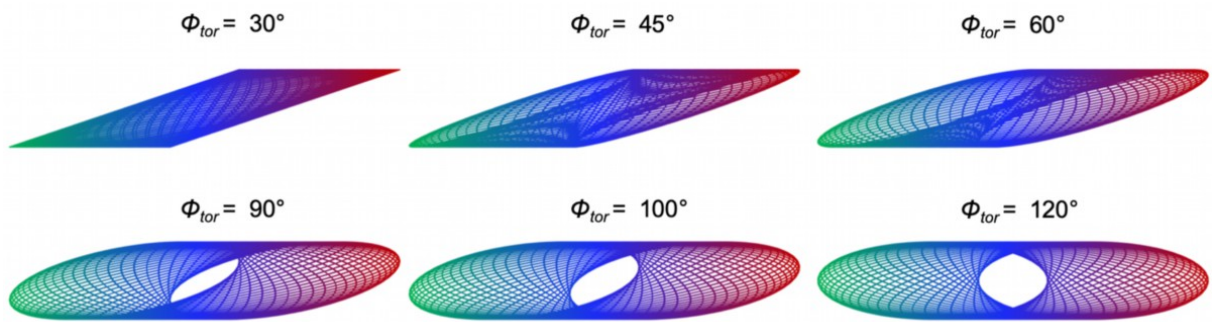


Figure 7-9: Tip-trajectories calculated using equations (7-12) and (7-13) for a “coupled” cantilever (resonance frequencies listed in Table 3-1 of the main text (Section 3.4)) oscillating in the AMFlex2-OLTor1-FMLat1 mode with $A_{flex,2} = 700$ pm, $A_{tor,1} = 1232$ pm and $A_{lat,1} = 863$ pm for different torsional phases.

From Figure 7-9 we can see that the torsional phase has a significant influence on the tip-trajectory which complicates the interpretation of the measurement data taken in the AMFlex2-OLTor1-FMLat1 mode. Consequently, we suggest to focus on imaging with “uncoupled” cantilevers if quantification is required.

7.2.3. Comparison of atomic resolution imaging on HOPG in the repulsive and the attractive regime

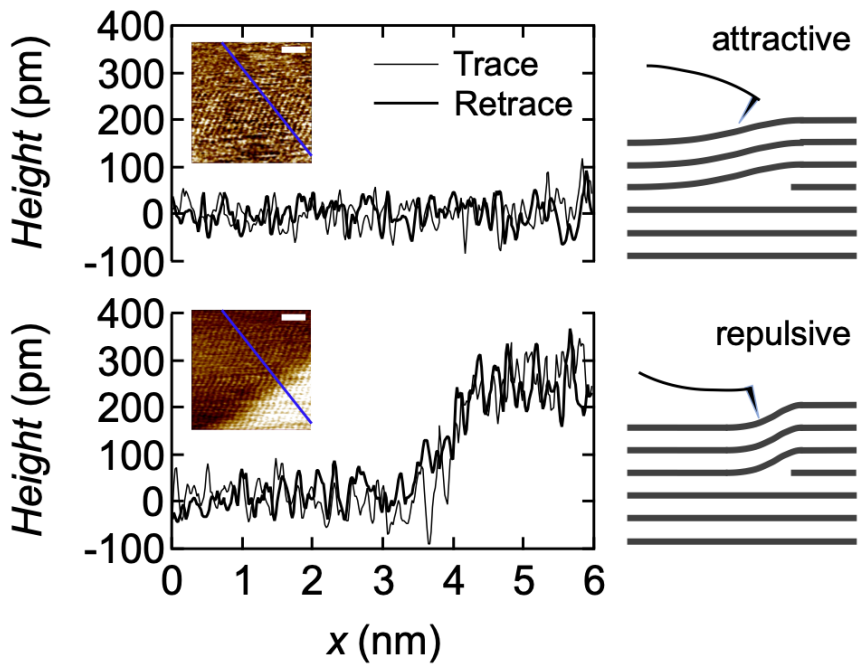


Figure 7-10: Cross sections through height images of HOPG at two different z-sensor positions and schemes of the alleged tip-sample interaction at the step edge in the attractive and the repulsive regime. The insets show the height images (retrace) of Figure 3-2j at $z \approx 3.1$ nm (top) and Figure 3-2k at $z \approx 3.7$ nm (bottom). The position of the cross sections is marked in blue, scale bar: 1 nm. The thin black cross sections are drawn through the trace images (not shown) and the thicker cross sections through the retrace images at the same position. Scale bar: 400 pm.

7.2.4. Calibration of lateral oscillation amplitude inverse optical lever sensitivity

The lateral cantilever oscillation is rarely used for AFM imaging because of the difficulties to calibrate its inverse optical lever sensitivity (invOLS). As discussed in detail by Ding *et al.* [89] the lateral oscillation itself cannot be detected by the photodiode. But due to the tip attached to the cantilever, a small torsion is induced which results in a measurable movement of the reflected laser beam on the photodiode, that allows for the detection of the lateral resonance by the help of a thermal spectra or cantilever tunes without being in contact with the sample. While the torsional oscillation amplitude invOLS can be determined *e.g.* from thermal noise spectra¹⁵, there is to the best of our knowledge currently no method for the lateral oscillation invOLS calibration. Here, we present an approach based on imaging a graphene wrinkle on an HOPG sample with different lateral-oscillation-amplitude setpoints in AMFlex2-OLTor1-FMLat1 mode. The idea behind this method is, that the effect of an increasing lateral oscillation amplitude can be compared to a smoothening of imaging data points. In Figure 7-11a and f we show the averaged cross sections (20 pixel) through the height images (b-e) and the lateral frequency-shift images (g-j) taken at different lateral-oscillation-amplitude setpoints. All images were taken at a constant second flexural-eigenmode amplitude of 238 pm and at a scan angle of 90° resulting in both, fast scan direction and lateral oscillation direction being perpendicular to the graphene wrinkle. The orange (b,g)/black (c,h)/blue (d,i)/red (e,j) marked cross sections result from the imaging data taken at lateral-oscillation-amplitude setpoints of 5 mV/10 mV/20 mV/40 mV. The black/blue/red dotted lines in Figure 7-11a and f result from smoothening of the orange curves ($A_{lat,1} = 5$ mV) over 23/45/89 pixel and multiplication (height)/division ($\Delta f_{lat,1}$) by the weighing factors 1.25/1.85/2.80 which we introduced in order to optimize the fit. The weighing factors $w_{lat,1}$ can be determined according to equation (7-14) which was found empirically

$$w_{lat,1} = 1.5^{\frac{A_{lat,1}(large)}{2A_{lat,1}(small)}}. \quad (7-14)$$

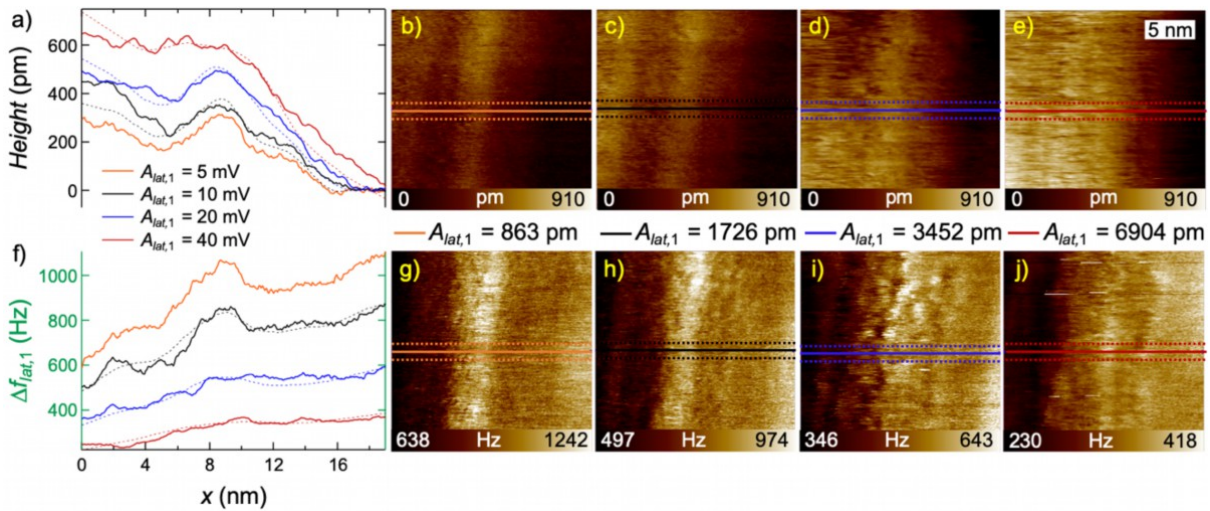


Figure 7-11: Calibration of lateral-oscillation-eigenmode amplitude at a graphene wrinkle on HOPG. The solid lines in a) and f) show the height and the lateral frequency shift for different lateral-eigenmode setpoints along the averaged cross sections (20 pixel) marked in b-e) and g-j). The images were taken in the AMFlex2-OLTor1-FMLat1 mode with a free second flexural-eigenmode amplitude of 765 pm and a setpoint of 238 pm. The scan angle was 90° so that both, the fast scan direction and the direction of the lateral oscillation were oriented perpendicular to the wrinkle. The dotted black/blue/red lines in a) and f) represent the orange curve smoothed over 23/45/89 pixel and multiplication (height)/division ($\Delta f_{lat,1}$) by the weighing factors 1.25/1.85/2.80 which we introduced in order to optimize the fit.

From the cross sections in Figure 7-11a and f and from the corresponding images in Figure 7-11b–e and g–j we can observe that the increase in $A_{lat,1}$ from 5 mV to 40 mV leads to stronger lateral averaging of the height and the lateral frequency-shift values. If we compare *e.g.* the orange ($A_{lat,1} = 5$ mV) with the red curve ($A_{lat,1} = 40$ mV) in Figure 7-11a we can directly see that for the smaller $A_{lat,1}$ two hillocks can be resolved whereas for the larger $A_{lat,1}$ only one broader hillock is visible. In Figure 7-11f the lateral frequency shift shows a clearly visible hillock for $A_{lat,1} = 5$ mV (orange) whereas for $A_{lat,1} = 40$ mV (red) the hillock is hardly visible. Based on these observations we assumed that the cross sections of the images taken with $A_{lat,1} = 10$ mV, $A_{lat,1} = 20$ mV and $A_{lat,1} = 40$ mV can be reproduced by smoothing of the orange curve which represents the cross sectional data resulting from $A_{lat,1} = 5$ mV. By smoothing the orange curves in Figure 7-11a and f with a Savitzky-Golay filter of first grade over 23, 45 and 89 pixel, respectively, we were able to reproduce the general trend of the black, blue and red curves with satisfying accuracy. After treating the smoothed averaged cross-sections with the appropriate weighing factors the black, blue and red dotted curves shown in Figure 7-11a and f were gained. Although there are small deviations between the dotted and the solid curves in Figure 7-11a, in particular at the end and the beginning of the cross sections, the overall trend is nicely reproduced. From the number of pixel over which the smoothing

was performed, we determined the optical invOLS of the lateral oscillation amplitude according to equations (3-7, 3-8)

$$(A_{lat,1} - A_{lat,1(ref)})[nm] = \frac{l}{n_{line}} \frac{n_{smooth} - 1}{2}, \quad (7-15)$$

$$s_{lat,1} = \frac{(A_{lat,1} - A_{lat,1(ref)})[nm]}{(A_{lat,1} - A_{lat,1(ref)})[V]}, \quad (7-16)$$

where $A_{lat,1(ref)}$ is the lateral-amplitude setpoint which was used for the reference image and the corresponding cross section chosen to be smoothed (here: $A_{lat,1(ref)} = 5$ mV, orange line). In our case the scan size (l) was 20 nm and the number of pixel/line (n_{line}) was 256. Due to the definition of the amplitude as half of the peak-to-peak value, the number of pixel over which was smoothed (n_{smooth}) needs to be divided by two after one pixel was subtracted (the pixel at the center position). The determination of the optical invOLS was done by comparing the differences of the lateral amplitudes in nanometers and in volts such as shown in equation (7-16). Following the explained procedure, we determined a lateral sensitivity of 122 nm/V. The resulting lateral-oscillation-amplitude setpoints in nanometers corresponding to the images in Figure 7-11 are shown in the center row. Consequently, the invOLS of the lateral oscillation is around eleven times larger compared to the invOLS of the torsional oscillation which we determined in our recent work to be 11 nm/V [8]. At first glance this seems to be counterintuitive because the lateral stiffness is higher than the torsional stiffness for the type of cantilever used here (see Section 7.2.7 “Calibration of inverse optical lever sensitivities and force constants” of this Supplementary Information), which should also result in a higher optical lever sensitivity (lower invOLS) for the lateral oscillation. However, if we take into account that the signal on the photodiode cannot sense the lateral but only the torsional component of the lateral oscillation induced by the tip, it is reasonable to believe that the invOLS is larger for the lateral eigenmode oscillation.

7.2.5. Vertical and lateral tip position estimated from dynamic spectroscopy and contact mode AFM

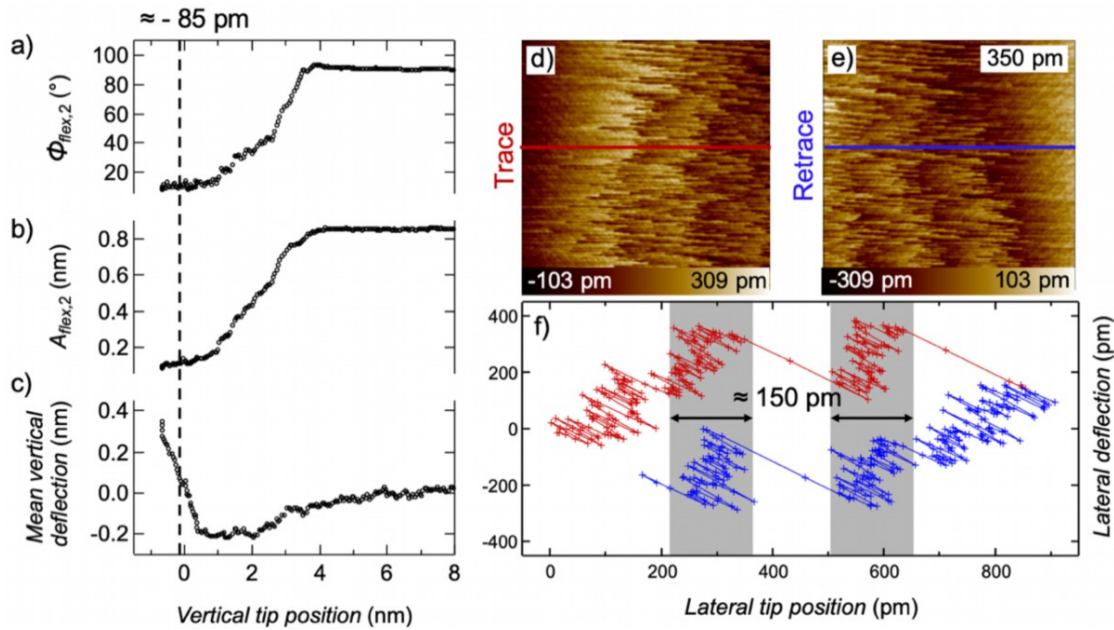


Figure 7-12: Vertical and lateral tip position estimated from dynamic spectroscopy (a-c) and contact mode AFM (d-f), respectively. Second flexural phase (a), amplitude (b) and mean vertical deflection (c) as a function of the vertical tip position (z -position corrected for vertical deflection). The dotted line at approximately -85 pm indicates the vertical tip position, where the second flexural eigenmode setpoint of 110 pm was reached. This corroborates the estimation of an indentation depth of 14-85 pm while imaging an HOPG surface. Nevertheless, it was not possible to determine differences in indentation depth when imaging the mean vertical deflection while varying the lateral or torsional oscillation amplitude. From a and b it becomes clear that the second flexural phase and amplitude form plateaus close to the HOPG surface. We assume that this is more likely a consequence of oscillating inside natural water layers covering the HOPG surface rather than a permanent contact between tip and sample. This would imply imaging in contact resonance mode where the frequency shift is expected to be much larger compared to the values observed in our study. In d and e, the trace and retrace lateral deflection images of an HOPG surface analyzed with friction force microscopy are shown, respectively. It needs to be mentioned that the vertical deflection setpoint (1100 nN) was much larger compared to the mean vertical deflection values reached in dynamic spectroscopy because no stable contact was achieved using smaller vertical deflection values. The horizontal lines indicate the positions at which the cross sections shown in f were taken, where the abscissa was selected as the lateral tip position, calculated from the x -position of the cross section corrected for the lateral tip-deflection. The calibration of the in-plane static sensitivity was performed on a silicon substrate, following the protocol of Dietz [88]. From the graph in f, on the one hand, the typical stick-slip motion (gray-white) can be observed. On the other hand, it becomes evident, that the tip-position was not completely fixed within the gray marked area, but that the tip showed an overall movement of around 150 pm. This observation can be interpreted as a corroboration of the observations from Figure 3-4, that while imaging, a local relative displacement of around 150 pm between two carbon layers could be induced.

7.2.6. Comparison of tip trajectories in AMFlex2-FMLat1-FMFlex3 and AMFlex2-FMTor1-FMFlex3 mode

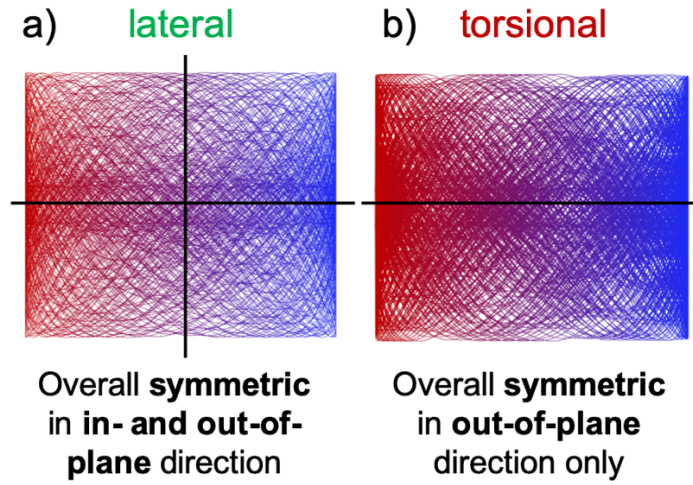


Figure 7-13: Comparison of the tip-trajectory resulting from (a) the AMFlex2-FMLat1-FMFlex3 mode and (b) the AMFlex2-FMTor1-FMFlex3 with $A_{flex,2} = 110$ pm, $A_{flex,3} = 145$ pm and $A_{lat,1} = A_{tor,1} = 328$ pm.

7.2.7. Calibration of inverse optical lever sensitivities and force constants

The determination of the inverse optical lever sensitivities (invOLS) as well as the force constants of the flexural and the torsional eigenmodes were described in detail in our recent paper [8]. A method for the determination of the lateral invOLS was provided in the main text. The lateral force constant was calculated from the first flexural force constant, the width b and the thickness t of the cantilever [146]

$$k_{lat} = k_{flex,1} \left(\frac{b}{t} \right)^2. \quad (7-17)$$

7.2.8. Comparison of resonance frequencies

Table 7-1: Averaged resonance-frequency ratios and standard deviations determined for different amounts of cantilevers (a: 18, b: 6, c: 17) of the type HiResC15/Gr-Au. The relative deviation, relating the standard deviation to the average value is shown in percentage. The last row includes the theoretical relations between the different resonance frequencies for rectangular cantilevers, where L is the length, b is the width and t is the thickness of the cantilever [68, 90].

| $f_{0 (flex,2)}/f_{0 (flex,1)}^a$ | $f_{0 (flex,3)}/f_{0 (flex,1)}^b$ | $f_{0 (tor,1)}/f_{0 (flex,2)}^a$ | $f_{0 (lat,1)}/f_{0 (flex,2)}^c$ | $f_{0 (lat,1)}/f_{0 (tor,1)}^c$ |
|-----------------------------------|-----------------------------------|----------------------------------|----------------------------------|---------------------------------|
| 6.29 ± 0.01 | 17.40 ± 0.04 | 1.04 ± 0.03 | 1.14 ± 0.02 | 1.09 ± 0.01 |
| 0.2 % | 0.2 % | 2.6 % | 2.1 % | 0.5 % |
| = 6.27 | = 17.55 | $\propto L/t$ | $\propto b/t$ | $\propto b/L$ |

From Table 7-1 we can see that the relations between the different flexural eigenmodes are very close to the theoretical values for rectangular cantilevers [68] and show only a small relative deviation. Additionally, we found that the relations between the resonance frequencies of the torsional, lateral and flexural eigenmodes were also comparably stable, although slightly larger relative deviations were observed, especially for the ratios of torsional to flexural (2.6 %) and lateral to flexural resonance frequencies (2.1 %). From theoretical considerations presented by Young *et al.* [90] regarding the dependency of the resonance frequencies on the cantilever dimensions, we concluded that the slightly larger spreading of the relation between torsional/flexural and lateral/flexural resonance frequencies can most likely be attributed to small variations in the thickness of the cantilevers. Due to the fact that the relation between the torsional and the second flexural resonance frequency is close to zero, even the small relative deviation of 2.6 % leads to the occurrence of “coupled” and “uncoupled” cantilevers as described in the main text.

7.3. Supplementary Information to Section 4

7.3.1. Temperature and relative humidity during storage in laboratory air

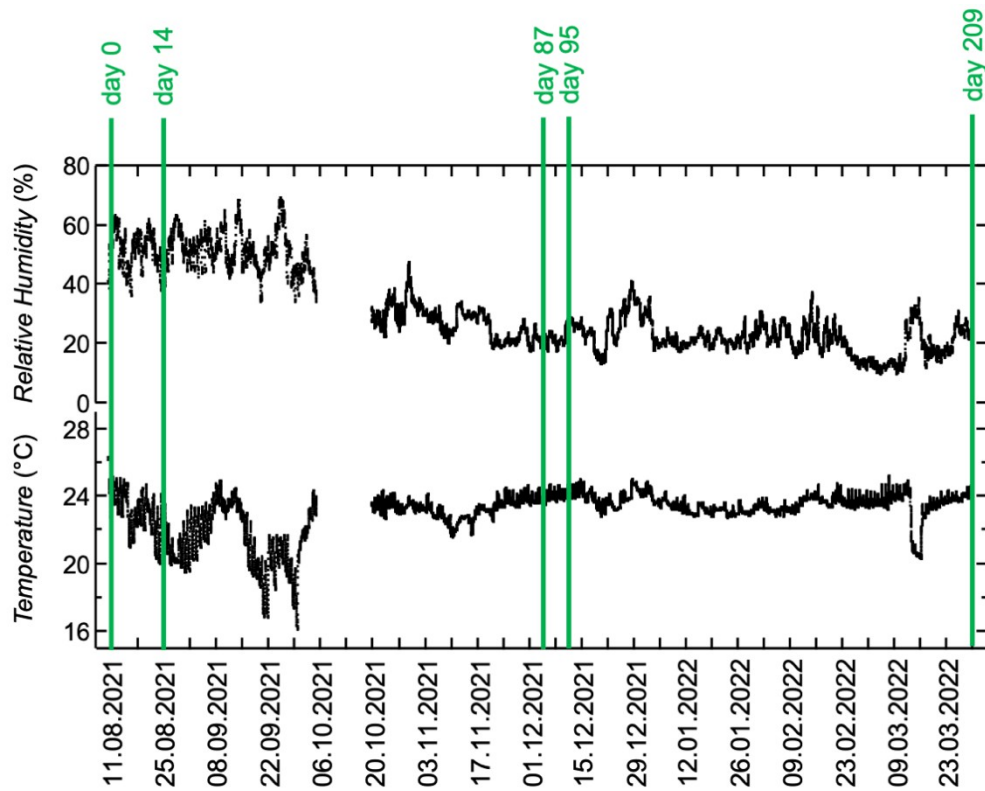


Figure 7-14: Temperature and relative humidity measured during storage of the few-layer graphene-/graphite-sample under laboratory air conditions in a polypropylene box.

7.3.2. Wrinkle formation during AMFlex2-OLTor1-FMLat1-FMFlex3 imaging

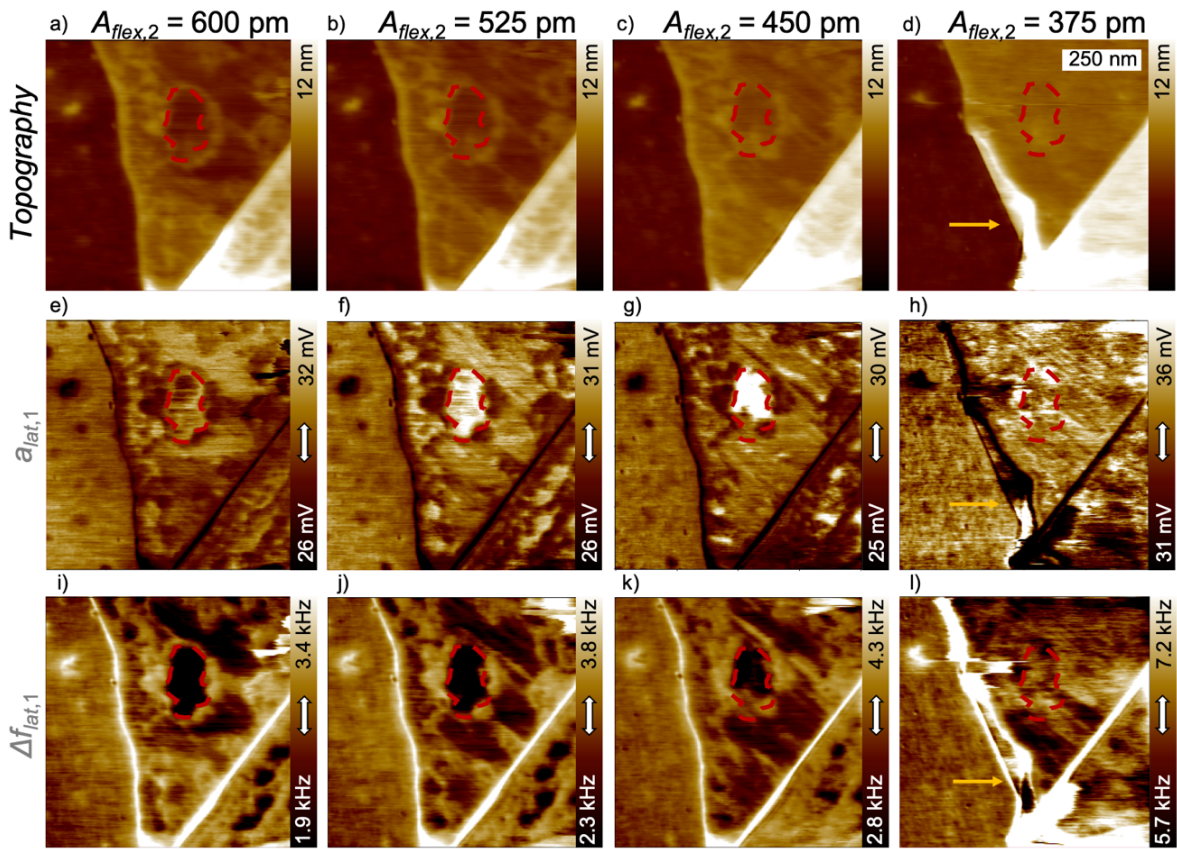


Figure 7-15: Wrinkle formation on a few-layer graphene-/graphite-flake while imaging in AMFlex2-OLTor1-FMLat1-FMFlex3 mode. Topography (a-d), lateral drive amplitude (e-h), lateral frequency shift images (i-l) taken at $A_{flex,2} = 600$ pm (a, e, i), 525 pm (b, f, j), 450 pm (c, g, k) and 375 pm (d, h, l). The free amplitude was $A_0(flex,2) = 675$ pm and $A_{lat,1} = 1.766$ nm.

7.3.3. Removal of large-scale adsorbates on a few-layer graphene-/graphite-flake after 7 days of storage

The first series of experiments was performed on the few-layer graphene-/graphite-flake after storage of 8 days under ambient conditions in laboratory air using the AMFlex2-OLTor1-FMLat1-FMFlex3 method with different second flexural and first lateral eigenmode amplitudes to adjust suitable values for adsorbate analysis. Figure 7-16 shows the influence of different second flexural as well as lateral eigenmode amplitudes on large scale adsorbate structures on a few-layer graphene-/graphite flake during imaging. The thinner part of the flake equals approximately 7 layers and the thicker part equals approximately 22 layers of graphene. On the left edge of the flake, a wrinkle was formed upon previous imaging with the AMFlex2-OLTor1-FMLat1-FMFlex3 method (see Figure 7-15 in Section 7.3.2). The images were taken

consecutively from a-h. Obviously, the large-scale adsorbates form predominantly at the edges between the areas of different layer numbers and between graphene and the Si/SiO₂-substrate. Especially the formed wrinkle seems to be strongly covered by large-scale adsorbates. For $A_{flex,2} = 0.60$ nm the adsorbate structures were neither modified by the small lateral amplitude of 0.86 nm (Figure 7-16a) nor by the large lateral amplitude of 17.26 nm (Figure 7-16b). For the images shown in Figure 7-16c and d the second flexural eigenmode amplitude setpoint was reduced to 0.53 nm. No substantial differences relative to the images shown in Figure 7-16a and b were visible for the small lateral eigenmode image in Figure 7-16c. In contrast to that, we observed a clear variation of the adsorbate structure for the large lateral amplitude case shown in Figure 7-16d. Lowering $A_{flex,2}$ to 0.45 nm and imaging with $A_{lat,1} = 0.86$ nm resulted in Figure 7-16e which again shows a similar adsorbate structure compared to the previously taken image in Figure 7-16d. Increasing the lateral amplitude to 17.26 nm led to a significant removal of adsorbates from the imaging area such as visible in Figure 7-16f. The same effect was observed for $A_{flex,2} = 0.38$ nm. For the small lateral amplitude resulting in Figure 7-16g, the adsorbate structure resembles that of Figure 7-16f but for the large lateral amplitude a further removal of adsorbates took place, such as visible in Figure 7-16h. Consequently, we found that large lateral eigenmode amplitudes can be used for modifications of large-scale adsorbate structures, where the degree of manipulation can be adjusted by the flexural amplitude setpoint. We conclude that the combination of small second flexural eigenmode amplitude setpoints and large lateral eigenmode amplitudes induces high lateral forces, allowing for a controlled manipulation of surface structures. On the other hand, using small lateral amplitudes, the large-scale adsorbate structures kept unmodified independent on the flexural eigenmode setpoint. In contrast to the large-scale adsorbate structures observed in Figure 7-16 there were several reports on the formation of ordered stripe-structures on graphene-/graphite-flakes, ranging between 4 – 6 nm [166]. The origin of these stripe structures is still under debate but it can most probably be attributed to the formation of nanotextured adsorbates [165, 166, 175]. Most of the performed studies in this context are either based on standard AFM imaging in contact or tapping mode (out-of-plane) or on lateral force microscopy or frictional/transversal force microscopy (in-plane). Using the AMFlex2-OLTor1-FMLat1-FMFlex3 method allows for simultaneous in-plane and out-of-plane analysis of dissipative and conservative tip-sample interactions, which can be considered as a promising approach towards a more complete understanding of structured adsorbate formation upon ambient storage.

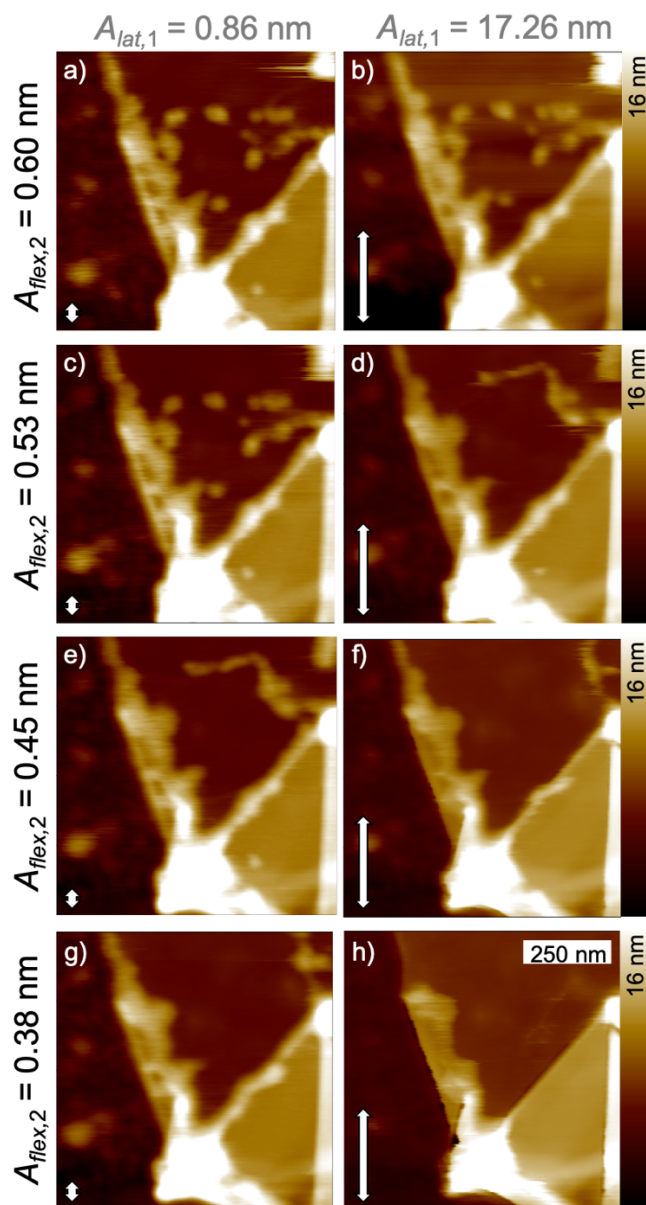


Figure 7-16: Adsorbate removal on a few-layer graphene-/graphite-flake while imaging in AMFlex2-OLTor1-FMLat1-FMFlex3 mode. Topography images taken at $A_{flex,2} = 0.60$ nm (a, b), 0.53 nm (c, d), 0.45 nm (e, f) and 0.38 nm (g, h). The free amplitude was $A_{0(flex,2)} = 0.68$ pm and $A_{lat,1} = 0.86$ nm (a, c, e, g) and 17.26 nm (b, d, f, h), respectively.

7.3.4. Determination of graphene/graphite layer numbers

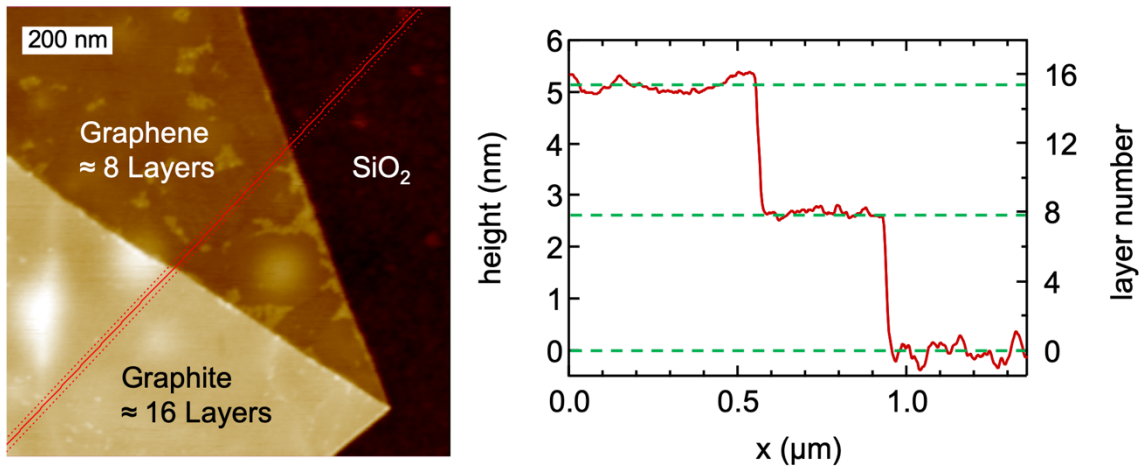


Figure 7-17: AFM topography image of a few-layer graphene-/graphite-flake and cross-sectional profile for the determination of layer numbers.

7.3.5. Adsorbate formation on a few-layer graphene-/graphite-flake analyzed in AMFlex2-OLTor1-FMLat1-FMFlex3 mode after different times of storage

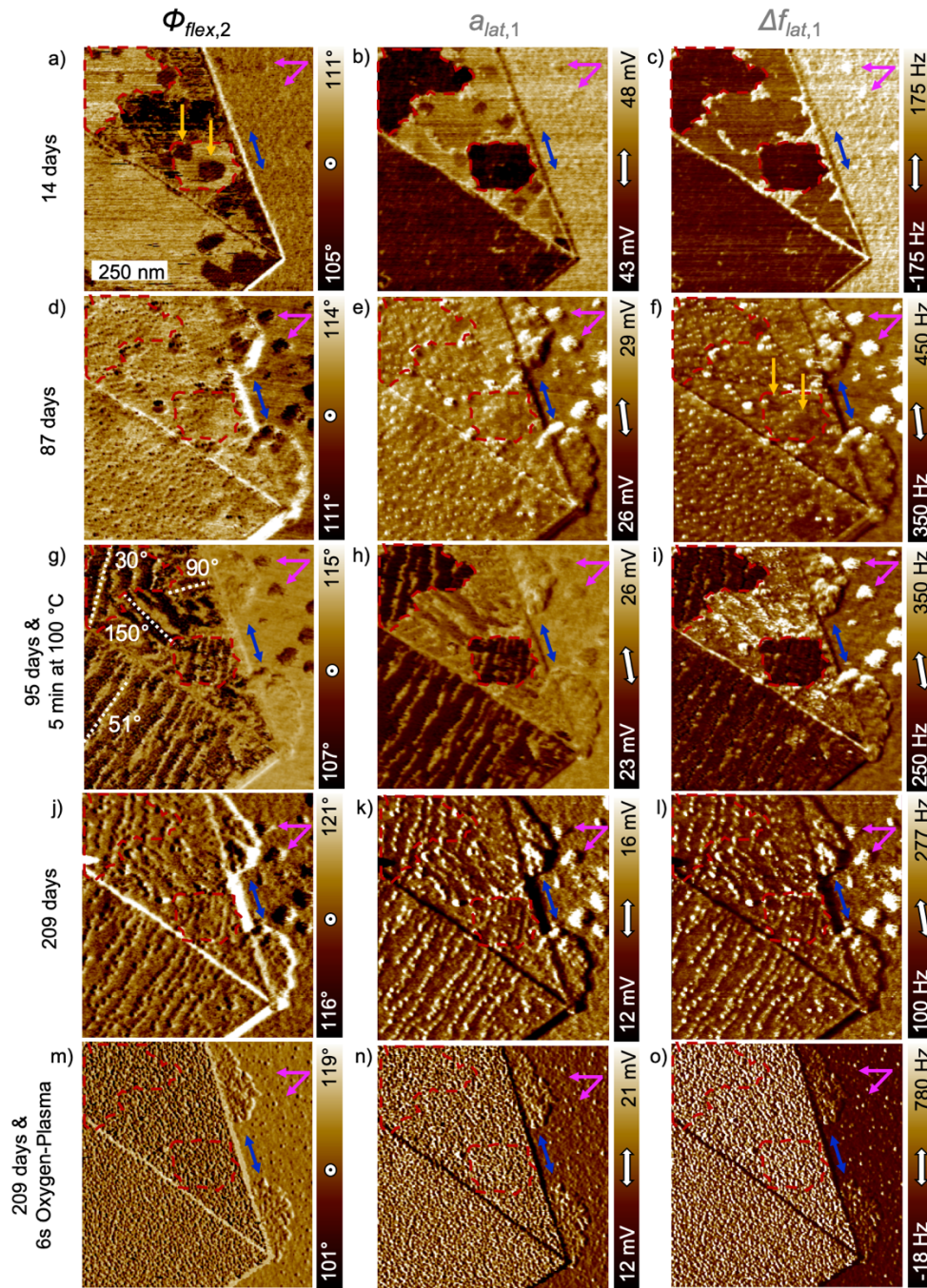


Figure 7-18: Adsorbate formation on a few-layer graphene-/graphite-flake analyzed in AMFlex2-OLTor1-FMLat1-FMFlex3 mode upon storage for 14 days (a-c), 87 days (d-f) and 95 days & heating for 5 min at 100 °C (g-i), 209 days (j-l) and 209 days & 6s oxygen-plasma treatment (m-o). Second flexural phase (a, d, g, j, m), lateral drive amplitude (b, e, h, k, n) and lateral frequency-shift images (c, f, i, l, o). $A_0 (flex,2) = 675$ pm, $A_{flex,2} = 600$ pm, $A_{lat,1} = 1.766$ nm.

7.3.6. Analysis of the influence of oxygen-plasma treatment on few-layer graphene-/graphite-flake *via* AFM

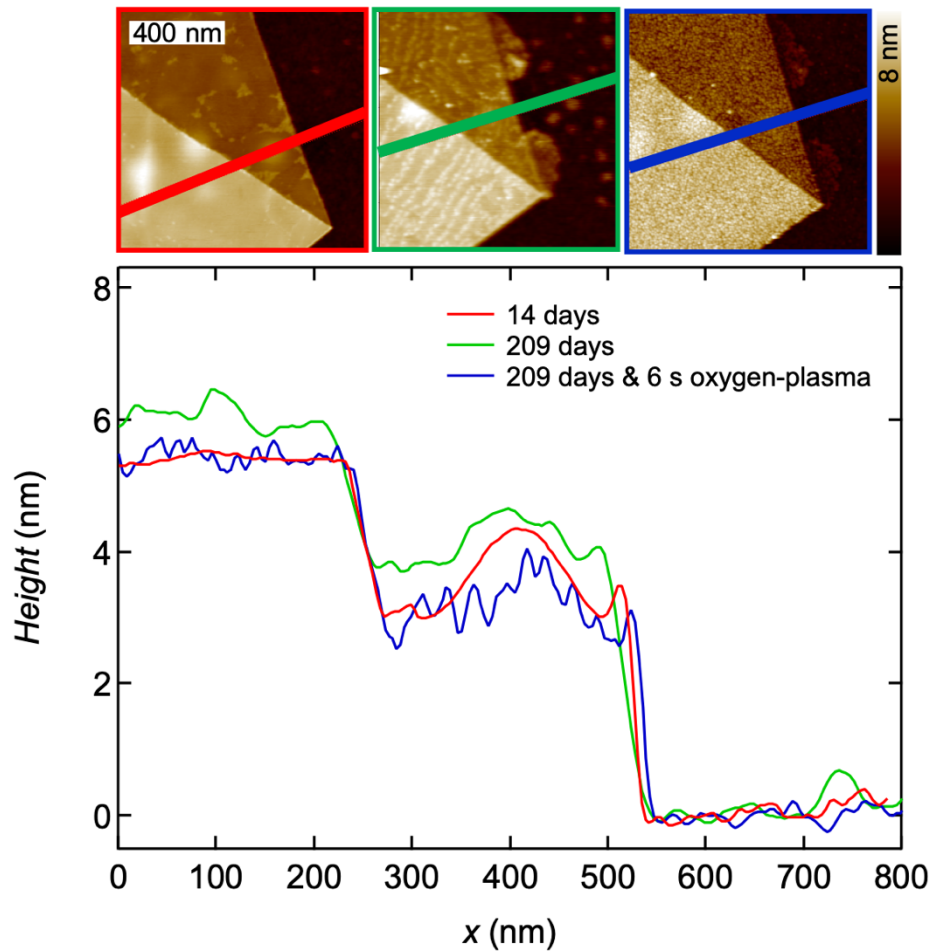


Figure 7-19: Weight cross-sections through topography images of the few-layer graphene-/graphite-flake stored for 14 days (red), 209 days (green) and after 6 s of oxygen-plasma treatment (blue). The increased amount of adsorbate material on the graphene-/graphite-area after 209 days of storage is clearly visible. After 6 s of plasma-treatment within the frame of uncertainty the cross-section determined after 14 days of storage was reproduced, however, the roughness of the few-layer graphene-/graphite-sample increased. We conclude that the sample was cleaned from adsorbates by the plasma-treatment and a slight modification of the surface took place, however, no ablation of graphene layers could be observed.

7.3.7. Analysis of the influence of oxygen-plasma treatment on few-layer graphene-/graphite-flake *via* Raman-spectroscopy

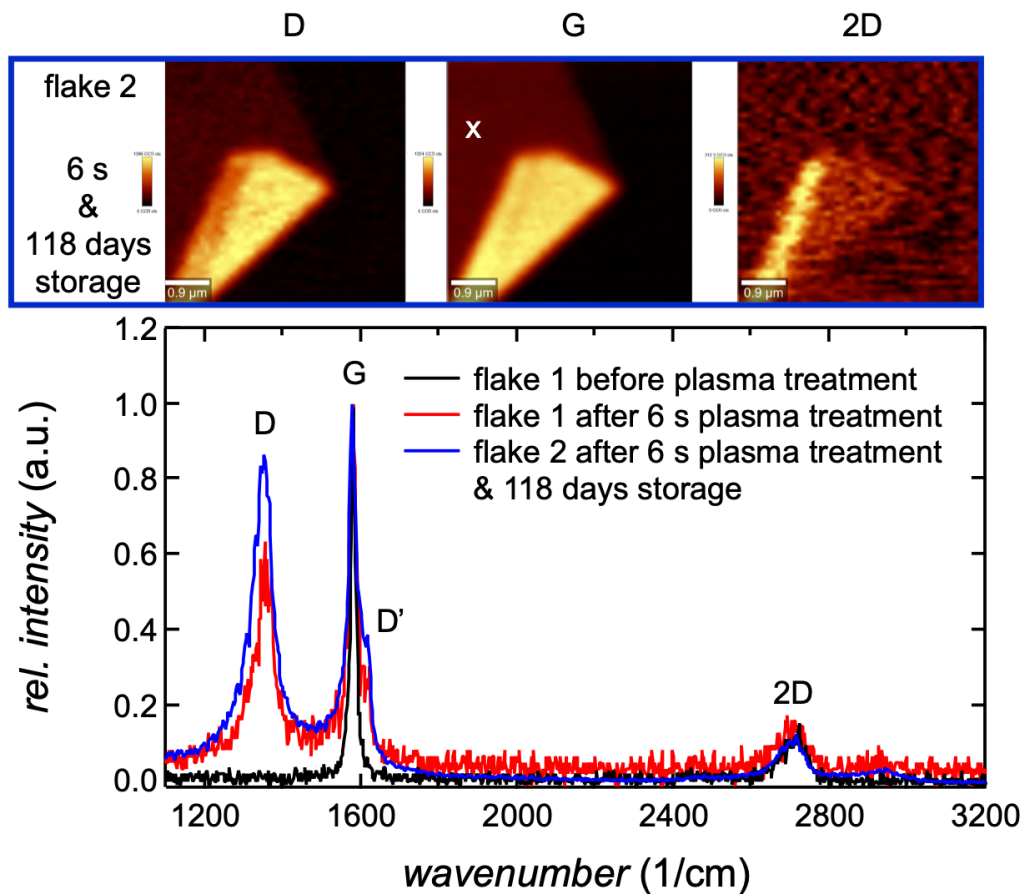


Figure 7-20: 2D Raman maps of the few-layer graphene-/graphite-flake (here named flake 2) analyzed for the characteristic peaks (D, G, and 2D). Raman spectra of a similar few-layer graphene-/graphite-flake (flake 1) are shown for comparison prior to plasma treatment (black) and after 6 s plasma treatment (red) in addition to an extracted Raman spectrum taken after plasma treatment and subsequent storage of flake 2 for 118 days (blue), approximately at the positions marked by the white cross in the Raman maps. The spectra were calibrated on the G-peak for a better comparison. It becomes clearly visible that after the 6 s oxygen-plasma treatment (red, blue) the D-peak as well as the D'-peak occurred which were not present in the spectrum prior to the plasma treatment (black). This clearly indicates that the plasma treatment introduced defects into the material. On the other hand, no additional peaks which could be attributed to adsorbate molecules were found after storage of flake 2 (blue). Possible explanations could be found in the small amount of adsorbate material covering the surface as well as the similarity of the adsorbates to the graphitic sample, complicating the identification of additional peaks.

7.3.8. Analysis of friction anisotropy on an “AFM-cleaned” few-layer graphene-/graphite flake

Figure 7-21 exemplarily shows the lateral frequency-shift images of the “cleaned” few-layer graphene-/graphite-flake area before (a, c) and after rotation by 87° (b, d) imaged with $A_{flex,2} = 4.5$ nm ($A_{o(flex,2)} = 6$ nm) and $A_{lat,1} = 0.86$ nm (a, b) and $A_{lat,1} = 8.6$ nm (c, d), respectively. Another four images taken at a lower second flexural amplitude setpoint ($A_{flex,2} = 3$ nm) have been additionally analyzed as shown in Figure 7-22. As schematically shown in Figure 7-21a–d we drew weight cross-sections through the images and analyzed the average values as well as the standard deviation of two representative areas, located on the Si/SiO₂-substrate (blue) and on the few-layer graphene-/graphite flake (red). The results are shown below the images and are additionally summarized in the diagram in Figure 7-21e, where the averaged lateral frequency-shift values on the Si/SiO₂-substrate (blue) are compared to the few-layer graphene-/graphite flake (red) before (circles) and after rotation by 87° (triangles) at second flexural amplitude setpoints of 4.5 nm and 3 nm and first lateral amplitudes of 0.86 nm and 8.60 nm. The same analysis was done for the third flexural frequency-shift (Figure 7-21f), the lateral drive amplitude (Figure 7-21g) and the second flexural phase images (Figure 7-21h).

First, we analyzed to what extent the in-plane (lateral) and the out-of-plane (flexural) eigenmode amplitudes influence on the one hand the associated and on the other hand the mutual in-plane and out-of-plane observables. Focussing on the few-layer graphene-/graphite-flake area (red) we observed, that the lateral frequency shift (Figure 7-21e) was neither substantially influenced by the variation of the lateral nor the second flexural amplitude setpoint. In contrast to that, the third flexural frequency shift (Figure 7-21f) increased as expected by the reduction of the second flexural eigenmode amplitude setpoint and surprisingly slightly decreased for the increase of the lateral eigenmode amplitude setpoint for both, the few-layer graphene-/graphite-flake area (red) and the Si/SiO₂-substrate area (blue). The same trend was visible for the lateral frequency shift (Figure 7-21e) examined on the Si/SiO₂-substrate area (blue). This cross-talk might be explained by the fact that the lateral amplitude (8.60 nm) was more than 100 times larger compared to the third flexural amplitude (0.08 nm). Analyzing the lateral drive amplitude (Figure 7-21g) it was found that on both areas, there was no substantial change originating from the variation in the second flexural amplitude setpoint for the small lateral amplitude case (0.86 nm). For the large lateral amplitude case (8.60 nm), the lateral drive amplitude increased as it was expected [141], however, the increase was slightly stronger for the smaller second flexural amplitude setpoint on both areas, again indicating a cross-talk for the large lateral amplitude case. For the second flexural phase (Figure

7-21h) we observed as expected a decrease originating from lowering the second flexural amplitude setpoint on both areas, but there was no clear indication for an interference with the lateral amplitude setpoint.

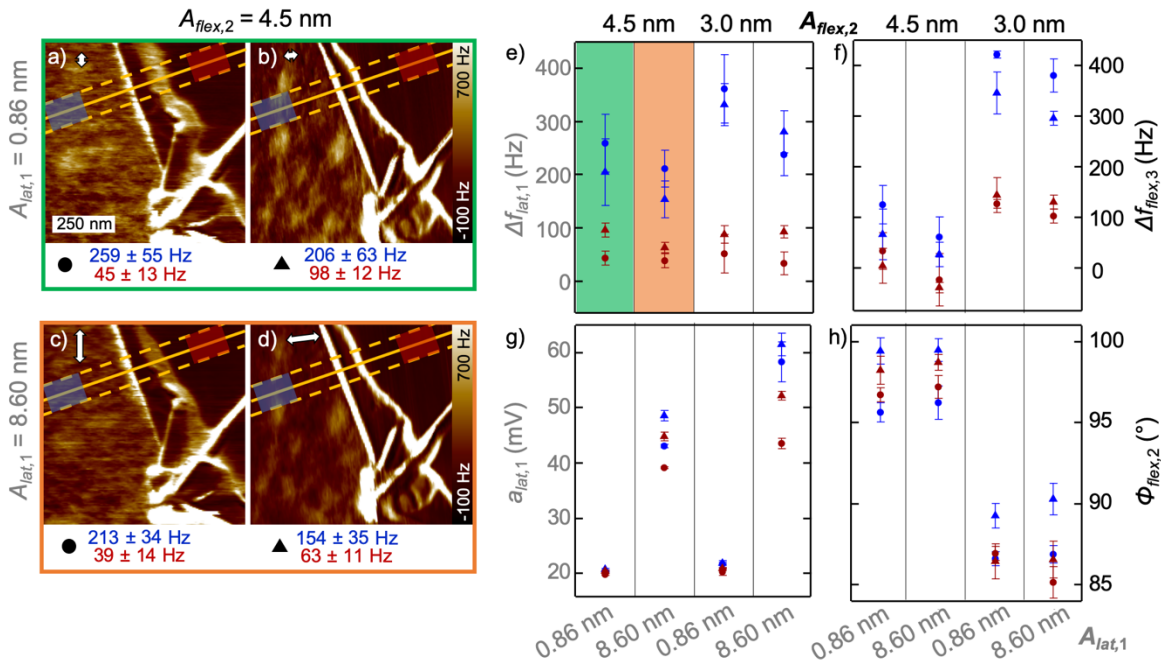


Figure 7-21: Analysis of the influence of different second flexural and first lateral amplitude setpoints on AFM images of a “cleaned” few-layer graphene-/graphite flake before and after rotation by 87°. Lateral frequency-shift images (a-d) were taken in the AMFlex2-OLTor1-FMLat1-FMFlex3 mode with $A_0(flex,2) = 6$ nm, $A_{flex,2} = 4.5$ nm, $A_{flex,3} = 0.08$ nm, $A_{lat,1} = 0.86$ nm (a, b) and $A_{lat,1} = 8.60$ nm (c, d) before (a, c) and after rotation of the flake by 87° (b, d). Weight cross-sections were drawn through the images to determine average values and standard deviation representative for the Si/SiO₂-substrate (blue) and the few-layer graphene-/graphite flake (red). The results originating from the images shown in a-d are summarized in the green (a, b) and orange highlighted areas (c, d) in e, where the averaged frequency-shift values were plotted as a function of two different second flexural amplitude setpoints (4.5 nm and 3 nm) and lateral amplitudes (0.86 nm and 8.60 nm) before (circles) and after rotation of the flake by 87° (triangles). The blue (red) color indicates that the values were determined on the Si/SiO₂-substrate (few-layer graphene-/graphite flake). The diagrams in f, g and h show the data resulting from the analysis of the third flexural frequency-shift, the lateral drive amplitude and the second flexural phase, respectively. Note, that the third flexural frequency-shift data of the rotated flake images shown in f was corrected for an offset in resonance frequency of 259 Hz.

By comparing the general trend of the predominantly conservative interaction values (Figure 7-21e, f) determined on the different areas we observed lower values on the few-layer graphene-/graphite flake (red) compared to the values determined on the Si/SiO₂-substrate (blue). This fits to the knowledge that the shear modulus, which correlates to the lateral frequency shift, as well as the elastic modulus, which corresponds to the flexural frequency

shift, are larger for SiO₂ than for multilayer-graphene/graphite [245, 246]. Regarding the dissipative interaction (Figure 7-21g, h) the trend of higher values determined on the Si/SiO₂-substrate (blue) compared to the few-layer graphene-/graphite flake (red) was only clearly observable for the lateral drive amplitude (Figure 7-21g) determined with large lateral amplitudes (8.6 nm). We assume that this can be explained by differences in frictional interaction on the two different areas, where the energy dissipated during imaging with a large lateral amplitude seems to be higher on the Si/SiO₂-substrate compared to the few-layer graphene-/graphite flake area. From these observations the question arises if it is possible to distinguish between frictional (dissipative) and shear interactions (conservative) by evaluating the lateral drive amplitude and frequency-shift, respectively. Therefore, we analyzed the images prior to (circles) and after rotation (triangles) of the sample by approximately 90°.

As reported by others, it should be possible to detect frictional anisotropy on the few-layer graphene-/graphite-flake [164, 166]. On the other hand, the shear modulus is supposed to be isotropic for the few-layer graphene-/graphite-flake [142]. Starting with the analysis of the lateral frequency shift on the few-layer graphene-/graphite-flake area (Figure 7-21e, red) we observed that the values after rotation of the sample were approximately 40 Hz larger than prior to the rotation. This could on the one hand be interpreted as anisotropy, which contradicts that the lateral frequency shift could be used for the determination of shear moduli. On the other hand, it can be assumed that the shift originates from a small general offset of the resonance frequency while tracking with the PLL, which is an often observed scenario in FM-AFM. Due to the fact that it is impossible to find the origin in retrospect, we compared the difference between the average value determined on the Si/SiO₂-substrate and the graphene-/graphite-flake prior to and after rotation such as shown in Figure 7-22.

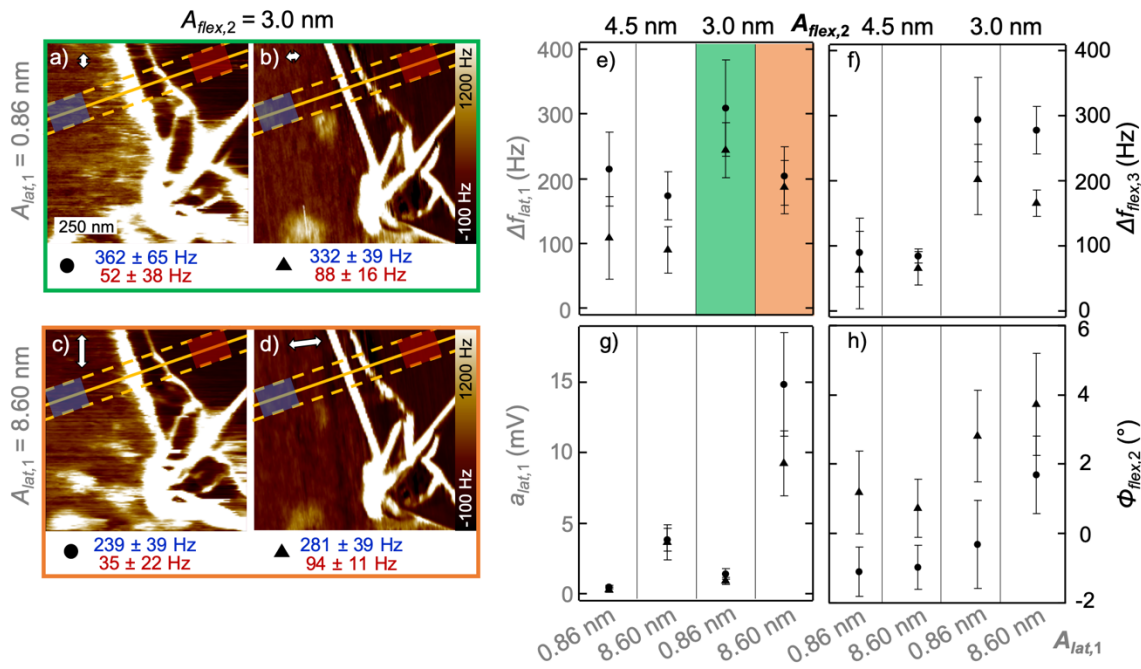


Figure 7-22: Analysis of the influence of different second flexural and first lateral amplitude setpoints on AFM images of a “cleaned” few-layer graphene-/graphite flake before and after rotation by 87°. Lateral frequency-shift images (a-d) were taken in the AMFlex2-OLTor1-FMLat1-FMFlex3 mode with $A_0(flex,2) = 6$ nm, $A_{flex,2} = 3.0$ nm, $A_{flex,3} = 0.08$ nm, $A_{lat,1} = 0.86$ nm (a, b) and $A_{lat,1} = 8.60$ nm (c, d) before (a, c) and after rotation of the flake by 87° (b, d). Weight cross-sections were drawn through the images to determine average values and standard deviation representative for the Si/SiO₂-substrate (blue) and the few-layer graphene-/graphite flake (red). The results originating from the images shown in a-d are summarized in the green (a, b) and orange highlighted areas (c, d) in e, where the difference between the averaged frequency-shift values on the Si/SiO₂-substrate and the few-layer graphene-/graphite flake were plotted as a function of two different second flexural amplitude setpoints (4.5 nm and 3 nm) and lateral amplitudes (0.86 nm and 8.60 nm) before (circles) and after rotation of the flake by 87° (triangles). The diagrams in f, g and h show the data resulting from the analysis of the third flexural frequency-shift, the lateral drive amplitude and the second flexural phase, respectively.

From Figure 7-22e we found that the lateral frequency-shift differences between the substrate and the graphene-/graphite-flake was slightly larger prior to the rotation than afterwards. However, taking into account the comparably large error bars, the differences are only small and cannot reliably be interpreted as anisotropic behavior. This is corroborated by the observation that similar trends are visible in the third flexural frequency-shift differences (Figure 7-22f) between the graphene-/graphite flake and the Si/SiO₂-substrate where no anisotropic behavior was to be expected. Interestingly the difference in lateral drive amplitude (Figure 7-22g) between the graphene-/graphite flake and the Si/SiO₂-substrate was very small except for the large lateral amplitude and small second flexural eigenmode amplitude. This can

be interpreted as a strong indicator against the presence of friction anisotropy. From Figure 7-22h we observed, that the difference in second flexural phase between the graphene/graphite flake and the Si/SiO₂-substrate was approximately 2° larger after the rotation of the sample. Taking into account that the error bars are of similar size compared to the determined difference in phase between the different areas, this effect is also negligible.

7.3.9. Analysis of third flexural frequency-shift and second flexural phase images after plasma treatment, prior to and after rotation by approximately 90°

From the cross-sections in Figure 4-5f in the main text we observed a small offset of approximately 1.0 mV on average between the lateral drive amplitude values determined prior to and after rotation of the sample. However, due to the fact that to the best of our knowledge no friction anisotropy was observed to take place on SiO₂ we assume that the small difference between the lateral drive amplitudes prior to and after rotation of the sample can most probably be attributed to subtle differences of detection laser positioning on the cantilever originating from the sample rotation process rather than friction anisotropy. This was corroborated by analyzing the simultaneously acquired second flexural phase images by means of cross-sections prior to and after rotation of the sample such as shown in Figure 7-23, where equivalently to the lateral drive amplitude a small general offset (approximately 2.5°) between both images was observed, which is unlikely to originate from a frictional interaction due to the out-of-plane nature of the analyzed interaction.

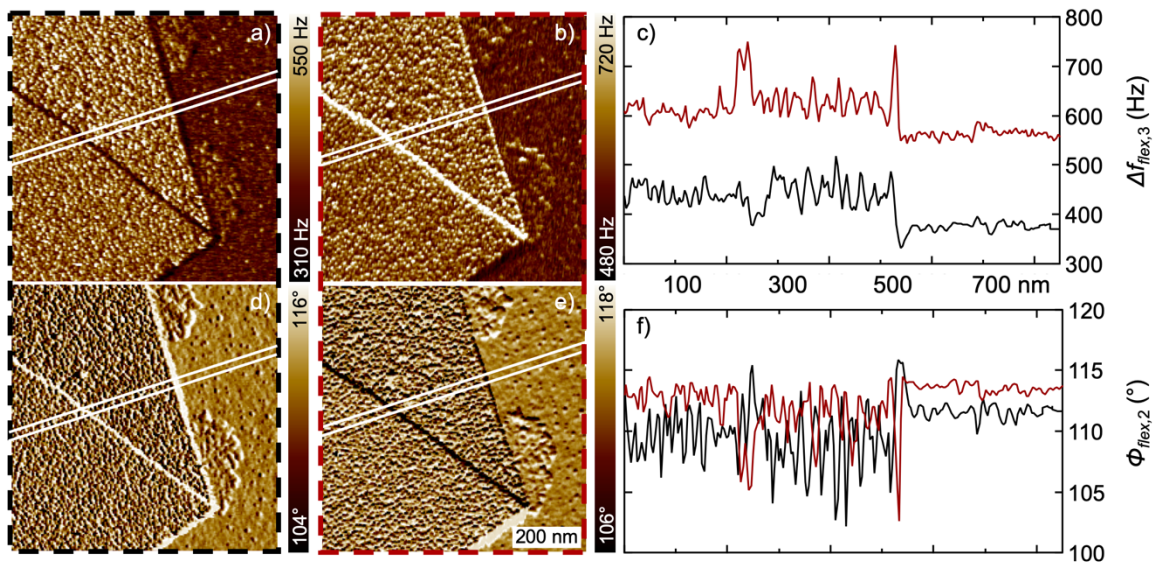


Figure 7-23: Third flexural frequency-shift (a, b) and second flexural phase images (d, e) of a few-layer graphene-/graphite-flake which was stored for 209 days and oxygen-plasma treated for 6 s afterwards. The black-framed images (a, d) show the sample prior to and the red-framed images (b, e) after rotation by approximately 90°. In c and f, the averaged cross-sections (four pixel) taken at the positions marked with black (a, d) and red lines (b, e) are shown. The general offsets between the cross-sections prior to and after rotation of the sample are most probably a consequence of the slightly changed imaging conditions originating from the rotation of the sample. $A_{0(flex,2)} = 675$ pm, $A_{flex,2} = 600$ pm, $A_{lat,1} = 883$ pm, $A_{flex,3} = 150$ pm.

7.4. Supplementary Information to Section 5

7.4.1. Oxygen-plasma treatment of HOPG

According to Zandiatashbar *et al.* [109], the HOPG sample was placed between two glass slides for plasma treatment, as schematically shown in Figure 7-24b. Raman spectra have been acquired prior to and after plasma treatment for different durations of gas discharge from both, the exposed and the shielded side. This procedure was consecutively repeated in time intervals of 15 s. The peak intensity ratios I_D/I_G (red) and I_{2D}/I_G (blue) were obtained from the average of 80 Raman spectra acquired at different positions of the sample using an integration time of 5 s and were plotted against the cumulative plasma-treatment time. The results are shown in Figure 7-24, where open circles correspond to the data from the exposed area of three different HOPG samples and filled circles to the data from the shielded area determined on one of the three HOPG samples.

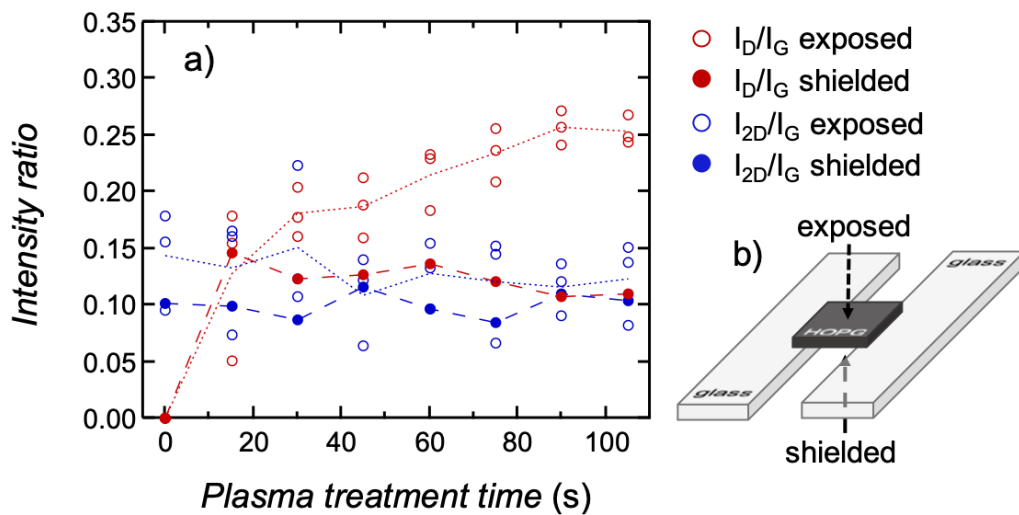


Figure 7-24: (a) Intensity ratios, derived from Raman spectroscopic measurements, as a function of the cumulative plasma treatment time for three HOPG samples (open circles). The intensity ratio between D- and G-peak is shown in red and between 2D- and G-peak in blue color. One HOPG sample was analyzed on both, the exposed (open circles) and the shielded area (filled circles), as schematically shown in (b).

From Figure 7-24a it becomes clear that, as it was expected, the intensity ratios I_{2D}/I_G (blue) are neither significantly influenced by the time nor by the type of plasma treatment, *i.e.* exposed (open circles) or shielded (filled circles). In contrast to that, it was shown that the ratio between the D- and the G-peak (red) depends on both, shielded/exposed plasma treatment and plasma-treatment time. Interestingly, after 15 s of plasma exposure, the ratio I_D/I_G (red) was similar for

the exposed (open circles) and the shielded (filled circles) side of the HOPG sample. However, the ratio between D- and G-peak clearly differed for larger cumulative plasma-treatment times depending on shielded or exposed configuration. For the exposed configuration we observed an asymptotical increase of I_D/I_G reaching the saturation after approximately 90 s at 0.25 ± 0.05 . For the shielded configuration the saturation was already reached after approximately 15 s at 0.13 ± 0.02 .

7.4.2. Adsorbate removal by oxygen-plasma treatment

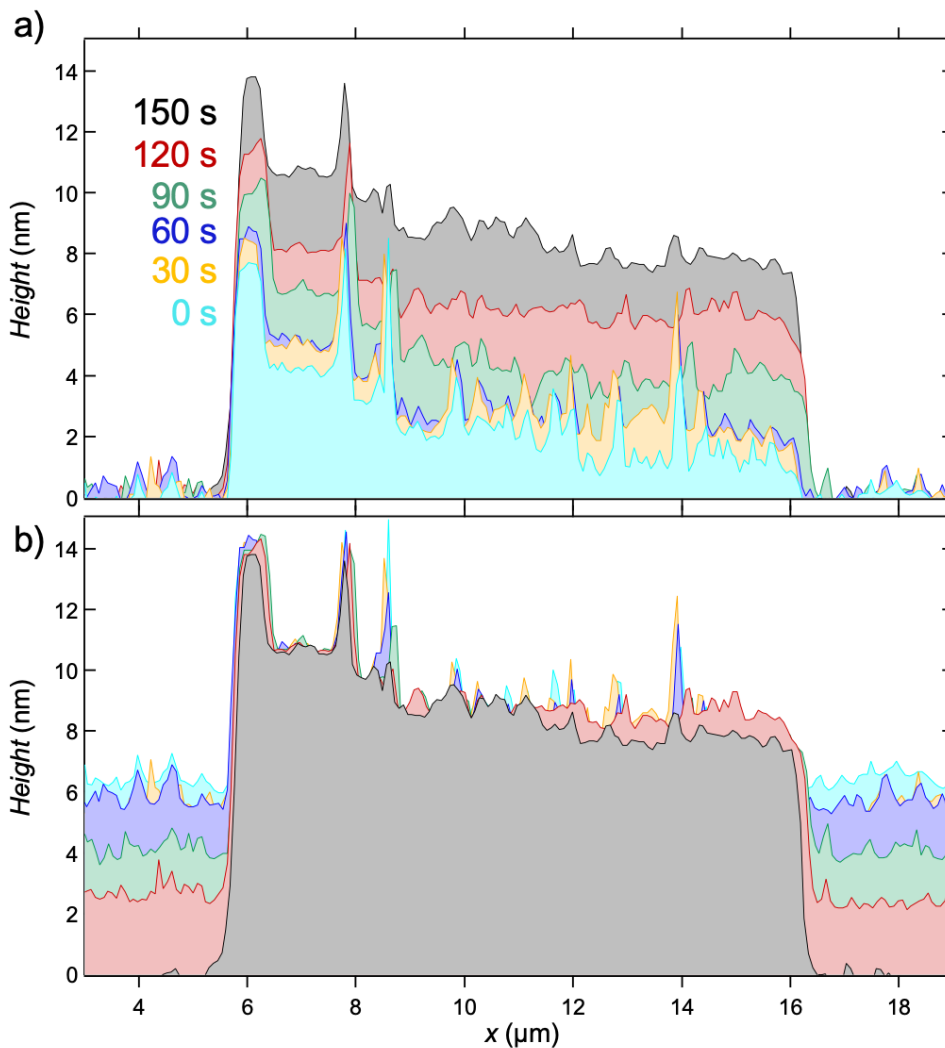


Figure 7-25: Adsorbate removal by oxygen-plasma treatment analyzed *via* cross-sections of AFM topography images. The sample was imaged prior to plasma treatment (light blue) and after 30 s (yellow), 60 s (blue), 90 s (green), 120 s (red), and 150 s (grey) of plasma treatment. For (a) the cross-sections aligned relative to the Si/SiO₂-substrate area and for (b) relative to the graphene/graphite sample area.

7.4.3. Raman intensity ratios as a function of graphene/graphite layer thickness

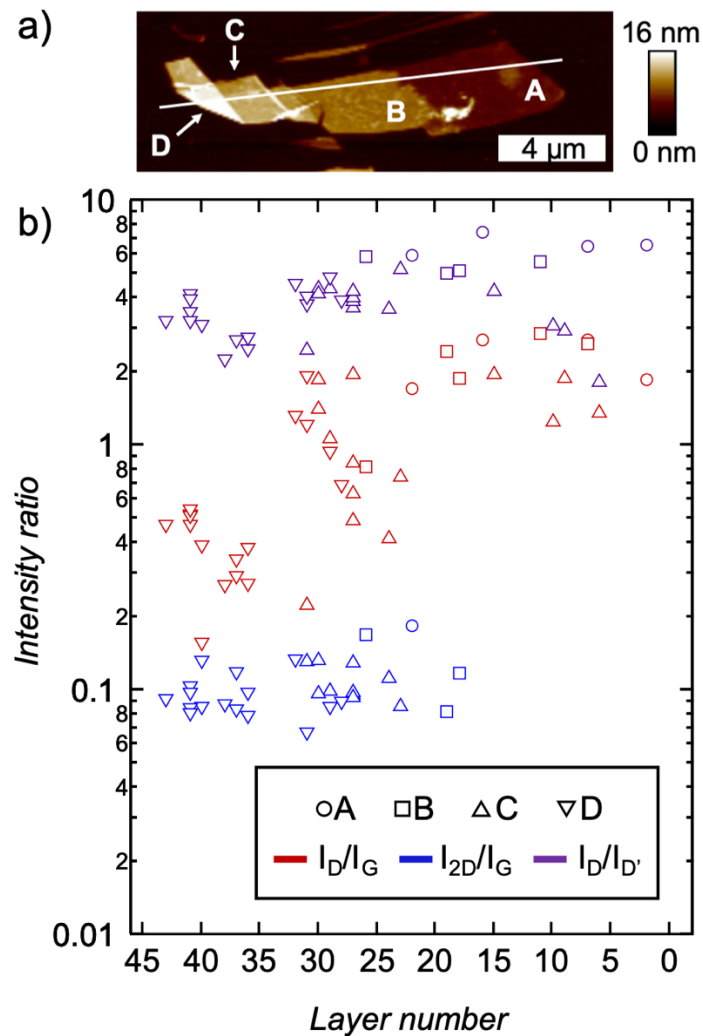


Figure 7-26: Raman intensity ratios measured within areas A (circle), B (square), C (triangle pointing up), and D (triangle pointing down), as marked in (a), as a function of layer number (b) resulting from stepwise oxygen-plasma treatment. The layer number was determined from cross-sections of AFM topography images, such as shown in Figure 5-1b (main text), where the height was divided by the graphene interlayer spacing (334.8 pm). The intensity ratio between D- and G-peak is shown in red, between 2D- and G-peak in blue and between D- and D'-peak in purple color.

7.4.4. Multifrequency AFM analysis of large-scale adsorbates and removal by oxygen-plasma treatment

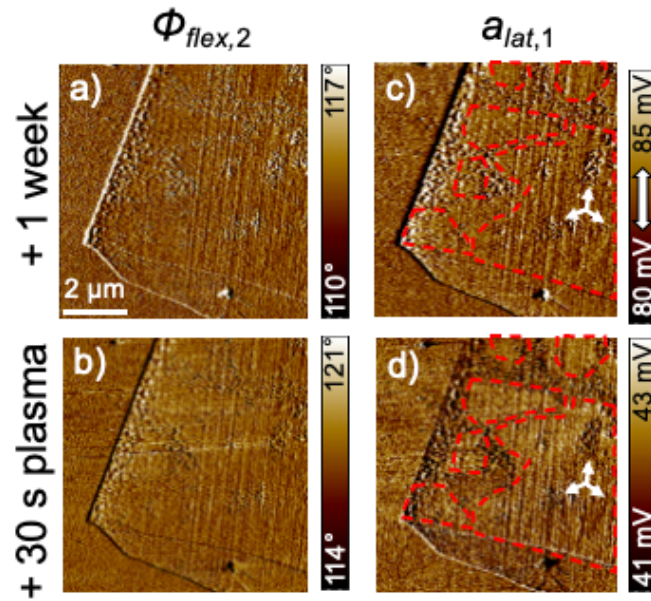


Figure 7-27: Adsorbate structure formation on a few-layer graphene/graphite flake analyzed after different durations of storage and oxygen-plasma treatment steps in AMFlex2-OLTor1-FMLat1 AFM mode. a–b: second flexural phase images and c–d: lateral drive amplitude images $A_0 (flex,2) = 675 \text{ nm}$, $A_{flex,2} = 600 \text{ nm}$ and $A_{lat,1} = 1.766 \text{ nm}$. The white arrow within the color bar (c) indicates the direction of lateral oscillation. These AFM images represent a continuation of the storage and oxygen-plasma treatment steps of the AFM images shown in Figure 5-3 of the main text.

7.4.5. Graphene height and layer number evolution upon storage and plasma treatment

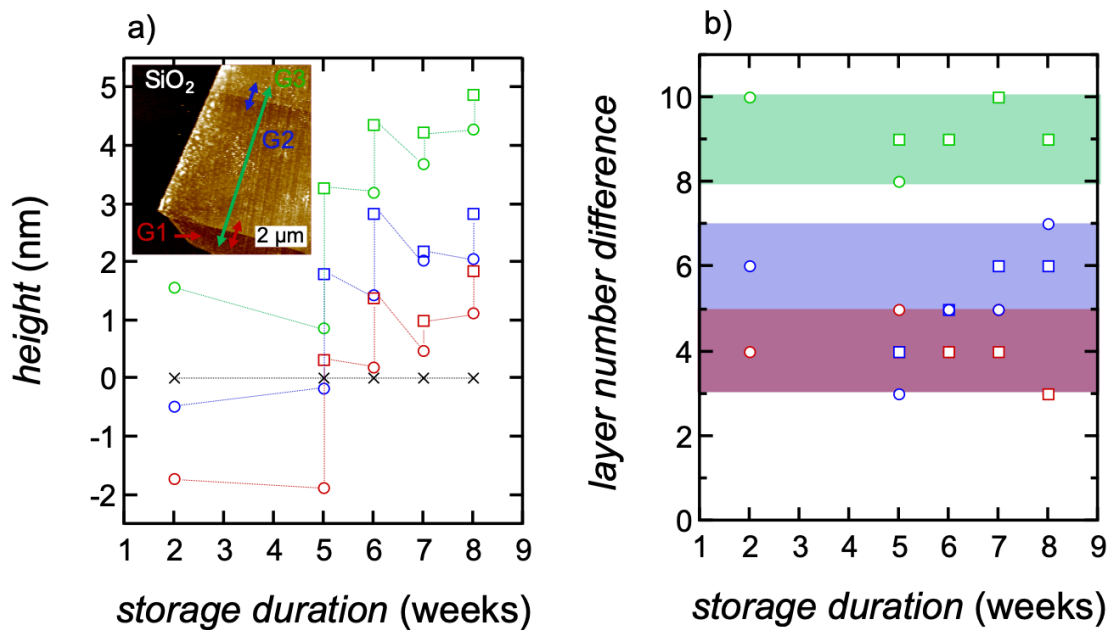


Figure 7-28: (a) Height and (b) graphene layer evolution of the investigated few-layer graphene/graphite flake upon storage in a polypropylene petri dish filled with laboratory air and plasma treatment extracted by using cross-sections in the recorded large-scale topographic images. The hollow circles represent the height values before and the hollow rectangles the values after the plasma treatment. The inset of Figure 7-28a shows an exemplary topography image of the examined few-layer graphene/graphite flake. The red colored double arrow indicates the layer number difference between G1 and G2, the green arrow the layer number difference between G1 and G3 and the blue one the layer number difference between G2 and G3.

7.4.6. Stripe-like and island structure formation on few-layer graphene/graphite

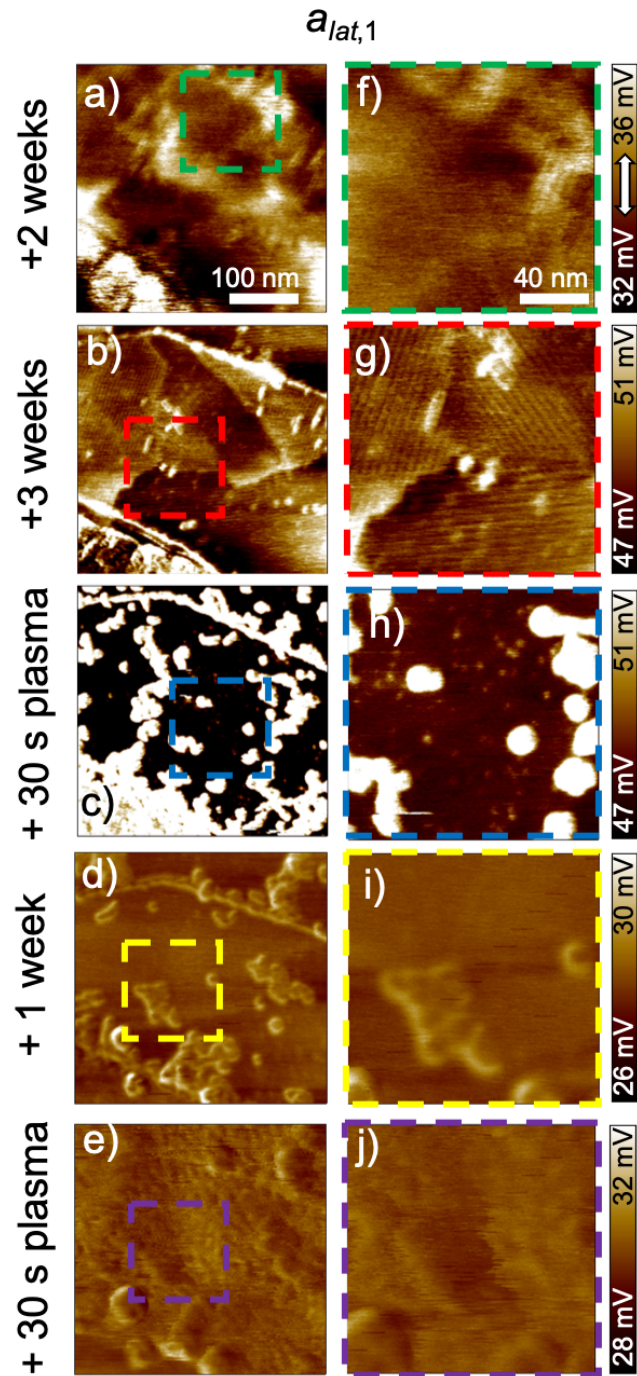


Figure 7-29: Stripe-like and island structure formation on a few-layer graphene/graphite flake analyzed based on the lateral drive amplitude images at two magnifications (a–e: $350 \times 350 \text{ nm}^2$ and f–j: $150 \times 150 \text{ nm}^2$) after different durations of storage and stepwise oxygen-plasma treatment in AMFlex2-OLTor1-FMLat1 AFM mode. $A_{0 \text{ (flex,2)}} = 675 \text{ nm}$, $A_{\text{flex,2}} = 600 \text{ nm}$ and $A_{\text{lat,1}} = 1.766 \text{ nm}$. The white arrow within the color bar (f) indicates the direction of lateral oscillation.

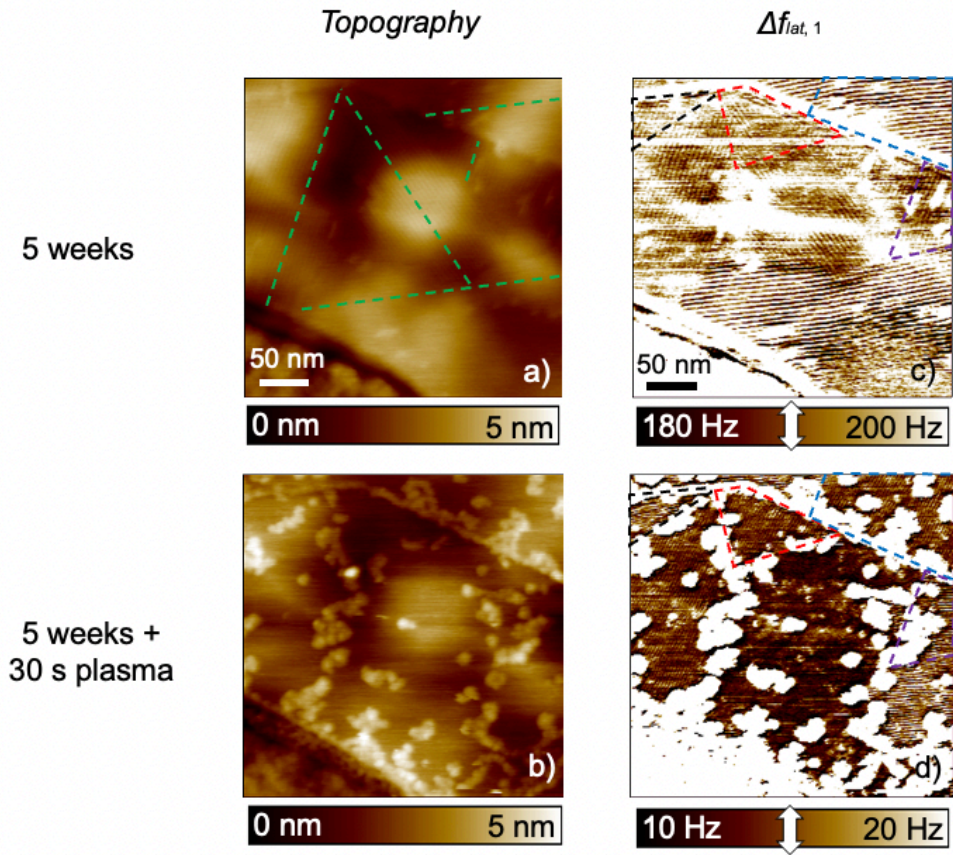


Figure 7-30: Stripe-like and island structure formation on a few-layer graphene/graphite flake analyzed based on the topographic and lateral frequency-shift images before (a, c) and after 30 s plasma treatment (b, d) in shielded configuration in AMFlex2-OLTor1-FMLat1 AFM mode. $A_0 (flex,2) = 675$ nm, $A_{flex,2} = 600$ nm and $A_{lat,1} = 1.766$ nm. White arrows within the color bars indicate the direction of lateral oscillation. The green dashed lines visible in the topographic image recorded before the plasma treatment in (a) are a guide to the eye to highlight the different orientations of the stripe-like pattern. The different colored polygons observable in the lateral frequency-shift images in (c) and (d) indicate the change in the orientation of the stripe pattern caused by the oxygen-plasma treatment.

8. List of Figures

| | |
|--|----|
| Figure 1-1: Schematic drawing of the crystallographic structure of graphite. a) Top view, b) side view. | 4 |
| Figure 1-2: Scheme of setup for static AFM modes. a) Contact mode AFM and b) lateral force microscopy (LFM) or friction force microscopy (FFM). | 7 |
| Figure 1-3: Scheme of setup for dynamic AFM modes with photothermal excitation. a) amplitude-modulated (AM) AFM and b) frequency-modulated (FM) AFM. | 8 |
| Figure 1-4: Experimental (a) amplitude A (black lines) and minimum distance of approach d_{min} (grey lines) and (b) normalized tip-sample force F_{ts}^* (dashed blue lines) and energy dissipation E_{dis}^* (black lines) as a function of cantilever separation z_c and distance d , respectively. (c)–(h) Experimental examples of images of dsDNA on mica obtained in the NC and SASS modes, respectively. Higher resolution is obtained in the SASS mode provided the tip is sharp enough. Here $R < 5$ nm. (Reprinted from ref. [69], © 2013, with permission from AIP Publishing LLC.) | 14 |
| Figure 1-5: Illustration of a cantilever oscillating (a) above the hydration layer with amplitudes (A_{sp}) comparable to the free amplitude A_0 (standard attractive regime imaging), (b) with amplitudes A smaller than A_0 when the tip is permanently immersed in the hydration layer (SASS regime), (c) above the hydration layer with small amplitudes (A_{sp}) much smaller than A_0 (Small amplitude attractive imaging). The inset in (d) is provided to illustrate that in the SASS regime the tip is immersed under the water layer where there might be structure and order. Airborne water molecules are also depicted for illustrative purposes. (Reprinted from ref. [70], https://doi.org/10.3390/molecules26237083 , © 2021 by the authors. Licensee MDPI, Basel, Switzerland. Figure caption was slightly adapted.) | 14 |
| Figure 1-6: Schematic setup of bimodal AM-FM-AFM including a lock-in amplifier for the topography feedback based on amplitude modulation of the first eigenmode and a phase-locked-loop (PLL) for frequency modulation of the second eigenmode oscillation. | 16 |
| Figure 1-7: Fractional operators of $(0.1^4/x^6 - 1/x^2)$. (a) The function, half-derivative and derivative are plotted. (b) The function, half-integral and integral are plotted. (Reprinted from ref. [7], https://doi.org/10.3762/bjnano.3.22 , © 2012 Herruzo and Garcia; licensee Beilstein-Institut.) | 17 |
| Figure 1-8: Effect of a tip on the fundamental lateral resonance of a cantilever with a rectangular cross section. (a) Finite element analysis (FEA) simulation for a cantilever with a tip height of 16 μm . The cantilever thickness is 1 μm . The colored part indicates the cantilever at the maximum movement of an oscillation; the uncolored part indicates the cantilever in the equilibrium position. The scale bar indicates the deflection of the cantilever in the z -direction. (b) Schematic of the lateral resonance for a cantilever with a tip. (c) FEA simulation for a tipless cantilever. The cantilever thickness is 1 μm . (d) Schematic of the lateral resonance for a tipless cantilever. (Reprinted from ref. [89], © 2016, with permission from Nanoscale.) | 18 |
| Figure 1-9: Schematic setup of a low-pressure plasma chamber. | 19 |
| Figure 1-10: Schematic energy diagram comparing Rayleigh and Raman scattering. | 20 |

| | |
|--|----|
| Figure 1-11: Raman spectra of 1-5 layers thick graphene and graphite samples acquired with a laser wavelength of 532 nm. (Reprinted from ref. [99], https://doi.org/10.1186/1556-276X-8-335 , © 2013. Figure caption was adapted.)..... | 21 |
| Figure 1-12: Phonon dispersion plot of a single-layer graphene, calculated (lines) [100] and experimental (points) [101]. Different experimental points correspond to the different branches, where the filled triangles correspond to the longitudinal optical (LO) branch, open squares to the in-plane transverse optical (iTO) branch and the filled dots to the longitudinal acoustic (LA) branch. (Reprinted from ref. [102], https://doi.org/10.1007/s10853-010-4673-3 , © 2010. Figure caption was slightly adapted.)..... | 22 |
| Figure 1-13: Schematic drawing of graphene in (a) real space and (b) reciprocal space. The shaded areas mark the unit cell in (a) and the first Brillouin zone in (b). The vibration of carbon atoms in (c) the A_{1g} D-mode or “breathing” mode and in d) the E_{2g} G-mode are shown [102, 103]..... | 22 |
| Figure 2-1: Schematic of AMFlex2-FMTor1-FMFlex3 mode for atomic-resolution imaging of HOPG. Out-of-plane forces can be determined from the third-eigenmode flexural frequency shift, whereas in-plane forces can be calculated from the torsional-eigenmode frequency shift. | 28 |
| Figure 2-2: AFM images of HOPG taken in AMFlex2-FMTor1-FMFlex3 mode: a) topography image, and b) torsional and c) flexural frequency-shift images. Imaging parameters: $A_{0(flex,2)} = 770$ pm, $A_{flex,2} = 100$ pm, $A_{tor} = 80$ pm, $A_{flex,3} = 220$ pm..... | 28 |
| Figure 2-3: Dynamic spectroscopy at alleged carbon-atom location of HOPG in air under ambient conditions. a) Amplitude, phase, mean deflection, and flexural and torsional frequency shifts versus tip-sample distance d . The approach curves are shown in black/red (flexural/torsional), the retract curves are shown in gray, and the solid lines represent the fitted frequency-shift data of the approach curves. b) Scheme of zigzag and armchair orientation of carbon hexagons. Here, the torsional oscillation direction (red double-headed arrow) is along the zigzag direction of the hexagonal carbon structure. c) Long-range interaction F_{lr} between tip and sample calculated from mean deflection and force deconvolution from fitted flexural and torsional frequency-shift data (solid lines in (a)) using the Sader method. The setpoint amplitude at which images were taken is marked by the black vertical lines. Some characteristic regions of the approach curves are colored gray, green, and orange and marked by double-headed arrows. The dashed vertical lines mark the starts of the characteristic areas. | 30 |
| Figure 2-4: Influence of torsional and third-eigenmode flexural-oscillation amplitudes on observed frequency shifts at a second-flexural-eigenmode amplitude setpoint of 110 pm. a) Histograms of third-eigenmode flexural- frequency-shift images for different third-eigenmode flexural amplitudes. b) Histograms of torsional-frequency-shift images for different torsional amplitudes. Third-eigenmode flexural and torsional frequency shifts at maximum counts (open circles) and at full width at half-maximum (FWHM) (dashed lines) as a function of c) third-flexural-eigenmode amplitude at constant torsional-eigenmode amplitude of 110 pm and d) torsional-eigenmode amplitude at constant third-flexural-eigenmode amplitude of 145 pm..... | 38 |

Figure 2-5: a, b, e, f) Forces and c, d, g, h) frequency-shift validation data determined from frequency-shift images using the Fourier method without offset correction. a, c, e, g) Torsional data were calculated using the monomodal Fourier method, b, d, f, h) flexural data were calculated using the bimodal Fourier method. Red: scan angle = 0° , $A_{tor} = 80$ pm, $A_{flex,2} = 100$ pm, $A_{0(flex,2)} = 770$ pm, $A_{flex,3} = 220$ pm. Blue: scan angle = 90° , $A_{tor} = 110$ pm, $A_{flex,2} = 90$ pm, $A_{0(flex,2)} = 770$ pm, and $A_{flex,3} = 150$ pm.41

Figure 2-6: Cross-sectional profiles through force and frequency-shift images of HOPG along the green, pink, and blue lines in Figure 2-5. Profiles and axis labels are shown in gray for the frequency shift, black for the flexural forces, and red for the torsional forces. The vertical dashed lines mark the positions of characteristic local extrema of the profiles, following the same color code. The torsional oscillation was aligned approximately along the zigzag (resp. armchair) direction of the carbon hexagons for the cross sections shown within the red frame a–c) (resp. blue frame d–f)). The cross sections in (a), (d), and (e) are in the zigzag direction of the carbon hexagons, and those in (b), (c), and (e) are in the armchair direction. The cross sections marked a, d) green and c, f) blue cut the center of the hollow side, whereas those marked b,e) pink are offset from the center of the hollow side by the particular torsional amplitude values to enable analysis of force extrema (black and red arrows).....43

Figure 3-1: Schematic illustration depicting the setup of the AMFlex2-OLTor1-FMLat1-FMFlex3 mode. Topographical feedback is driven at the coupled resonance frequency of the second flexural and the first torsional eigenmode using the flexural component for amplitude modulation. The first-torsional-eigenmode amplitude and phase are recorded at the same frequency in an open-loop configuration. Optionally, the setup can be expanded by one or two phase-locked loops, tracking the phase at resonance of the first lateral and/or the third flexural eigenmode which allowed us to quantify forces in in-plane and/or out-of-plane direction from the respective frequency-shift data. Dissipative tip-sample interactions can be analyzed from the drive amplitudes ($a_{lat,1}$, $a_{flex,3}$) and the respective phase shifts ($\Phi_{flex,2}$, $\Phi_{tor,1}$). The cantilever dimension was substantially reduced for simplicity.53

Figure 3-2: Imaging and spectroscopy on HOPG at a covered step edge in AMFlex2-OLTor1-FMLat1 mode with 863 pm lateral-eigenmode-amplitude setpoint. (a–e) Schemes of the tip trajectory for the coupled second flexural and first torsional cantilever oscillation for decreasing second flexural-eigenmode-amplitude setpoints $A_{flex,2}$. The setpoints of $A_{flex,2}$ are listed in the first, the corresponding setpoints of the first-torsional-eigenmode amplitude $A_{tor,1}$ in the second row and the approximate z -sensor position at the third row. The values in brackets represent the percentages of the setpoints from the free amplitudes $A_{0(flex,2)}$ and $A_{0(tor,1)}$. (f) Second flexural-, (l) first torsional-eigenmode amplitude $A_{tor,1}$ and (r) first lateral frequency shift $\Delta f_{lat,1}$ vs. z -sensor position, where the crossed circles mark the positions at which the images were taken. (g–k) Height, (m–q) first torsional-eigenmode amplitude error $\Delta A_{tor,1}$ and (s–w) $\Delta f_{lat,1}$ images at decreasing $A_{flex,2}$. Note, that $\Phi_{tor,1}$ was assumed to be 90° for the calculation of the tip-trajectories shown in (a–e).....55

Figure 3-3: Influence of the lateral- and the torsional-amplitude setpoints on the frequency shifts in AMFlex2-FMLat1-FMFlex3 mode and in AMFlex2-FMTor1-FMFlex3 mode respectively. Frequency-shift images are shown exemplarily taken at

- $A_{lat,1} = 518$ pm in (a), $A_{lat,1} = 3451$ pm in (e) and $A_{tor,1} = 158$ pm in (d), $A_{tor,1} = 628$ pm in (h). Histograms of lateral (b) and torsional frequency-shift images (c) at different lateral-/torsional-amplitude setpoints. Third-eigenmode flexural and lateral (f)/torsional (g) frequency shifts at maximum counts (open circles) and at FWHM (dotted lines) as a function of the lateral-/torsional-amplitude setpoints at a constant third flexural-eigenmode amplitude of 145 pm and a constant second flexural-eigenmode amplitude of 110 pm.....58
- Figure 3-4: Extract of the calculated tip-trajectory of a cantilever oscillating in the AMFlex2-FMLat1-FMFlex3 mode (a, b) or in the AMFlex2-FMTor1-FMFlex3 mode (c, d) with $A_{flex,2} = 110$ pm and $A_{flex,3} = 145$ pm. The trajectories are shown for two different torsional- and lateral-oscillation eigenmodes: (a) $A_{lat,1} = 518$ pm, (b) $A_{lat,1} = 863$ pm, (c) $A_{tor,1} = 186$ pm and (d) $A_{tor,1} = 742$ pm. Additionally, the effective amplitudes ($A_{lat,1}^{(eff)}$ and $A_{tor,1}^{(eff)}$) as well as the determined corrugation amplitudes A_{C-H} are shown. The minimum possible distance between two hydrophobic surfaces (tip and sample) of 300 pm [158] was neglected for the schematic drawing to improve the comprehensibility.....59
- Figure 3-5: Scheme of the interaction between tip and HOPG surface for (a) a shearing interaction resulting from imaging in the AMFlex2-FMLat1-FMFlex3 mode with $A_{lat,1} = 518$ pm (F_s : shear force) and (d) a frictional interaction resulting from imaging in the AMFlex2-FMTor1-FMFlex3 mode with $A_{tor,1} = 158$ pm, where F_N is the normal force acting perpendicular to the surface, F_{push} is the force originating from the movement of the tip in the direction of the in-plane oscillation and F_f is the frictional force counteracting F_{push} ($A_{flex,2} = 110$ pm and $A_{flex,3} = 145$ pm). (b, e) lateral and torsional frequency-shift images. (c, f) corresponding lateral and torsional force images calculated by the Fourier method and using the effective lateral/torsional amplitudes $A_{lat,1}^{(eff)} = 123$ pm and $A_{tor,1}^{(eff)} = 79$ pm.....62
- Figure 4-1: Large- and small-scale adsorbate formation on a few layer graphene-/graphite-flake analyzed at different magnifications in AMFlex2-OLTor1-FMLat1-FMFlex3 mode in out-of-plane (a-h, q-t) and in-plane direction (i-p) after 14 days of storage under ambient conditions in air. Topography (a-d), second flexural phase (e-h), lateral drive-amplitude (i-l), lateral frequency-shift (m-p) and third flexural frequency-shift images (q-t). $A_0^{(flex,2)} = 675$ pm, $A_{flex,2} = 600$ pm, $A_{lat,1} = 1.766$ nm, $A_{flex,3} = 75$ pm. White arrows within the color bars indicate the direction of lateral oscillation. White arrows within the frequency-shift images (m-t) point out regions where different adsorbates numerated from #1 to #5 are assumed. Yellow arrows in (a) exemplarily mark unordered large-scale adsorbates and the pink arrows in the second column highlight the hillock observed on the graphene-portion of the flake.75
- Figure 4-2: Scheme of stable adsorption configurations of different polycyclic aromatic hydrocarbons (PAH) on graphene in a) “top”-configuration (benzo[k]fluoranthene) and b, c) “bridge”-configuration (benzo[b]fluoranthene, fluoranthene) according to Li *et al.* [193].....80
- Figure 4-3: Adsorbate formation on the same few-layer graphene-/graphite-flake as shown in Figure 4-1 analyzed by means of the lateral drive amplitude acquired in the AMFlex2-OLTor1-FMLat1-FMFlex3 mode upon storage for 14 days (a), 87 days (b) and 95 days & heating for 5 min at 100 °C (c), 209 days (d) and 209 days & 6 s

oxygen-plasma treatment (e). $A_{0(flex,2)} = 675$ pm, $A_{flex,2} = 600$ pm, (a–c): $A_{lat,1} = 1.766$ nm, $A_{flex,3} = 75$ pm, (d, e): $A_{lat,1} = 833$ pm, $A_{flex,3} = 150$ pm. The white arrows within the color bar indicate the direction of the in-plane cantilever oscillation. Pink and blue arrows point out positions where adsorbates were formed on the Si/SiO₂-substrate. The green arrow exemplarily indicates the position of a small-scale ordered stripe domain.....82

Figure 4-4: Lateral frequency-shift images of a few layer graphene-/graphite-flake taken in the AMFlex2-OLTor1-FMLat1-FMFlex3 mode before (a–d) and after rotation by approximately 90° (e–h). The areas framed in a and h by the yellow, green and red dotted squares are shown enlarged in b and e ($1 \times 1 \mu\text{m}^2$), c and f ($1.4 \times 1.4 \mu\text{m}^2$) and d and g ($1.9 \times 1.9 \mu\text{m}^2$), respectively. $A_{0(flex,2)} = 675$ pm, $A_{flex,2} = 600$ pm, $A_{lat,1} = 1.766$ nm, $A_{flex,3} = 75$ pm. Arrows point out regions where the color contrast was inverted after sample rotation by approximately 90°.85

Figure 4-5: Lateral frequency-shift (a, b) and drive-amplitude images (d, e) of a few-layer graphene-/graphite-flake which was stored for 209 days and oxygen-plasma treated for 6 s afterwards. The black-framed images (a, d) show the sample prior to and the red-framed images (b, e) after rotation by approximately 90°. The lateral tip oscillation directions with respect to the sample orientation are indicated by the white arrows in a and b. In c and f, the averaged cross-sections (four pixel) taken at the positions marked with white lines (a, b, d, e) are shown. $A_{0(flex,2)} = 675$ pm, $A_{flex,2} = 600$ pm, $A_{lat,1} = 883$ pm, $A_{flex,3} = 150$ pm.87

Figure 5-1: AFM topography imaging and analysis of a few-layer graphene-/graphite-sample treated by oxygen plasma. AFM topography images (a) and cross-sections (b) of a few-layer graphene-/graphite-flake before (light blue) and after 2.5 min (grey), 4.5 min (red), 6.5 min (blue), 8.5 min (green), 10.5 min (pink), 24.5 min (purple), and 36.5 min (orange) of oxygen-plasma treatment in a shielded configuration (inset in b). (c) Number of carbon layers of the different areas A (red circle), B (blue square), C (black triangle), and D (green triangle), as marked in (b), as a function of plasma-treatment time.....94

Figure 5-2: Raman intensity ratios measured within areas A (circle), B (square), C (triangle pointing up), and D (triangle pointing down), as marked in (a), as a function of oxygen-plasma treatment time (b). The intensity ratio between the D- and G-peak is shown in red, between the 2D- and G-peak in blue and between the D- and D'-peak in purple color. Zoom-in images of the grey marked area in (b) for the intensity ratios D/G and 2D/G are shown in (c) and (d), respectively. For comparison, the intensity ratios determined on highly oriented pyrolytic graphite (HOPG) for stepwise oxygen-plasma treatment in the shielded configuration are added to (c) and (d) by means of filled hexagons.96

Figure 5-3: Adsorbate formation on a few-layer graphene-/graphite-flake analyzed by means of second flexural phase (a–g) and lateral drive-amplitude (h–n) after different durations of storage and oxygen-plasma treatment and in AMFlex2-OLTor1-FMLat1 AFM mode. $A_{0(flex,2)} = 675$ nm, $A_{flex,2} = 600$ nm, and $A_{lat,1} = 1.766$ nm. The few-layer graphene-/graphite-flake consists of three areas (G1, G2, and G3, as marked in (a)) with different numbers of graphene layers, where the layer number increases from G1 to G3. The white arrow within the color bar (h) indicates the

direction of lateral oscillation. Dashed lines (blue, green, pink, and red) highlight the shape of the different domains found on the few-layer graphene-/graphite-flake surface. Large-scale islands are enclosed by white dashed lines in the flexural phase images (a–g). The yellow square in (g) marks the area ($350 \times 350 \text{ nm}^2$) where the high-resolution images shown in Figure 5-4 were taken.....99

Figure 5-4: Stripe-like and island structure formation on a few-layer graphene-/graphite-flake analyzed using the second flexural phase images at two magnifications (a–e: $350 \times 350 \text{ nm}^2$ and f–j: $150 \times 150 \text{ nm}^2$). Analysis took place after different durations of storage and stepwise oxygen-plasma treatment measured by the AMFlex2-OLTor1-FMLat1 AFM mode. $A_{0 \text{ (flex,2)}} = 675 \text{ nm}$, $A_{\text{flex,2}} = 600 \text{ nm}$, and $A_{\text{lat,1}} = 1.766 \text{ nm}$103

Figure 5-5: Scheme for oxygen-plasma induced water island formation on graphitic surfaces based on the theories of Paredes *et al.* [229] and Li *et al.* [233].....106

Figure 7-1: Inverted AFM images of HOPG taken in AMFlex2-FMTor1-FMFlex3 mode: a) topography image, and b) torsional and c) flexural frequency-shift images. Imaging parameters: $A_{0 \text{ (flex,2)}} = 770 \text{ pm}$, $A_{\text{flex,2}} = 100 \text{ pm}$, $A_{\text{tor}} = 80 \text{ pm}$, $A_{\text{flex,3}} = 220 \text{ pm}$113

Figure 7-2: Comparison of mean deflection for different eigenmode oscillations as well as the static case on HOPG upon approach. a) Scheme for determining tip–sample distance from *z*-sensor position, tip height, and mean deflection (purple). b) Plot of mean deflection vs. tip–sample distance for static case (black), first flexural eigenmode (red), second flexural eigenmode (green), and third flexural eigenmode (blue).116

Figure 7-3: Comparison of hysteretic behavior upon approach and retract for silicon and HOPG with a DLC AFM tip. a) Deflection vs. tip–sample distance on silicon (green) and HOPG (black). b) and c) Scheme of tip–sample interactions on silicon and HOPG, respectively.....117

Figure 7-4: Comparison of topography, mean-deflection, and third-eigenmode frequency-shift images and cross sections for three different third-flexural-eigenmode amplitude setpoints. a), d), g) Topography images, b), e), h) cross sections drawn along the pink lines, and c), f), i) third-eigenmode frequency-shift images at $A_{\text{flex,3}} = 364 \text{ pm}$ (a–c), $A_{\text{flex,3}} = 436 \text{ pm}$ (d–f), and $A_{\text{flex,3}} = 509 \text{ pm}$ (g–h). Further imaging parameters: $A_{\text{flex,2}} = 68 \text{ pm}$, $A_{\text{tor}} = 0 \text{ pm}$119

Figure 7-5: Influence of second-eigenmode flexural-oscillation amplitude setpoint on the observed frequency shifts. Histograms of a) third-eigenmode flexural and b) torsional frequency-shift images for different second-eigenmode flexural-amplitude setpoints. Third-eigenmode flexural and torsional frequency shifts at maximum counts (open circles) and at FWHM (dotted lines) as a function of the second-flexural-eigenmode amplitude setpoint at a constant torsional-eigenmode amplitude of 110 pm and a constant flexural-eigenmode amplitude of 145 pm.....121

Figure 7-6: Original frequency-shift images (a, b, e, f) and frequency-shift validation images (c, d, g, h) determined by using the Fourier method. The torsional validation data (a, c, e, g) were calculated using the monomodal Fourier method, and the flexural validation data (b, d, f, h) were calculated using the bimodal Fourier method. Red: scan angle = 0° , $A_{\text{tor}} = 80 \text{ pm}$, $A_{\text{flex,2}} = 100 \text{ pm}$, $A_{0 \text{ (flex,2)}} = 770 \text{ pm}$, $A_{\text{flex,3}} =$

220 pm. Blue: scan angle = 90° , $A_{tor} = 110$ pm, $A_{flex,2} = 90$ pm, $A_{0(flex,2)} = 770$ pm, $A_{flex,3} = 150$ pm.124

Figure 7-7: Cross-sectional profiles drawn through the original and validation frequency-shift images of HOPG along the pink, blue, and green lines in Figure 7-6. Profiles and axis labels are shown in gray for the original frequency-shift data, black for the flexural validation frequency-shift data, and red for the torsional validation frequency-shift data. The torsional oscillation was aligned approximately along the zigzag (resp. armchair) direction of the carbon hexagons for the cross sections shown in the red frame (a–c) (resp. blue frame (d–f)). The cross sections in a), d), and e) were drawn along the zigzag direction and in b), c), and e) along the armchair direction of the carbon hexagons. The a), d) green and c), f) blue marked cross sections cut the center of the hollow side, whereas the b), e) pink marked cross sections are offset from the center of the hollow side by the particular torsional amplitude values.....125

Figure 7-8: Illustration of a torsional (a, c) and a lateral eigenmode oscillation (b, d) for tip-less (a, b) and tip-containing cantilevers (c, d) and scheme of the detection (red) and photothermal excitation laser (blue) (e). Due to the rotational motion induced by the torsional eigenmode oscillation, the amplitude can be optically detected on a segmented photodiode for tip-less (a) and tip-containing cantilevers (c) in the same way. On the other hand, it is not possible to detect the lateral oscillation of a tip-less cantilever (b) by means of the standard optical beam detection technique. Nevertheless, as explained by Ding *et al.* [89], due to the small torsional motion induced by the tip attached to the cantilever, the lateral oscillation can be detected using the standard optical beam detection technique. To determine the optical lever sensitivity, additional considerations are required as discussed in detail in Section 7.2.4 “Calibration of lateral oscillation amplitude inverse optical lever sensitivity” of this Supplementary Information.....126

Figure 7-9: Tip-trajectories calculated using equations (7-12) and (7-13) for a “coupled” cantilever (resonance frequencies listed in Table 3-1 of the main text (Section 3.4)) oscillating in the AMFlex2-OLTor1-FMLat1 mode with $A_{flex,2} = 700$ pm, $A_{tor,1} = 1232$ pm and $A_{lat,1} = 863$ pm for different torsional phases.127

Figure 7-10: Cross sections through height images of HOPG at two different z-sensor positions and schemes of the alleged tip-sample interaction at the step edge in the attractive and the repulsive regime. The insets show the height images (retrace) of Figure 3-2j at $z \approx 3.1$ nm (top) and Figure 3-2k at $z \approx 3.7$ nm (bottom). The position of the cross sections is marked in blue, scale bar: 1 nm. The thin black cross sections are drawn through the trace images (not shown) and the thicker cross sections through the retrace images at the same position. Scale bar: 400 pm.....128

Figure 7-11: Calibration of lateral-oscillation-eigenmode amplitude at a graphene wrinkle on HOPG. The solid lines in a) and f) show the height and the lateral frequency shift for different lateral-eigenmode setpoints along the averaged cross sections (20 pixel) marked in b-e) and g-j). The images were taken in the AMFlex2-OLTor1-FMLat1 mode with a free second flexural-eigenmode amplitude of 765 pm and a setpoint of 238 pm. The scan angle was 90° so that both, the fast scan direction and the direction of the lateral oscillation were oriented perpendicular to the wrinkle. The dotted

black/blue/red lines in a) and f) represent the orange curve smoothed over 23/45/89 pixel and multiplication (height)/division ($\Delta f_{lat,1}$) by the weighing factors 1.25/1.85/2.80 which we introduced in order to optimize the fit..... 130

Figure 7-12: Vertical and lateral tip position estimated from dynamic spectroscopy (a-c) and contact mode AFM (d-f), respectively. Second flexural phase (a), amplitude (b) and mean vertical deflection (c) as a function of the vertical tip position (z-position corrected for vertical deflection). The dotted line at approximately -85 pm indicates the vertical tip position, where the second flexural eigenmode setpoint of 110 pm was reached. This corroborates the estimation of an indentation depth of 14-85 pm while imaging an HOPG surface. Nevertheless, it was not possible to determine differences in indentation depth when imaging the mean vertical deflection while varying the lateral or torsional oscillation amplitude. From a and b it becomes clear that the second flexural phase and amplitude form plateaus close to the HOPG surface. We assume that this is more likely a consequence of oscillating inside natural water layers covering the HOPG surface rather than a permanent contact between tip and sample. This would imply imaging in contact resonance mode where the frequency shift is expected to be much larger compared to the values observed in our study. In d and e, the trace and retrace lateral deflection images of an HOPG surface analyzed with friction force microscopy are shown, respectively. It needs to be mentioned that the vertical deflection setpoint (1100 nN) was much larger compared to the mean vertical deflection values reached in dynamic spectroscopy because no stable contact was achieved using smaller vertical deflection values. The horizontal lines indicate the positions at which the cross sections shown in f were taken, where the abscissa was selected as the lateral tip position, calculated from the x-position of the cross section corrected for the lateral tip-deflection. The calibration of the in-plane static sensitivity was performed on a silicon substrate, following the protocol of Dietz [88]. From the graph in f, on the one hand, the typical stick-slip motion (gray-white) can be observed. On the other hand, it becomes evident, that the tip-position was not completely fixed within the gray marked area, but that the tip showed an overall movement of around 150 pm. This observation can be interpreted as a corroboration of the observations from Figure 3-4, that while imaging, a local relative displacement of around 150 pm between two carbon layers could be induced..... 132

Figure 7-13: Comparison of the tip-trajectory resulting from (a) the AMFlex2-FMLat1-FMFlex3 mode and (b) the AMFlex2-FMTor1-FMFlex3 with $A_{flex,2} = 110$ pm, $A_{flex,3} = 145$ pm and $A_{lat,1} = A_{tor,1} = 328$ pm. 133

Figure 7-14: Temperature and relative humidity measured during storage of the few-layer graphene-/graphite-sample under laboratory air conditions in a polypropylene box.... 135

Figure 7-15: Wrinkle formation on a few-layer graphene-/graphite-flake while imaging in AMFlex2-OLTor1-FMLat1-FMFlex3 mode. Topography (a-d), lateral drive amplitude (e-h), lateral frequency shift images (i-l) taken at $A_{flex,2} = 600$ pm (a, e, i), 525 pm (b, f, j), 450 pm (c, g, k) and 375 pm (d, h, l). The free amplitude was $A_0 (flex,2) = 675$ pm and $A_{lat,1} = 1.766$ nm. 136

Figure 7-16: Adsorbate removal on a few-layer graphene-/graphite-flake while imaging in AMFlex2-OLTor1-FMLat1-FMFlex3 mode. Topography images taken at $A_{flex,2} =$

| | |
|--|-----|
| 0.60 nm (a, b), 0.53 nm (c, d), 0.45 nm (e, f) and 0.38 nm (g, h). The free amplitude was $A_{0 (flex,2)} = 0.68$ pm and $A_{lat,1} = 0.86$ nm (a, c, e, g) and 17.26 nm (b, d, f, h), respectively..... | 138 |
| Figure 7-17: AFM topography image of a few-layer graphene-/graphite-flake and cross-sectional profile for the determination of layer numbers. | 139 |
| Figure 7-18: Adsorbate formation on a few-layer graphene-/graphite-flake analyzed in AMFlex2-OLTor1-FMLat1-FMFlex3 mode upon storage for 14 days (a-c), 87 days (d-f) and 95 days & heating for 5 min at 100 °C (g-i), 209 days (j-l) and 209 days & 6s oxygen-plasma treatment (m-o). Second flexural phase (a, d, g, j, m), lateral drive amplitude (b, e, h, k, n) and lateral frequency-shift images (c, f, i, l, o). $A_{0 (flex,2)} = 675$ pm, $A_{flex,2} = 600$ pm, $A_{lat,1} = 1.766$ nm..... | 140 |
| Figure 7-19: Weight cross-sections through topography images of the few-layer graphene-/graphite-flake stored for 14 days (red), 209 days (green) and after 6 s of oxygen-plasma treatment (blue). The increased amount of adsorbate material on the graphene-/graphite-area after 209 days of storage is clearly visible. After 6 s of plasma-treatment within the frame of uncertainty the cross-section determined after 14 days of storage was reproduced, however, the roughness of the few-layer graphene-/graphite-sample increased. We conclude that the sample was cleaned from adsorbates by the plasma-treatment and a slight modification of the surface took place, however, no ablation of graphene layers could be observed. | 141 |
| Figure 7-20: 2D Raman maps of the few-layer graphene-/graphite-flake (here named flake 2) analyzed for the characteristic peaks (D, G, and 2D). Raman spectra of a similar few-layer graphene-/graphite-flake (flake 1) are shown for comparison prior to plasma treatment (black) and after 6 s plasma treatment (red) in addition to an extracted Raman spectrum taken after plasma treatment and subsequent storage of flake 2 for 118 days (blue), approximately at the positions marked by the white cross in the Raman maps. The spectra were calibrated on the G-peak for a better comparison. It becomes clearly visible that after the 6 s oxygen-plasma treatment (red, blue) the D-peak as well as the D'-peak occurred which were not present in the spectrum prior to the plasma treatment (black). This clearly indicates that the plasma treatment introduced defects into the material. On the other hand, no additional peaks which could be attributed to adsorbate molecules were found after storage of flake 2 (blue). Possible explanations could be found in the small amount of adsorbate material covering the surface as well as the similarity of the adsorbates to the graphitic sample, complicating the identification of additional peaks. | 142 |
| Figure 7-21: Analysis of the influence of different second flexural and first lateral amplitude setpoints on AFM images of a “cleaned” few-layer graphene-/graphite flake before and after rotation by 87°. Lateral frequency-shift images (a-d) were taken in the AMFlex2-OLTor1-FMLat1-FMFlex3 mode with $A_{0 (flex,2)} = 6$ nm, $A_{flex,2} = 4.5$ nm, $A_{flex,3} = 0.08$ nm, $A_{lat,1} = 0.86$ nm (a, b) and $A_{lat,1} = 8.60$ nm (c, d) before (a, c) and after rotation of the flake by 87° (b, d). Weight cross-sections were drawn through the images to determine average values and standard deviation representative for the Si/SiO ₂ -substrate (blue) and the few-layer graphene-/graphite flake (red). The results originating from the images shown in a-d are summarized in the green (a, b) and orange highlighted areas (c, d) in e, where the averaged | |

frequency-shift values were plotted as a function of two different second flexural amplitude setpoints (4.5 nm and 3 nm) and lateral amplitudes (0.86 nm and 8.60 nm) before (circles) and after rotation of the flake by 87° (triangles). The blue (red) color indicates that the values were determined on the Si/SiO₂-substrate (few-layer graphene-/graphite flake). The diagrams in f, g and h show the data resulting from the analysis of the third flexural frequency-shift, the lateral drive amplitude and the second flexural phase, respectively. Note, that the third flexural frequency-shift data of the rotated flake images shown in f was corrected for an offset in resonance frequency of 259 Hz.....144

Figure 7-22: Analysis of the influence of different second flexural and first lateral amplitude setpoints on AFM images of a “cleaned” few-layer graphene-/graphite flake before and after rotation by 87°. Lateral frequency-shift images (a-d) were taken in the AMFlex2-OLTor1-FMLat1-FMFlex3 mode with $A_{0(flex,2)} = 6$ nm, $A_{flex,2} = 3.0$ nm, $A_{flex,3} = 0.08$ nm, $A_{lat,1} = 0.86$ nm (a, b) and $A_{lat,1} = 8.60$ nm (c, d) before (a, c) and after rotation of the flake by 87° (b, d). Weight cross-sections were drawn through the images to determine average values and standard deviation representative for the Si/SiO₂-substrate (blue) and the few-layer graphene-/graphite flake (red). The results originating from the images shown in a-d are summarized in the green (a, b) and orange highlighted areas (c, d) in e, where the difference between the averaged frequency-shift values on the Si/SiO₂-substrate and the few-layer graphene-/graphite flake were plotted as a function of two different second flexural amplitude setpoints (4.5 nm and 3 nm) and lateral amplitudes (0.86 nm and 8.60 nm) before (circles) and after rotation of the flake by 87° (triangles). The diagrams in f, g and h show the data resulting from the analysis of the third flexural frequency-shift, the lateral drive amplitude and the second flexural phase, respectively.....146

Figure 7-23: Third flexural frequency-shift (a, b) and second flexural phase images (d, e) of a few-layer graphene-/graphite-flake which was stored for 209 days and oxygen-plasma treated for 6 s afterwards. The black-framed images (a, d) show the sample prior to and the red-framed images (b, e) after rotation by approximately 90°. In c and f, the averaged cross-sections (four pixel) taken at the positions marked with black (a, d) and red lines (b, e) are shown. The general offsets between the cross-sections prior to and after rotation of the sample are most probably a consequence of the slightly changed imaging conditions originating from the rotation of the sample. $A_{0(flex,2)} = 675$ pm, $A_{flex,2} = 600$ pm, $A_{lat,1} = 883$ pm, $A_{flex,3} = 150$ pm.....148

Figure 7-24: (a) Intensity ratios, derived from Raman spectroscopic measurements, as a function of the cumulative plasma treatment time for three HOPG samples (open circles). The intensity ratio between D- and G-peak is shown in red and between 2D- and G-peak in blue color. One HOPG sample was analyzed on both, the exposed (open circles) and the shielded area (filled circles), as schematically shown in (b).....149

Figure 7-25: Adsorbate removal by oxygen-plasma treatment analyzed via cross-sections of AFM topography images. The sample was imaged prior to plasma treatment (light blue) and after 30 s (yellow), 60 s (blue), 90 s (green), 120 s (red), and 150 s (grey) of plasma treatment. For (a) the cross-sections aligned relative to the Si/SiO₂-substrate area and for (b) relative to the graphene/graphite sample area.....150

- Figure 7-26: Raman intensity ratios measured within areas A (circle), B (square), C (triangle pointing up), and D (triangle pointing down), as marked in (a), as a function of layer number (b) resulting from stepwise oxygen-plasma treatment. The layer number was determined from cross-sections of AFM topography images, such as shown in Figure 1b (main text), where the height was divided by the graphene interlayer spacing (334.8 pm). The intensity ratio between D- and G-peak is shown in red, between 2D- and G-peak in blue and between D- and D'-peak in purple color.151
- Figure 7-27: Adsorbate structure formation on a few-layer graphene/graphite flake analyzed after different durations of storage and oxygen-plasma treatment steps in AMFlex2-OLTor1-FMLat1 AFM mode. a–b: second flexural phase images and c–d: lateral drive amplitude images $A_{0(flex,2)} = 675$ nm, $A_{flex,2} = 600$ nm and $A_{lat,1} = 1.766$ nm. The white arrow within the color bar (c) indicates the direction of lateral oscillation. These AFM images represent a continuation of the storage and oxygen-plasma treatment steps of the AFM images shown in Figure 3 of the main text.152
- Figure 7-28: (a) Height and (b) graphene layer evolution of the investigated few-layer graphene/graphite flake upon storage in a polypropylene petri dish filled with laboratory air and plasma treatment extracted by using cross-sections in the recorded large-scale topographic images. The hollow circles represent the height values before and the hollow rectangles the values after the plasma treatment. The inset of Figure 7-28a shows an exemplary topography image of the examined few-layer graphene/graphite flake. The red colored double arrow indicates the layer number difference between G1 and G2, the green arrow the layer number difference between G1 and G3 and the blue one the layer number difference between G2 and G3.153
- Figure 7-29: Stripe-like and island structure formation on a few-layer graphene/graphite flake analyzed based on the lateral drive amplitude images at two magnifications (a–e: 350×350 nm² and f–j: 150×150 nm²) after different durations of storage and stepwise oxygen-plasma treatment in AMFlex2-OLTor1-FMLat1 AFM mode. $A_{0(flex,2)} = 675$ nm, $A_{flex,2} = 600$ nm and $A_{lat,1} = 1.766$ nm. The white arrow within the color bar (f) indicates the direction of lateral oscillation.154
- Figure 7-30: Stripe-like and island structure formation on a few-layer graphene/graphite flake analyzed based on the topographic and lateral frequency-shift images before (a, c) and after 30 s plasma treatment (b, d) in shielded configuration in AMFlex2-OLTor1-FMLat1 AFM mode. $A_{0(flex,2)} = 675$ nm, $A_{flex,2} = 600$ nm and $A_{lat,1} = 1.766$ nm. White arrows within the color bars indicate the direction of lateral oscillation. The green dashed lines visible in the topographic image recorded before the plasma treatment in (a) are a guide to the eye to highlight the different orientations of the stripe-like pattern. The different colored polygons observable in the lateral frequency-shift images in (c) and (d) indicate the change in the orientation of the stripe pattern caused by the oxygen-plasma treatment.155

9. List of Tables

| | |
|---|-----|
| Table 3-1: Resonance frequencies, quality factors and force constants of the “coupled” and “uncoupled” cantilevers HiResC15/Cr-Au. The cantilever indexed by “Tor” was used for the images taken in AMFlex2-FMTor1-FMFlex3 mode and by “Lat” in the AMFlex2-FMLat1-FMFlex3 mode. | 66 |
| Table 4-1: Flexural, torsional and lateral resonance frequencies and approximate force constants of the cantilever types HQ:NSC15/Cr–Au and HiRes-C15/Cr–Au. | 72 |
| Table 5-1: Oxygen-plasma times for treatment of the few-layer graphene-/graphite-flake as analyzed in Figure 5-1 and Figure 5-2..... | 109 |
| Table 7-1: Averaged resonance-frequency ratios and standard deviations determined for different amounts of cantilevers (a: 18, b: 6, c: 17) of the type HiResC15/Cr-Au. The relative deviation, relating the standard deviation to the average value is shown in percentage. The last row includes the theoretical relations between the different resonance frequencies for rectangular cantilevers, where L is the length, b is the width and t is the thickness of the cantilever [68, 90]. | 134 |

10. List of Abbreviations

| | | | |
|---------------|--|--------------|---|
| A | Acoustic phonon mode | LFM | Lateral Force Microscopy |
| AFM | Atomic Force Microscopy | MEMS | MicroElectroMechanical System |
| AM | Amplitude Modulated | mono | monomodal |
| BHT | Butylated HydroxyToluene | NC | Non-Contact |
| bi | bimodal | NEMS | NanoElectroMechanical System |
| C | Carbon side | O | Optical phonon mode |
| CA | Constant Amplitude | o | out-of-plane phonon mode |
| CE | Constant Excitation | OL | Open Loop |
| DBP | DiButyl Phthalate | op | out-of-plane |
| DFT | Density Functional Theory | P | Proportional |
| dis | dissipation | PAH | Polycyclic Aromatic Hydrocarbons |
| DLC | Diamond Like Carbon | PLL | Phase Locked Loop |
| DM | Dissipative Mode | PSD | Power Spectral Density |
| DR | Double Resonance | PTCDA | 3,4,9,10-PeryleneTetra-Carboxylic DiAnhydride |
| dsDNA | double-stranded DeoxyriboNucleic Acid | ref | reference |
| eff | effective | SASS | Small Amplitude Small Setpoint |
| exc | excitation | SNOM | Scanning Nearfield Optical Microscopy |
| FEA | Finite Element Analysis | sp | setpoint |
| FFM | Frictional Force Microscopy | SPM | Scanning Probe Microscopy |
| Flex | Flexural | STM | Scanning Tunneling Microscopy |
| FM | Frequency Modulated | T | Transverse phonon mode |
| FWHM | Full Width at Half Maximum | Tor | Torsional |
| H | Hollow side | ts | tip-sample |
| HF | High-Frequency | UHV | Ultra High Vacuum |
| HOPG | Highly Oriented (also: Ordered) Pyrolytic Graphite | val | validation |
| I | Integral | vdw | Van-der-Waals |
| i | in-plane phonon mode | VOC | Volatile Organic Compounds |
| invOLS | inverse Optical Lever Sensitivity | | |
| ip | in-plane | | |
| L | Longitudinal phonon mode | | |
| Lat | Lateral | | |

11. References

1. Hibino, H., *Graphene Research at NTT*. NTT Technical Review, 2013. **11**(8).
2. Phiri, J., P. Gane, and T.C. Maloney, *General overview of graphene: Production, properties and application in polymer composites*. Materials Science and Engineering: B, 2017. **215**: p. 9-28.
3. Lee, C., et al., *Measurement of the elastic properties and intrinsic strength of monolayer graphene*. Science, 2008. **321**(5887): p. 385-388.
4. Seeholzer, T., et al., *A Fourier method for estimating potential energy and lateral forces from frequency-modulation lateral force microscopy data*. New Journal of Physics, 2019. **21**(8): p. 083007.
5. Kawai, S., et al., *Systematic Achievement of Improved Atomic-Scale Contrast via Bimodal Dynamic Force Microscopy*. Physical Review Letters, 2009. **103**(22): p. 220801.
6. Kawai, S., et al., *Ultrasensitive detection of lateral atomic-scale interactions on graphite (0001) via bimodal dynamic force measurements*. Physical Review B, 2010. **81**(8): p. 085420.
7. Herruzo, E.T. and R. Garcia, *Theoretical study of the frequency shift in bimodal FM-AFM by fractional calculus*. Beilstein Journal of Nanotechnology, 2012. **3**: p. 198-206.
8. Eichhorn, A.L. and C. Dietz, *Simultaneous Deconvolution of In-Plane and Out-of-Plane Forces of HOPG at the Atomic Scale under Ambient Conditions by Multifrequency Atomic Force Microscopy*. Advanced Materials Interfaces, 2021. **8**(20).
9. *Noble Prize to A. Geim and K. Novoselov*. The Royal Swedish Academy of Sciences, 2010.
10. Novoselov, K.S., et al., *Electric field effect in atomically thin carbon films*. Science, 2004. **306**(5696): p. 666-669.
11. Bolotin, K.I., et al., *Ultrahigh electron mobility in suspended graphene*. Solid State Communications, 2008. **146**(9): p. 351-355.
12. Bae, S., et al., *Roll-to-roll production of 30-inch graphene films for transparent electrodes*. Nature Nanotechnology, 2010. **5**(8): p. 574-578.
13. Balandin, A.A., et al., *Superior Thermal Conductivity of Single-Layer Graphene*. Nano Letters, 2008. **8**(3): p. 902-907.
14. Rao, C.N.R., et al., *Graphene: The New Two-Dimensional Nanomaterial*. Angewandte Chemie-International Edition, 2009. **48**(42): p. 7752-7777.
15. Berry, V., *Impermeability of graphene and its applications*. Carbon, 2013. **62**: p. 1-10.
16. Hembacher, S., et al., *Revealing the hidden atom in graphite by low-temperature atomic force microscopy*. Proceedings of the National Academy of Sciences of the United States of America, 2003. **100**(22): p. 12539-12542.
17. Blackman, L.C.F. and A.R.J.P. Ubbelohde, *Stress recrystallization of graphite*. Proceedings of the Royal Society of London. Series A. Mathematical and Physical Sciences, 1962. **266**(1324): p. 20-32.
18. Ezawa, M., *Supersymmetry and unconventional quantum Hall effect in monolayer, bilayer and trilayer graphene*. Physica E: Low-dimensional Systems and Nanostructures, 2007. **40**(2): p. 269-272.
19. Zhu, W., et al., *Carrier scattering, mobilities, and electrostatic potential in monolayer, bilayer, and trilayer graphene*. Physical Review B, 2009. **80**(23): p. 235402.

-
20. Parvez, K., *et al.*, *Exfoliation of graphene via wet chemical routes*. *Synthetic Metals*, 2015. **210**: p. 123-132.
 21. Liu, N., *et al.*, *One-step ionic-liquid-assisted electrochemical synthesis of ionic-liquid-functionalized graphene sheets directly from graphite*. *Advanced Functional Materials*, 2008. **18**(10): p. 1518-1525.
 22. Berger, C., *et al.*, *Ultrathin Epitaxial Graphite: 2D Electron Gas Properties and a Route toward Graphene-based Nanoelectronics*. *The Journal of Physical Chemistry B*, 2004. **108**(52): p. 19917-9916.
 23. Reina, A., *et al.*, *Large Area, Few-Layer Graphene Films on Arbitrary Substrates by Chemical Vapor Deposition*. *Nano Letters*, 2009. **9**(1): p. 30-35.
 24. Li, X.S., *et al.*, *Large-Area Synthesis of High-Quality and Uniform Graphene Films on Copper Foils*. *Science*, 2009. **324**(5932): p. 1317-314.
 25. Hesjedal, T., *Continuous roll-to-roll growth of graphene films by chemical vapor deposition*. *Applied Physics Letters*, 2011. **98**(13): p. 133106.
 26. Lin, J., *et al.*, *Laser-induced porous graphene films from commercial polymers*. *Nature Communications*, 2014. **5**(1): p. 5714.
 27. Qian, M., *et al.*, *Formation of graphene sheets through laser exfoliation of highly ordered pyrolytic graphite*. *Applied Physics Letters*, 2011. **98**(17): p. 173108.
 28. Luong, D.X., *et al.*, *Gram-scale bottom-up flash graphene synthesis*. *Nature*, 2020. **577**(7792): p. 647-651.
 29. Gutierrez-Cruz, A., *et al.*, *A review of top-down and bottom-up synthesis methods for the production of graphene, graphene oxide and reduced graphene oxide*. *Journal of Materials Science*, 2022. **57**(31): p. 14543-14578.
 30. Lee, Y., *et al.*, *Wafer-Scale Synthesis and Transfer of Graphene Films*. *Nano Letters*, 2010. **10**(2): p. 490-493.
 31. Regan, W., *et al.*, *A direct transfer of layer-area graphene*. *Applied Physics Letters*, 2010. **96**(11).
 32. Blake, P., *et al.*, *Making graphene visible*. *Applied Physics Letters*, 2007. **91**(6).
 33. Huang, Y., *et al.*, *Reliable Exfoliation of Large-Area High-Quality Flakes of Graphene and Other Two-Dimensional Materials*. *Acs Nano*, 2015. **9**(11): p. 10612-10620.
 34. *Noble Prize to G. Binnig and H. Rohrer*. *The Royal Swedish Academy of Sciences*, 1986.
 35. Binnig, G. and H. Rohrer, *Scanning tunneling microscopy*. *Surface Science*, 1983. **126**(1): p. 236-244.
 36. Lewis, A., *et al.*, *Development of a 500 Å spatial resolution light microscope: I. light is efficiently transmitted through $\lambda/16$ diameter apertures*. *Ultramicroscopy*, 1984. **13**(3): p. 227-231.
 37. Pohl, D.W., W. Denk, and M. Lanz, *Optical stethoscopy: Image recording with resolution $\lambda/20$* . *Applied Physics Letters*, 1984. **44**(7): p. 651-653.
 38. Binnig, G., C.F. Quate, and C. Gerber, *ATOMIC FORCE MICROSCOPE*. *Physical Review Letters*, 1986. **56**(9): p. 930-933.
 39. Sasaki, N., K. Kobayashi, and M. Tsukada, *Atomic-scale friction image of graphite in atomic-force microscopy*. *Physical Review B*, 1996. **54**(3): p. 2138-2149.
 40. Martin, Y., C.C. Williams, and H.K. Wickramasinghe, *ATOMIC FORCE MICROSCOPE FORCE MAPPING AND PROFILING ON A SUB 100-Å SCALE*. *Journal of Applied Physics*, 1987. **61**(10): p. 4723-4729.

-
41. Zhong, Q., *et al.*, *FRACTURED POLYMER SILICA FIBER SURFACE STUDIED BY TAPPING MODE ATOMIC-FORCE MICROSCOPY*. *Surface Science*, 1993. **290**(1-2): p. L688-L692.
 42. Albrecht, T.R., *et al.*, *FREQUENCY-MODULATION DETECTION USING HIGH-Q CANTILEVERS FOR ENHANCED FORCE MICROSCOPE SENSITIVITY*. *Journal of Applied Physics*, 1991. **69**(2): p. 668-673.
 43. Pini, V., *et al.*, *Dynamical characterization of vibrating AFM cantilevers forced by photothermal excitation*. *Physical Review B*, 2010. **81**(5): p. 054302.
 44. Kiracofe, D., *et al.*, *High efficiency laser photothermal excitation of microcantilever vibrations in air and liquids*. *Review of Scientific Instruments*, 2011. **82**(1): p. 013702.
 45. Anselmetti, D., *et al.*, *ATTRACTIVE-MODE IMAGING OF BIOLOGICAL-MATERIALS WITH DYNAMIC FORCE MICROSCOPY*. *Nanotechnology*, 1994. **5**(2): p. 87-94.
 46. Ruths, M. and J.N. Israelachvili, *Surface Forces and Nanorheology of Molecularly Thin Films*, in *Nanotribology and Nanomechanics: An Introduction*, B. Bhushan, Editor. 2008, Springer Berlin Heidelberg: Berlin, Heidelberg. p. 417-515.
 47. Israelachvili, J.N., *6 - Van der Waals Forces*, in *Intermolecular and Surface Forces (Third Edition)*, J.N. Israelachvili, Editor. 2011, Academic Press: San Diego. p. 107-132.
 48. Argento, C. and R.H. French, *Parametric tip model and force–distance relation for Hamaker constant determination from atomic force microscopy*. *Journal of Applied Physics*, 1996. **80**(11): p. 6081-6090.
 49. Hamaker, H.C., *The London—van der Waals attraction between spherical particles*. *Physica*, 1937. **4**(10): p. 1058-1072.
 50. Hutter, J.L. and J. Bechhoefer, *Manipulation of van der Waals forces to improve image resolution in atomic-force microscopy*. *Journal of Applied Physics*, 1993. **73**: p. 4123-4129.
 51. Hertz, H., *Ueber die Berührung fester elastischer Körper*. 1882. **1882**(92): p. 156-171.
 52. Derjaguin, B.V., V.M. Muller, and Y.P. Toporov, *Effect of contact deformations on the adhesion of particles*. *Journal of Colloid and Interface Science*, 1975. **53**(2): p. 314-326.
 53. Johnson, K.L., K. Kendall, and A.D. Roberts, *Surface Energy and Contact of Elastic Solids*. *Proceedings of The Royal Society A: Mathematical, Physical and Engineering Sciences*, 1971. **324**: p. 301-313.
 54. Chen, J., *et al.*, *NUMERICAL SIMULATIONS OF A SCANNING FORCE MICROSCOPE WITH A LARGE-AMPLITUDE VIBRATING CANTILEVER*. *Nanotechnology*, 1994. **5**(4): p. 199-204.
 55. Gotsmann, B., *et al.*, *Conservative and dissipative tip-sample interaction forces probed with dynamic AFM*. *Physical Review B*, 1999. **60**(15): p. 11051-11061.
 56. Chen, G.Y., *et al.*, *HARMONIC RESPONSE OF NEAR-CONTACT SCANNING FORCE MICROSCOPY*. *Journal of Applied Physics*, 1995. **78**(3): p. 1465-1469.
 57. Giessibl, F.J., *Forces and frequency shifts in atomic-resolution dynamic-force microscopy*. *Physical Review B*, 1997. **56**(24): p. 16010-16015.
 58. Giessibl, F.J., *A direct method to calculate tip–sample forces from frequency shifts in frequency-modulation atomic force microscopy*. *Applied Physics Letters*, 2000. **78**(1): p. 123-125.
 59. Sader, J.E. and S.P. Jarvis, *Interpretation of frequency modulation atomic force microscopy in terms of fractional calculus*. *Physical Review B*, 2004. **70**(1): p. 012303.

-
60. Sader, J.E. and S.P. Jarvis, *Accurate formulas for interaction force and energy in frequency modulation force spectroscopy*. Applied Physics Letters, 2004. **84**(10): p. 1801-1803.
 61. Weymouth, A.J., *et al.*, *Atomic Structure Affects the Directional Dependence of Friction*. Physical Review Letters, 2013. **111**(12): p. 126103.
 62. Garcia, R. and R. Perez, *Dynamic atomic force microscopy methods*. Surface Science Reports, 2002. **47**(6-8): p. 197-301.
 63. Kawai, S. and H. Kawakatsu, *Atomically resolved amplitude modulation dynamic force microscopy with a high-frequency and high-quality factor cantilever*. Applied Physics Letters, 2006. **89**(1): p. 013108.
 64. Korolkov, V.V., *et al.*, *Supramolecular networks stabilise and functionalise black phosphorus*. Nature Communications, 2017. **8**: p. 1385.
 65. Kawai, S., *et al.*, *An ultrasmall amplitude operation of dynamic force microscopy with second flexural mode*. Applied Physics Letters, 2005. **86**(19): p. 193107.
 66. Kiracofe, D. and A. Raman, *On eigenmodes, stiffness, and sensitivity of atomic force microscope cantilevers in air versus liquids*. Journal of Applied Physics, 2010. **107**(3): p. 033506.
 67. Stark, R.W. and W.M. Heckl, *Fourier transformed atomic force microscopy: tapping mode atomic force microscopy beyond the Hookian approximation*. Surface Science, 2000. **457**(1-2): p. 219-228.
 68. Garcia, R. and E.T. Herruzo, *The emergence of multifrequency force microscopy*. Nature Nanotechnology, 2012. **7**(4): p. 217-226.
 69. Santos, S., *et al.*, *Stability, resolution, and ultra-low wear amplitude modulation atomic force microscopy of DNA: Small amplitude small set-point imaging*. Applied Physics Letters, 2013. **103**(6): p. 063702.
 70. Santos, S., *et al.*, *Hydration Dynamics and the Future of Small-Amplitude AFM Imaging in Air*. Molecules, 2021. **26**(23).
 71. Rodriguez, T.R. and R. Garcia, *Compositional mapping of surfaces in atomic force microscopy by excitation of the second normal mode of the microcantilever*. Applied Physics Letters, 2004. **84**(3): p. 449-451.
 72. Patil, S., *et al.*, *Force microscopy imaging of individual protein molecules with sub-pico Newton force sensitivity*. Journal of Molecular Recognition, 2007. **20**(6): p. 516-523.
 73. Martinez-Martin, D., *et al.*, *Noninvasive Protein Structural Flexibility Mapping by Bimodal Dynamic Force Microscopy*. Physical Review Letters, 2011. **106**(19).
 74. Dietz, C., *et al.*, *Nanomechanical coupling enables detection and imaging of 5 nm superparamagnetic particles in liquid*. Nanotechnology, 2011. **22**(12).
 75. Martinez, N.F., *et al.*, *Enhanced compositional sensitivity in atomic force microscopy by the excitation of the first two flexural modes*. Applied Physics Letters, 2006. **89**(15): p. 153115.
 76. Proksch, R., *Multifrequency, repulsive-mode amplitude-modulated atomic force microscopy*. Applied Physics Letters, 2006. **89**(11).
 77. Ebeling, D. and S.D. Solares, *Bimodal atomic force microscopy driving the higher eigenmode in frequency-modulation mode: Implementation, advantages, disadvantages and comparison to the open-loop case*. Beilstein journal of nanotechnology, 2013. **4**: p. 198-207.

-
78. Chawla, G. and S.D. Soares, *Mapping of conservative and dissipative interactions in bimodal atomic force microscopy using open-loop and phase-locked-loop control of the higher eigenmode*. Applied Physics Letters, 2011. **99**(7): p. 074103.
 79. Holscher, H., et al., *Measurement of conservative and dissipative tip-sample interaction forces with a dynamic force microscope using the frequency modulation technique*. Physical Review B, 2001. **64**(7).
 80. Holscher, H., B. Gotsmann, and A. Schirmeisen, *Dynamic force spectroscopy using the frequency modulation technique with constant excitation*. Physical Review B, 2003. **68**(15).
 81. Schirmeisen, A., et al., *Dynamic force spectroscopy using the constant-excitation and constant-amplitude modes*. Nanotechnology, 2005. **16**(3): p. S13.
 82. Dietz, C., et al., *Bimodal frequency-modulated atomic force microscopy with small cantilevers*. Nanoscale, 2015. **7**(5): p. 1849-1856.
 83. Benaglia, S., et al., *Fast and high-resolution mapping of elastic properties of biomolecules and polymers with bimodal AFM*. Nature Protocols, 2018. **13**(12): p. 2890-2907.
 84. Soares, S.D. and G. Chawla, *Frequency response of higher cantilever eigenmodes in bimodal and trimodal tapping mode atomic force microscopy*. Measurement Science and Technology, 2010. **21**(12): p. 125502.
 85. Ebeling, D., B. Eslami, and S.D.J. Soares, *Visualizing the Subsurface of Soft Matter: Simultaneous Topographical Imaging, Depth Modulation, and Compositional Mapping with Triple Frequency Atomic Force Microscopy*. ACS Nano, 2013. **7**(11): p. 10387-10396.
 86. Soares, S.D., S.M. An, and C.J. Long, *Multi-frequency tapping-mode atomic force microscopy beyond three eigenmodes in ambient air*. Beilstein Journal of Nanotechnology, 2014. **5**: p. 1637-1648.
 87. Meier, T., B. Eslami, and S.D. Soares, *Multifrequency force microscopy using flexural and torsional modes by photothermal excitation in liquid: atomic resolution imaging of calcite ($10\bar{1}4$)*. Nanotechnology, 2016. **27**(8): p. 085702.
 88. Dietz, C., *Sensing in-plane nanomechanical surface and sub-surface properties of polymers: local shear stress as function of the indentation depth*. Nanoscale, 2018. **10**(1): p. 460-468.
 89. Ding, R.-F., et al., *High-sensitivity imaging with lateral resonance mode atomic force microscopy*. Nanoscale, 2016. **8**(43): p. 18421-18427.
 90. Young, W.C.B., R. G., *Roark's Formulas for Stress and Strain*. 7th ed. 2002: McGraw-Hill. 765-768.
 91. Cai, T., *Theoretical Analysis of Torsionally Vibrating Microcantilevers for Chemical Sensor Applications in Viscous Liquids*. 2009, Marquette University.
 92. *Noble Prize to C.V. Raman*. The Royal Swedish Academy of Sciences, 1930.
 93. Kudelski, A., *Analytical applications of Raman spectroscopy*. Talanta, 2008. **76**(1): p. 1-8.
 94. Orlando, A., et al. *A Comprehensive Review on Raman Spectroscopy Applications*. Chemosensors, 2021. **9**, DOI: 10.3390/chemosensors9090262.
 95. Baia, M., S. Astilean, and T. Iliescu, *Fundamentals of Infrared and Raman Spectroscopy, SERS, and Theoretical Simulations*, in *Raman and SERS Investigations of Pharmaceuticals*, M. Baia, S. Astilean, and T. Iliescu, Editors. 2008, Springer Berlin Heidelberg: Berlin, Heidelberg. p. 9-35.

-
96. Varberg, T.D., *Raman Spectroscopy, Group Theory, and Computational Chemistry: A Physical Chemistry Laboratory Experiment on para-Difluorobenzene*. Journal of Chemical Education, 2022. **99**(5): p. 2129-2134.
 97. Ferrari, A.C., *et al.*, *Raman spectrum of graphene and graphene layers*. Physical Review Letters, 2006. **97**(18).
 98. Ni, Z.H., *et al.*, *Raman Spectroscopy and Imaging of Graphene*. Nano Research, 2008. **1**(4): p. 273-291.
 99. Liu, Y., *et al.*, *Temperature dependence of the electrical transport properties in few-layer graphene interconnects*. Nanoscale research letters, 2013. **8**: p. 335.
 100. Piscanec, S., *et al.*, *Kohn anomalies and electron-phonon interactions in graphite*. Physical Review Letters, 2004. **93**(18).
 101. Maultzsch, J., S. Reich, and C. Thomsen, *Double-resonant Raman scattering in graphite: Interference effects, selection rules, and phonon dispersion*. Physical Review B, 2004. **70**(15).
 102. Ferralis, N., *Probing mechanical properties of graphene with Raman spectroscopy*. Journal of Materials Science, 2010. **45**(19): p. 5135-5149.
 103. Ferrari, A.C. and J. Robertson, *Interpretation of Raman spectra of disordered and amorphous carbon*. Physical Review B, 2000. **61**(20): p. 14095-14107.
 104. Pimenta, M.A., *et al.*, *Studying disorder in graphite-based systems by Raman spectroscopy*. Physical Chemistry Chemical Physics, 2007. **9**(11): p. 1276-1291.
 105. Ferrari, A.C., *Raman spectroscopy of graphene and graphite: Disorder, electron-phonon coupling, doping and nonadiabatic effects*. Solid State Communications, 2007. **143**(1-2): p. 47-57.
 106. Thomsen, C. and S. Reich, *Double resonant Raman scattering in graphite*. Physical Review Letters, 2000. **85**(24): p. 5214-5217.
 107. Nemanich, R.J. and S.A. Solin, *1ST-ORDER AND 2ND-ORDER RAMAN-SCATTERING FROM FINITE-SIZE CRYSTALS OF GRAPHITE*. Physical Review B, 1979. **20**(2): p. 392-401.
 108. Eckmann, A., *et al.*, *Probing the Nature of Defects in Graphene by Raman Spectroscopy*. Nano Letters, 2012. **12**(8): p. 3925-3930.
 109. Zandiatashbar, A., *et al.*, *Effect of defects on the intrinsic strength and stiffness of graphene*. Nature Communications, 2014. **5**: p. 3186.
 110. Fu, D., *et al.*, *A molecularly imprinted electrochemical sensing platform based on the signal amplification system fabricated with the theoretically optimized monomer for specific determination of formaldehyde*. Sensors and Actuators B: Chemical, 2021. **344**: p. 130260.
 111. Chen, T., *et al.*, *Specific detection of monosaccharide by dual-channel sensing platform based on dual catalytic system constructed by bio-enzyme and bionic enzyme using molecular imprinting polymers*. Sensors and Actuators B: Chemical, 2020. **320**: p. 128430.
 112. Frank, I.W., *et al.*, *Mechanical properties of suspended graphene sheets*. Journal of Vacuum Science & Technology B, 2007. **25**(6): p. 2558-2561.
 113. Cellini, F., Y. Gao, and E. Riedo, *angstrom-Indentation for non-destructive elastic moduli measurements of supported ultra-hard ultra-thin films and nanostructures*. Scientific Reports, 2019. **9**: p. 4075.

-
114. Schwarz, A., *et al.*, *Dynamic force microscopy with atomic resolution at low temperatures*. Applied Surface Science, 2002. **188**(3): p. 245-251.
 115. Holscher, H., *et al.*, *Interpretation of "true atomic resolution" images of graphite (0001) in noncontact atomic force microscopy*. Physical Review B, 2000. **62**(11): p. 6967-6970.
 116. Albers, B.J., *et al.*, *Combined low-temperature scanning tunneling/atomic force microscope for atomic resolution imaging and site-specific force spectroscopy*. Review of Scientific Instruments, 2008. **79**(3): p. 033704.
 117. Weber, S.A.L., *et al.*, *High viscosity environments: an unexpected route to obtain true atomic resolution with atomic force microscopy*. Nanotechnology, 2014. **25**(17): p. 175701.
 118. Giessibl, F.J., *Atomic resolution on Si(111)-(7x7) by noncontact atomic force microscopy with a force sensor based on a quartz tuning fork*. Applied Physics Letters, 2000. **76**(11): p. 1470-1472.
 119. Wastl, D.S., A.J. Weymouth, and F.J. Giessibl, *Atomically Resolved Graphitic Surfaces in Air by Atomic Force Microscopy*. ACS Nano, 2014. **8**(5): p. 5233-5239.
 120. Giessibl, F.J., M. Herz, and J. Mannhart, *Friction traced to the single atom*. Proceedings of the National Academy of Sciences, 2002. **99**(19): p. 12006-12010.
 121. Kirpal, D., *et al.*, *Biaxial atomically resolved force microscopy based on a qPlus sensor operated simultaneously in the first flexural and length extensional modes*. Review of Scientific Instruments, 2021. **92**(4): p. 043703.
 122. Giessibl, F.J., *The qPlus sensor, a powerful core for the atomic force microscope*. Review of Scientific Instruments, 2019. **90**(1): p. 011101.
 123. Miller, E.J., *et al.*, *Sub-nanometer Resolution Imaging with Amplitude-modulation Atomic Force Microscopy in Liquid*. Jove-Journal of Visualized Experiments, 2016(118): p. e54924.
 124. Gross, L., *et al.*, *The Chemical Structure of a Molecule Resolved by Atomic Force Microscopy*. Science, 2009. **325**(5944): p. 1110-1114.
 125. Moll, N., *et al.*, *The mechanisms underlying the enhanced resolution of atomic force microscopy with functionalized tips*. New Journal of Physics, 2010. **12**: p. 125020.
 126. Guo, C.-S., *et al.*, *High-Resolution Model for Noncontact Atomic Force Microscopy with a Flexible Molecule on the Tip Apex*. The Journal of Physical Chemistry C, 2015. **119**(3): p. 1483-1488.
 127. Uhlig, M.R., D. Martin-Jimenez, and R. Garcia, *Atomic-scale mapping of hydrophobic layers on graphene and few-layer MoS₂ and WSe₂ in water*. Nature Communications, 2019. **10**(1): p. 2606.
 128. Fukuma, T. and R. Garcia, *Atomic- and Molecular-Resolution Mapping of Solid-Liquid Interfaces by 3D Atomic Force Microscopy*. ACS Nano, 2018. **12**(12): p. 11785-11797.
 129. Umeda, K., *et al.*, *Atomic-resolution three-dimensional hydration structures on a heterogeneously charged surface*. Nature Communications, 2017. **8**(1): p. 2111.
 130. Sweetman, A.M., *et al.*, *Mapping the force field of a hydrogen-bonded assembly*. Nature Communications, 2014. **5**(1): p. 3931.
 131. Baykara, M.Z., *et al.*, *Exploring atomic-scale lateral forces in the attractive regime: a case study on graphite (0001)*. Nanotechnology, 2012. **23**(40): p. 405703.
 132. Kawai, S., *et al.*, *Time-averaged cantilever deflection in dynamic force spectroscopy*. Physical Review B, 2009. **80**(8): p. 085422.

-
133. Yalcin, S.E., *et al.*, *Direct observation of anisotropic growth of water films on minerals driven by defects and surface tension*. Science Advances, 2020. **6**(30): p. eaaz9708.
 134. Kawai, S. and H. Kawakatsu, *Surface-relaxation-induced giant corrugation on graphite (0001)*. Physical Review B, 2009. **79**(11): p. 115440.
 135. Aksoy, M.D. and A. Atalar, *Force spectroscopy using bimodal frequency modulation atomic force microscopy*. Physical Review B, 2011. **83**(7): p. 075416.
 136. Naitoh, Y., *et al.*, *Simultaneous observation of surface topography and elasticity at atomic scale by multifrequency frequency modulation atomic force microscopy*. Journal of Vacuum Science & Technology B, 2010. **28**(6): p. 1210-1214.
 137. Chiesa, M. and C.-Y. Lai, *Surface aging investigation by means of an AFM-based methodology and the evolution of conservative nanoscale interactions*. Physical Chemistry Chemical Physics, 2018. **20**(29): p. 19664-19671.
 138. Calo, A., *et al.*, *Capillary and van der Waals interactions on CaF₂ crystals from amplitude modulation AFM force reconstruction profiles under ambient conditions*. Beilstein Journal of Nanotechnology, 2015. **6**: p. 809-819.
 139. Krajina, B.A., L.S. Kocherlakota, and R.M. Overney, *Direct determination of the local Hamaker constant of inorganic surfaces based on scanning force microscopy*. Journal of Chemical Physics, 2014. **141**(16): p. 164707.
 140. Sader, J.E., *et al.*, *Interatomic force laws that evade dynamic measurement*. Nature Nanotechnology, 2018. **13**(12): p. 1088-1091.
 141. Weymouth, A.J., *et al.*, *Strumming a Single Chemical Bond*. Physical Review Letters, 2020. **124**(19): p. 196101.
 142. Michel, K.H. and B. Verberck, *Theory of the elastic constants of graphite and graphene*. Physica Status Solidi B-Basic Solid State Physics, 2008. **245**(10): p. 2177-2180.
 143. Green, C.P., *et al.*, *Normal and torsional spring constants of atomic force microscope cantilevers*. Review of Scientific Instruments, 2004. **75**(6): p. 1988-1996.
 144. Cannara, R.J., M. Eglin, and R.W. Carpick, *Lateral force calibration in atomic force microscopy: A new lateral force calibration method and general guidelines for optimization*. Review of Scientific Instruments, 2006. **77**(5): p. 053701.
 145. Higgins, M.J., *et al.*, *Noninvasive determination of optical lever sensitivity in atomic force microscopy*. Review of Scientific Instruments, 2006. **77**(1): p. 013701.
 146. Mullin, N. and J.K. Hobbs, *A non-contact, thermal noise based method for the calibration of lateral deflection sensitivity in atomic force microscopy*. Review of Scientific Instruments, 2014. **85**(11): p. 113703.
 147. Wang, J., D. Zhang, and B. Zhou, *Achieving an Ohmic contact in graphene-based van der Waals heterostructures by intrinsic defects and the inner polarized electric field of Janus AlGaSSe*. New Journal of Chemistry, 2021. **45**(45): p. 21178-21187.
 148. Heerema, S.J. and C. Dekker, *Graphene nanodevices for DNA sequencing*. Nature Nanotechnology, 2016. **11**(2): p. 127-136.
 149. Martin-Jimenez, D., *et al.*, *Chemical bond imaging using torsional and flexural higher eigenmodes of qPlus sensors*. Nanoscale, 2022. **14**(14): p. 5329-5339.
 150. Ogletree, D.F., R.W. Carpick, and M. Salmeron, *Calibration of frictional forces in atomic force microscopy*. Review of Scientific Instruments, 1996. **67**(9): p. 3298-3306.

-
151. Varenberg, M., I. Etsion, and G. Halperin, *An improved wedge calibration method for lateral force in atomic force microscopy*. Review of Scientific Instruments, 2003. **74**(7): p. 3362-3367.
 152. Zhang, G., *et al.*, *Lateral force calibration for atomic force microscope cantilevers using a suspended nanowire*. Nanotechnology, 2020. **31**(47): p. 475703.
 153. Munz, M., *Force calibration in lateral force microscopy: a review of the experimental methods*. Journal of Physics D-Applied Physics, 2010. **43**(6).
 154. Lai, C.Y., S. Santos, and M. Chiesa, *Systematic Multidimensional Quantification of Nanoscale Systems From Bimodal Atomic Force Microscopy Data*. Acs Nano, 2016. **10**(6): p. 6265-6272.
 155. Benaglia, S., C.A. Amo, and R. Garcia, *Fast, quantitative and high resolution mapping of viscoelastic properties with bimodal AFM*. Nanoscale, 2019. **11**(32): p. 15289-15297.
 156. Aboalizadeh, Z., L.J. Sudak, and P. Egberts, *Nanoscale spatial mapping of mechanical properties through dynamic atomic force microscopy*. Beilstein journal of nanotechnology, 2019. **10**: p. 1337-347.
 157. Eslami, B. and M. Damircheli, *Biharmonic versus bimodal AFM: Numerical and experimental study on soft matter*. Journal of Applied Physics, 2019. **126**(9): p. 095301.
 158. Zhang, Z., *et al.*, *Molecular features of hydration layers probed by atomic force microscopy*. Physical Chemistry Chemical Physics, 2018. **20**(48): p. 30492-30501.
 159. Weymouth, A.J., *Non-contact lateral force microscopy*. Journal of Physics: Condensed Matter, 2017. **29**(32): p. 323001.
 160. Blakslee, O.L., *et al.*, *Elastic Constants of Compression-Annealed Pyrolytic Graphite*. Journal of Applied Physics, 1970. **41**(8): p. 3373-3382.
 161. Holscher, H., *et al.*, *Consequences of the stick-slip movement for the scanning force microscopy imaging of graphite*. Physical Review B, 1998. **57**(4): p. 2477-2481.
 162. Lee, H., *et al.*, *Comparison of frictional forces on graphene and graphite*. Nanotechnology, 2009. **20**(32): p. 325701.
 163. Choi, J.S., *et al.*, *Correlation between micrometer-scale ripple alignment and atomic-scale crystallographic orientation of monolayer graphene*. Scientific Reports, 2014. **4**(1): p. 7263.
 164. Choi Jin, S., *et al.*, *Friction Anisotropy-Driven Domain Imaging on Exfoliated Monolayer Graphene*. Science, 2011. **333**(6042): p. 607-610.
 165. Gallagher, P., *et al.*, *Optical Imaging and Spectroscopic Characterization of Self-Assembled Environmental Adsorbates on Graphene*. Nano Letters, 2018. **18**(4): p. 2603-2608.
 166. Gallagher, P., *et al.*, *Switchable friction enabled by nanoscale self-assembly on graphene*. Nature Communications, 2016. **7**.
 167. Berman, D., A. Erdemir, and A.V. Sumant, *Reduced wear and friction enabled by graphene layers on sliding steel surfaces in dry nitrogen*. Carbon, 2013. **59**: p. 167-175.
 168. Mescola, A., *et al.*, *Graphene Confers Ultralow Friction on Nanogear Cogs*. Small, 2021. **17**(47).
 169. Uzoma, P.C., *et al.*, *Tribology of 2D Nanomaterials: A Review*. Coatings, 2020. **10**(9).
 170. Lee, J.H., *et al.*, *Nanotribology of 2D materials and their macroscopic applications*. Journal of Physics D: Applied Physics, 2020. **53**(39): p. 393001.
 171. Koenig, S.P., *et al.*, *Selective molecular sieving through porous graphene*. Nature Nanotechnology, 2012. **7**(11): p. 728-732.

-
172. Yuan, Z., *et al.*, *Predicting Gas Separation through Graphene Nanopore Ensembles with Realistic Pore Size Distributions*. ACS Nano, 2021. **15**(1): p. 1727-1740.
 173. Wastl, D.S., *et al.*, *Observation of 4 nm Pitch Stripe Domains Formed by Exposing Graphene to Ambient Air*. ACS Nano, 2013. **7**(11): p. 10032-10037.
 174. Zhang, D., *et al.*, *Origin of friction hysteresis on monolayer graphene*. Friction, 2021.
 175. Temiryazev, A., A. Frolov, and M. Temiryazeva, *Atomic-force microscopy study of self-assembled atmospheric contamination on graphene and graphite surfaces*. Carbon, 2019. **143**: p. 30-37.
 176. Choi, J.S., *et al.*, *Facile characterization of ripple domains on exfoliated graphene*. Review of Scientific Instruments, 2012. **83**(7): p. 073905.
 177. Singh, S.K., *et al.*, *Thermomechanical properties of a single hexagonal boron nitride sheet*. Physical Review B, 2013. **87**(18): p. 184106.
 178. Tamayo, J. and R. García, *Relationship between phase shift and energy dissipation in tapping-mode scanning force microscopy*. Applied Physics Letters, 1998. **73**(20): p. 2926-2928.
 179. Cleveland, J.P., *et al.*, *Energy dissipation in tapping-mode atomic force microscopy*. Applied Physics Letters, 1998. **72**(20): p. 2613-2615.
 180. Gotsmann, B. and H. Fuchs, *The measurement of hysteretic forces by dynamic AFM*. Applied Physics A, 2001. **72**(1): p. S55-S58.
 181. Tan, X., D. Guo, and J. Luo, *Dynamic friction energy dissipation and enhanced contrast in high frequency bimodal atomic force microscopy*. Friction, 2022. **10**(5): p. 748-761.
 182. Eichhorn, A.L. and C. Dietz, *Torsional and lateral eigenmode oscillations for atomic resolution imaging of HOPG in air under ambient conditions*. Scientific Reports, 2022. **12**(1): p. 8981.
 183. Chen, Q., *et al.*, *Long-term electrical conductivity stability of graphene under uncontrolled ambient conditions*. Carbon, 2018. **133**: p. 410-415.
 184. Martinez-Martin, D., *et al.*, *Atmospheric contaminants on graphitic surfaces*. Carbon, 2013. **61**: p. 33-39.
 185. Androulidakis, C., *et al.*, *Non-Eulerian behavior of graphitic materials under compression*. Carbon, 2018. **138**: p. 227-233.
 186. Kazakova, O., V. Panchal, and T.L. Burnett, *Epitaxial Graphene and Graphene-Based Devices Studied by Electrical Scanning Probe Microscopy*. Crystals, 2013. **3**(1).
 187. Li, Z., *et al.*, *Effect of airborne contaminants on the wettability of supported graphene and graphite*. Nature Materials, 2013. **12**: p. 925.
 188. Choi, K., T.-J. Eom, and C. Lee, *Comparison of the removal efficiency for organic contaminants on silicon wafers stored in plastic boxes between UV/O₃ and ECR oxygen plasma cleaning methods*. Thin Solid Films, 2003. **435**(1): p. 227-231.
 189. Lee, W. and H. Jeon, *The effect of UV/ozone and HF on the removal of metallic impurities and the surface roughness on Si(100) substrate*. Journal of the Korean Physical Society, 1997. **30**: p. S307-S310.
 190. Seibert, S., *et al.*, *Origin of Ubiquitous Stripes at the Graphite–Water Interface*. Langmuir, 2020. **36**(27): p. 7789-7794.
 191. Pálinkás, A., *et al.*, *The composition and structure of the ubiquitous hydrocarbon contamination on van der Waals materials*. 2022. **Preprint** (10.48550/arXiv.2207.01057).

-
192. Endo, O., *et al.*, *Incommensurate Crystalline phase of n-Alkane Monolayers on Graphite (0001)*. *Journal of Physical Chemistry C*, 2011. **115**(13): p. 5720-5725.
 193. Li, B., *et al.*, *Polycyclic Aromatic Hydrocarbons Adsorption onto Graphene: A DFT and AIMD Study*. *Materials*, 2018. **11**(5).
 194. Diana, N., *et al.*, *Carbon materials with high pentagon density*. *Journal of Materials Science*, 2021. **56**(4): p. 2912-2943.
 195. Lu, Y.H., C.W. Yang, and I.S. Hwang, *Molecular Layer of Gaslike Domains at a Hydrophobic-Water Interface Observed by Frequency-Modulation Atomic Force Microscopy*. *Langmuir*, 2012. **28**(35): p. 12691-12695.
 196. Wang, S., *et al.*, *Adsorptive remediation of environmental pollutants using novel graphene-based nanomaterials*. *Chemical Engineering Journal*, 2013. **226**: p. 336-347.
 197. Xie, W., *et al.*, *Clean graphene surface through high temperature annealing*. *Carbon*, 2015. **94**: p. 740-748.
 198. Al-Mumen, H., *et al.*, *Singular Sheet Etching of Graphene with Oxygen Plasma*. *Nano-Micro Letters*, 2014. **6**(2): p. 116-124.
 199. Tuinstra, F. and J.L. Koenig, *Raman Spectrum of Graphite*. *The Journal of Chemical Physics*, 1970. **53**(3): p. 1126-1130.
 200. Berman, D., *et al.*, *Nanoscale friction properties of graphene and graphene oxide*. *Diamond and Related Materials*, 2015. **54**: p. 91-96.
 201. Sun, L., *et al.*, *Super-aligned carbon nanotube/graphene hybrid materials as a framework for sulfur cathodes in high performance lithium sulfur batteries*. *Journal of Materials Chemistry A*, 2015. **3**(10): p. 5305-5312.
 202. Song, Y., *et al.*, *Graphene-Perovskite Schottky Barrier Solar Cells*. *Advanced Sustainable Systems*, 2018. **2**(4).
 203. Bai, L., *et al.*, *Graphene for Energy Storage and Conversion: Synthesis and Interdisciplinary Applications*. *Electrochemical Energy Reviews*, 2019.
 204. Natter, N., *et al.*, *Plasma-Derived Graphene-Based Materials for Water Purification and Energy Storage*. *C*, 2019. **5**(2).
 205. McCann, E. and V.I. Fal'ko, *Landau-Level Degeneracy and Quantum Hall Effect in a Graphite Bilayer*. *Physical Review Letters*, 2006. **96**(8): p. 086805.
 206. Suárez Morell, E., *et al.*, *Electronic properties of twisted trilayer graphene*. *Physical Review B*, 2013. **87**(12): p. 125414.
 207. Sun, L.-F., *et al.*, *A comparison of the transport properties of bilayer graphene, monolayer graphene, and two-dimensional electron gas*. *Chinese Physics B*, 2013. **22**(7): p. 077201.
 208. Jeon, I.-Y., *et al.*, *Edge-carboxylated graphene nanosheets via ball milling*. *Proceedings of the National Academy of Sciences*, 2012. **109**(15): p. 5588-5593.
 209. Zhao, W., *et al.*, *Preparation of graphene by exfoliation of graphite using wet ball milling*. *Journal of Materials Chemistry*, 2010. **20**(28): p. 5817-5819.
 210. Hernandez, Y., *et al.*, *High-yield production of graphene by liquid-phase exfoliation of graphite*. *Nature Nanotechnology*, 2008. **3**(9): p. 563-568.
 211. Somani, P.R., S.P. Somani, and M. Umeno, *Planer nano-graphenes from camphor by CVD*. *Chemical Physics Letters*, 2006. **430**(1): p. 56-59.
 212. Hazra, K.S., *et al.*, *Thinning of multilayer graphene to monolayer graphene in a plasma environment*. *Nanotechnology*, 2010. **22**(2): p. 025704.

-
213. Zhao, G., *et al.*, *Synthesis of few-layered graphene by H₂O₂ plasma etching of graphite*. Applied Physics Letters, 2011. **98**(18): p. 183114.
 214. Seah, C.-M., *et al.*, *Mechanisms of graphene fabrication through plasma-induced layer-by-layer thinning*. Carbon, 2016. **105**: p. 496-509.
 215. Kim, D.C., *et al.*, *The structural and electrical evolution of graphene by oxygen plasma-induced disorder*. Nanotechnology, 2009. **20**(37): p. 375703.
 216. Mao, H., *et al.*, *Mildly O₂ plasma treated CVD graphene as a promising platform for molecular sensing*. Carbon, 2014. **76**: p. 212-219.
 217. Childres, I., *et al.*, *Effect of oxygen plasma etching on graphene studied using Raman spectroscopy and electronic transport measurements*. New Journal of Physics, 2011. **13**(2): p. 025008.
 218. Lee, G., *et al.*, *Precise control of defects in graphene using oxygen plasma*. Journal of Vacuum Science & Technology A, 2015. **33**(6): p. 060602.
 219. Ferrari, A.C. and J. Robertson, *Resonant Raman spectroscopy of disordered, amorphous, and diamondlike carbon*. Physical Review B, 2001. **64**(7): p. 075414.
 220. Zhang, D., *et al.*, *Origin of friction hysteresis on monolayer graphene*. Friction, 2022. **10**(4): p. 573-582.
 221. Lu, Y.-H., *et al.*, *Interface-Induced Ordering of Gas Molecules Confined in a Small Space*. Scientific Reports, 2014. **4**(1): p. 7189.
 222. Haghghian, N., *et al.*, *Rippling of graphitic surfaces: a comparison between few-layer graphene and HOPG*. Physical Chemistry Chemical Physics, 2018. **20**(19): p. 13327-3330.
 223. Rastei, M.V., B. Heinrich, and J.L. Gallani, *Puckering Stick-Slip Friction Induced by a Sliding Nanoscale Contact*. Physical Review Letters, 2013. **111**(8): p. 084301.
 224. Pálinkás, A., *et al.*, *The composition and structure of the ubiquitous hydrocarbon contamination on van der Waals materials*. Nature Communications, 2022. **13**(1): p. 6770.
 225. Eichhorn, A.L., M. Hoffer, and C. Dietz, *In-plane and out-of-plane interaction analysis of adsorbates on multilayer graphene and graphite by multifrequency atomic force microscopy*. Carbon, 2022. **200**: p. 124-133.
 226. Eichhorn, A.L., M. Hoffer, K. Bitsch and C. Dietz, *Adsorbate formation/removal and plasma-induced evolution of defects in graphitic materials*. Advanced Materials Interfaces, 2023. 2300256.
 227. Ferreira, E.H.M., *et al.*, *Evolution of the Raman spectra from single-, few-, and many-layer graphene with increasing disorder*. Physical Review B, 2010. **82**(12).
 228. Zhou, H., *et al.*, *Understanding Defect-Stabilized Noncovalent Functionalization of Graphene*. Advanced Materials Interfaces, 2015. **2**(17): p. 1500277.
 229. Paredes, J.I., A. Martínez-Alonso, and J.M.D. Tascón, *Early Stages of Plasma Oxidation of Graphite: Nanoscale Physicochemical Changes As Detected by Scanning Probe Microscopies*. Langmuir, 2002. **18**(11): p. 4314-4323.
 230. Paredes, J.I., A. Martínez-Alonso, and J.M.D. Tascón, *Multiscale Imaging and Tip-Scratch Studies Reveal Insight into the Plasma Oxidation of Graphite*. Langmuir, 2007. **23**(17): p. 8932-8943.

-
231. Solís-Fernández, P., *et al.*, *A Combined Experimental and Theoretical Investigation of Atomic-Scale Defects Produced on Graphite Surfaces by Dielectric Barrier Discharge Plasma Treatment*. The Journal of Physical Chemistry C, 2009. **113**(43): p. 18719-18729.
 232. Paredes, J.I., A. Martinez-Alonso, and J.M.D. Tascon, *Atomic vacancy-induced friction on the graphite surface: observation by lateral force microscopy*. Journal of Microscopy-Oxford, 2003. **210**: p. 119-124.
 233. Li, S., *et al.*, *Structure Evolution of Graphitic Surface upon Oxidation: Insights by Scanning Tunneling Microscopy*. JACS Au, 2022. **2**(3): p. 723-730.
 234. McCallum, C.L., *et al.*, *A Molecular Model for Adsorption of Water on Activated Carbon: Comparison of Simulation and Experiment*. Langmuir, 1999. **15**(2): p. 533-544.
 235. Butt, H.J. and M. Jaschke, *CALCULATION OF THERMAL NOISE IN ATOMIC-FORCE MICROSCOPY*. Nanotechnology, 1995. **6**(1): p. 1-7.
 236. Hutter, J.L. and J. Bechhoefer, *Calibration of atomic force microscope tips*. Review of Scientific Instruments, 1993. **64**(7): p. 1868-1873.
 237. Labuda, A., *et al.*, *Calibration of higher eigenmodes of cantilevers*. Review of Scientific Instruments, 2016. **87**(7): p. 073705.
 238. E. Sader, J., J. Chon, and P. Mulvaney, *Calibration of Rectangular Atomic Force Microscope Cantilevers*. Review of Scientific Instruments, 1999. **70**: p. 3967-3969.
 239. Sasaki, N. and M. Tsukada, *EFFECT OF THE TIP STRUCTURE ON ATOMIC-FORCE MICROSCOPY*. Physical Review B, 1995. **52**(11): p. 8471-8482.
 240. Wong, H.S., C. Durkan, and N. Chandrasekhar, *Tailoring the Local Interaction between Graphene Layers in Graphite at the Atomic Scale and Above Using Scanning Tunneling Microscopy*. ACS Nano, 2009. **3**(11): p. 3455-3462.
 241. Wong, H.S. and C. Durkan, *Shifting atomic patterns: on the origin of the different atomic-scale patterns of graphite as observed using scanning tunnelling microscopy*. Nanotechnology, 2012. **23**(18): p. 185703.
 242. Xu, P., *et al.*, *New scanning tunneling microscopy technique enables systematic study of the unique electronic transition from graphite to graphene*. Carbon, 2012. **50**(12): p. 4633-4639.
 243. Alam, A.U., M.M.R. Howlader, and M.J. Deen, *The effects of oxygen plasma and humidity on surface roughness, water contact angle and hardness of silicon, silicon dioxide and glass*. Journal of Micromechanics and Microengineering, 2014. **24**(3): p. 035010.
 244. Ondarcuhu, T., *et al.*, *Wettability of partially suspended graphene*. Scientific Reports, 2016. **6**: p. 24237.
 245. Cost, J.R., K.R. Janowski, and R.C. Rossi, *ELASTIC PROPERTIES OF ISOTROPIC GRAPHITE*. Philosophical Magazine, 1968. **17**(148): p. 851-+.
 246. Kimizuka, H. and H. Kaburaki, *Molecular dynamics study of the high-temperature elasticity of SiO₂ polymorphs: Structural phase transition and elastic anomaly*. Physica Status Solidi B-Basic Solid State Physics, 2005. **242**(3): p. 607-620.

12. Publications

- A.L. Eichhorn and C. Dietz, *Simultaneous Deconvolution of In-Plane and Out-of-Plane Forces of HOPG at the Atomic Scale under Ambient Conditions by Multifrequency Atomic Force Microscopy*. *Advanced Materials Interfaces*, 2021. 8(20).
- A.L. Eichhorn and C. Dietz, *Torsional and lateral eigenmode oscillations for atomic resolution imaging of HOPG in air under ambient conditions*. *Scientific Reports*, 2022. 12(1): p. 8981.
- A.L. Eichhorn*, M. Hoffer* and C. Dietz, *In-plane and out-of-plane interaction analysis of adsorbates on multilayer graphene and graphite by multifrequency atomic force microscopy*. *Carbon*, 2022. 200: p. 124-133.
- A.L. Eichhorn*, M. Hoffer*, K. Bitsch and C. Dietz, *Adsorbate Formation/Removal and Plasma-Induced Evolution of Defects in Graphitic Materials*, *Advanced Materials Interfaces*, 2023. 2300256.

* These authors contributed equally.

13. Curriculum Vitae

Persönliche Daten

Name Anna Lisa Eichhorn (geb. Hawlitschek)

Ausbildungsweg

- 01/2019 – 02/2023 **Promotionsstudium an der TU Darmstadt**
Thesis: „*Multifrequency atomic force microscopy for the in-plane and out-of-plane nanomechanical characterization of graphitic surfaces*“
- 10/2015 – 10/2018 **Master of Science in „Materials Science“ an der TU Darmstadt in Kooperation mit der Merck KGaA**
Thesis: „*Microtopographic Characterization and Micromechanical Analysis of Novel Liquid Crystal Materials via Atomic Force Microscopy*“
- 10/2012 – 11/2015 **Bachelor of Science in Materialwissenschaften an der TU Darmstadt**
Thesis: „*Subsurface-Detektion und Charakterisierung von superparamagnetischen Nanopartikeln mittels magnetischer Rasterkraftmikroskopie*“

14. Acknowledgments/Danksagung

Zuerst möchte ich Christian Dietz danken für die Möglichkeit, meine Doktorarbeit unter seiner Betreuung schreiben zu dürfen. Herzlichen Dank für die großartige Unterstützung während meiner Zeit als Doktorandin. Ich habe enorm viel von Christian gelernt und die konstruktive Zusammenarbeit immer sehr geschätzt. Vielen Dank, dass du mich für die Rasterkraftmikroskopie begeistert und motiviert hast, diese Arbeit zu schreiben!

Ich möchte mich außerdem bei Robert Stark dafür bedanken, dass ich mein Promotionsthema in seinem Fachgebiet bearbeiten durfte. Vielen Dank für die Unterstützung meines beruflichen Werdeganges!

Vielen Dank an Regine von Klitzing, Ralph Krupke und Karsten Durst, dass Sie sich die Zeit genommen haben Teil meiner Prüfungskommission zu sein.

Für die stets angenehme Arbeitsatmosphäre, möchte ich mich ganz herzlich bei allen aktuellen und ehemaligen Mitgliedern des Fachgebiets *Physics of Surfaces* bedanken. Mein besonderer Dank gilt Alena, Julia, Marcus und Lukas für die freundliche Aufnahme ins Team der PoS-Doktoranden. Ich habe viel von euch gelernt und bin euch für die fachliche aber auch menschliche Unterstützung sehr dankbar. Außerdem möchte ich Asma und Anahid danken für die angenehme gemeinsame Bürozeit während meiner ersten 1,5 Jahre der Doktorandenzeit. Herzlichen Dank an Alena, die mich nach meinem COVID-19-bedingten Umzug in Büro 206 sehr lieb aufgenommen hat. Für die Arbeitszeit unter besonderen Umständen während der Pandemie, möchte ich mich insbesondere bei Alena und Julia bedanken. Das Wissen, jederzeit auf eure Unterstützung bauen zu können, war enorm wertvoll. Vielen Dank, für die stets lösungsorientierte Zusammenarbeit! Mein Dank gilt auch Melanie Butin und Simone Liesenberg, auf deren Unterstützung ich bei administrativen Fragestellungen stets bauen konnte.

Bedanken möchte ich mich außerdem bei allen Studierenden, die ihre Abschlussarbeiten oder Forschungspraktika unter meiner Betreuung absolviert haben. Insbesondere möchte ich Niklas danken, der mich im Rahmen einer HiWi-Tätigkeit bei der Programmierung eines Matlabcodes unterstützt hat. Vielen Dank für die konstruktive Zusammenarbeit! Außerdem möchte ich Katharina danken für ihre hervorragende experimentelle Arbeit am Raman und am AFM während ihrer Bachelorthesis. Ihre Ergebnisse haben maßgeblich zur Anfertigung des in Kapitel 5 gezeigten Manuskripts beigetragen. Mein herzlicher Dank gilt auch Marvin, der sowohl experimentell als auch bei der Interpretation seiner Forschungsergebnisse außergewöhnliches

Talent bewies. Die in Kapitel 4 gezeigte Publikation ist ebenso ein Resultat dieser konstruktiven Zusammenarbeit wie auch das in Kapitel 5 gezeigte Manuskript.

Zudem möchte ich Marvin, Martin und Alena für das Korrekturlesen meiner Dissertation danken.

Außerdem möchte ich mich noch bei Tobi bedanken, auf dessen Unterstützung ich mich schon während des Studiums immer verlassen konnte. Danke, dass du mich in die Photolithographie eingewiesen und in diesem Zusammenhang Experimente für mich gemacht hast, auch wenn diese letztendlich nicht Teil dieser Thesis wurden.

Mein Dank gilt zudem meinen Kolleginnen und Kollegen, die mich stets darin bestärkt haben meine Promotion zu Ende zu bringen und mir dafür den Rücken freigehalten haben. Insbesondere vielen Dank an Katrina und Stefanie für den mentalen Support.

Ganz herzlich möchte ich mich abschließend noch bei meiner Familie bedanken. Ohne eure Unterstützung wäre diese Arbeit nie entstanden. Danke, dass ihr immer für mich da seid und mich aus kurzen Tiefs ganz schnell wieder herausgeholt habt. Insbesondere vielen Dank an Thomas für deine Unterstützung in jeglicher Hinsicht.